UNIVERSITY OF STRATHCLYDE
Department of Physics

Organic Lasers and Nanostructured Organic Films for Hybrid Integration

by

Johannes Hermann Ludwig Herrnsdorf

A thesis presented in fulfilment of the
requirements for the degree of
Doctor of Philosophy

November 2012

Declaration of Authorship

This thesis is the result of the author's original research. It has been composed by the author and has not been previously submitted for examination which has led to the award of a degree.

Signed: _____

Date: _____

Frontispiece

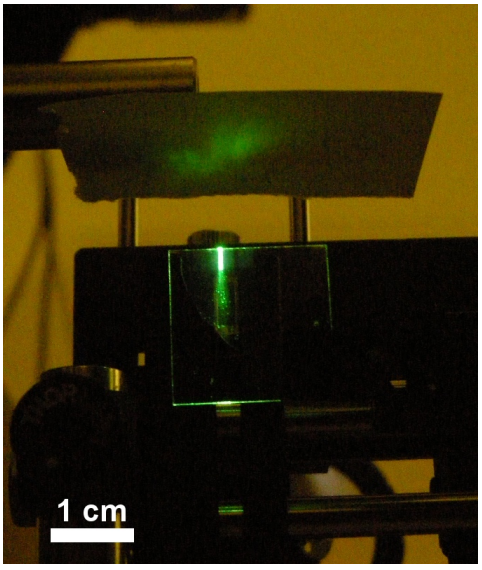

Random laser action in an organic semiconductor film under stripe excitation.

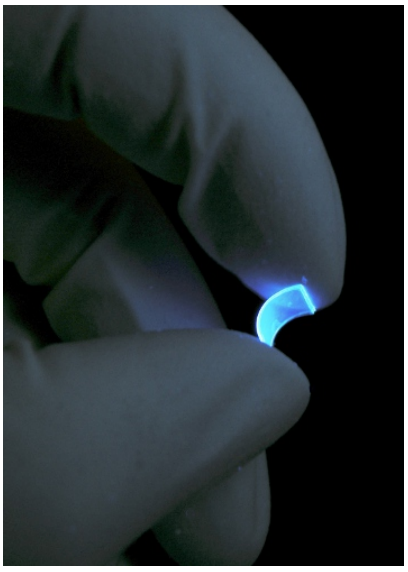

A mechanically flexible blue-emitting distributed feedback laser under ultraviolet illumination.

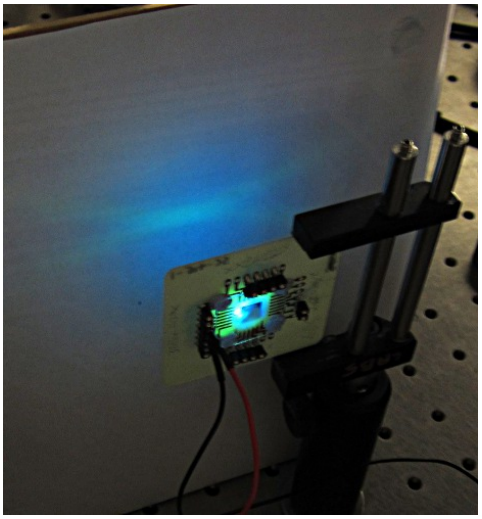

Fan-shaped emission from a hybrid organic/inorganic photonic crystal light emitting diode.

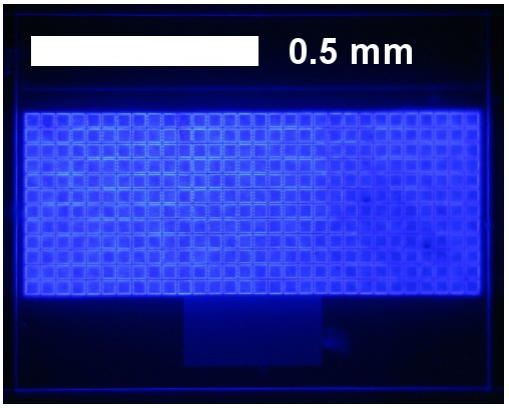

Micrograph of a micro-light-emitting diode array for pumping of organic lasers.

Abstract

Light emitting polymers (LEPs) are a promising category of organic materials for photonic applications owing to their potential for simple fabrication and availability of materials emitting across the whole visible spectrum. LEPs are already exploited commercially in the case organic light emitting diodes and their interesting properties for colour conversion and as laser gain material are under investigation.

To keep the LEPs' benefit of simple and low-cost fabrication, integration onto inorganic semiconductor devices such as in particular gallium nitride light emitting diodes (LEDs) is an important research topic. In this thesis, developments towards integration of organic devices onto micro-pixellated flip-chip LEDs are presented. This particular format may be beneficial for applications such as displays, various sensing schemes and data transmission owing to spatio-temporal control, high modulation bandwidths and potential for simple integration with complementary metal oxide semiconductor electronics.

The properties of LEP films as optical gain medium were assessed on smooth and corrugated substrates. In the former case, random laser action (RL) was observed which is attributed to the high optical gain delivered by these materials. Arguments are presented suggesting that RL may be very common in high gain media. In the latter case, mechanically flexible distributed feedback lasers were fabricated in a very simple way and their properties including operational lifetime were characterised.

Nano-patterned LEP films for colour conversion of LED light exhibited strong modification of the LEP emission due to the photonic crystal (PhC) effect of the periodic pattern. PhCs allow tailoring of the emission properties by appropriate design of the nano-pattern and they can be created relatively easy in organic films. Furthermore, the modulation bandwidth of an organic PhC film excited by micro-LEDs was measured to be 168 MHz and was mainly limited by the inorganic LED. This underpins the potential of LEPs for communications applications.

The suitability of micro-LEDs in flip-chip format as pump source for organic semiconductor lasers was investigated. For this purpose, stripe-shaped arrays of micro-LEDs were developed that were employed for the demonstration of the first micro-LED pumped polymer laser.

Acknowledgements

It has been a great pleasure to work in Professor Martin Dawson's team and I am grateful for him enabling me this opportunity. A lot of the work presented in this thesis is a result of very close teamwork between Nicolas Laurand, Benoit Guilhabert, Yujie Chen and myself. I can only hope that each of us will experience an as fruitful working environment in future. Other people at the Institute of Photonics that I have been working with closely on various aspects of my project are Erdan Gu, Jonathan McKendry, Zheng Gong and David Massoubre. In general I found that the Institute of Photonics provided a very friendly atmosphere and thanks go to each of its members.

A big thanks goes to Yue Wang, Georgios Tsiminis, Graham Turnbull and Ifor Samuel from the University of St. Andrews for the enthusiasm they put into our collaboration. This work would not have been possible without the supply with materials by Alexander Kanibolotsky, Allan Mackintosh and Peter Skabara from the Chemistry Department of the University of Strathclyde. Being part of the HYPIX project was an inspiring experience and at this point, the Engineering and Physical Sciences Research Council shall be acknowledged for their funding of my PhD project and also of a three month visit to Nanyang Technological University (NTU).

At the end of my PhD I had the opportunity to visit the Luminous! Centre for Lighting and Displays at NTU in Singapore. Results of our joint work are summarised in appendix C. Thanks go to Professors Martin Dawson, Volkan Demir, Sun Xiaowei and Sun Handong for making this possible. The people at Luminous! welcomed me very warm-heartedly and I would like to highlight my closest co-workers, Gao Yuan, Evren Mutlugun and Ta Van Duong.

I would also like to thank my former supervisors during my undergraduate studies at ETH Zürich, in particular Thomas Südmeier, Aude-Reine Bellancourt, Deran Maas, Ursula Keller, Taryl Kirk and Danilo Pescia. My fellow students and friends of that time deserve mentioning here as well.

Then, I would like to express my gratitude to all the people that triggered and supported my interest in physical sciences early on and helped me to develop fundamental skills. Among these are my former teachers, Udo Wlotzka, Jürgen Radke, Herr Hasse, Ute Wille, Frau Thiel and the members of the Volkssternwarte Hagen.

Probably the most important thanks goes to my family. If I am gifted with anything, then it surely is the surrounding I was brought up in. Therefore, I feel very grateful towards all my relatives and in particular to my parents, Johannes and Rita Herrnsdorf.

Contents

List of Figures

List of Tables

Abbreviations

ASE	**A**mplified **S**pontaneous **E**mission
BER	**B**it **E**rror **R**ate
CIE	**C**ommission **I**nternationale de l'**É**clairage
CMOS	**C**omplementary **M**etal **O**xide **S**emiconductor
CQD	**C**olloidal **Q**uantum **D**ot
CW	**C**ontinuous **W**ave
DC	**D**irect **C**urrent
DBR	**D**istributed **B**ragg **R**eflector
DFB	**D**istributed **F**eed**b**ack
DFT	**D**ensity **F**unctional **T**heorem
DPN	**D**ip **P**en **N**ano-Lithography
EQE	**E**xternal **Q**uantum **E**fficiency
FRET	**F**örster **R**esonant **E**nergy **T**ransfer
FWHM	**F**ull **W**idth **H**alf **M**aximum
GUI	**G**raphical **U**ser **I**nterface
HOMO	**H**ighest **O**ccupied **M**olecular **O**rbital
HYPIX	Name of the research project to which this work contributed
IQE	**I**nternal **Q**uantum **E**fficiency
IR	**I**nfra**r**ed
LC	**L**iquid **C**rystal
LD	**L**aser **D**iode
LED	**L**ight **E**mitting **D**iode
LEP	**L**ight **E**mitting **P**olymer
LUMO	**L**owest **U**noccupied **M**olecular **O**rbital
MIMO	**M**ultiple **I**nput **M**ultiple **O**utput

MOSFET	**M**etal **O**xide **S**emiconductor **F**ield **E**ffect **T**ransistor
MW	**M**olecular **W**eight
NIL	**N**ano **I**mprint **L**ithography
NW	**N**ano**w**ire
OFET	**O**rganic **F**ield **E**ffect **T**ransistor
OLED	**O**rganic **L**ight **E**mitting **D**iode
OPO	**O**ptical **P**arametric **O**scillator
OSL	**O**rganic **S**emiconductor **L**aser
OSL	**O**rganic **S**olid-state **L**aser
PAG	**P**hoto **A**cid **G**enerator
PCB	**P**rinted **C**ircuit **B**oard
PDI	**P**oly**d**ispersity **I**ndex
PFT	**P**ower **F**ourier **T**ransform
PhC	**Ph**otonic **C**rystal
PL	**P**hoto**l**uminescence
PLQY	**P**hoto**l**uminescence **Q**uantum **Y**ield
PMT	**P**hoto**m**ultiplier **T**ube
POF	**P**olymer **O**ptical **F**ibre
PR	**P**hoto**r**esist
PSS	**P**atterned **S**apphire **S**ubstrate
QD	**Q**uantum **D**ot
QW	**Q**uantum **W**ell
RCLED	**R**esonant **C**avity **L**ight **E**mitting **D**iode
RGB	**R**ed **G**reen **B**lue
RL	**R**andom **L**aser Action
SPAD	**S**ingle **P**hoton **A**valanche **D**etector
TE	**T**ransverse **E**lectric
TM	**T**ransverse **M**agnetic
UV	**U**ltra**v**iolet
VCSEL	**V**ertical **C**avity **S**urface **E**mitting **L**aser
VECSOL	**V**ertical **E**xternal **C**avity **S**urface Emitting **O**rganic **L**aser
VLC	**V**isible **L**ight **C**ommunications
VSL	**V**ariable **S**tripe-**L**ength Method

WGM	**W**hispering **G**allery **M**ode

Materials

AK*xyz***DCM***n*	Material batch, see section 3.1.2
Alq3	Aluminum tris(quinolate)
BBEHP-PPV	Poly[2,5-bis(2',5'-bis(2"-ethylhexyloxy)phenyl)-p-phenylenevinylene]
BT	Benzothiadiazole
CHDG	1,4-cyclohexanedimethanol diglycidyl ether
CHDV	1,4-cyclohexyldimethanol divinyl ether
DCM (solvent)	Dichloromethane
DCM (dye)	4-(dicyanomethylene)-2-methyl-6-(4-dimethylaminostyryl)-4H-pyran
DCM2	4-(dicyanomethylene)-2-methyl-6-(julolidin-4-yl-vinyl)-4H-pyran
DNB	Dinitrobenzene
DNT	2,4-dinitrotoluene
NOA	Norland Optical Adhesive
PEDOT	Poly(ethylene dioxythiophene)
PFO	Polyfluorene
PM	Pyrromethane
PMMA	Poly(methyl methacrylate)
PPP	Poly(para phenylene)
PPV	Poly(phenylene vinylene)
PSS	Poly(styrene sulfonate)
PT	Poly(thiophene)
R6G	Rhodamine 6G
SU8	Trade name of a photoresist
T3	Tris(trifluorene)truxene
T4	Tris(tetrafluorene)truxene
TNT	Trinitrotoluene
TOPO	Trioctylphosphine oxide
YAG	Yttrium Aluminum Garnet

Meiner Familie gewidmet

Part I

Introduction

Chapter 1

Hybrid Organic/Inorganic Light Sources

Throughout human history there has been a great desire to control light which has had a dramatic impact on the way we live. At the time of writing this thesis, a major change in lighting technology is taking place. Driven by the need for versatile and energy-efficient light sources, incandescent light generation that has been used for centuries is increasingly being replaced by luminescent and phosphorescent light emitters. This does not just mean a simple change in the mechanism of light generation, but also an astonishing degree of control on the emitted light's properties is gained, including colour and directionality but also rather subtle aspects such as polarisation and coherence. As a consequence, today's state-of-the-art light sources are not only suitable for lighting, but may serve a range of applications including data transmission, displays, optical manipulation, medical diagnosis, biological and chemical sensing, just to mention those most relevant for the particular work presented in this thesis. The development of new devices is proceeding rapidly and offers a rich working ground for scientists and engineers.

In particular, an area of great attention is that of Gallium Nitride based light emitting diodes (LEDs). Nitride semiconductors offer LEDs at wavelengths from near ultra violet (UV) to yellow/amber. However, GaN devices suffer from a problem referred to as efficiency droop: the internal quantum efficiency (IQE) of these LEDs can be very high (e.g. IQE of 70 % has been reported at room temperature [1]) at a certain optimum current, but drops drastically if operated below or above [2]. There is also a strong wavelength dependence of the LED efficiency. In general, the most efficient GaN LEDs operate in the blue near 450 nm. Green/yellow devices have a lower peak quantum efficiency (typically a third of that of blue LEDs fabricated in the same way [3]) and

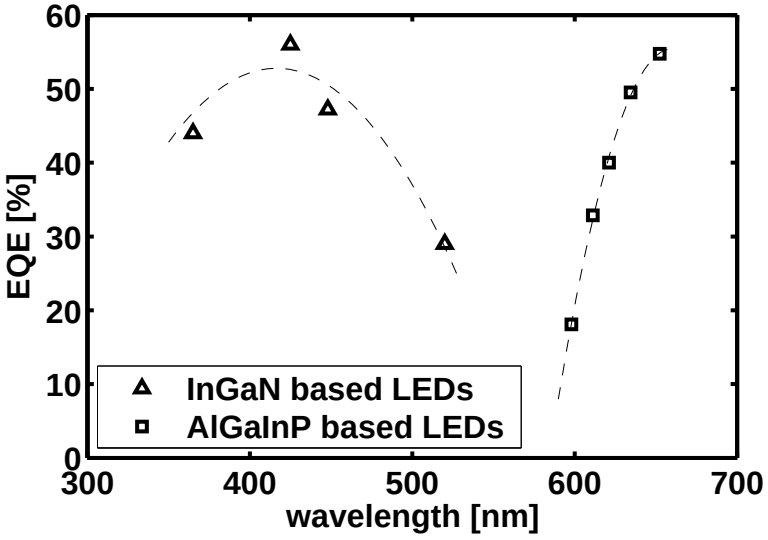

FIGURE 1.1: External quantum efficiencies (EQE) of inorganic high power (>1 W) visible LEDs showing the lack of efficient inorganic LEDs in the green spectral region. This graph is a recreation of figure 2 in reference [6] using data from references [6–9]. The dashed lines are a guide to the eye.

suffer from a more pronounced droop [4]. As a result, green LEDs available for the work here deliver about a fifth of the output power of similar blue LEDs under typical operating conditions [5]. The reasons for the droop are not fully understood and this is a much-debated research topic of nitride semiconductor science [2].

The relatively poor efficiency of green/yellow GaN LEDs and the fact that phosphide based LEDs are only efficient in the red mean that there is a spectral gap (illustrated in figure 1.1) – the so-called "green gap" – for which no high performance inorganic LEDs are available. Such a spectral gap does not exist for organic chromophores. Light emitting polymers (LEPs) have been shown to allow high photoluminescence quantum yields (PLQY, 80 % and higher are not uncommon) from near UV to near infrared (IR), covering more than the entire visible spectrum. Electroluminescent polymeric devices are possible and organic LEDs (OLEDs) are already used commercially, e.g. in mobile phone displays. However, low carrier mobility and the typically phosphorescent nature of OLED emission (see sections 2.1 and 2.1.1 below) limit their usefulness for certain purposes, in particular if a fast response is required. Therefore, the green/yellow spectral gap may suitably be accessed with hybrid organic/inorganic devices, where efficient blue GaN LEDs are equipped with a colour converting organic overlayer. A particular benefit of this approach is that the overlayer can be structured by very simple means, such as nano imprint lithography (NIL), that do not require a clean room facility. These structures can for example be cavities or photonic crystals (PhC) that modify the emission. Table 1.1 gives an overview how the different LED types compare to each other.

Inorganic	Hybrid	Organic
✓ Established technology	✓ Simple fabrication/processing	✓ Established technology
✓ High electroluminescent efficiency	✓ Whole visible wavelength range efficiently accessible	✓ Simple fabrication/processing
✓ Fast optical data transmission	✓ Fast optical data transmission	✓ Whole visible wavelength range efficiently accessible
✗ Efficiency strongly wavelength-dependent	✗ Photodegradation issues	✗ Photodegradation issues
✗ Hard to nanopattern		✗ Present technology probably not suited for data transmission

TABLE 1.1: Overview of various benefits and drawbacks of purely organic, inorganic and hybrid devices.

The hybrid organic/inorganic approach has also been promising in the field of organic solid state lasers (OSLs). Up to now it has not been possible to operate an organic laser by current injection, due to a combination of reasons explained in section 2.3. All OSLs so far have been optically pumped, often using bulky, expensive and difficult-to-maintain solid state or gas lasers. More compact pump sources have recently been used as well (c.f. section 2.2.1.5) including in particular GaN laser diodes [10–15] and LEDs [16]. This latter class of hybrid organic/inorganic device is currently a very promising approach to circumvent the difficulties encountered with electrical injection and may be an important step towards commercialisation of OSLs.

1.1 Outline of this Thesis

The main goal of the work presented in this thesis is to develop hybrid GaN/organic polymer devices using micro-pixellated arrays of LEDs as the inorganic part. The rest of this chapter describes the motivation for this specific format. Chapter 2 explains the physics of LEPs and gives a literature review on OSL performance. In chapter 3 the material properties (including random laser action) of the specific gain media available for this work are discussed and chapter 4 presents mechanically flexible OSLs made from these materials. Hybrid devices are presented in chapters 5 and 6. Chapter 5 reports a PhC LED where the PhC structure is in the organic overlayer. Work towards a micro-LED pumped OSL is presented in chapter 6. Concluding remarks can be found in chapter 7.

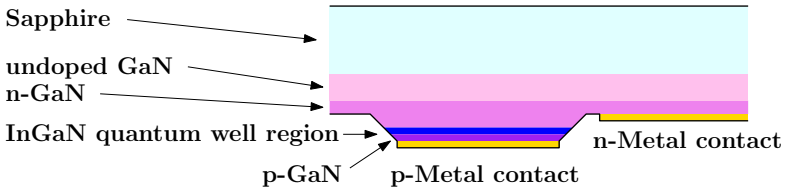

FIGURE 1.2: Cross-sectional schematic of a GaN flip-chip LED.

1.2 Micro-pixellated Gallium Nitride Light Emitting Diodes

For a great variety of purposes (e.g. displays, optical neuro-stimulation, optical trapping) it is beneficial or even mandatory to have spatio-temporal control of the excitation light. One way to achieve this is via a pattern-programmable array of sub-millimetre sized LEDs [17, 18]. When the LEDs are in the sub-100 μm size regime, they are typically referred to as "micro-LEDs". Micro-LEDs in top-emitting format can be connected in a matrix-addressable fashion allowing functional micro-displays [17]. However, in this case, complex two-dimensional patterns require rapid scanning through the rows of the array, i.e. not all LEDs are turned on at the same time.

True pattern programmability can be achieved if the LED array is in so-called "flip-chip" format, i.e. the LED light is emitted through a sapphire window on which the LED structure was grown [18]. A schematic of a GaN LED in flip-chip format is given in figure 1.2. Current spreading across the active area is achieved by having the p-metal contact extending across the entire LED mesa. In comparison to the top-emitting format, uniform current spreading is achieved more easily and in particular without employing indium tin oxide. Furthermore, the p-metal contact also acts as a back-reflector for the LED emission. An important benefit of flip-chip LED arrays is that they can be bump-bonded to a CMOS (complementary metal oxide semiconductor) control circuit, thus providing a highly compact and versatile device in chip format [18–20]. A micrograph demonstrating pattern generation by CMOS-controlled flip-chip micro-LEDs is shown in figure 1.3.

1.2.1 Lab-on-a-chip devices for Biosensing and Chemosensing

In the life sciences, there exists an abundance of measurement techniques that use fluorescent tags [21]. Particular types of cells, proteins or DNA sequences, for example, can be probed using selective tags [21, 22]. Optical techniques have advanced to a stage that allows the study of processes within living subjects [23] and can even be used to stimulate or inhibit certain processes [24]. There is also potential for widespread use of fluorescence-based techniques in the diagnosis of diseases and for this particular purpose

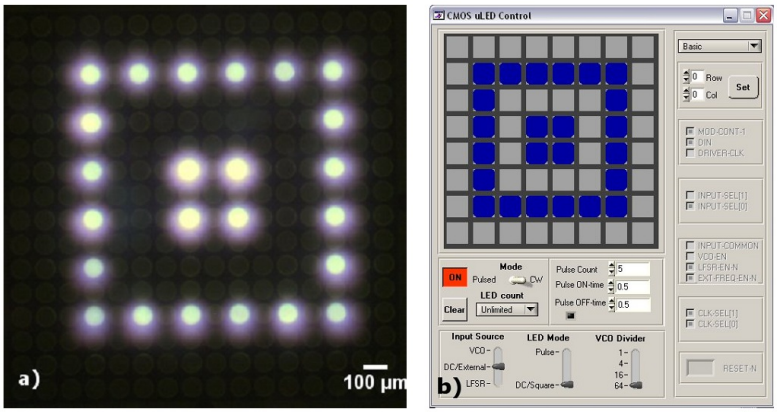

FIGURE 1.3: *a)* Output pattern from a CMOS-controlled micro-LED array and *b)* Software interface used to control the device.

it is very important to move away from bulky and expensive systems that were used for the pioneering work in the area [25], making the technology affordable and usable for any hospital or even general practitioners. Pattern-programmable LED-arrays can form the basis of a simple device that allows quick analysis of specimens. Due to the chip-format of flip-chip bonded LED-arrays, such devices can be very compact, low cost and easy to maintain in comparison to traditional excitation sources such as solid state lasers or gas-discharge lamps [5, 25]. A possible implementation would be to have microfluidic channels or wells aligned with the array, allowing selective probing of a single channel/well by switching on the LED underneath. Since it is possible to generate picosecond pulses with GaN micro-LEDs [20], there is the possibility to not only detect an on/off fluorescence signal but also record the fluorescence lifetime [26, 27]. In both cases (CW and pulsed excitation), the detector can be embedded on the same CMOS chip that controls the LED array, using suitable CMOS technology such as single photon avalanche detectors (SPADs) [27]. A vision for such a compact lab-on-a-chip system is shown in figure 1.4. Initial work towards integration of micro-fluidic systems onto micro-LED arrays was done by A. Zarowna-Dabrowska [5]. Colour converters can be used to match the absorption of fluorescent tags. In particular, individual LEDs in an array can be overcoated with different colour converters enabling simple fabrication of a device capable of probing numerous tags at once. Suitable nanostructures in the colour converting layer, or organic lasers, can add the benefit of directional emission and narrow spectral linewidth of the excitation light as compared to the underlying flip-chip LED.

One area of rapid development is the optical monitoring and stimulation of neural activity. For this purpose, compact array-format devices are particularly interesting [28] and proof-of-concept results using a matrix-addressable micro-LED arrays have been published [29]. In general, for applications such as neuro-stimulation that require the light source to be in contact with soft tissue, it may be desirable to have a mechanically

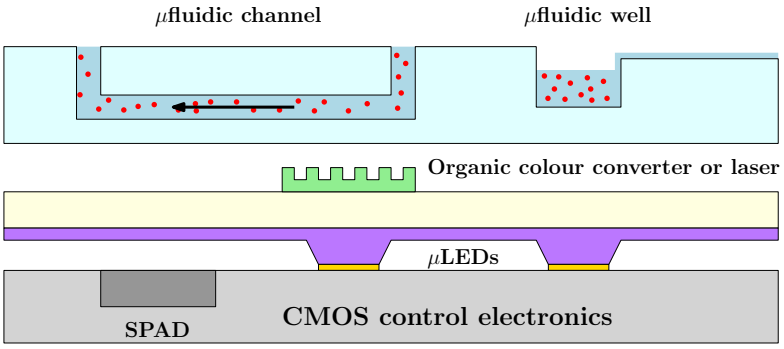

FIGURE 1.4: Vision for a lab-on-a-chip biosensing system based on CMOS controlled micro-LEDs (see e.g. [27]).

flexible optical device that can conform to an uneven specimen surface. Exciting recent work by Rogers *et al.* [30, 31] has shown that GaN and other micro-LEDs can indeed be fabricated in such flexible format. Generally though, flexible photonics remains a key domain of functional organic materials.

A sensing scheme that is particularly suited for the hybrid organic/inorganic approach is explosive detection using fluorescent polymers. The vast majority of explosive devices emit vapours containing trinitrotoluene (TNT), 2,4-dinitrotoluene (DNT) and dinitrobenzene (DNB) molecules. These nitroaromatic compounds are strongly electron-negative and if they enter the polymer matrix of a LEP they will induce a non-radiative relaxation pathway, thus quenching the LEP emission [32–34]. In general, very low quantities of TNT, DNT or DNB are required to see a measurable effect. High sensitivity is obtained if the LEP is photo-pumped above laser threshold [34, 35] (see figure 1.5b), but also below threshold reductions in luminescence intensity and fluorescence lifetime are pronounced enough for usage in practical devices [32, 36]. A compact system for DNB detection based on fluorescence of a micro-LED pumped LEP and CMOS-SPADs has been demonstrated [36] (see figure 1.5a for a photo of the setup).

While this section has focussed on sensing techniques, it is worth noting that the forces generated by optical fields can be exploited to manipulate particles and cells. The intensity of LEDs is too low for conventional optical tweezers but when the specimen is placed in a so-called photo-conductive cell (see references [5, 37, 38] for details), the change in electric field pattern and the fluid motions triggered by illumination with LED light lead to trapping of micron-sized particles at the illuminated spot. Such opto-electronic tweezing has been demonstrated using green-emitting GaN micro-LEDs [5, 38].

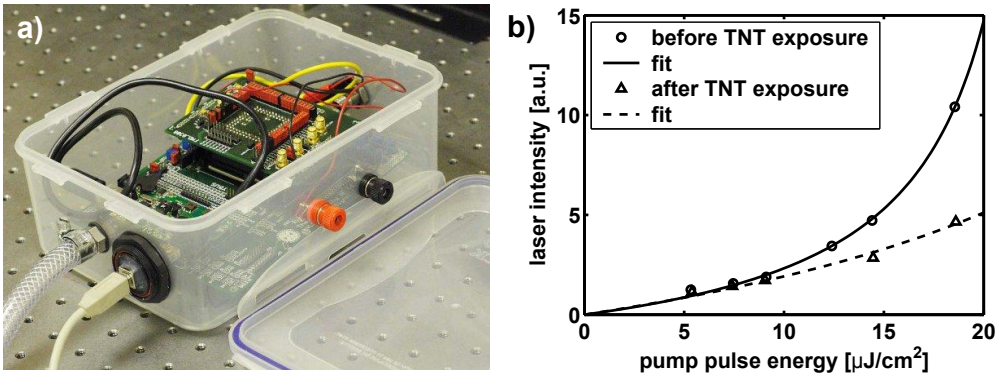

FIGURE 1.5: Illustration of chemosensing using LEPs: *a)* Photographic image of a compact explosive detection system utilising a CMOS-controlled micro-LED pumped LEP film and CMOS SPAD detectors [36]. *b)* Impact of TNT exposure on the power transfer characteristics of an OSL based on an LEP that is used in this thesis (see section 3.1.2). The data is taken from [35] and was here fitted with the soft threshold model (4.2) from section 4.1.2.1 for better clarity.

1.2.2 Micro-LEDs for Visible Light Communications

In communications the amount of data transmission and demand for bandwidth keep increasing steadily at exponential rates. Traditional technologies such as radio-frequency wireless connections and electrical wired networks are already exploited close to their physical limits. Also, they may be impractical or unfavourable for certain applications, e.g. due to risk of sparking when metallic network cables are installed alongside mains cables, an issue that is not present in the case of optical fibres. It is therefore attractive to study the usage of optical frequency carriers for data transmission.

Long-range data transmission is already dominated by infra-red (IR) technology and IR-Vertical Cavity Surface Emitting Lasers (VCSELs) are increasingly used for optical interconnects in high performance computers. However, IR-based short- to mid-range communications is problematic due to factors like cost of components, relatively poor mechanical stress tolerance of silica optical fibres, requirement for high-precision alignment and eye-safety concerns. For example, in cars, aeroplanes or private houses it is arguably more practical to use polymer optical fibre (POF) for wired data transfer, taking advantage of its low weight, low cost and ease of installation. Due to strong attenuation of IR wavelengths it is favourable to operate POF in the visible spectral range. In particular, the attenuation minimum of conventional PMMA fibre is at a wavelength of approximately 530 nm [39].

There is also interest in future replacement of, or complementary technology to, radio-frequency wireless communications. Current research is investigating the feasibility of THz [40, 41], IR [42, 43] and visible [44] frequency free-space optical communications. THz radiation does not scatter as much as other wavelengths on dust particles and

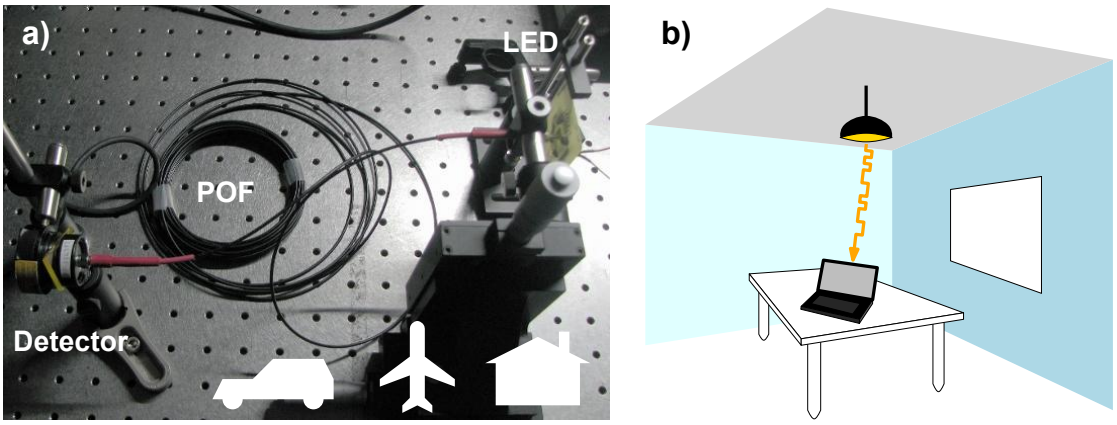

FIGURE 1.6: *a)* Transmission of LED light through POF, with applications in, for example, vehicles, aeroplanes and buildings. *b)* Vision for free-space VLC using LED room lighting.

droplets [41]. Owing to the rapid development of THz technology driven by other applications such as remote sensing, compact sources and detectors are available [40]. On the downside, it is challenging to install efficient non-line-of-sight links and THz radiation can be strongly absorbed by water.

Wireless IR optical links were in fact the first demonstration of optical indoor free-space communications [42]. An important drawback of IR wireless is that the detectors are sensitive to room light which causes the room lighting to be a strong source of noise [45]. A key idea of visible light free-space communications is to use the room-lighting itself for data transmission [44]. If incandescent light bulbs are replaced by LEDs this is readily feasible because GaN (micro-)LEDs can be modulated at high speed [46, 47]. A major challenge might be the uplink from the client that is receiving data from the room lighting. The most likely candidate so far is to provide the uplink by traditional radio frequency wireless transmission, i.e. the visible data transmission will be installed complementary to traditional technology. Other ideas include the use of modulated retro-reflectors. Table 1.2 gives a brief comparison of THz, IR and visible themes for short- to mid-range communications. Free-space VLC and transmission of LED light through POF are illustrated in figure 1.6.

1.2.3 Other Applications

If asked for a synonym for "micro-LED array" one would probably describe it as a micro-display. It is only natural to see these devices as an addition to display technology. Arrays with a pitch of a few tens of microns allow a significantly higher pixel density compared to established technology and the compact nature of CMOS-controlled LED arrays makes them suitable for portable head-up displays [48]. Since one display is made from a single wafer, it is by default monochromatic. Sophisticated epitaxial structures

THz	IR	VLC
✓ Not susceptible to atmospheric perturbations – In particular dust and fog ✓ Potential for high level of security ✗ Waveguides have high losses ✗ Non line-of-sight transmission may require additional installations such as reflective wall paper	✓ Low-loss fibres are available ✓ Low atmospheric attenuation for 9-13 μm ✓ Mature VCSEL technology ✗ Susceptible to atmospheric perturbations ✗ Available fibres are best suited for long range networks ✗ Room lighting causes considerable noise	✓ Can easily be implemented in solid state lighting ✓ High and easily controllable security of indoor wireless networks ✓ Suitable for POF ✗ Bidirectional operation can be problematic ✗ Susceptible to atmospheric perturbations

TABLE 1.2: Overview of various benefits and drawbacks of possible future wireless or cabled short range data transmission schemes.

with green/amber quantum wells (QW) as main emitters and wider bandgap QWs as so called "electron reservoir layers" [49] allow limited colour control via the current density [50], but as of yet a true red green blue (RGB) micro-display can only be achieved using colour converting overlayers [51]. Due to incomplete absorption of pump light and saturation of the colour converter, the CIE (Commission internationale de l'éclairage) coordinates of each pixel will in general depend on the wavelength of the inorganic LED and the drive current. Good colour fidelity can be achieved by overcoating UV LEDs with suitable organic emitters [52].

Finally, I would like to mention the suitability of blue/UV micro-LEDs for maskless lithography where the the LED light is imaged through a de-magnification system onto photoresist, allowing for sub-micron spatial resolution [53]. Colour converting overlayers will probably not be of much use for this purpose but it is an important application of micro-LEDs in general.

1.3 Hybrid Devices Based on Micro-LEDs

Colour conversion of blue or UV LED light is already done industrially. The vast majority of available white-light LEDs consists of blue (or UV) LEDs with a phosphorescent overlayer (typically Yttrium Aluminum Garnet – YAG – with a grain size comparable to the diameter of micro-LEDs). This approach yields simple device structure, longevity of the whole device and is perfectly suitable for current applications such as torches. However, when LEDs are to be used in a broader range of applications, the current technology has important limitations such as poor colour rendering or unsuitable colour

temperature. Furthermore, the long radiative lifetime of phosphors is a serious problem for any application needing fast switching. With some phosphor based white LEDs, it is actually possible to recognise the phosphor afterglow upon switch-off by eye. Hence, there is general interest in research on suitable colour converters for future LEDs.

1.3.1 Solution Processible Materials

The most widespread phosphor for white LEDs, YAG, is an inorganic polycrystalline material. While this has some benefits such as a good resistance against photo-chemical degradation, it means that a great number of processing techniques that can be used with organic materials are simply not available. These include spin-coating, ink-jet printing, dip-pen nanolithography (DPN) and nano-imprint lithography. With such techniques, it is possible to create micro- and nanostructured layers in a simple manner without the need for high-level clean room facilities or ultra-high vacuum systems. To enable usability of these methods, one needs luminescent chromophores that can be diluted in a solvent or a curable monomer solution. After processing, the created features will consist of either pure chromophores in the former case or a chromophore-doped polymer-matrix in the latter case. It is one of the great strengths of organic chemistry that solubility can be controlled by attaching functional chemical groups to the chromophore, which is typically possible without significant impact on the luminescence properties of the chromophores.

Having simple micro- and nanopatterning techniques available allows one in particular to take advantage of the micro-LED geometry. Ink-jet printing, for example, enables individual overcoating of adjacent pixels at tens of microns pitch [51].

1.3.1.1 Organic Semiconductors

Only six years after the first demonstration of a laser [54], laser operation from organic molecules was reported [55]. These early devices were based on small fluorescent dye molecules that needed to be suspended in a solution or polymer matrix because their luminescence would quench if individual dye molecules come in close proximity to each other. Dye solutions were the basis of a successful branch of optically pumped lasers that were widely used until the 1990s. Their main advantage was the broad gain bandwidth allowing broad spectral tuning and ultra-short pulse generation. However, due to the liquid-state of the gain material they were complicated and maintenance-intensive and are nowadays largely edged out by solid state laser technology. In the late 1980s and early 1990s, progress in organic synthesis brought up a new class of polymers that have similar optical, but different chemical and electrical properties, compared to dyes [56].

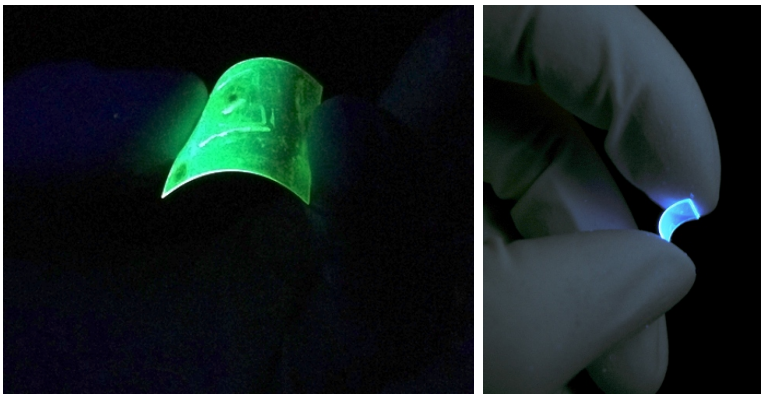

FIGURE 1.7: Mechanically flexible devices incorporating green- and blue-emitting organic semiconductor films under UV-illumination.

These so called "conjugated", "semiconducting" or "light-emitting" polymers (LEP) are highly luminescent in solid state films and have semiconducting charge transport characteristics. Their physics and performance will be reviewed in detail in chapter 2. Since LEPs are solution-processible and allow in principle mechanically flexible devices, there is great interest in exploiting their properties for usage in OSLs, OLEDs, organic photodiodes, organic solar cells and organic transistors. LEPs are a prime candidate for colour conversion in future LEDs and therefore they play a central role in this thesis. Photographs of LEP based devices are shown in figure 1.7, demonstrating in particular the potential for mechanically flexible and highly compact devices.

1.3.1.2 Colloidal Quantum Dots

An interesting type of inorganic chromophore is that of semiconductor nanocrystals. If certain metal-organic precursors of II-VI or III-V semiconductors are brought to chemical reaction within a solvent (under the addition of heat), the resulting semiconductor crystals are just a few nm in size [57]. The mean size and size distribution of these so-called colloidal quantum dots (CQDs) can in be controlled by the synthesis parameters such as the temperature and reaction time [57], enabling control of the luminescence wavelength. It is possible to overcoat the CQDs with a different material leading to "core-shell" CQDs [57] (see illustration in figure 1.8). A very interesting property of CQDs is that organic molecules can be attached to their surface. These will normally be functional groups to allow solubility in a specific target solvent and to determine the inter-particle separation in a close-packed film [57]. As a result, CQDs are solution-processible inorganic chromophores, see figure 1.8. CQDs have high PLQYs and are therefore attractive for colour conversion applications. Their suitability for VLC was studied and they were found to yield a bandwidth of 25 MHz which is an order of

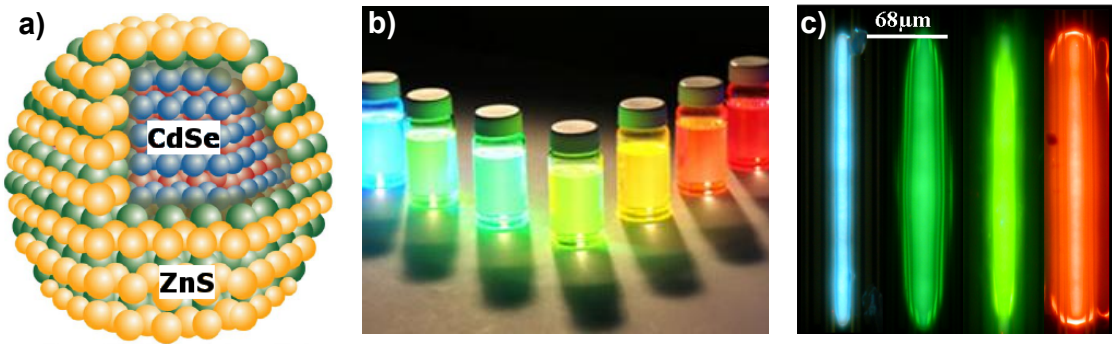

FIGURE 1.8: *a)* Illustration of a CdSe/ZnS core-shell CQD. *b)* CQDs in solution, dot size increasing from left to right. *c)* Self-written colour converting overlayers utilising CQDs in an epoxy matrix on top of UV-emitting GaN micro-stripe LEDs [61]. Image courtesy for *a)* and *b)*: Evident Technologies, inc. http://www.evidenttech.com/.

magnitude better than LEDs using conventional phosphors [58] and similar to the best OLED based results [59]. Furthermore, CQD lasers have been demonstrated [60].

1.3.2 Prospects for Hybrid Micro-LEDs

As already pointed out there exists an abundance of patterning techniques for solution-processible materials, most of which are suitable to exploit the pattern-programmability of micro-LED arrays. Whether this format is competitive or not depends on how hybrid devices compare to their purely organic or inorganic rivals in terms of optical power/fluence, overall efficiency, ease and cost of fabrication, ease and cost of operation, operational lifetime and specific optical and electrical properties (e.g. wavelength, linewidth, modulation response). Due to the broad range of potential applications it is promising and important to explore the options that are available.

1.4 Summary

CMOS-controlled GaN-based micro-LED arrays are a platform technology with widespread applications. They may find use in lab-on-a-chip devices for biology, medicine and chemistry, displays, maskless lithography systems and communications technology. This thesis explores how structured organic colour-converting overlayers can enhance the functionality of such systems. It is proposed that the hybrid organic/inorganic approach allows efficient access to the green/yellow spectral gap of inorganic LEDs, takes advantage of the simple fabrication methods of polymeric materials and may serve, for some applications, as an alternative to the yet-unsolved problem of creating an organic laser diode.

References

[1] Ya-Ju Lee, Ching-Hua Chiu, Chih Chun Ke, Po Chun Lin, Tien-Chang Lu, Hao-Chung Kuo, and Shing-Chung Wang. Study of the Excitation Power Dependent Internal Quantum Efficiency in InGaN/GaN LEDs Grown on Patterned Sapphire Substrate. *IEEE J. Sel. Top. Quantum Electron.*, 15(4):1137–1143, 2009.

[2] Joachim Piprek. Efficiency droop in nitride-based light-emitting diodes. *Phys. Status Solidi A*, 207 (10):2217–2225, 2010.

[3] Muthusamy Senthil Kumar, Jae Young Park, Yong Seok Lee, Sang Jo Chung, Chang-Hee Hing, and Eun-Kyung Suh. Improved Internal Quantum Efficiency of Green Emitting InGaN/GaN Multiple Quantum Wells by In Preflow for InGaN Well Growth. *Jpn. J. Appl. Phys.*, 47(2):839–842, 2008.

[4] Yi Yang, Xian An Cao, and Chunhui Yan. Investigation of the Nonthermal Mechanism of Efficiency Rolloff in InGaN Light-Emitting Diodes. *IEEE Trans. Electron Devices*, 55(7):1771–1775, 2008.

[5] Alicja Zarowna-Dabrowska. *Miniaturised opto-fluidic systems for cell manipulation and analysis.* PhD thesis, University of Strathclyde, Glasgow, UK, 2011.

[6] Michael R. Krames, Oleg B. Shchekin, Regina Mueller-Mach, Gerd O. Mueller, Ling Zhou, Gerard Harbers, and M. George Craford. Status and Future of High-Power Light-Emitting Diodes for Solid-State Lighting. *J. Display Technol.*, 3(2):160–175, 2007.

[7] M. R. Krames, M. Ochiai-Holcomb, G. E. Höfler, C. Carter-Coman, E. I. Chen, I.-H. Tan, P. Grillot, N. F. Gardner, H. C. Chui, J.-W. Huang, S. A. Stockman, F. A. Kish, M. G. Craford, T. S. Tan, C. P. Kocot, M. Hueschen, J. Posselt, B. Loh, G. Sasser, and D. Collins. High-power truncated-inverted-pyramid $(Al_xGa_{1-x})_{0.5}In_{0.5}P/GaP$ light-emitting diodes exhibiting >50% external quantum efficiency. *Appl. Phys. Lett.*, 75(16):2365–2367, 1999.

[8] Daisuke Morita, Masashi Yamamoto, Kazuyuki Akaishi, Kousuke Matoba, Katsuhiro Yasumoto, Yoshio Kasai, Masahiko Sano, Shin ichi Nagahama, and Takashi Mukai. Watt-Class High-Output-Power 365 nm Ultraviolet Light-Emitting Diodes. *Jpn. J. Appl. Phys.*, 43(9A):5945–5950, 2004.

[9] Yukio Narukawa, Junya Narita, Takahiko Sakamoto, Kouichiro Deguchi, Takao Yamada, and Takashi Mukai. Ultra-High Efficiency White Light Emitting Diodes. *Jpn. J. Appl. Phys.*, 45 (41):L1084–L1086, 2006.

[10] T. Riedl, T. Rabe, H.-H. Johannes, W. Kowalsky, J. Wang, T. Weimann, P. Hinze, B. Nehls, T. Farrell, and U. Scherf. Tunable organic thin-film laser pumped by an inorganic violet diode laser. *Appl. Phys. Lett.*, 88:241116, 2006.

[11] Christian Karnutsch, Marc Stroisch, Martin Punke, Uli Lemmer, Jing Wang, and Thomas Weimann. Laser Diode-Pumped Organic Semiconductor Lasers Utilizing Two-Dimensional Photonic Crystal Resonators. *IEEE Photon. Technol. Lett.*, 19(10):741–743, 2007.

[12] H. Sakata, K. Yamashita, H. Takeuchi, and M. Tomiki. Diode-pumped distributed-feedback dye laser with an organic-inorganic microcavity. *Appl. Phys. B*, 92:243–246, 2008.

[13] A. E. Vasdekis, G. Tsiminis, J.-C. Ribierre, Liam O' Faolain, T. F. Krauss, G. A. Turnbull, and I. D. W. Samuel. Diode pumped distributed Bragg reflector lasers based on a dye-to-polymer energy transfer blend. *Opt. Express*, 14(20):9211–9216, 2006.

[14] H. Matsuura, M. Fukuda, and H. Sakata. Threshold reduction induced by silica nanoparticledispersed active layer in diode-pumped microcavity dye laser. *Laser Phys. Lett.*, 6(3):194–197, 2009.

[15] Sönke Klinkhammer, Tobias Großmann, Karl Lüll, Mario Hauser, Christoph Vannahme, Timo Mappes, Heinz Kalt, and Uli Lemmer. Diode-Pumped Organic Semiconductor Microcone Laser. *IEEE Photon. Technol. Lett.*, 23(8):489–491, 2011.

[16] Y. Yang, G. A. Turnbull, and I. D. W. Samuel. Hybrid optoelectronics: A polymer laser pumped by a nitride light-emitting diode. *Appl. Phys. Lett.*, 92:163306, 2008.

[17] Z. Gong, H. X. Zhang, E. Gu, C. Griffin, M. D. Dawson, V. Poher, G. Kennedy, P. M. W. French, and M. A. A. Neil. Matrix-Addressable Micropixellated InGaN Light-Emitting Diodes With Uniform Emission and Increased Light Output. *IEEE Trans. Electron. Dev.*, 54(10):2650–2658, 2007.

[18] Z. Gong, E. Gu, S.R. Jin, D. Massoubre, B. Guilhabert, H.X. Zhang, M.D. Dawson, V. Poher, G.T. Kennedy, P.M.W. French, and M.A.A. Neil. Efficient flip-chip InGaN micro-pixellated light-emitting diode arrays: promising candidates for micro-displays and colour conversion. *J. Phys. D: Appl. Phys.*, 41:094002, 2008.

[19] H. X. Zhang, D. Massoubre, J. McKendry, Z. Gong, B. Guilhabert, C. Griffin, E. Gu, P.E. Jessop, J. M. Girkin, and M. D. Dawson. Individually-addressable flip-chip AlInGaN micropixelated light emitting diode arrays with high continuous and nanosecond output power. *Opt. Expr.*, 16(13): 9918–9926, 2008.

[20] Jonathan J. D. McKendry, Bruce R. Rae, Zheng Gong, Keith R. Muir, Benoit Guilhabert, David Massoubre, Erdan Gu, David Renshaw, Martin D. Dawson, and Robert K. Henderson. Individually Addressable AlInGaN Micro-LED Arrays With CMOS Control and Subnanosecond Output Pulses. *IEEE Photon. Technol. Lett.*, 21(12):811–813, 2009.

[21] Ben N. G. Giepmans, Stephen R. Adams, Mark H. Ellisman, and Roger Y. Tsien. The Fluorescent Toolbox for Assessing Protein Location and Function. *Science*, 312:217–224, 2006.

[22] James M. Prober, George L. Trainor, Rudy J. Dam, Frank W. Hobbs, Charles W. Robertson, Robert J. Zagursky, Anthony J. Cocuzza, Mar A. Jensen, and Kirk Baumeister. A System for Rapid DNA Sequencing with Fluorescent Chain-Terminating Dideoxynucleotides. *Science*, 238: 336–341, 1987.

[23] Tarik F.Massoud and Sanjiv S.Gambhir. Molecular imaging in living subjects: seeing fundamental biological processes in a new light. *Genes Develop.*, 17:545–580, 2003.

[24] Karl Deisseroth. Optogenetics. *Nature Methods*, 8(1):26–29, 2011.

[25] Thomas Hänscheid. The future looks bright: low-cost fluorescent microscopes for detection of Mycobacterium tuberculosis and Coccidiae. *Trans. Roy. Soc. Trop. Med. Hyg.*, 102:520–521, 2008.

[26] B. R. Rae, C. Griffin, J. McKendry, J. M. Girkin, H. X. Zhang, E. Gu, D. Renshaw, E. Charbon, M. D. Dawson, and R. K. Henderson. CMOS driven micro-pixel LEDs integrated with single photon avalanche diodes for time resolved fluorescence measurements. *J. Phys. D: Appl. Phys.*, 41:094011, 2008.

[27] Bruce R. Rae, Keith R. Muir, Zheng Gong, Jonathan McKendry, John M. Girkin, Erdan Gu, David Renshaw, Martin D. Dawson, and Robert K. Henderson. A CMOS Time-Resolved Fluorescence Lifetime Analysis Micro-System. *Sensors*, 9:9255–9274, 2009.

[28] Akihiko Hirota, Katsushige Sato, Yoko Momose-Sato, Tetsuro Sakai, and Kohtaro Kamino. A new simultaneous 1020-site optical recording system for monitoring neural activity using voltage-sensitive dyes. *J. Neurosci. Meth.*, 56:187–194, 1995.

[29] Nir Grossman, Vincent Poher, Matthew S. Grubb, Gordon T. Kennedy, Konstantin Nikolic, Brian McGovern, Rolando Berlinguer Palmini, Zheng Gong, Emmanuel M. Drakakis, Mark A. A. Neil, Martin D. Dawson, Juan Burrone, and Patrick Degenaar. Multi-site optical excitation using ChR2 and micro-LED array. *J. Neural Eng.*, 7:016004, 2010.

[30] Sang-Il Park, Yujie Xiong, Rak-Hwan Kim, Paulius Elvikis, Matthew Meitl, Dae-Hyeong Kim, Jian Wu, Jongseung Yoon, Chang-Jae Yu, Zhuangjian Liu, Yonggang Huang, Keh chih Hwang, Placid Ferreira, Xiuling Li, Kent Choquette, and John A. Rogers. Printed Assemblies of Inorganic Light-Emitting Diodes for Deformable and Semitransparent Displays. *Science*, 325:977–981, 2009.

[31] Rak-Hwan Kim, Dae-Hyeong Kim, Jianliang Xiao, Bong Hoon Kim, Sang-Il Park, Bruce Panilaitis, Roozbeh Ghaffari, Jimin Yao, Ming Li, Zhuangjian Liu, Viktor Malyarchuk, Dae Gon Kim, An-Phong Le, Ralph G. Nuzzo, David L. Kaplan, Fiorenzo G. Omenetto, Yonggang Huang, Zhan Kang, and John A. Rogers. Waterproof AlInGaP optoelectronics on stretchable substrates with applications in biomedicine and robotics. *Nature Materials*, 9:929–937, 2010.

[32] Jye-Shane Yang and Timothy M. Swager. Fluorescent Porous Polymer Films as TNT Chemosensors: Electronic and Structural Effects. *J. Am. Chem. Soc.*, 120:11864–11873, 1998.

[33] Sarah J. Toal and William C. Trogler. Polymer sensors for nitroaromatic explosives detection. *J. Mater. Chem.*, 16:2871–2883, 2006.

[34] Ying Yang, Graham A. Turnbull, and Ifor D. W. Samuel. Sensitive Explosive Vapor Detection with Polyfluorene Lasers. *Adv. Funct. Mater.*, 20:2093–2097, 2010.

[35] Aimée Rose, Zhengguo Zhu, Conor F. Madigan, Timothy M. Swager, and Vladimir Bulović. Sensitivity gains in chemosensing by lasing action in organic polymers. *Nature*, 434:876–879, 2005.

[36] Yue Wang, Bruce R. Rae, Robert K. Henderson, Zheng Gong, Jonathan Mckendry, Erdan Gu, Martin D. Dawson, Graham A. Turnbull, and Ifor D. W. Samuel. Ultra-portable explosives sensor based on a CMOS fluorescence lifetime analysis micro-system. *AIP Advances*, 1:032115, 2011.

[37] Pei Yu Chiou, Aaron T. Ohta, and Ming C. Wu. Massively parallel manipulation of single cells and microparticles using optical images. *Nature*, 436:370–372, 2005.

[38] Alicja Zarowna-Dabrowska, Steven L. Neale, David Massoubre, Jonathan McKendry, Bruce R. Rae, Robert K. Henderson, Mervyn J. Rose, Huabing Yin, Jonathan M. Cooper, Erdan Gu, and Martin D. Dawson. Miniaturized optoelectronic tweezers controlled by GaN micro-pixel light emitting diode arrays. *Opt. Express*, 19(3):2720–2728, 2011.

[39] T. Matsuoka, T. Ito, and T. Kaino. First plastic optical fibre transmission experiment using 520nm LEDs with intensity modulation/direct detection. *Electron. Lett.*, 36(22):1836–1837, 2000.

[40] Masayoshi Tonouchi. Cutting-edge terahertz technology. *Nature Photonics*, 1:97–105, 2007.

[41] John Federici and Lothar Moeller. Review of terahertz and subterahertz wireless communications. *J. Appl. Phys.*, 107:111101, 2010.

[42] Fritz R. Gfeller and Urs Bapst. Wireless In-House Data Communication via Diffuse Infrared Radiation. *Proc. IEEE*, 67(11):1474–1486, 1979.

[43] Haim Manor and Shlomi Arnon. Performance of an optical wireless communication system as a function of wavelength. *Appl. Opt.*, 42(21):4285–4294, 2003.

[44] Toshihiko Komine and Masao Nakagawa. Fundamental Analysis for Visible-Light Communication System using LED Lights. *IEEE Trans. Consumer Electron.*, 50(1):100–107, 2004.

[45] A. C. Boucouvalas. Indoor ambient light noise and its effect on wireless optical links. *IEE Proc. Optoelectron.*, 143(6):334–338, 1996.

[46] Jonathan McKendry, Richard P. Green, A. E. Kelly, Zheng Gong, Benoit Guilhabert, David Massoubre, Erdan Gu, and Martin D. Dawson. High-Speed Visible Light Communications Using Individual Pixels in a Micro Light-Emitting Diode Array. *IEEE Photon. Technol. Lett.*, 22(18): 1346–1348, 2010.

[47] Jonathan J. D. McKendry, David Massoubre, Shuailong Zhang, Bruce R. Rae, Richard P. Green, Erdan Gu, Robert K. Henderson, A. E. Kelly, and Martin D. Dawson. Visible-Light Communications Using a CMOS-Controlled Micro-Light-Emitting-Diode Array. *J. Lightwave Technol.*, 30(1): 61–67, 2012.

[48] Z.Y. Fan, J.Y. Lin, and H.X. Jiang. III-nitride micro-emitter arrays: development and applications. *J. Phys. D: Appl. Phys.*, 41:094001, 2008.

[49] N. Otsuji, K. Fujiwara, and J. K. Sheu. Electroluminescence efficiency of blue InGaN/GaN quantum-well diodes with and without an n-InGaN electron reservoir layer. *J. Appl. Phys.*, 100: 113105, 2006.

[50] Chih-Feng Lu, Chi-Feng Huang, Yung-Sheng Chen, Wen-Yu Shiao, Cheng-Yen Chen, Yen-Cheng Lu, and Chih-Chung Yang. Phosphor-Free Monolithic White-Light LED. *IEEE J. Sel. Top. Quantum Electron.*, 15(4):1210–1217, 2009.

[51] M. Wu, E. Gu, A. Zarowna, A.L. Kanibolotsky, A.J.C. Kuehne, A.R. Mackintosh, P.R. Edwards, O.J. Rolinski, I.F. Perepichka, P.J. Skabara, R.W. Martin, R.A. Pethrick, D.J.S. Birch, and M.D. Dawson. Star-shaped oligofluorene nanostructured blend materials: controlled micro-patterning and physical characteristics. *Appl. Phys. A*, 97(1):119–123, 2009.

[52] C.R. Belton, G. Itskos, G. Heliotis, P.N. Stavrinou, P.G. Lagoudakis, J. Lupton, S. Pereira, E. Gu, C. Griffin, B. Guilhabert, I.M. Watson, A.R. Mackintosh, A.R. Pethrick, J. Feldmann, R. Murray, M.D. Dawson, and D.D.C. Bradley. New light from hybrid inorganic-organic emitters. *J. Phys. D: Appl. Phys.*, 41:094006, 2008.

[53] Alexander J. C. Kuehne, David Elfström, Allan R. Mackintosh, Alexander L. Kanibolotsky, Benoit Guilhabert, Erdan Gu, Igor F. Perepichka, Peter J. Skabara, Martin D. Dawson, and Richard A. Pethrick. Direct Laser Writing of Nanosized Oligofluorene Truxenes in UV-Transparent Photoresist Microstructures. *Adv. Mat.*, 21:781–785, 2009.

[54] T. H. Maiman. Stimulated Optical Radiation in Ruby. *Nature*, 187:493–494, 1960.

[55] P. P. Sorokin and L. R. Lankard. Stimulated Emission Observed from an Organic Dye, Chloroaluminum Phthalocyanine . *IBM J. Res. Dev.*, 10(2):162–163, 1966.

[56] Alan J. Heeger. Nobel Lecture: Semiconducting and metallic polymers: The fourth generation of polymeric materials. *Rev. Mod. Phys.*, 73(3):681–700, 2001.

[57] C.B. Murray, C.R. Kagan, and M.G. Bawendi. Synthesis and Characterization of Monodisperse Nanocrystals and Close-Packed Nanocrystal Assemblies. *Annu. Rev. Mater. Sci.*, 30:545–610, 2000.

[58] N. Laurand, B. Guilhabert, J. McKendry, A. E. Kelly, B. Rae, D. Massoubre, Z. Gong, E. Gu, R. Henderson, and M. D. Dawson. Colloidal quantum dot nanocomposites for visible wavelength conversion of modulated optical signals. *Opt. Mater. Express*, 2(3):250–260, 2012.

[59] Iain A. Barlow, Theo Kreouzis, and David G. Lidzey. High-speed electroluminescence modulation of a conjugated-polymer light emitting diode. *Appl. Phys. Lett.*, 94:243301, 2009.

[60] A.V. Malko, A.A. Mikhailovsky, M.A. Petruska, J.A. Hollingsworth, H. Htoon, M.G. Bawendi, and V.I. Klimov. From amplified spontaneous emission to microring lasing using nanocrystal quantum dot solids. *Appl. Phys. Lett.*, 81(7):1303–1305, 2002.

[61] B. Guilhabert, D. Elfström, A. J. C. Kuehne, D. Massoubre, H. X. Zhang, S. R. Jin, A. R. Mackintosh, E. Gu, R. A. Pethrick, and M. D. Dawson. Integration by self-aligned writing of nanocrystal/epoxy composites on InGaN micropixelated light-emitting diodes. *Opt. Express*, 16(23):18933–18941, 2008.

Chapter 2

Organic Gain Media

2.1 Conjugated Organic Molecules

An important stimulus for the current interest in polymeric media for electronic and optical applications was the advance in synthesis of materials that share an effect usually referred to as "π-conjugation". In these materials, chains of carbon atoms are connected by alternating single- and double-bonds. As illustrated in figure 2.1, the electrons in the hybridised π-orbitals are delocalised along the chain, leading to a semiconductor-like electronic band-structure. In contrast to inorganic semiconductors, the delocalisation is efficient only within individual molecules (a few nm in length) which have much more conformational freedom than a neat crystal, but is less efficient between molecules. As an immediate result, the electronic energy bands of a semiconducting organic film are much narrower than those of inorganic semiconductors but transitions are broadened by conformational changes of the molecules such as vibrational modes along the bonds.

2.1.1 Fluorescence and Phosphorescence

A conjugated molecule in the electronic ground state will have all bonding π-orbitals filled by two electrons. Due to the Pauli exclusion principle, the spin states of two electrons in one of these orbitals have to be in singlet configuration. The first excited state may be thought of as having one electron from the highest binding orbital (often referred to as HOMO, highest occupied molecular orbital) raised to the lowest anti-bonding orbital (LUMO, lowest unoccupied molecular orbital). In this case both spin-singlet and triplet configurations are possible yielding two species of excited state. The HOMO and LUMO wave functions can in principle be calculated numerically. However, in the case of large and complex molecules such as the polymeric materials used in this

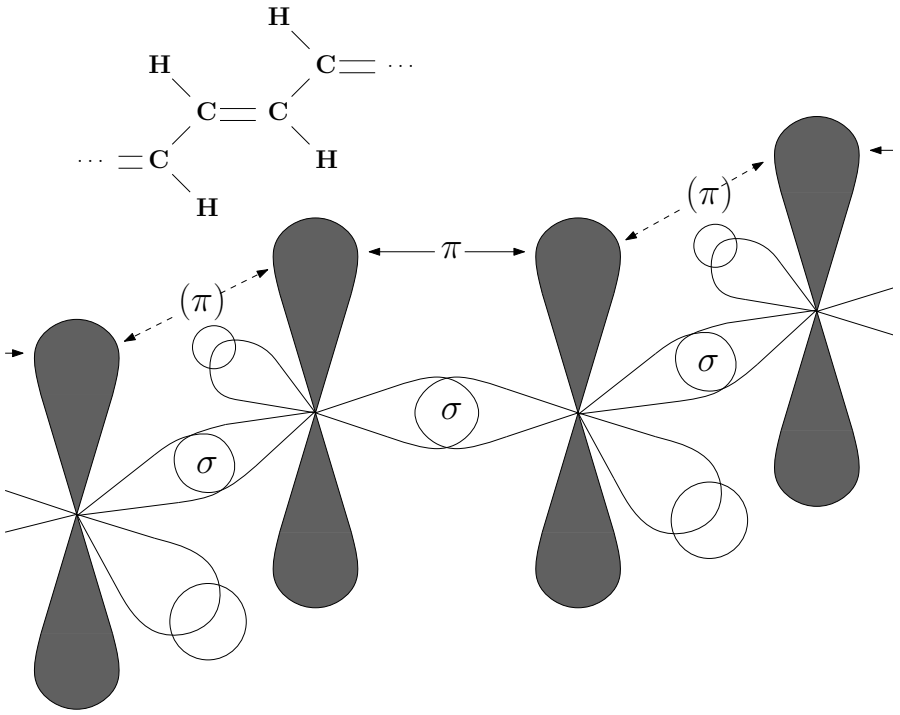

FIGURE 2.1: Schematic illustrating the delocalisation of the π-electrons in a chain of alternating single- and double-bonds between carbon atoms.

thesis this sort of calculation requires immense computational effort and often needs empirical input to choose good starting values for the numerical procedure.

Figure 2.2 illustrates the energies of the ground state and the two lowest excited states as a function of molecular conformation. Since the transition from the triplet state T1 to the ground state S0 is spin-forbidden, pump light will excite molecules in effect exclusively into the singlet (excited) state S1. Molecules in the singlet state may relax directly into the ground state or cross at a rate k_{ST} into the triplet state (that typically has a lower energy than S1). Both singlet state and triplet state may decay to the ground state either radiatively or non-radiatively. The quantum yield of each transition depends on the material and can be as high as 80 % or more. Since the triplet state decay is spin-forbidden, its lifetime τ_T is very long (typically microseconds to milliseconds) compared to the singlet state lifetime τ_S (typically at the order of one nanosecond). The two types of luminescence can thus be distinguished by their lifetime. Luminescence originating from singlet state to ground state transitions is called "fluorescence" and luminescence originating from triplet state to ground state transitions is called "phosphorescence". Historically, the terms were initially used to refer to luminescence with different lifetimes but their physical origin was not then known. It was in the 1930's that A. Jablonski associated them with two types of excited states depicted in a diagram similar to figure 2.2 [1] and during the 1940's it became widely accepted that these two states are in fact spin singlet and triplet configurations [2]. In

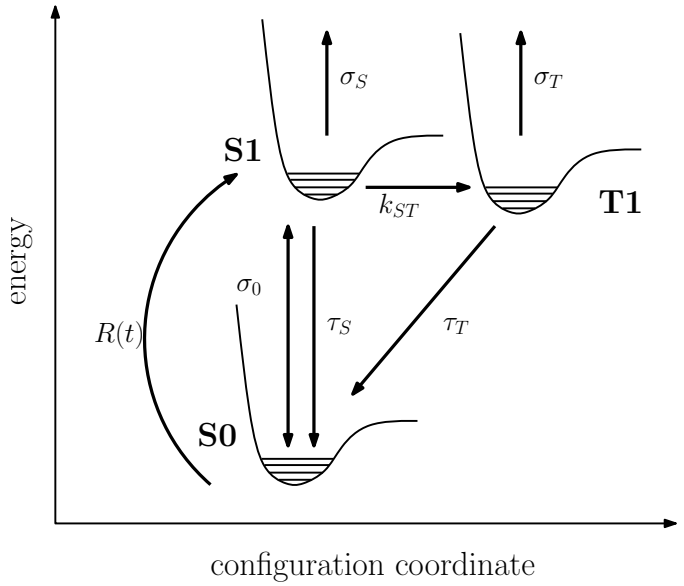

FIGURE 2.2: Jablonksi diagram illustrating the energy levels and transitions relevant for the most organic light emitters. The diagram includes a simplified scheme of transition cross sections, $\sigma_0, \sigma_S, \sigma_T$, that is used in section 2.1.5. A reduced Jablonski diagram that illustrates the vibrational features of the spectra in more detail is given in figure 2.7.

principle, both fluorescence and phosphorescence can occur in the same material and the phosphorescence spectrum will then be redshifted compared to the fluorescence [3]. In most cases however, one of the processes will be so dominant that we can classify a material as either fluorescent or phosphorescent.

Organic lasers are exclusively made from fluorescent molecules because they have a large stimulated emission cross section and in the case of pulsed pumping they offer a time window of very low excited state absorption (see section 2.1.5 below). Organic LEDs (OLEDs) can be made from either fluorescent or phosphorescent chromophores and in fact the current trend in the OLED industry is in favour of phosphorescent OLEDs.

2.1.2 Types of Organic Gain Media

The field of organic chemistry is vast and so is the number of different light emitters incorporating organics. One typically differentiates between dyes, molecular solids (often referred to as "small-molecule organic semiconductors"), conjugated polymers and oligomers. Each of them is introduced in more detail below. The term "organic semiconductor" can refer to any of these material classes, with the exception of dyes. If we speak of a "light emitting polymer" (LEP) then this usually refers to either conjugated polymers or oligomers. Each of the above are purely organic light emitters. There are

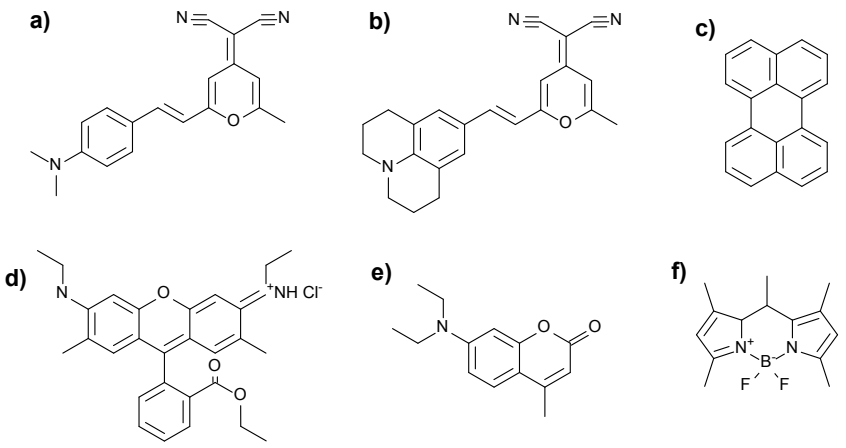

FIGURE 2.3: Some popular dyes: *a)* 4-(dicyanomethylene)-2-methyl-6-(4-dimethylaminostyryl)-4H-pyran (DCM), *b)* 4-(dicyanomethylene)-2-methyl-6-(julolidin-4-yl-vinyl)-4H-pyran (DCM2), *c)* perylene, *d)* Rhodamine 6G (R6G), *e)* Coumarin 47, *f)* pyrromethane (PM).

also types of inorganic light emitters that utilise organics such as colloidal quantum dots (CQDs) with organic ligaments and rare-earth doped organics.

2.1.2.1 Dyes

The first laser demonstration using an organic gain medium was based on a material class referred to as dyes [4]. Dyes are very small conjugated molecules (conjugation extends over ∼10 carbon atoms). However, if individual dye molecules are brought in close proximity to each other, then this will induce efficient non-radiative relaxation pathways that diminish luminescence [5]. Therefore, dye molecules need to be either diluted in a solvent or embedded in a polymer matrix. Dye-doped polymers are in fact very commonly used for organic solid state lasers (OSLs). Some of the most common laser dyes are shown in figure 2.3.

2.1.2.2 Molecular Solids

There are "small" conjugated molecules that can be fabricated into neat solid films without inducing non-radiative relaxation pathways. Instead, carriers can efficiently move from one molecule to its neighbours, thus providing inter-molecule delocalisation and charge transport [6]. Important examples of molecular solids are anthracene and aluminum tris(quinolate) which are shown in figure 2.4. Molecular solids are often doped with dyes yielding luminescent films with high quantum yields. Light is absorbed by the molecular solid matrix and the energy is efficiently transferred to the dye molecules via Förster resonant energy transfer (FRET, a near-field dipole-dipole interaction process)

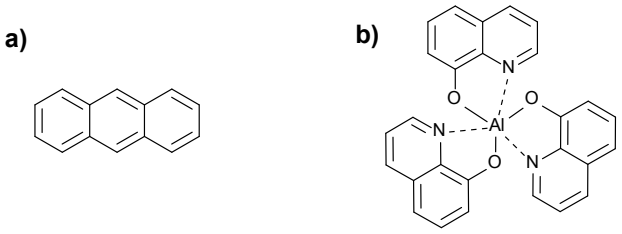

FIGURE 2.4: Two important molecular solids: *a)* anthracene and *b)* aluminum tris(quinolate) (Alq3).

[7, 8]. Their most important drawback is that they are not solution processible and therefore many interesting device fabrication techniques (in particular various printing and imprinting technologies) that can be applied to conjugated polymers are not available [5].

2.1.2.3 Conjugated Polymers

The prototype of all conjugated polymers is polyacetylene and in fact its structure was already shown above in figure 2.1 to explain the phenomenon of π-conjugation. Polyacetylene was studied from the 1970's onwards [9]. However its electronic properties are very susceptible to disorder along the molecule chain and therefore creating films with good semiconducting properties is very difficult [6]. Breakthrough results were obtained in the mid 1980's to early 1990's when advances in synthesis allowed conjugated polymers with more complex repeat units incorporating benzene, thiophene or similar ring structures that stabilise molecular conformation [6]. A selection of the most common building blocks in these modern conjugated polymers is shown in figure 2.5. These monomers can be functionalised with various side groups that allow design of the solubility properties of the molecules. Typically, each molecule consists of a few tens of repeat units each of which is of similar size to a typical dye molecule. Therefore intra-chain delocalisation plays an important role in charge transport. In addition, the relatively weak inter-molecule delocalisation (similar to molecular solids) still exists and therefore charge transport properties can compete with molecular solids.

2.1.2.4 Conjugated Oligomers

This class of material is actually very similar to conjugated polymers. The same building blocks are used and the optical and electronic properties follow the same rules. The key difference in oligomers as opposed to polymers is that an oligomer film will consist of practically monodisperse molecules that all have exactly the same number (usually small, < 10) of repeat units. Oligomers are a very recent addition to semiconducting

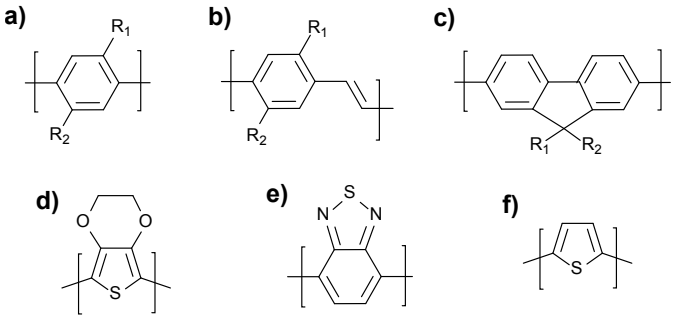

FIGURE 2.5: Common building blocks of LEPs: *a)* (poly) para phenylene (PPP), *b)* (poly) para phenylene vinylene (PPV), *c)* (poly) fluorene (PFO, in copolymers fluorene units are typically abbreviated as F), *d)* (poly) ethylene dioxythiophene ((PEDOT), *e)* benzothiadiazole (BT) and *f)* (poly) thiophene (PT). Compare figure 3.3 for the structure and spectral properties of a PPV derivative used for the work presented here.

polymers and an exciting research topic. They may offer enhanced spectral overlap of optical transitions between individual molecules and potential for controllability of electronic and optical properties via conjugation length, introduction of single monomers of a different species and self-organisation.

Usually, polymers are long, one-dimensional thread-like chains and oligomers can simply be the same but with a well defined number of repeat units. It is though also possible to create more complex structures from the monomers. For example highly branched structures (so called "dendrimers"), star shaped molecules and structures incorporating spiro-linked cyclopentadiene groups have seen considerable interest. Normally, these complex molecules are oligomeric. Some examples are shown in figure 2.6. How the structure influences the electronic and optical properties of these materials is a current research topic [10].

2.1.2.5 Inorganic Emitters utilising Organics

At this point it should be pointed out that there are photoluminescent materials which are solution processible but are not based on conjugation. These are inorganic nanocrystals with functional organic surface groups ("ligaments") or organic molecules incorporating rare-earth atoms as their luminescent centres. While devices based on these materials are fabricated by the same methods as OSLs or OLEDs, their photophysics is very different from organic emitters and therefore they shall not be further discussed in this chapter but are considered in section 3.1.3.

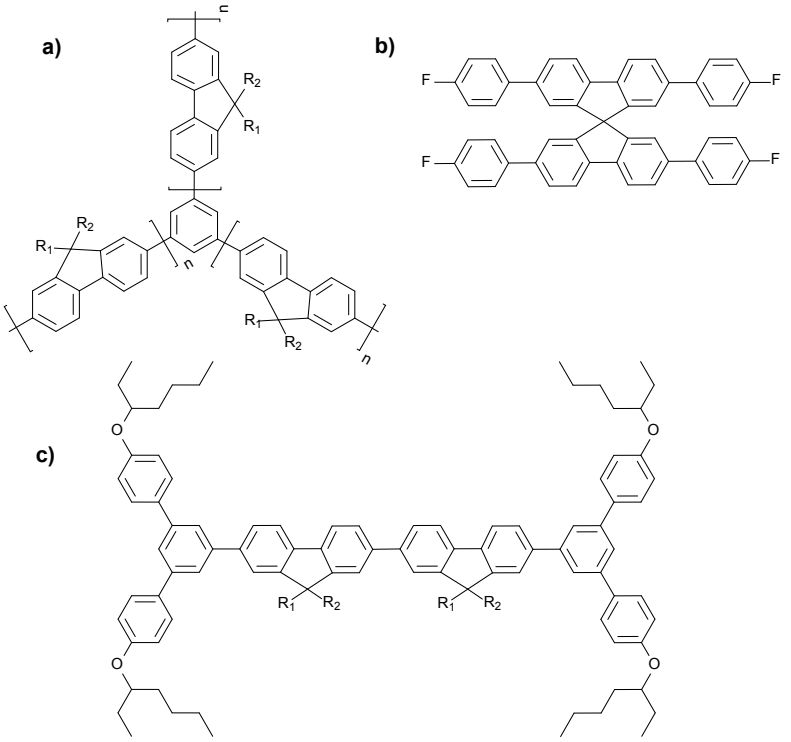

FIGURE 2.6: Examples of oligomers with complex structures: *a)* star-shaped oligofluorene benzene, *b)* spiro-bifluorene, *c)* bisfluorene-cored dendrimer. Compare figure 3.2 for the structure and spectral properties of an oligofluorene used for the work presented here.

2.1.3 Vibronic Structure of LEP Spectra

It was discussed in the above sections what conjugated molecules are, which varieties of them exist and what the underlying principles of their luminescence are. Here, more detailed spectral features of luminescence and absorption will be explained. Figure 2.7 shows a reduced Jablonski diagram that only includes transitions in between the S0 and S1 states. The x-axis is the "conformation coordinate" Q which is basically a measure of the overlap of electron wave functions. Q is not exactly a spatial coordinate but represents the combined effect of displacement along each of the molecule's chemical bonds. Each of the two states, S0 and S1, has a potential well at a certain value of Q, leading to several discrete vibrational states within this well. These vibronic modes are simply numbered from 0 onwards i.e. the vibronic states are $|m_n\rangle$ where n specifies the electronic state (e.g. S0, S1, T1,...) and $m = 0, 1, 2, \ldots$. The overall quantum mechanical state of the molecule can then be described as the product of electronic and vibronic states $|n, m_n\rangle = |n\rangle|m_n\rangle$. It is important to note that the location of the conformational potential minimum is different for the S0 and S1 state with a separation ΔQ [6]. This has two significant consequences. First of all, it means that relaxation of the electronic state will always be accompanied by a structural relaxation of the molecule.

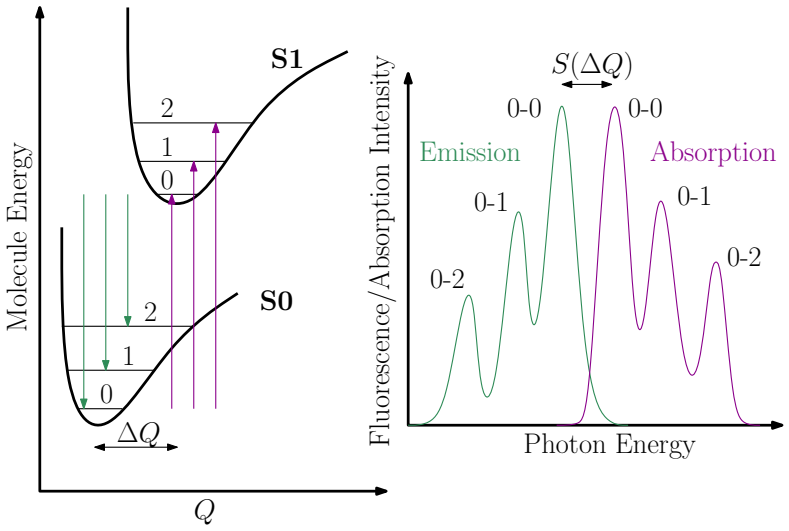

FIGURE 2.7: Simplified Jablonski diagram (compare also figure 2.2) and idealised fluorescence/absorption spectra illustrating optical transitions in between the S0 and S1 electronic states. The x-axis in the Jablonski diagram is the conformation coordinate Q and the spectra illustrate the Stokes shift $S(\Delta Q)$. In real organic media, the emission and absorption spectra will normally not be as symmetric as illustrated here and at high photon energies additional absorption features from higher excited states will be present. Compare figures 3.2 and 3.3 for experimental spectra of real LEPs.

Therefore, the emission wavelength will be redshifted compared to the absorption by an amount $S(\Delta Q)$, the so called "Stokes shift". The Stokes shift is indicated in the idealised spectrum in figure 2.7. Typically, it is at the order of 50 meV (compare section 3.1 for fluorescence and absorption spectra of the materials used in this work), though LEPs with extraordinarily large Stokes shifts of several 100 meV exist [11, 12]. The second important consequence of $\Delta Q \neq 0$ is that due to this offset, the vibronic substates of S0 and S1 are no longer orthogonal to each other, i.e. $\langle 0_{S1}|0_{S0}\rangle \neq 0$, $\langle 0_{S1}|1_{S0}\rangle \neq 0$, $\langle 0_{S1}|2_{S0}\rangle \neq 0$ etc. As a result, the $|S1, 0_{S1}\rangle$ state can not only relax into the $|S0, 0_{S0}\rangle$ state, but also into $|S0, 1_{S0}\rangle$, $|S0, 2_{S0}\rangle$, ... For $\Delta Q = 0$ these latter transitions would be quantum mechanically forbidden. The importance of this aspect becomes clear when noting that the lowest OSL thresholds are typically obtained at a laser wavelength corresponding to the $|S1, 0_{S1}\rangle \rightarrow |S0, 1_{S0}\rangle$ transition. A more detailed discussion on the significance of ΔQ can be found in a recent review by A. Heeger [6].

A convenient and commonly used notation is to label the $|S1, 0_{S1}\rangle \rightarrow |S0, 0_{S0}\rangle$ transition as "0-0", the $|S1, 0_{S1}\rangle \rightarrow |S0, 1_{S0}\rangle$ transition as "0-1" etc. This notation is used in figure 2.7. In practice, the labelling of spectral features is done on a purely phenomenological basis. There is no rule on how the labelling is associated with the specific bonds along which the vibration occurs and it can happen that distinct vibronic transitions are close enough and broadened to such a degree that they end up pooled under a single label [13].

2.1.4 Photodegradation

It is well known that illumination of matter with light can trigger chemical reactions. The groups that studied the fundamental mechanisms of fluorescence and phosphorescence in the 1940s realised at the same time that these mechanisms are also responsible for photo-induced chemical reactions in dyes [14]. Of particular importance is the photo-induced oxidation of organic light emitters which causes bleaching of the light emission. The details of photodegradation has been studied in PFO, where it was found that oxygen atoms ketone-bind to the alkyl side chains or even replace them [15, 16], see figure 2.8. Similar types of reactions were found in photo-degradation studies on MEH-PPV [17]. The oxidised PFO molecules, typically referred to as fluorenones, have reduced pump absorption, lower PLQY, reduced intensity at the first (blue) vibronic transitions and increased intensity at higher (green) vibronic modes [15]. As a result, LEPs based on fluorene units will appear greenish after photo-oxidation, an effect clearly visible in figure 2.8. In general, it is understood that in LEPs the strong electron-negativity of oxygen distorts electron de-localisation and induces non-radiative relaxation mechanisms [16], particularly if the binding of the oxygen atom to the molecule is ketonic. Since photo-oxidation is simply an alternative relaxation pathway for the excited S1 state, bleaching of organic light emitters will always occur under the presence of oxygen. There are a number of options to suppress this effect:

1. Operate the device in vacuum or inert (e.g. nitrogen) atmosphere.
2. Embed the chromophores in a protective polymer matrix.
3. Attach functional side-groups to the chromophore that prevent oxygen molecules from coming close to the LEP backbone.
4. Use an inorganic (e.g. glass) layer as oxygen-barrier.

To date, the last option appears to be the most practical and powerful method, see also section 2.2.2 below for photo-stability investigations on OSLs. In fact, commercially available OLEDs currently employ encapsulation based on inorganic oxygen-barriers. However, this type of encapsulation disables mechanical flexibility and therefore alternative techniques remain an interesting research topic.

2.1.5 Gain Dynamics in Organic Gain Media

So far, organic lasers are operated using pulsed optical pumping. This is due to the build-up of triplet-state excitons in the organic molecules that prevent population inversion

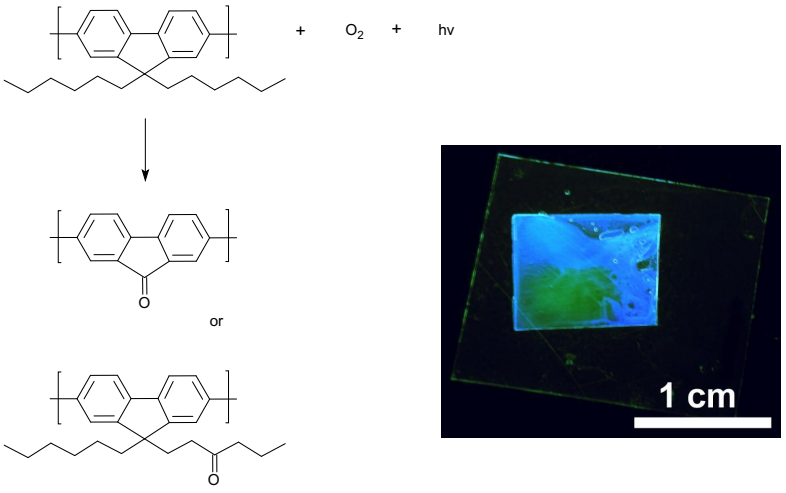

FIGURE 2.8: Photo-oxidation of fluorene units. The picture shows a degraded sample of oligofluorene truxene und UV-illumination with characteristic green emission from the photo-bleached pump spot.

and cause additional losses under continuous wave (CW) pumping. See section 2.2.3 below for a discussion of current research towards CW OSLs. This section provides a rate equation analysis of various pumping conditions to provide an understanding of how different pump pulse durations and pulse shapes affect the achievable optical gain and in particular the threshold. It also aims to clarify whether laser thresholds should be measured in terms of fluence (energy per pulse per unit area, $[\mu J/cm^2]$) or peak intensity $[W/cm^2]$.

2.1.5.1 Relevant Parameters

Obviously, very important parameters are the timescales: the singlet and triplet state lifetimes, τ_S and τ_T, the intersystem crossing rate, $k_{ST} = 1/\tau_{ST}$, and the pump pulse duration τ_{pulse}. The singlet lifetime is typically of the order of 1 ns, τ_T is significantly longer, at least a microsecond and up to milliseconds. The exact value is probably irrelevant. Intersystem crossing rates have only been measured for a selected number of materials (e.g. R6G [18] and PFO [19]), but it seems reasonable to assume $\tau_{ST} \approx 10 \cdot \tau_S$. The pump pulse duration is one of the key parameters examined here and may consist of asymmetric rise and fall times $\tau_{rise} + \tau_{fall} = \tau_{pulse}$.

The model has been simplified such that the only other parameters are the pump peak intensity γ_{max} and the absorption cross sections of the ground-, singlet- and triplet-states at the laser line, respectively $\sigma_0, \sigma_S, \sigma_T$.

2.1.5.2 Details of the Model

The calculation follows a rate equation model by Weber and Bass [18] and an illustration of the transitions considered in this model can be found in figure 2.2:

$$\begin{aligned}
\frac{\mathrm{d}N_S}{\mathrm{d}t} &= -\frac{1}{\tau_S}N_S + R(t)N_0 \\
\frac{\mathrm{d}N_T}{\mathrm{d}t} &= -\frac{1}{\tau_T}N_T + k_{ST}N_S \\
\frac{\mathrm{d}N_0}{\mathrm{d}t} &= -R(t)N_0 + (\frac{1}{\tau_S} - k_{ST})N_S + \frac{1}{\tau_T}N_T
\end{aligned}$$

Where $N_{0,S,T}$ are respectively the ground, singlet and triplet state populations and R(t) is the time dependent pump rate. By normalising $n_0 + n_S + n_T \equiv 1$ we obtain a reduced set of rate equations:

$$\frac{\mathrm{d}n_S}{\mathrm{d}t} = -\left(\frac{1}{\tau_S} + R(t)\right) n_S - R(t)n_T + R(t) \tag{2.1}$$

$$\frac{\mathrm{d}n_T}{\mathrm{d}t} = -\frac{1}{\tau_T}n_T + k_{ST}n_S \tag{2.2}$$

$$n_S, n_T \in [0, 1]$$

It should be pointed out, that equations (2.1) and (2.2) are only useful to determine the small-signal gain g_0 (and therefore the threshold). Above threshold, stimulated emission will occur on a picosecond timescale [13]. Assuming a simple set of three cross sections $\sigma_0, \sigma_S, \sigma_T$ as mentioned above, we can calculate an approximation of the small signal gain:

$$g_0 \approx (2n_S + n_T - 1)\sigma_0 - n_T\sigma_T - n_S\sigma_S \tag{2.3}$$

Here, σ_0 is the optical cross section of the fluorescent transition between S0 and S1, and σ_S, σ_T account for excited state absorption into higher lying states. In fact, equation (2.3) is a simplification of an expression used by Weber and Bass [18] where also the same three cross-sections were used but including a wavelength-dependent extension.

2.1.5.3 Results

Rate equations (2.1) and (2.2) were solved numerically for sech^2 shaped pump pulses (τ_{pulse} is treated as FWHM, hence the factor 1.76):

$$R(t) = R_{max} \cdot \mathrm{sech}^2\left(1.76\frac{t}{\tau_{pulse}}\right) \tag{2.4}$$

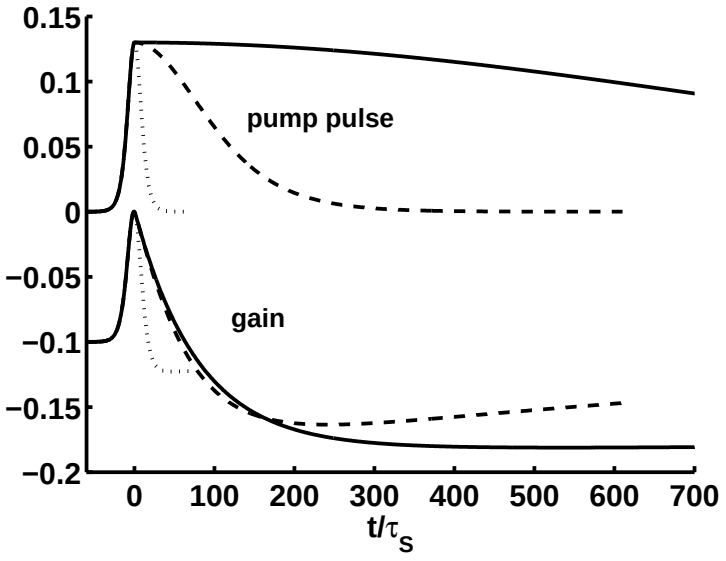

FIGURE 2.9: Time dependent pump pulse and optical gain for pulses with fixed rise time and peak intensity but different fall times at threshold. Parameters are $\tau_S = 1, \tau_{ST} = 10, \tau_T = 1000, \tau_{rise} = 10, \sigma_S = 0, \sigma_T = 0.2, \sigma_0 = 0.1$. The fall times are $\tau_{fall} = 10, 100, 1000$.

or in case of asymmetrical pulses:

$$R(t) = R_{max} \cdot \begin{cases} \operatorname{sech}^2\left(0.88\frac{t}{\tau_{rise}}\right) & , \quad t < 0 \\ \operatorname{sech}^2\left(0.88\frac{t}{\tau_{fall}}\right) & , \quad t \geq 0 \end{cases} \tag{2.5}$$

The populations found this way are then fed into equation (2.3). The values for the different cross sections $\sigma_{0,S,T}$ are currently arbitrary guess-values that are roughly aligned with those published for R6G [18].

As a first illustration of how the gain in organics evolves, figure 2.9 shows the temporal evolution of the pump rate and gain by asymmetrical pump pulses according to equation (2.5) in a regime of relatively long rise time (longer than the singlet state lifetime) and even longer fall times. The peak intensity and rise time has been kept constant but the fall time and thus the pump fluence was changed. It can be seen that for all of the pump pulses the gain just about reaches transparency, i.e. all pulses are at threshold. Hence we conclude that in this regime, a consistent measure for threshold is the peak intensity while the threshold fluence will vary strongly.

To investigate further the influence of the rise time, we record the maximum gain obtained during the pulse and plot it as a function of the rise time. This is done in figure 2.10. It can be seen that for fall times longer than τ_{ST} it is only the rise time that governs the gain and not the overall pulse duration. In this case of long fall time the peak

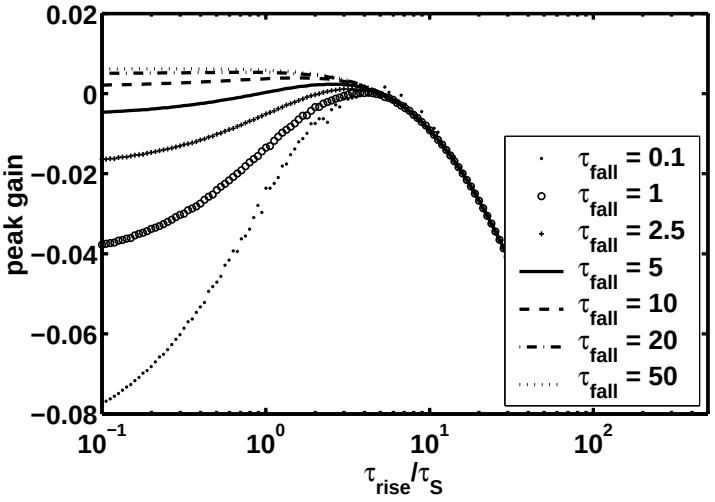

FIGURE 2.10: Maximum gain as a function of rise time at constant pump peak intensity and various fall times. Parameters are $R_{max} = 0.115, \tau_S = 1, \tau_T = 1000, \tau_{rise} = 10, \sigma_S = 0, \sigma_T = 0.2, \sigma_0 = 0.1$.

intensity is the most important figure of merit for the threshold condition, in particular when the rise time is at the order of or shorter than τ_S.

On the other hand, we expect a priori that for very short pulses the pump fluence is the relevant parameter. Hence, with increasing pulse duration there has to be be a transition regime until we are in a regime as above where the peak intensity is more relevant. This transition is studied with symmetrical pulses. Figure 2.11 shows the maximum gain achieved depending on the pump pulse duration. In the top graph, the pump fluence was fixed to a value just above the lowest threshold (in terms of fluence). We see that above $0.01 \cdot \tau_S$ the maximum gain drops off with increasing pulse duration but it is constant below. Hence, for very short pulses the maximum gain (for a given fluence) and therefore also the threshold fluence are the same irrespective of pump pulse duration. The bottom graph in figure 2.11 is similar but for fixed pump peak intensity. We see that the gain and thus the threshold depends strongly on the pump pulse duration. For pulses longer than $0.01 \cdot \tau_S$ both threshold values, threshold fluence and threshold peak intensity, depend on the pump pulse duration and fair comparisons can be very difficult. Note that for the longest pulses in this graph it is effectively the rise time only that governs how much gain is obtained.

2.1.5.4 Summary

In general, neither the fluence nor the peak intensity are good measures of threshold by themselves. Both values should always be provided (or at least the pump pulse duration should be specified) in order to allow fair comparison and even then the exact pulse

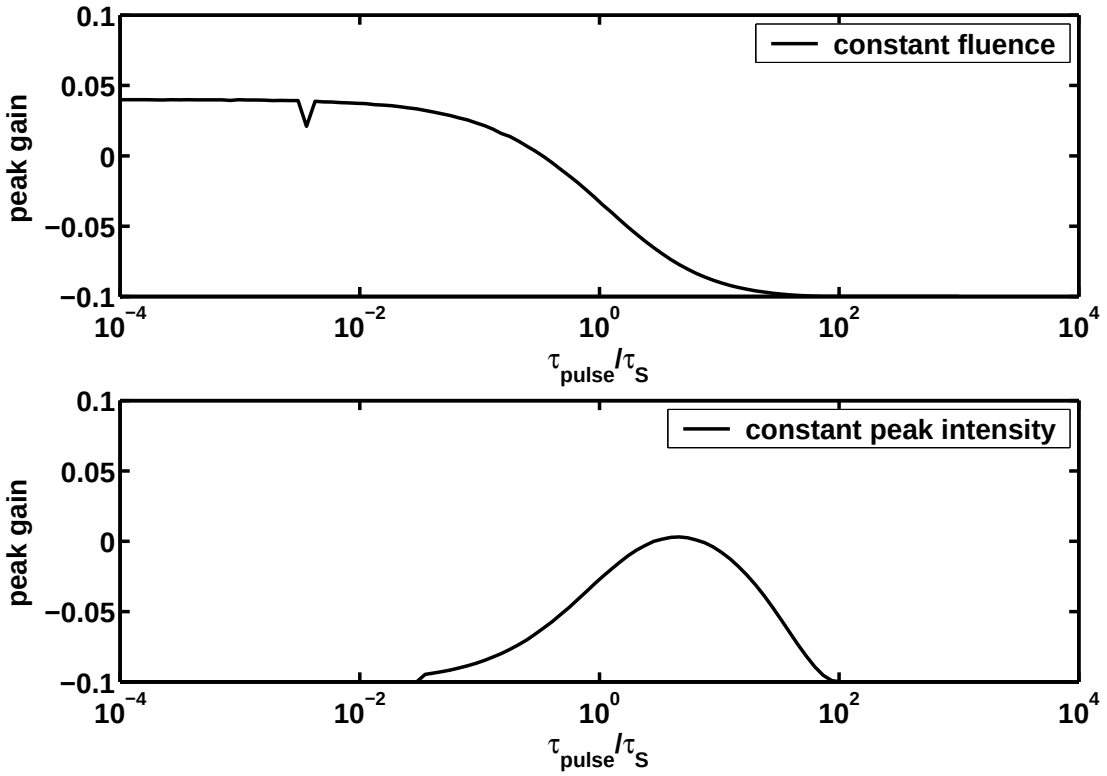

FIGURE 2.11: *Top:* maximum optical gain depending on the pulse duration for a fixed pulse fluence ($R_{max} \cdot \tau_{pulse} = 0.12$). *Bottom:* maximum optical gain depending on the pulse duration for a fixed peak intensity ($R_{max} = 0.13$). Parameters are $\tau_S = 1, \tau_T = 1000, \tau_{rise} = 10, \sigma_S = 0, \sigma_T = 0.2, \sigma_0 = 0.1$.

shape may have a significant influence. In particular, the following regimes have been identified:

1. **Short pulse**

   τ_{pulse} about two (or more) orders of magnitude smaller than τ_S:

   In this case the threshold fluence is the relevant measure and is independent of the pulse duration. The threshold peak intensity is irrelevant.

2. **Short rise time, long fall time**

   Asymmetrical pulse with long fall time, $\tau_{fall} > \tau_{ST}$, and τ_{rise} at the order of or shorter than τ_S:

   In this case the peak intensity is a good and consistent measure for threshold. Overall pulse duration and threshold pump fluence are irrelevant.

3. a) **Medium rise time, long fall time**

   $\tau_{fall} > \tau_{ST}$, $\tau_{rise} > \tau_S$, $\tau_{rise} < \tau_{ST}$:

   In this case the peak intensity is a good measure for threshold but depends strongly on the rise time (the shorter, the better). Overall pulse duration and threshold pump fluence are irrelevant.

b) **Long rise time (fall time irrelevant)**
Fixed rise time at the order of τ_{ST} or longer:
In this case the peak intensity is a good measure for threshold but depends strongly on the rise time (the shorter the better). Fall time, overall pulse duration and threshold pump fluence are irrelevant.

4. **Medium rise and fall times**
$\tau_{pulse} > 0.01 \cdot \tau_S$ but neither $\tau_{rise} > \tau_{ST}$ nor $\tau_{fall} > \tau_{ST}$:
This is the somewhat unfortunate regime, where neither the threshold fluence nor the threshold peak intensity are really consistent measures in any way. Comparison of results - different pump lasers or even different materials pumped by the same laser - are notoriously problematic and only order-of-magnitude differences can clearly be classed as meaningful.

Only regimes 1 and 2 allow precise and straight forward comparisons of experiments using different materials and/or different pump sources. However, for practical reasons - in particular availability of suitable pump sources - most reported experiments were done in regime 4.

Implications for LED pumping: The optical pulses emitted by LEDs that are driven by a laser diode driver are asymmetrical. The rise time depends on the LED itself and the driver electronics. Typical values are $\tau_{rise} \approx 10 - 15$ ns. The rise time appears to stay fixed, independent of the peak current delivered by the driver. However, the fall time changes dramatically with drive current. Values from 10 ns just above turn on up to more than 50 ns at several kA/cm^2 have been observed. However, this is no reason for concern. It is only the rise time and the peak intensity that matter. This can be seen in figure 2.9 which in fact represents a typical LED-pumping scenario. It should in practice be aimed to have as short rise times as possible without compromising the peak intensity.

2.2 Organic Solid State Lasers

Organic solid state lasers (OSL) [1] were first demonstrated in the early 1970s in distributed feedback (DFB) [20] and distributed Bragg resonator (DBR) [21] formats, using dye-doped transparent host polymers as gain material. It was not until the mid-1990s that improvements in material processing and the materials themselves led to renewed

[1] It should be noted that from the point of view of this thesis (with emphasis on optical excitation) organic semiconductor lasers in particular and organic solid state lasers in general are not distinguished, i.e. the acronym "OSL" can refer to either.

interest in the field and, by 1996, groups working in the field of organic LEDs reported laser emission from films of π-conjugated polymers [22] for the first time. Since then, OSLs were fabricated in various different formats, the most common one being DFB lasers. These can be one-dimensional [20, 23–126], two-dimensional [23, 25–28, 127–143] or circular [144–146] gratings (or more generally: photonic crystals) that are created within a planar waveguide film of active material. As opposed to hard-coding the grating into the film, another popular method is to impose the grating by interference of the pump laser beam with itself thus obtaining periodic gain modulation in the film [119, 147–156], achievable for example in a Lloyd-mirror-arrangement. The above DFB-resonators rely on in-plane feedback in the active layer. It is also possible to create a vertical cavity DFB layout, where (in contrast to conventional vertical cavity surface emitting lasers) the active medium is not sandwiched in between Bragg mirrors but one of the two alternating layers in the Bragg grating is actually made from the gain material [157–159]. A special type of DFB lasers are liquid-crystal lasers, where a transparent polymer is doped with dyes and liquid crystals (LCs) [160–174]. Optical feedback is provided by the periodic structure formed by the self-organisation of the liquid crystal molecules. At the moment, however, their interesting properties seem hampered by high thresholds of typically several mJ/cm^2. The various types of DFB laser resonators are illustrated in figure 2.12.

Of course, resonator types other than DFB structures are feasible as well. OSLs have been realised in the format of traditional cavities (rod + two mirrors) [175–183], a variation of this with only one mirror and utilising a high quality polished facet of the rod as outcoupler [184–194], vertical cavity surface emitting lasers (VCSELs) [7, 22, 195–200], the vertical external cavity surface emitting organic laser (VECSOL) [201], DBR lasers [12, 21, 23, 24, 127, 202], slab waveguides with feedback by reflection from end-facets [7, 203–208], doped optical fibres [209–211], Shoshan cavities (using a grating for colour-tuning and out-coupling) [193, 212–214], whispering gallery mode (WGM) lasers [23, 215–226] and random lasers [12, 198, 227–246]. Schematics of all these cavity types are shown in figure 2.13.

2.2.1 Distributed Feedback Lasers

In this section, the performance characteristics of organic DFB lasers reported in the literature will be compared. The restriction to DFB lasers, only, is justified by the fact that other laser types have significantly higher thresholds (compare section 2.2.1.3 below) and thus are currently not as relevant from the point of view of integration onto micro-LEDs.

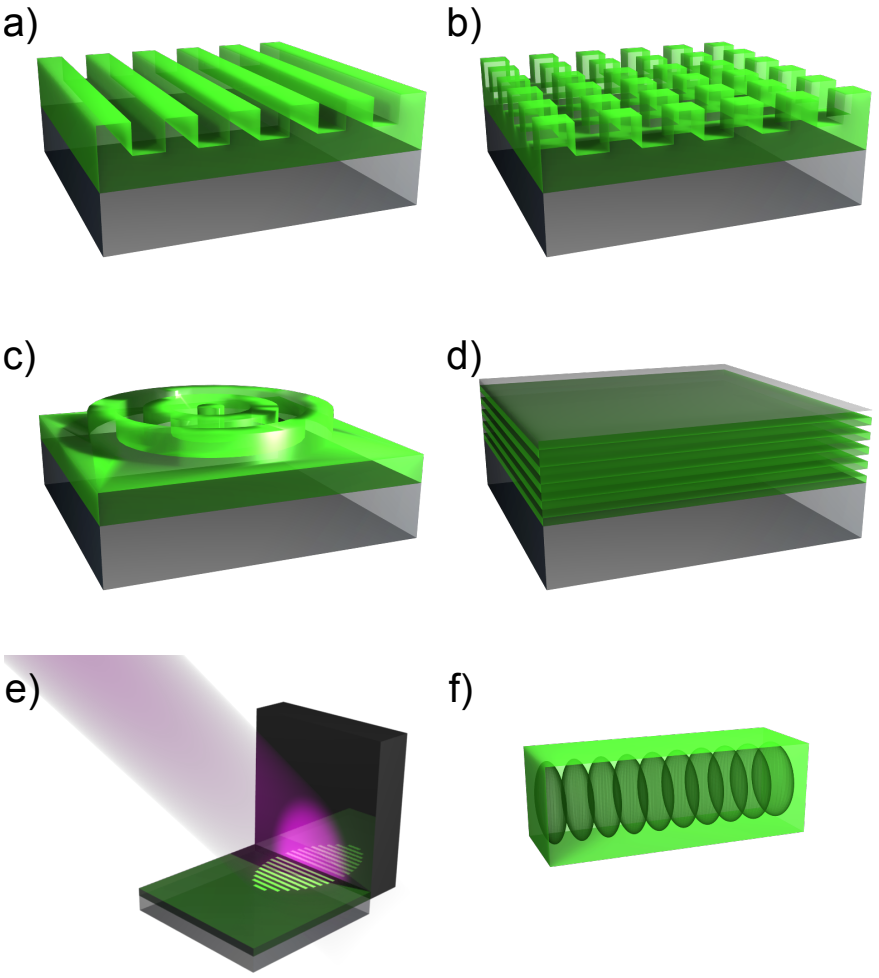

FIGURE 2.12: Various types of DFB lasers: *a)* one-dimensional grating, *b)* two-dimensional grating, *c)* circular DFB resonator, *d)* vertically stacked DFB structure, *e)* DFB by pump beam interference, *f)* liquid crystal laser.

A DFB laser is defined as a laser device with a periodic structure within the amplifying medium such that the laser output characteristics are dominated by resonant scattering at the (wavelength-scale) periodic features. In the simplest case this can be achieved by a slab waveguide made from the active medium with a one-dimensional grating pattern of the effective refractive index. The effective refractive index pattern is often achieved by a variation of active film thickness, see figure 2.12a, but can also be obtained by spatial variation of the actual refractive index. A one-dimensional DFB-grating is said to be of "n^{th} order" if the laser vacuum wavelength λ and the grating period Λ are related by [5]:

$$2\langle n_{eff}\rangle\Lambda = n\lambda \tag{2.6}$$

where $\langle n_{eff}\rangle$ is the spatially averaged in-plane effective refractive index of the patterned slab waveguide. In the case of organics, typical values are $\langle n_{eff}\rangle \approx 1.5 - 1.6$. Compare section 4.1.3 for values of devices fabricated during this work. If equation (2.6) is fulfilled

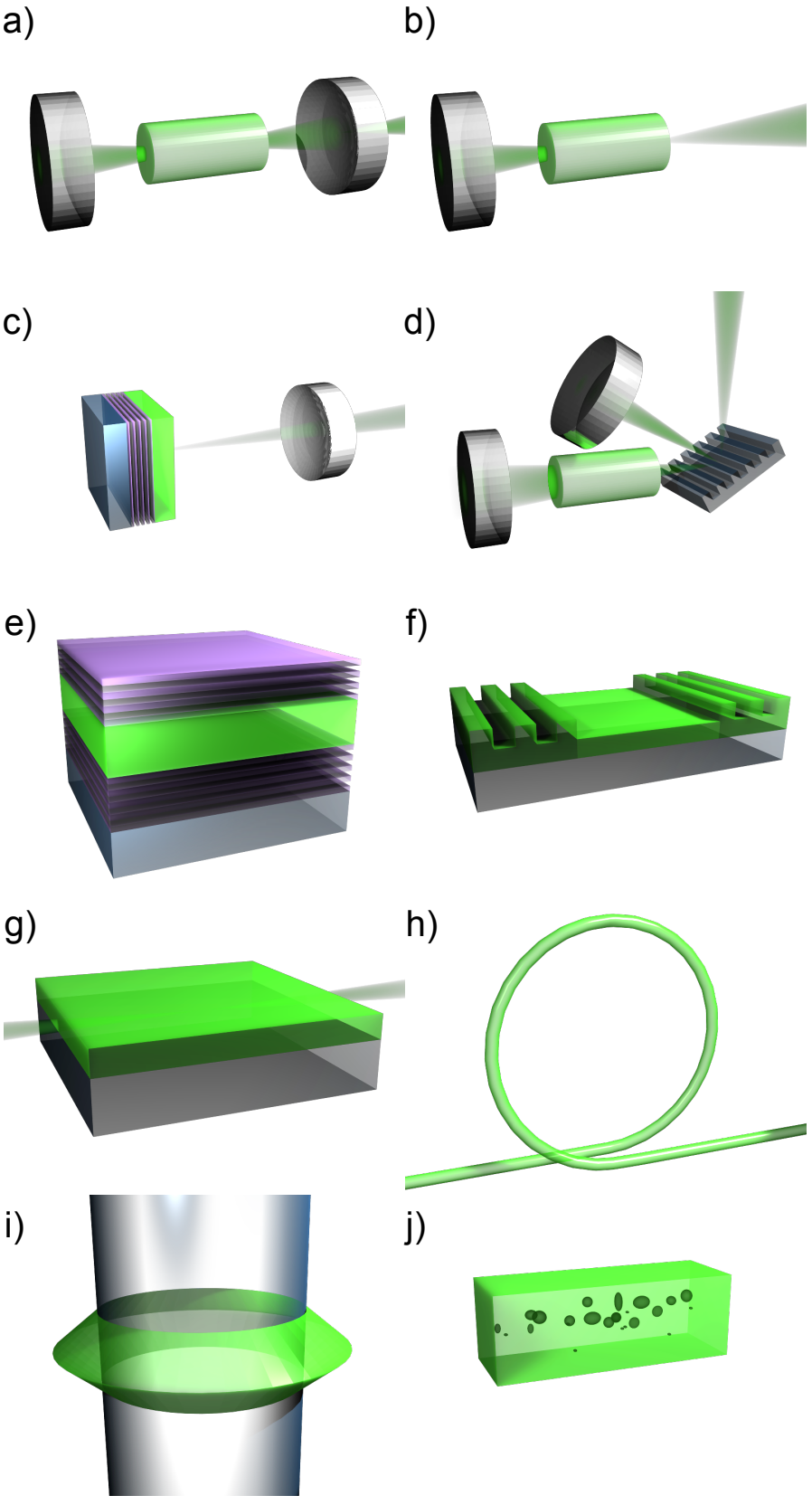

FIGURE 2.13: Resonator geometries used for organic lasers: *a)* classic cavity, *b)* variation using the polished end facet of the rod as out-coupler, *c)* VECSOL, *d)* Shoshan cavity, *e)* VCSEL, *f)* DBR laser, *g)* slab waveguide with high-quality end-facets, *h)* doped fibre, *i)* WGM laser, *j)* random laser.

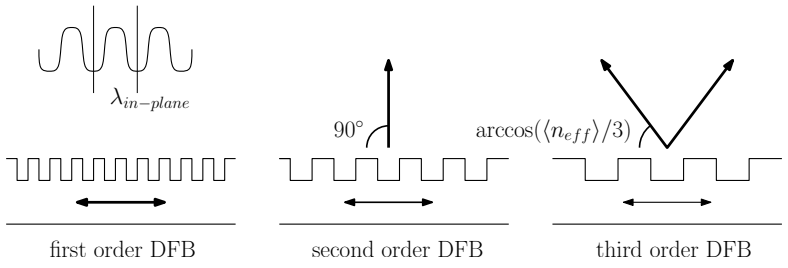

FIGURE 2.14: Illustration of first, second and third order DFB gratings.

then Bragg scattering of n^{th} order prohibits propagation of light in the waveguide in a perpendicular direction to the grating, i.e. it causes a photonic stop band. This mechanism provides the feedback necessary for laser operation. Bragg scattering of order $< n$ may couple the laser light out of the plane of the waveguide if the angle of emission θ (measured with respect to the surface normal) fulfils the following condition:

$$\frac{n}{2}\left(1-\frac{\sin(\theta)}{\langle n_{eff}\rangle}\right)=m, \qquad m=1,2,3,\ldots \tag{2.7}$$

Equation (2.7) immediately implies that that there is no surface emission from first order gratings and second order gratings have a solution for $\theta = 0$, i.e. laser light is emitted perpendicularly to the surface. An illustration can be found in figure 2.14.

The vast majority of organic DFB lasers use either 1^{st} or 2^{nd} order gratings. In the first case, devices are edge-emitting and 1^{st} order Bragg scattering provides strong feedback. In the case of a 2^{nd} order DFB laser, feedback due to 2^{nd} order Bragg scattering is relatively weak compared to the out-coupling normal to the device surface. Second order DFB lasers are very commonly used because the larger feature size enables easier fabrication than first order gratings and the surface emitting property is convenient for characterisation and applications. Owing to the high optical gain of organics, the relatively weak second order feedback does not deteriorate the device performance unduly. However, it is interesting to note that the lowest OSL thresholds so far (see section 2.2.1.3 below) [77] were obtained by a combination of first and second order structures.

2.2.1.1 Wavelength

An important feature of organic gain media is their broad gain bandwidth of up to ∼300 meV, which is available from chromophores throughout the entire visible spectrum. This fact is illustrated in figure 2.15 which gives an overview of the wavelengths at which organic lasers operate and shows the reported tuning ranges. The shortest and longest wavelength are 361.9 nm from spiro-terphenyl chromophores [62] and 930 nm from IR-140 dye [74], respectively. Normally, OSLs are pumped at a wavelength equal to or

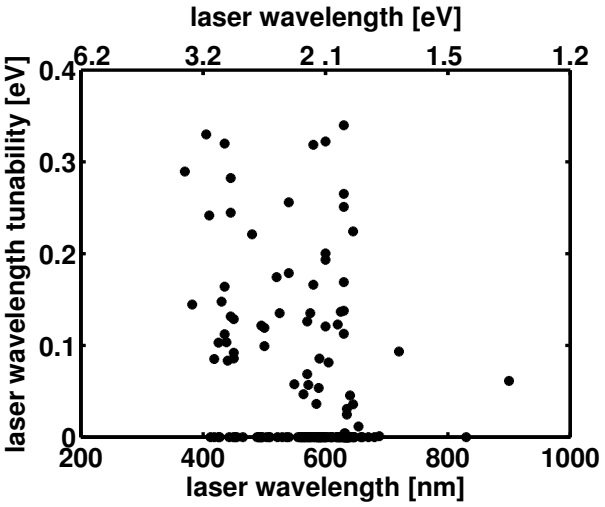

FIGURE 2.15: Summary of reported organic DFB wavelengths and tuning ranges.

shorter than the first main absorption peak. Pumping with a wavelength longer than the laser wavelength by multiphoton absorption is also possible [142], but requires high pump intensities.

A number of publications demonstrate the impressive wavelength tuning ranges of organics which can be greater than 50 nm [52, 58, 90, 104, 107, 118, 126, 133, 161, 167]. Several of them [52, 90, 107, 126, 161, 167] are based DCM dye, which allows tuning across up to 115.3 nm (0.34 eV) [52] which is to the author's knowledge the largest tuning range reported for an organic emitter in a DFB resonator. Other papers report 75 nm (0.21 eV) tuning range for red-emitting fluorene-copolymers [133], 60 nm (0.25 eV) for thianthrene substituted distyrylbenzene [58], 58 nm (0.2 eV) for PM567 [118] and 51 nm (0.32 eV) for oligofluorene truxene [104]. Bearing in mind that it is probably more relevant to look at tuning ranges in terms of photon energy, there are also outstanding near-UV results of 31.9 nm (0.28 eV) for spiro-terphenyl [62] and 45 nm (0.33 eV) for sexiphenyl based oligomers [66].

2.2.1.2 Threshold

Thresholds are typically recorded as either threshold pump fluences (F_{th}, measured in μJ/cm^2) or as threshold pump intensities (I_{th}, measured in kW/cm^2). It was pointed out above in section 2.1.5 that in most cases neither value is meaningful on its own. Thus both values are plotted against each other in figure 2.16. They are also plotted individually against the pump pulse duration in figure 2.17. Interestingly, the lowest thresholds in terms of both fluence and intensity were obtained with few-nanosecond pump pulses. From figure 2.16 it can be seen that looking at threshold fluences and

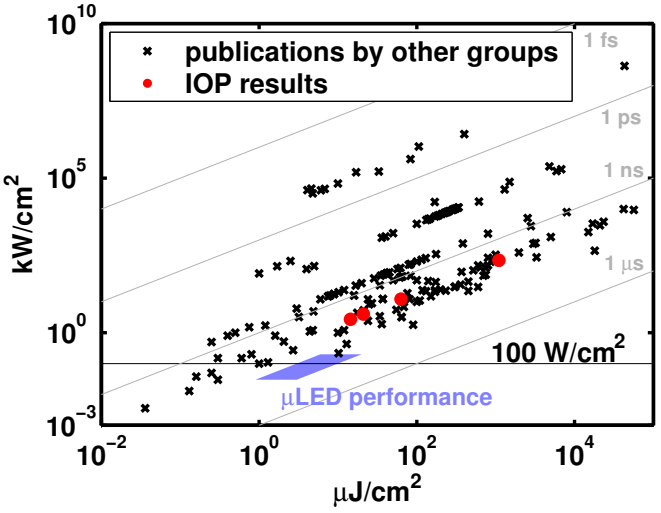

FIGURE 2.16: Summary of reported organic DFB laser thresholds. Results obtained at the Institute of Photonics during the course of this work are highlighted [29, 30]. For reference, the typical regime of micro-LED performance in pulsed operation is indicated, see also chapter 6. The grey lines indicate constant pump pulse durations. Compare also figure 6.18.

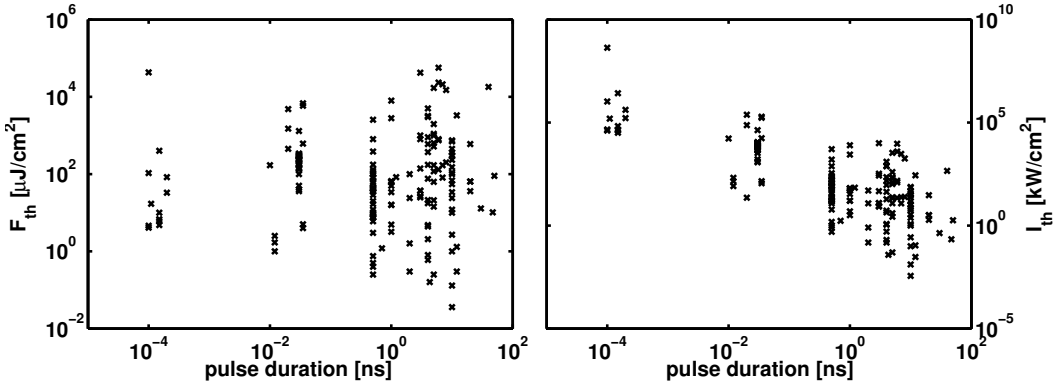

FIGURE 2.17: Summary of reported DFB thresholds in terms of threshold fluence (left) and threshold peak intensity (right) as a function of pulse duration.

intensities each on their own, GaN micro-LEDs can deliver the required fluence/intensity values. However when looking at the two in combination, there is no good overlap between micro-LED pulses (developed so far) and reported threshold values. This is probably due to two reasons. First of all, sources such as in particular GaN laser diodes (LDs) that are attractive despite having long pump pulses have only recently become available and were only used in a limited number of publications (see section 2.2.1.5). The majority of reports use nano-second pulsed solid-state or gas lasers that have different optical pulse durations and shapes than LDs or LEDs. Furthermore, as explained in section 2.1.5, LEDs operate in a regime where the optical pulse rise time is crucial. So far no optimisation for this aspect has been reported except for flashlamp-pumped dye-lasers.

2.2.1.3 Outstandingly low thresholds

Five devices with threshold below 100 W/cm^2 have been reported [50, 71, 77, 84, 93]. The chromophores that allowed these results are DCM, fluorene-based copolymers and pyrenes. The lowest threshold to my knowledge is 36 nJ/cm^2 (3.6 W/cm^2) obtained with a fluorene-copolymer and a mixed order grating [77]. There are also further reports of thresholds below 250 W/cm^2 [23, 40, 85, 91]. In principle, therefore, there is prospect for all of these to be pumped by LEDs.

Reported thresholds for other cavity-types are significantly higher than all the above reports. Probably the most outstanding result in terms of W/cm^2 is a micro-cone laser tested with two different pump sources yielding thresholds of 3.5 μJ/cm^2 ($>$ 700 W/cm^2) and 16 μJ/cm^2 (800 W/cm^2), respectively [224]. There is also a report of a ring laser (coated silica fibre) with 0.2 μJ/cm^2 (2 kW/cm^2) though this is in terms of absorbed pump energy only [216]. There are several more reports of non-DFB OSLs that have thresholds in the range $1-10$ μJ/cm^2 and $1-10$ kW/cm^2 [7, 203] (faceted slab waveguide), [23, 127, 202] (DBR).

2.2.1.4 Pump spot geometry

Circular, slightly elliptical and stripe-shaped pump spots have been used to pump organic DFB lasers within a wide range of pump spot sizes, the smallest being 4 μm diameter [106] and the largest 3 mm $\times$ 2.5 cm [127]. An overview of reported pump spot geometries in terms of area and ellipticity (ratio of long to short axis) is given in figure 2.18. The lowest reported thresholds were obtained with roughly symmetrical pump spots of 5×10^{-4} cm^2 area which corresponds to a circle of 250 μm diameter. However these are only very few data points within the bulk of OSL reports and no dedicated optimisation of the pump spot geometry was reported. Overall, there is no clear trend in the literature as to how the pump spot geometry influences the threshold. A systematical study of pump spot geometries for DFB lasers was done by Y. Wang [247] as part of a joint research project with the author and will briefly be discussed in section 6.3.1. In short, a stripe of a few 100 μm width and several mm length gave the best results.

2.2.1.5 Pump sources

Typical pump sources for OSLs are frequency-doubled or -tripled Nd:YAG lasers (532 nm or 355 nm, respectively), nitrogen lasers (337 nm), frequency doubled Ti:sapphire lasers (400 nm) and optical parametric oscillators (variable wavelength). Less common are

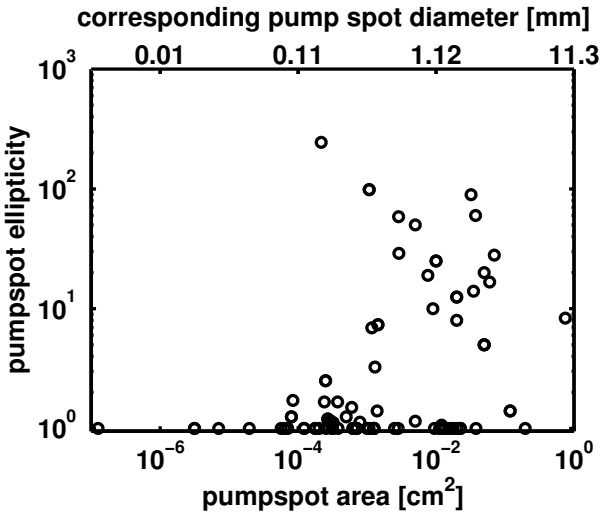

FIGURE 2.18: Pump spot geometries used to pump organic DFB lasers in terms of pump spot area and ellipticity. For reference, the top x-axis indicates the diameter of a circular pump spot with given area.

dye lasers (wavelength depending on the dye and resonator) and frequency doubled ruby lasers (347.15 nm). There has been a move towards more compact sources, the first being a diode-pumped passively Q-switched Nd:YAG microlaser (355 nm) demonstrated in 2001 [37]. Nd:YVO_4 microchip lasers (532 nm or 355 nm) have now been employed so many times [25, 49, 79, 80, 98, 104, 130, 134, 139] that they may be regarded as a standard technique. Inorganic semiconductor sources have been used in a few cases, namely GaN laser diodes at 405 nm [72, 122, 140, 158] or 445 nm [143] and broad-area GaN LEDs (450 nm) [85]. An organic DBR-laser [202], an organic VCSEL [197] and a micro-cone laser [224] have been pumped with GaN laser diodes as well.

2.2.2 Stability

In section 2.1.4, it was pointed out that upon excitation with pump light, organic chromophores are prone to degradation due to photo-induced oxidation which ultimately limits the useful lifetime of the device. Here, we use two figures of merit to characterise device lifetime, which are the total pump dosage F_{deg} (measured in J/cm^2) that the sample has been exposed to during its lifetime and the ratio of this value to the threshold fluence, F_{deg}/F_{th}. Since different specifications of the lifetime were used in the literature ($1/2, 1/e, 10\%$-lifetime, or unspecified), these numbers allow only an order-of-magnitude comparison. Investigations by Richardson *et al.* [26, 139] and Sakhno *et al.* [118] indicate that the degradation dosage F_{deg} does not have a strong dependency on the pump fluence and repetition rate.

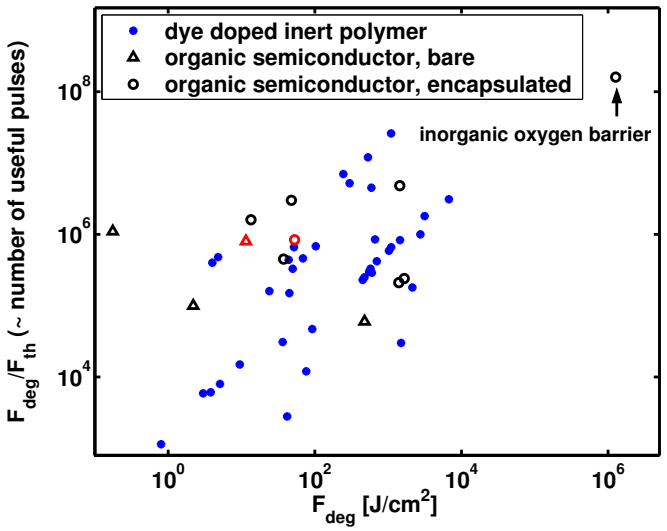

FIGURE 2.19: Overview of the useful operational lifetime that has been reported for OSLs in the literature. Results presented in this thesis in section 4.1.4 are highlighted in red.

A summary of reported lifetime data of organic DFB lasers is given in tables 2.1, 2.2, 2.3, 2.4 and 2.5 and also illustrated in figure 2.19. Both figures of merit vary over a huge range of values. The degradation energy dosage (which also serves as an indicator of how stable the device will be to any UV illumination, e.g. sunlight) varies in between 18 mJ/cm^2 for pyrenes [93] and more than 1 MJ/cm^2 in case of an encapsulated PPV derivative [139]. The F_{deg}/F_{th} value spans six orders of magnitude, $10^3 - 10^8$. It is also noteworthy that so far only very few lasers using organic semiconductors (as opposed to dye doped inert materials) have been investigated for their lifetime. Currently, the most efficient encapsulation techniques involve layers of inorganic materials. Such encapsulation is successfully used in OLEDs to a standard suitable for commercial application. However, these devices do not have the mechanical flexibility of all-organic devices. In section 4.1.4 of chapter 4 we demonstrate an all-organic encapsulation that enhances the degradation dosage F_{deg} by a factor 5. Recently it was demonstrated that in a suitable polymer matrix dye molecules can undergo a diffusive motion and thus an OSL employing such material can partly recover from degradation similar to dye-solution lasers [125].

A substantial number of operational lifetime experiments mostly on dye-doped polymers used different resonator geometries than DFB. Tables 2.6 and 2.6 summarise those that specify both figures of merit, F_{deg} and F_{deg}/F_{th}. There are numerous further investigations that report only one or none of these two values [175, 176, 178, 181, 184–188, 188, 190–194, 211, 213, 214, 217, 218]. An outstanding result among these was obtained from a PM567-doped rod with a single mirror for feedback (geometry b) in figure 2.13), having a degradation fluence of $F_{deg} = 10.8$ kJ/cm^2 yielding 60000 pulses operation at 180 mJ/cm^2 pump fluence, however no threshold was measured [185].

2.2.3 Towards CW Organic Laser Operation

Only two years after the first organic dye-laser [4], it was recognised that dye molecules can only deliver gain for a short period of time (of the order of nanoseconds) and for the laser to work at all it was necessary to use pump pulses with a short rise time [248]. This is a result of the triplet state build-up that was already looked at in section 2.1.5. When pumping a dye or LEP with a CW pump source, then the singlet and triplet populations are clamped:

$$\left.\frac{n_S}{n_T}\right|_{CW} = \frac{\tau_{ST}}{\tau_T} \qquad (\dot{\approx} 0.01) \tag{2.8}$$

Equation (2.8) is the steady-state solution of the rate equations (2.1) and (2.2). Noting that $n_S + n_T \leq 1$, equation (2.3) gives us an upper limit for the gain that can be obtained by CW pumping[2]:

$$g_{0,CW} \;\leq\; \frac{1}{1+\tau_T/\tau_{ST}}\sigma_0 - \frac{1}{1+\tau_{ST}/\tau_T}\sigma_T \;\approx_{\tau_{ST}\ll\tau_T}\; \frac{\tau_{ST}}{\tau_T}\sigma_0 - \sigma_T \tag{2.9}$$

Since τ_{ST} is significantly smaller than τ_T, gain could only be achieved if σ_T is several orders of magnitude smaller than σ_0. Some simplifications made here, e.g. ignoring the Stokes shift, make the situation look worse than it really is. However, the general result holds true that in order to obtain CW gain, σ_T has to be very small compared to the stimulated emission cross section. In dyes this is simply not the case and CW or mode-locked dye-lasers were normally operated by circulating a liquid dye solution to circumvent this problem. CW operation has also been obtained using a solid state organic film on a rotating disk, though it is difficult to obtain low-noise laser output due to inhomogenities in the film [249, 250].

In organic semiconductors the same fundamental problem exists though some LEPs have a good spectral separation between triplet state absorption and laser wavelength so that the ratio σ_T/σ_0 is much smaller than in most organic chromophores [117]. Zhang and Forrest [122] recently claimed that introducing a triplet quenching mechanism (that reduces τ_T) can be sufficient to allow CW operation. They back up their claims by experimental verification that stimulated emission can occur over a duration of a few tens of micro-seconds which is orders of magnitudes longer than previously reported and possibly only limited by material degradation. It is not clear whether true CW operation

[2]Strictly speaking, the upper boundary is:

$$g_{0,CW} \leq \begin{cases} -\sigma_0 & , \quad \sigma_T \geq \sigma_0(1+2\tau_S/\tau_T) \\ g_{0,CW,max} & , \quad \text{else} \end{cases}$$

where $g_{0,CW,max}$ is the value given by equation (2.9). The first case, however, represents a scenario of strong triplet absorption where any CW pumping will only increase the losses and the lowest loss (i.e. highest "gain", mathematically) will be found when the pump is switched off.

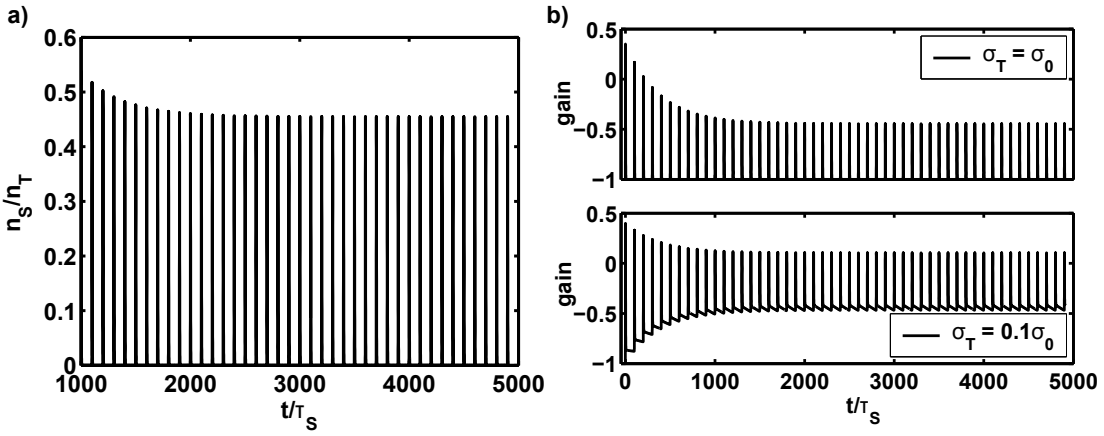

FIGURE 2.20: Modelling of quasi-CW pumping: *a)* Ratio of singlet and triplet populations after some relaxation time. *b)* Optical gain for two different triplet state absorptions σ_T at the laser line. The x-axis is the time in units of the singlet state lifetime τ_S starting with the first incident pulse. Parameters were: $R_{max} = 3$, $\tau_P = \tau_S$, $\tau_{ST} = 10\tau_S$, $\tau_T = 1000\tau_S$ and the separation between two consecutive pump pulses was $\tau_{rep} = 100\tau_S$.

can be achieved this way but the results are encouraging. A similar experiment (declared as "CW pumping") using very long pump pulses was reported earlier by Yamashita *et al.* [251] though their measurements lack the crucial time-resolved recording of the organic laser emission and therefore it is unkown for how long gain was really present.

As opposed to true CW operation, it is also feasible to strive for quasi-CW lasers that operate in pulsed mode but at very high repetition rates. OSL operation at 5 MHz repetition rate has indeed been reported [76] and was later attributed to the low triplet state absorption of the material that was used for this experiment [117]. The rate equation model from section 2.1.5 can give some insight into this. Figure 2.20 shows numerical solutions of equations (2.1), (2.2) and (2.3) under a scenario of high repetition rate pumping. First of all, we see from figure 2.20a that, even after numerous pump pulses, the peak singlet population of $n_{S,peak}/n_T \approx 0.45$ is still considerably larger than the CW value $n_S/n_T|_{CW} = 0.01$. The importance of having low triplet absorption is visible in figure 2.20b. If the triplet absorption cross section is of the same order of magnitude as the stimulated emission cross section, then gain can only be provided for the first few pulses. However if the triplet state absorption is one order of magnitude lower then positive gain is reached for all pulses. It is important to note here that even in the latter case, true CW operation is not possible.

Various schemes for CW organic lasers are illustrated in figure 2.21.

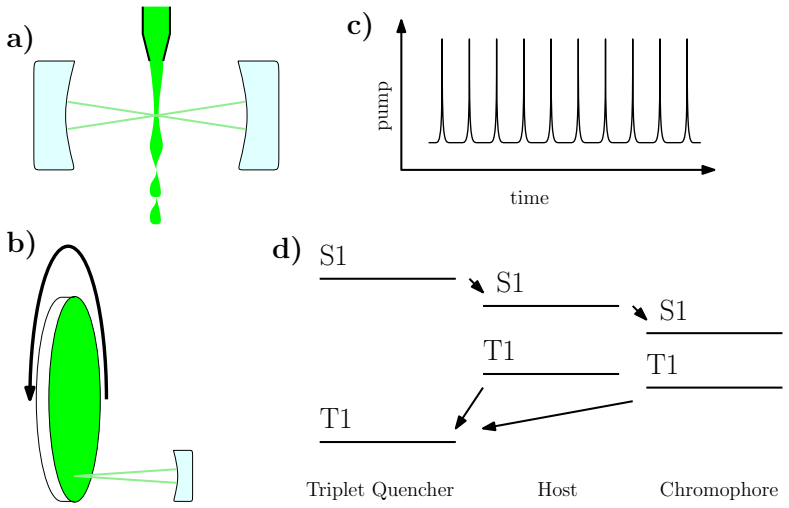

FIGURE 2.21: Schemes for CW operation in organic lasers: a) liquid dye-solution jet passing through the cavity, b) rotating disk with solid state organic film, c) Quasi-CW pumping at high repetition rate, d) triplet quenching using sophisticated material-compositions.

2.3 Electroluminescent Devices

In 1965, about a year before the first demonstration of organic dye lasers, it was recognised that certain organic molecules can be electroluminescent [252]. However, the poor carrier mobility in these early attempts required voltages of several 100 V to several kV and it took until 1987 and 1990, respectively, that OLEDs based on molecular solids [253] and conjugated polymers [254] could be driven with voltages on the order of 10 V. To date, OLEDs have matured to commercially available products. During the 1990's, the same materials that were used in OLEDs were successfully used as gain materials [22, 127], sparking great excitement about the possibility of an electrically pumped organic laser diode which culminated in the infamous Schön-affair at Bell Laboratories when a report of an organic laser diode had to be retracted [255, 256]. During the efforts undertaken since, it has become clear that an organic laser diode is an enormous challenge due to the reasons given below in this section. Interest still exists and recent advances include laser action from a complete OLED structure under optical excitation [110] and OLEDs with partially coherent output [257, 258]. The latter results were vividly debated and in conclusion these devices cannot satisfactorily be claimed to be laser diodes [259].

2.3.1 Challenges of Achieving an Organic Laser Diode

First of all, any electrical injection laser suffers from noticeably increased intra-cavity losses as compared to similar optically pumped devices. This is due to the usually

metallic electrical contacts which absorb the laser light and cause the threshold carrier density to be higher than for a structure without electrodes. Recent results of laser operation from optically pumped organic field effect transistor (OFET) [99] OLED [110] structures (including metallic contacts) prove that this issue can be overcome in the case of organics. In fact, in the case of the OFET only a modest increase in threshold from 4.1 μJ/cm^2 to 4.6 μJ/cm^2 (100 fs pump pulses) was caused by the metallic electrodes [99]. There are however a number of further challenges intrinsic to the particular electronic properties of current organic gain media.

Due to the relatively weak inter-molecule delocalisation, charge carriers in organics have a low mobility of less than 0.1 cm^2/Vs [6] (which compares to more than 100 cm^2/Vs in group-III nitride semiconductors [260]). Therefore it is generally difficult to drive sufficiently high currents through the film to reach threshold carrier density. Furthermore, low carrier mobility causes a slow response to changes in the drive voltage. Electroluminescence response times of a few μs are considered fast for an OLED [261] and the fastest OLED rise times to my knowledge reported so far are on the order of 40 ns [262] which is longer than the few-nanosecond regime favoured for OSL operation. Hence, organic laser diodes suffer from the same problem of triplet state absorption as CW organic lasers.

Not only will triplet excitons accumulate over time in an electrically driven device but, contrary to optical pumping, electrical injection will create a significant triplet population right from the start. A priori, one would expect that three out of four electron-hole pairs that where injected electrically will form a triplet exciton. Experimentally, spin-dependent formation rates were observed in some polymeric materials and the fraction of electrically generated singlets can be enhanced to over 50% [263], but still triplet absorption remains an important issue even if nanosecond current pulses could be achieved. Due to the large number of generated triplet excitons, phosphorescent emitters are favourably used in current OLEDs.

Current injection into organic films also generates polarons, i.e. charged states of LEP molecules. These polarons will absorb light at the laser wavelength.

Finally, given that due to the above reasons a much higher carrier density is needed compared to optical pumping, higher order recombination effects such as exciton-exciton annihilation may play a role as well.

2.4 Conclusion

Conjugated polymers can be tailored to deliver fluorescence and broad gain-bandwidth throughout the visible spectrum. Delocalisation of π-electrons along the polymer backbone enables semiconductor-like charge transport and highly efficient photo- and electroluminescence. The nature of their electronic states, in particular the existence of two types of excited states, singlet and triplet, has significant impact on their optical properties. To date, organic lasers are optically pumped using pulsed excitation sources. CW operation is inhibited by the build-up of triplet-state population and its associated excited state absorption at the laser wavelength. Schemes towards CW and quasi-CW operation exist, but a true CW organic solid state laser has not yet been achieved.

Attempts on micro-LED pumped lasers will therefore concentrate on short pulsed excitation. Crucial factors in LED-pumping experiments will be the LED peak power and the rise-time of the pulse. OSLs with thresholds below 100 W/cm^2, obtained in DFB format with few-nanosecond pulses, are possible though the vast majority of reported OSLs exceeds this value by orders of magnitude. Ideally, the rise time should be as short as the singlet state lifetime, i.e. roughly one nanosecond. This can probably not easily be achieved without compromising the peak power (compare section 6.2) and therefore in practice the rise time should be kept as short as possible. The most promising resonator layout for achieving low thresholds appears to be the DFB laser.

While efficient OLEDs have been a great success, it has not yet been possible to electrically pump an organic laser. Given the enormous challenges associated with this goal, LED-pumping may be an attractive alternative. The main competitors to LEDs as pump sources are GaN laser diodes and solid state micro-chip lasers.

A fundamental problem of organic light emitters is their susceptibility to photo-oxidation. Driven by the OLED industry, effective encapsulation schemes exist, however only in non-flexible format. Photo-stability of organic devices particularly in mechanically flexible format remains an interesting research area.

chromophore	encapsulation	F_{th} [μJ/cm^2]	I_{th} [kW/cm^2]	F_{deg} [J/cm^2]	F_{deg}/F_{th}	reference
DCM	doped molecular solid	16	> 16	$4.8 - 48$	$3 \times 10^5 - 3 \times 10^6$	[37]
DCM	vacuum	16	> 16	160	10^7	[37]
PM567	doped polymer	42	84	513	1.2×10^7	[43]
Rhodamine 590	doped polymer	35	70	245	7×10^6	[43]
DCM	doped polymer	57	114	298	5.2×10^6	[43]
Rhodamine 640	doped polymer	42	84	1098	2.6×10^7	[43]
LDS722 dye	doped polymer	79	158	52	6.6×10^5	[43]
R6G	doped polymer	520	104	3 (?)	5.9×10^3 (?)	[39]
R6G	doped polymer	640	128	5.1 (?)	8×10^3 (?)	[39]
R6G	doped polymer	1970	394	92.4	4.7×10^4	[39]
Fluorene-copolymer	vacuum	10	1	1400	1.4×10^8	[133]
IR-140 dye	vacuum	37	12.3	0.38	1.03×10^4	[74]
PPV	NOA68 + glass	7960	7960	1.27×10^6	1.6×10^8	[139]
PPV	none	7960	7960	477	6×10^4	[139]
Rhodamine 640	doped polymer	131	22	≤ 590	$\leq 4.5 \times 10^6$	[146]
Coumarin 540	doped polymer	700	70	0.8	1.14×10^3	[86]
pyrenes	none	$0.16 - 0.28$	$0.038 - 0.065$	0.176	$6.4 \times 10^5 - 1.1 \times 10^6$	[93]
perylene	doped polymer	301	30	45	1.5×10^5	[105]
T3	none	14.4	2.7	11.5 ± 5.8	$(8 \pm 4) \times 10^5$	[29]
T3	Norland 88	63	12.2	53	8.4×10^5	[29]
perylene	doped polymer	151	15	69	4.6×10^5	[101]
perylene	doped polymer	151	15	24	1.6×10^5	[101]
perylene	doped polymer	151	15	50	3.3×10^5	[101]
perylene	doped polymer	151	15	103	6.8×10^5	[101]
FB135 dye	doped polymer	613	1.75×10^4	3.8	6.1×10^3	[100]
FB135 dye	doped polymer	613	1.75×10^4	9.5	1.5×10^4	[100]

TABLE 2.1: Operational lifetime of organic DFB lasers, see also tables 2.3, 2.4 and 2.5. Continued in table 2.2.

chromophore	encapsulation	F_{th} [μJ/cm^2]	I_{th} [kW/cm^2]	F_{deg} [J/cm^2]	F_{deg}/F_{th}	reference
oligofluorene	glassy LC film	6800	1.94×10^5	> 1400	$> 2.1 \times 10^5$	[170]
oligofluorene	fluid LC film	6800	1.94×10^5	1660	2.4×10^5	[170]
PM567	doped polymer	6	12	4	4×10^5	[118]
PM567	doped polymer	6	12	4.8	4.8×10^5	[118]
perylene	doped polymer	100	10	44	4.4×10^5	[123]

TABLE 2.2: Operational lifetime of organic DFB lasers. Continuation of table 2.1.

chromophore	pump level	repetition rate	lifetime	number of pulses	F_{deg} [J/cm^2]	F_{deg}/F_{th}	reference
DCM (molecular solid host)	3× threshold	10.8 kHz	9-90 sec	$10^5 - 10^6$	$4.8 - 48$	$3 \times 10^5 - 3 \times 10^6$	[37]
DCM (molecular solid host and vacuum)	3× threshold	10.8 kHz	15 min	10^7	160	10^7	[37]
PM567 (in polymer matrix)	27× threshold	100 Hz	75 min	4.5×10^5	513	1.2×10^7	[43]
Rhodamine 590 (in polymer matrix)	2.5× threshold	100 Hz	7.8 h	2.8×10^6	245	7×10^6	[43]
DCM (in polymer matrix)	3.5× threshold	100 Hz	4.2 h	1.5×10^6	298	5.2×10^6	[43]
Rhodamine 640 (in polymer matrix)	5× threshold	100 Hz	>13.9 h	$> 5 \times 10^6$	1098	2.6×10^7	[43]
LDS722 dye (in polymer matrix)	2.7× threshold	100 Hz	40 min	2.4×10^5	52	6.6×10^5	[43]

TABLE 2.3: Additional data to the lifetime summary in tables 2.1 and 2.2. Continued in table 2.4.

chromophore	pump level	repetition rate	lifetime	number of pulses	F_{deg} [J/cm^2]	F_{deg}/F_{th}	reference
R6G (in polymer matrix)	0.17× threshold (?)	10 Hz	57 min	3.4×10^4	3 (?)	5.9×10^3 (?)	[39]
R6G (in polymer matrix)	0.14× threshold (?)	10 Hz	95 min	5.7×10^4	5.1 (?)	8×10^3 (?)	[39]
R6G (in polymer matrix)	1.12× threshold	10 Hz	70 min	4.2×10^4	92.4	4.7×10^4	[39]
fluorene-copolymer (in vacuum)	7× threshold			2×10^7	1400	1.4×10^8	[133]
IR-140 dye (in polymer matrix and vacuum)	1.7× threshold	10 Hz	10 min	6×10^3	0.38	1.03×10^4	[74]
PPV (NOA68 + glass)	40× threshold	5 kHz	13.3 min	4×10^6	1.27×10^6	1.6×10^8	[139]
PPV (unencapsulated)	10× threshold	5 kHz	1.2 sec	6×10^3	477	6×10^4	[139]
Rhodamine 640 (in polymer)	$\leq$ 4.5× threshold			1×10^6	≤ 590	$\leq 4.5 \times 10^6$	[146]
Coumarin 540 (in polymer matrix)	1.4× threshold	1 Hz	13.3 min	800	0.8	1.14×10^3	[86]
pyrenes (unencapsulated)	10× threshold	10 Hz	3 h	1.1×10^5	0.176	$6.4 \times 10^5 - 1.1 \times 10^6$	[93]
perylene (in polymer matrix)	1.5× threshold	10 Hz	3 h	10^5	45	1.5×10^5	[105]
T3 (unencapsulated)	34.7× threshold	10 Hz	38 min	2.3×10^4	11.5 ± 5.8	$(8 \pm 4) \times 10^5$	[29]
T3 (NOA88)	7.9× threshold	10 Hz	3.5 h	1.26×10^5	53	8.4×10^5	[29]

TABLE 2.4: Additional data to the lifetime summary in tables 2.1 and 2.2. Continuation of table 2.3. Continued in table 2.5.

chromophore	pump level	repetition rate	lifetime	number of pulses	F_{deg} [J/cm^2]	F_{deg}/F_{th}	reference
perylene (in polymer matrix)	138× threshold	10 Hz	5 min	3×10^3	69	4.6×10^5	[101]
perylene (in polymer matrix)	23.7× threshold	10 Hz	11 min	6.7×10^3	24	1.6×10^5	[101]
perylene (in polymer matrix)	3.3× threshold	10 Hz	2.8 h	1×10^5	50	3.3×10^5	[101]
perylene (in polymer matrix)	2.2× threshold	10 Hz	8.6 h	3.1×10^5	103	6.8×10^5	[101]
FB 135 dye (in polymer matrix)	1.27× threshold	10 Hz	8.3 min	5×10^3	3.8	6.1×10^3	[100]
FB 135 dye (in polymer matrix)	7.3× threshold	10 Hz	3.7 min	2.2×10^3	9.5	1.5×10^4	[100]
oligofluorene (glassy LC film)	68.5× threshold	10 Hz	$>$ 5 min	> 3000	> 1400	$> 2.1 \times 10^5$	[170]
oligofluorene (fluid LC film)	81× threshold	10 Hz	5 min	3000	1660	2.4×10^5	[170]
PM567 (in polymer matrix)	10× threshold	100 Hz	7 min	4×10^4	4	4×10^5	[118]
PM567 (in polymer matrix)	10× threshold	10 Hz	1 h	4×10^4	4	4×10^5	[118]
PM567 (in polymer matrix)	20× threshold	10 Hz	36 min	2.4×10^4	4.8	4.8×10^5	[118]
perylene (in polymer matrix)	4× threshold	10 Hz	3 h	1.1×10^5	44	4.4×10^5	[123]

TABLE 2.5: Additional data to the lifetime summary in tables 2.1 and 2.2. Continuation of table 2.4.

chromophore	cavity design	encapsulation	F_{th} [μJ/cm^2]	I_{th} [kW/cm^2]	F_{deg} [J/cm2]	F_{deg}/F_{th}	reference
PM567	classic cavity	doped polymer	1900	240	475	2.5×10^5	[177]
PM580	classic cavity	doped polymer	1800	230	550	3×10^5	[177]
PM580	classic cavity	doped polymer	1750	219	1025	5.9×10^5	[177]
PM580	classic cavity	doped polymer	2000	250	450	2.3×10^5	[177]
PM597	classic cavity	doped polymer	1750	219	575	3.3×10^5	[177]
PM597	classic cavity	doped polymer	1650	208	1100	6.6×10^5	[177]
PM597	classic cavity	doped polymer	1750	219	3150	1.8×10^6	[177]
PM597	classic cavity	doped polymer	1750	219	1450	8.3×10^5	[177]
PM567	classic cavity	doped polymer	1650	208	700	4.2×10^5	[177]
PM580	classic cavity	doped polymer	2100	260	600	2.9×10^5	[177]
PM580	classic cavity	doped polymer	2650	333	2750	10^6	[177]
PM597	classic cavity	doped polymer	2150	271	6750	3.1×10^6	[177]
Rhodamine 640	VECSOL	doped polymer	11700	1670	2141	1.8×10^5	[201]
Rhodamine 640	VECSOL	doped polymer	6200	12400	76.5	1.2×10^4	[201]
DCM	VCSEL	200 nm silver	300	600	1440	4.8×10^6	[7, 195]
Coumarin 540A	VCSEL	doped polymer + silica nanoparticles	780	260	662	8.5×10^5	[197]
Coumarin 540A	VCSEL	doped polymer	1162	387	36.4	3.1×10^4	[197]

TABLE 2.6: Summary of lifetime investigations on OSLs other than DFB. Continued in table 2.7

chromophore	cavity design	encapsulation	F_{th} [μJ/cm^2]	I_{th} [kW/cm^2]	F_{deg} [J/cm2]	F_{deg}/F_{th}	reference
PPV	VCSEL	inorganic DBR layers	80	unknown	13.5	1.6×10^5	[199]
PPV	VCSEL	inorganic DBR layers + optical adhesive	80	unknown	37.5	4.5×10^5	[199]
DCM	facetted waveguide	doped molecular solid in nitrogen atmosphere	1.2	2.4	> 4.8	$> 4 \times 10^6$	[203]
DCM	facetted waveguide	doped molecular solid in nitrogen atmosphere	3	6	> 500	$> 1.7 \times 10^8$	[7]
DCM2	facetted waveguide	doped molecular solid in nitrogen atmosphere	2.5	5	> 50	$> 2 \times 10^7$	[7]
R6G	facetted waveguide	doped molecular solid in nitrogen atmosphere	37	70	0.5	1.4×10^4	[7]
PM546	facetted waveguide	doped molecular solid in nitrogen atmosphere	15	30	> 50	$> 3.3 \times 10^6$	[7]
perylene	facetted waveguide	doped molecular solid in nitrogen atmosphere	5	10	> 50	$> 1 \times 10^7$	[7]
Coumarin 47	facetted waveguide	doped molecular solid in nitrogen atmosphere	15	30	0.5	3.3×10^4	[7]
R6G	DBR	doped polymer	50000	2500	1500 (estimated)	3×10^4 (estimated)	[21]
R6G	RL	doped polymer	15000	3000	42	2800	[227]
di(biphenyl)-aminobenzene	RL	none	22	44	> 2.2	$> 10^5$	[12]

TABLE 2.7: Summary of lifetime investigations on organic lasers other than DFB. Continuation of table 2.6.

References

[1] A. Jabloński. Über den Mechanismus der Photolumineszenz von Farbstoffphosphoren. *Z. Phys.*, 94:38–46, 1935.

[2] Gilbert N. Lewis and M. Kasha. Phosphorescence and the triplet state. *J. Am. Chem. Soc.*, 66: 2100–2116, 1944.

[3] Dirk Hertel, Sepas Setayesh, Heinz-Georg Nothofer, Ullrich Scherf, Klaus Müllen, and Heinz Bässler. Phosphorescence in Conjugated Poly(para-phenylene)-Derivatives. *Adv. Mater.*, 13(1): 65–70, 2001.

[4] P. P. Sorokin and L. R. Lankard. Stimulated Emission Observed from an Organic Dye, Chloroaluminum Phthalocyanine . *IBM J. Res. Dev.*, 10(2):162–163, 1966.

[5] I.D.W. Samuel and G.A. Turnbull. Organic Semiconductor Lasers. *Chem. Rev.*, 107:1272–1295, 2007.

[6] Alan J. Heeger. Semiconducting polymers: the Third Generation. *Chem. Soc. Rev.*, 39:2354–2371, 2010.

[7] V. G. Kozlov, V. Bulovic, P. E. Burrows, M. Baldo, V. B. Khalfin, G. Parthasarathy, and S. R. Forrest. Study of lasing action based on Förster energy transfer in optically pumped organic semiconductor thin films. *J. Appl. Phys.*, 84(8):4096–4108, 1998.

[8] Th. Förster. Zwischenmolekulare Energiewanderung und Fluoreszenz. *Ann. Phys.*, 437(2):55–75, 1948.

[9] C. K. Chiang, Jr. C. B. Fincher, Y. W. Park, A. J. Heeger, H. Shirakawa, E. J. Louis, S. C. Gau, and Alan G. MacDiarmid. Electrical Conductivity in Doped Polyacetylene. *Phys. Rev. Lett.*, 39 (17):1098–1101, 1977.

[10] Neil A. Montgomery, Jean-Christophe Denis, Stefan Schumacher, Arvydas Ruseckas, Peter J. Skabara, Alexander Kanibolotsky, Martin J. Paterson, Ian Galbraith, Graham A. Turnbull, and Ifor D. W. Samuel. Optical Excitations in Star-Shaped Fluorene Molecules. *J. Phys. Chem. A*, 115:2913–2919, 2011.

[11] Ji Eon Kwon and Soo Young Park. Advanced Organic Optoelectronic Materials: Harnessing Excited-State Intramolecular Proton Transfer (ESIPT) Process. *Adv. Mater.*, 23:3615–3642, 2011.

[12] Hadi Rabbani-Haghighi, Sébastien Forget, Sébastien Chénais, Alain Siove, Marie-Claude Castex, and Elena Ishow. Laser operation in nondoped thin films made of a small-molecule organic red-emitter. *Appl. Phys. Lett.*, 95:033305, 2009.

[13] G. Wegmann, B. Schweitzer, D. Hertel, H. Giessen, M. Oestreich, U. Scherf, K. Müllen, and R.F. Mahrt. The dynamics of gain-narrowing in a ladder-type π-conjugated polymer. *Chem. Phys. Lett.*, 312:376–384, 1999.

[14] James Franck and Robert Livingston. Remarks on the Fluorescence, Phosphorescence and Photochemistry of Dyestuffs. *J. Chem. Phys.*, 9:184–190, 1941.

[15] Linlin Liu, Shi Tang, Meirong Liu, Zengqi Xie, Wu Zhang, Ping Lu, Muddasir Hanif, and Yuguang Ma. Photodegradation of Polyfluorene and Fluorene Oligomers with Alkyl and Aromatic Disubstitutions. *J. Phys. Chem. B*, 110:13734–13740, 2006.

[16] Egbert Zojer, Alexander Pogantsch, Emmanuelle Hennebicq, David Beljonne, Jean-Luc Brédas, Patricia Scandiucci de Freitas, Ullrich Scherf, and Emil J. W. List. Green emission from poly(fluorene)s: The role of oxidation. *J. Chem. Phys.*, 117(14):6794–6802, 2002.

[17] M. Atreya, S. Li, E. T. Kang, K. G. Neoh, Z. H. Ma, K. L. Tan, and W. Huang. Stability studies of poly(2-methoxy-5-(2'-ethyl hexyloxy)-p-(phenylene vinylene) [MEH-PPV]. *Polym. Degrad. Stab.*, 65:287–296, 1999.

[18] Marvin J. Weber and Michael Bass. Frequency- and Time-Dependent Gain Characteristics of Dye Lasers. *IEEE J. Quant. Electron.*, QE5(4):175–188, 1969.

[19] Andy Monkman, Carsten Rothe, Simon King, and Fernando Dias. Polyfluorene Photophysics. *Adv. Polym. Sci.*, 212:187–225, 2008.

[20] H. Kogelnik and C. V. Shank. Stimulated Emission in a Periodic Structure. *Appl. Phys. Lett.*, 18 (4):152–154, 1971.

[21] I. P. Kaminow, H. P. Weber, and E. A. Chandross. Poly(Methyl Methacrylate) Dye Laser with Internal Diffraction Grating Resonator. *Appl. Phys. Lett.*, 18(11):497–499, 1971.

[22] N. Tessler, G. J. Denton, and R. H. Friend. Lasing from conjugated-polymer microcavities. *Nature*, 382:695–697, 1996.

[23] A. Dodabalapur, M. Berggren, R. E. Slusher, Z. Bao, A. Timko, P. Schiortino, E. Laskowski, H. E. Katz, and O. Nalamasu. Resonators and Materials for Organic Lasers Based on Energy Transfer. *IEEE J. Sel. Top. Quantum. Electron.*, 4(1):67–74, 1998.

[24] Naoto Tsutsumi and Takashi Ishibashi. Organic dye lasers with distributed Bragg reflector grating and distributed feedback resonator. *Opt. Expr.*, 17(24):21698–21703, 2009.

[25] George Heliotis, Ruidong Xia, Graham A. Turnbull, Piers Andrew, William L. Barnes, Ifor D. W. Samuel, and Donal D. C. Bradley. Emission Characteristics and Performance Comparison of Polyfluorene Lasers with One- and Two-Dimensional Distributed Feedback. *Adv. Func. Mater.*, 14(1):91–97, 2004.

[26] Scott Richardson. *The Fabrication and Lithography of Conjugated Polymer Distributed Feedback Lasers and Development of their Applications.* PhD thesis, University of St. Andrews, School of Physics and Astronomy, 2007.

[27] Ying Yang, Ifor D. W. Samuel, and Graham A. Turnbull. The Development of Luminescent Concentrators for Pumping Organic Semiconductor Lasers. *Adv. Mat.*, 21:3205–3209, 2009.

[28] Tianrui Zhai, Xinping Zhang, Zhaoguang Pang, and Fei Dou. Direct Writing of Polymer Lasers Using Interference Ablation. *Adv. Mater.*, 23:1860–1864, 2011.

[29] J. Herrnsdorf, B. Guilhabert, Y. Chen, A. L. Kanibolotsky, A. R. Mackintosh, R. A. Pethrick, P. J. Skabara, E. Gu, N. Laurand, and M. D. Dawson. Flexible blue-emitting encapsulated organic semiconductor DFB laser. *Opt. Express*, 18(25):25535–25545, 2010.

[30] Yujie Chen, Johannes Herrnsdorf, Benoit Guilhabert, Alexander L. Kanibolotsky, Allan R. Mackintosh, Yue Wang, Richard A. Pethrick, Erdan Gu, Graham A. Turnbull, Peter J. Skabara, Ifor D.W. Samuel, Nicolas Laurand, and Martin D. Dawson. Laser action in a surface-structured free-standing membrane based on a π-conjugated polymer-composite. *Org. Electron.*, 12:62–69, 2011.

[31] Christian Kallinger, Martin Hilmer, Andreas Haugeneder, Martin Perner, Wolfgang Spirkl, Uli Lemmer, Jochen Feldmann, Ullrich Scherf, Klaus Müllen, Andreas Gombert, and Volker Wittwer. A Flexible Conjugated Polymer Laser. *Adv. Mat.*, 10(12):920–923, 1998.

[32] M. Berggren, A. Dodabalapur, R. E. Slusher A. Timko, and O. Nalamasu. Organic solid-state lasers with imprinted gratings on plastic substrates. *Appl. Phys. Lett.*, 72(4):410–411, 1998.

[33] John A. Rogers, Martin Meier, Ananth Dodabalapur, Edward J. Laskowski, and Mark A. Cappuzzo. Distributed feedback ridge waveguide lasers fabricated by nanoscale printing and molding on nonplanar substrates. *Appl. Phys. Lett.*, 74(22):3257–3259, 1999.

[34] Michifumi Nagawa, Musubu Ichikawa, Toshiki Koyama, Hirofusa Shirai, Yoshio Taniguchi, Akihito Hongo, Shinji Tsuji, and Yoshiaki Nakano. Organic solid-state distributed feedback dye laser with a nonmorphological modification grating. *Appl. Phys. Lett.*, 77(17):2641–2643, 2000.

[35] S. Riechel, U. Lemmer, J. Feldmann, T. Benstem, W. Kowalsky, U. Scherf, A. Gombert, and V. Wittwer. Laser modes in organic solid-state distributed feedback lasers. *Appl. Phys. B*, 71: 897–900, 2000.

[36] G. A. Turnbull, P. Andrew, M. J. Jory, W. L. Barnes, and I. D. W. Samuel. Relationship between photonic band structure and emission characteristics of a polymer distributed feedback laser. *Phys. Rev. B*, 64:125122, 2001.

[37] S. Riechel, U. Lemmer, J. Feldmann, S. Berleb, A. G. Mückl, W. Brütting, A. Gombert, and V. Wittwer. Very compact tunable solid-state laser utilizing a thin-film organic semiconductor. *Opt. Lett.*, 26(9):593–595, 2001.

[38] Musubu Ichikawa, Yuji Tanaka, Naotoshi Suganuma, Toshiki Koyama, and Yoshio Taniguchi. Photopumped Organic Solid-State Dye Laser with a Second-Order Distributed Feedback Cavity. *Jpn. J. Appl. Phys.*, 40(8A):L799–L801, 2001.

[39] Yuji Oki, Takeshi Yoshiura, Yuichi Chisaki, and Mitsuo Maeda. Fabrication of a distributed-feedback dye laser with a grating structure in its plastic waveguide. *Appl. Opt.*, 41(24):5030–5035, 2002.

[40] R. Gupta, M. Stevenson, and A. J. Heeger. Low threshold distributed feedback lasers fabricated from blends of conjugated polymers: Reduced losses through Förster transfer. *J. Appl. Phys.*, 92 (9):4874–4877, 2002.

[41] W. Holzer, A. Penzkofer, T. Pertsch, N. Danz, A. Bräuer, E. B. Kley, H. Tillmann, C. Bader, and H.-H. Hörhold. Corrugated neat thin-film conjugated polymer distributed-feedback lasers. *Appl. Phys. B*, 74:333–342, 2002.

[42] Thomas Kavc, Gregor Langer, Wolfgang Kern, Gerald Kranzelbinder, Eric Toussaere, Graham A. Turnbull, Ifor D. W. Samuel, Kurt F. Iskra, Theo Neger, and Alexander Pogantsch. Index and Relief Gratings in Polymer Films for Organic Distributed Feedback Lasers. *Chem. Mater.*, 14: 4178–4185, 2002.

[43] Yuji Oki, Shinichi Miyamotoa, Masamitsu Tanakab, Duluo Zuoa, and Mitsuo Maeda. Long lifetime and high repetition rate operation from distributed feedback plastic waveguided dye lasers. *Opt. Commun.*, 214:277–283, 2002.

[44] G. Heliotis, R. Xia, D. D. C. Bradley, G. A. Turnbull, I. D. W. Samuel, P. Andrew, and W. L. Barnes. Blue, surface-emitting, distributed feedback polyfluorene lasers. *Appl. Phys. Lett.*, 83(11): 2118–2120, 2003.

[45] D. Schneider, S. Hartmann, T. Benstem, T. Dobbertin, D. Heithecker, D. Metzdorf, E. Becker, T. Riedl, H.-H. Johannes, W. Kowalsky, T. Weimann, J. Wang, and P. Hinze. Wavelength-tunable organic solid-state distributed-feedback laser. *Appl. Phys. B*, 77:399–402, 2003.

[46] Musubu Ichikawa, Yuji Tanaka, Naotoshi Suganuma, Toshiki Koyama, and Yoshio Taniguchi. Low-Threshold Photopumped Distributed Feedback Plastic Laser Made by Replica Molding. *Jpn. J. Appl. Phys.*, 42(9A):5590–5593, 2003.

[47] D. Pisignano, M. Anni, G. Gigli, R. Cingolani, G. Barbarella, L. Favaretto, and G. Sotgui. Flexible organic distributed feedback structures by soft lithography. *Synth. Met.*, 137:1057–1058, 2003.

[48] Dario Pisignano, Luana Persano, Paolo Visconti, Roberto Cingolani, Giuseppe Gigli, Giovanna Barbarella, and Laura Favaretto. Oligomer-based organic distributed feedback lasers by room-temperature nanoimprint lithography. *Appl. Phys. Lett.*, 83(13):2545–2547, 2003.

[49] Justin R. Lawrence, Graham A. Turnbull, and Ifor D. W. Samuel. Polymer laser fabricated by a simple micromolding process. *Appl. Phys. Lett.*, 82(23):4023–4025, 2003.

[50] Gerald Kranzelbinder, Eric Toussaere, Joseph Zyss, Thomas Kavc, Gregor Langer, and Wolfgang Kern. Organic surface emitting laser based on a deep-ultraviolet photopolymer containing thiocyanate groups. *Appl. Phys. Lett.*, 82(14):2203–2205, 2003.

[51] Kazuharu Suzuki, Kunimitsu Takahashi, Yoshimi Seida, Kouki Shimizu, Mikio Kumagai, and Yoshio Taniguchi. A Continuously Tunable Organic Solid-State Laser Based on a Flexible Distributed-Feedback Resonator. *Jpn. J. Appl. Phys.*, 42(3A):L249–L251, 2003.

[52] D. Schneider, T. Rabe, T. Riedl, T. Dobbertin, M. Kröger, E. Becker, H.-H. Johannes, W. Kowalsky, T. Weimann, J. Wang, and P. Hinze. Ultrawide tuning range in doped organic solid-state lasers. *Appl. Phys. Lett.*, 85(11):1886–1888, 2004.

[53] Dario Pisignano, Elisa Mele, Luana Persano, Giuseppe Gigli, Paolo Visconti, Roberto Cingolani, Giovanna Barbarella, and Laura Favaretto. Full organic distributed feedback cavities based on a soluble electroluminescent oligothiophene. *Phys. Rev. B*, page 205206, 2004.

[54] D. Schneider, T. Rabe, T. Riedl, T. Dobbertin, O. Werner, M. Kröger, E. Becker, H.-H. Johannes, W. Kowalsky, T. Weimann, J. Wang, P. Hinze, A. Gerhard, P. Stössel, and H. Vestweber. Deep blue widely tunable organic solid-state laser based on a spirobifluorene derivative. *Appl. Phys. Lett.*, 84(23):4693–4695, 2004.

[55] M. Reufer, S. Riechel, J. M. Lupton, J. Feldmann, U. Lemmer, D. Schneider, T. Benstem, T. Dobbertin, W. Kowalsky, A. Gombert, K. Forberich, V. Wittwer, and U. Scherf. Low-threshold polymeric distributed feedback lasers with metallic contacts. *Appl. Phys. Lett.*, 84(17):3262–3264, 2004.

[56] Kokou D. Dorkenoo, Olivier Crégut, and Alain Fort. Organic plastic laser in holographic materials by photopolymerization. *Appl. Phys. Lett.*, 84(15):2733–2735, 2004.

[57] E. Brasselet, D. Wright, J. Zyss, G. Langer, and W. Kern. Spectral encoding of the polarization state of light in multiplexed polarization-sensitive lasing structures. *Opt. Lett.*, 29(12):1309–1311, 2004.

[58] W. Holzer, A. Penzkofer, A. Lux, H.-H. Hörhold, and E.B. Kley. Photo-physical and lasing characterisation of neat films of a thianthrene-substituted distyrylbenzene dye (Thianthrene-DSB). *Synth. Met.*, 145:119–127, 2004.

[59] Daniel Wright, Etienne Brasselet, Joseph Zyss, Gregor Langer, and Wolfgang Kern. Dye-doped organic distributed-feedback lasers with index and surface gratings: the role of pump polarization and molecular orientation. *J. Opt. Soc. Am. B*, 21(5):944–950, 2004.

[60] R. Xia, G. Heliotis, P. N. Stavrinou, and D. D. C. Bradley. Polyfluorene distributed feedback lasers operating in the green-yellow spectral region. *Appl. Phys. Lett.*, 87:031104, 2005.

[61] R. Xia, G. Heliotis, M. Campoy-Quiles, P. N. Stavrinou, D. D. C. Bradley, Doojin Vak, and Dong-Yu Kim. Characterization of a high-thermal-stability spiroanthracenefluorene-based blue-light-emitting polymer optical gain medium. *J. Appl. Phys*, 98:083101, 2005.

[62] T. Spehr, A. Siebert, T. Fuhrmann-Lieker, J. Salbeck, T. Rabe, T. Riedl, H. H. Johannes, W. Kowalsky, J. Wang, T. Weimann, and P. Hinze. Organic solid-state ultraviolet-laser based on spiro-terphenyl. *Appl. Phys. Lett.*, 87:161103, 2005.

[63] Dario Pisignano, Luana Persano, Elisa Mele, Paolo Visconti, Marco Anni, Guiseppe Gigli, Roberto Cingulani, Laura Favaretto, and Giovanni Barabarella. First-order imprinted organic distributed feedback lasers. *Synth. Met.*, 153:237–240, 2005.

[64] J. Wang, Th. Weimann, P. Hinze, G. Ade, D. Schneider, T. Rabe, T. Riedl, and W. Kowalsky. A continuously tunable organic DFB laser. *Microelectron. Eng.*, 78–79:364–368, 2005.

[65] Daniel Schneider, Torsten Rabe, Thomas Riedl, Thomas Dobbertin, Michael Kröger, Eike Becker, Hans-Hermann Johannes, Wolfgang Kowalsky, Thomas Weimann, Jing Wang, Peter Hinze, Anja Gerhard, Philipp Stössel, and Horst Vestweber. An Ultraviolet Organic Thin-Film Laser for Biomarker Applications. *Adv. Mat.*, 17(1):31–34, 2005.

[66] D. Schneider, T. Rabe, T. Riedl, T. Dobbertin, E. Becker M. Kröger, H.-H. Johannes, W. Kowalsky, T. Weimann, J. Wang, and P. Hinze. Organic solid-state lasers based on sexiphenyl as active chromophore. *J. Appl. Phys.*, 98:043104, 2005.

[67] Dario Pisignano, Luana Persano, Elisa Mele, Paolo Visconti, Roberto Cingolani, Giuseppe Gigli, Giovanna Barbarella, and Laura Favaretto. Emission properties of printed organic semiconductor lasers. *Opt. Lett.*, 30(3):260–262, 2005.

[68] Takashi Ubukata, Takashi Isoshima, and Masahiko Hara. Wavelength-Programmable Organic Distributed-Feedback Laser Based on a Photoassisted Polymer-Migration System. *Adv. Mater.*, 17:1630–1633, 2005.

[69] G. Heliotis, S. A. Choulis, G. Itskos, R. Xia, R. Murray, P. N. Stavrinou, and D. D. C. Bradley. Low-threshold lasers based on a high-mobility semiconducting polymer. *Appl. Phys. Lett.*, 88: 081104, 2006.

[70] Elisa Mele, Andrea Camposeo, Ripalta Stabile, Pompilio Del Carro, Francesca Di Benedetto, Luana Persano, Roberto Cingolani, and Dario Pisignano. Polymeric distributed feedback lasers by room-temperature nanoimprint lithography. *Appl. Phys. Lett.*, 89:131109, 2006.

[71] C. Karnutsch, C. Gärtner, V. Haug, U. Lemmer, T. Farrell, B. S. Nehls, U. Scherf, J. Wang, T. Weimann, G. Heliotis, C. Pflumm, J. C. deMello, and D. D. C. Bradley. Low threshold blue conjugated polymer lasers with first- and second-order distributed feedback. *Appl. Phys. Lett.*, 89: 201108, 2006.

[72] T. Riedl, T. Rabe, H.-H. Johannes, W. Kowalsky, J. Wang, T. Weimann, P. Hinze, B. Nehls, T. Farrell, and U. Scherf. Tunable organic thin-film laser pumped by an inorganic violet diode laser. *Appl. Phys. Lett.*, 88:241116, 2006.

[73] Zhenyu Li, Zhaoyu Zhang, Teresa Emery, Axel Scherer, and Demetri Psaltis. Single mode optofluidic distributed feedback dye laser. *Opt. Expr.*, 14(2):696–701, 2006.

[74] P. Del Carro, A. Camposeo, R. Stabile, E. Mele, L. Persano, R. Cingolani, and D. Pisignano. Near-infrared imprinted distributed feedback lasers. *Appl. Phys. Lett.*, 89:201105, 2006.

[75] M. Zavelani-Rossi, S. Perissinotto, G. Lanzani, M. Salerno, and G. Gigli. Laser dynamics in organic distributed feedback lasers. *Appl. Phys. Lett.*, 89:181105, 2006.

[76] T. Rabe, K. Gerlach, T. Riedl, H.-H. Johannes, W. Kowalsky, J. Niederhofer, W. Gries, J. Wang, T. Weimann, P. Hinze, F. Galbrecht, and U. Scherf. Quasi-continuous-wave operation of an organic thin-film distributed feedback laser. *Appl. Phys. Lett.*, 89:081115, 2006.

[77] C. Karnutsch, C. Pflumm, G. Heliotis, J. C. deMello, D. D. C. Bradley, J. Wang, T. Weimann, V. Haug, C. Gärtner, and U. Lemmer. Improved organic semiconductor lasers based on a mixed-order distributed feedback resonator design. *Appl. Phys. Lett.*, 90:131104, 2007.

[78] Sidney S. Yang, Yun-Ching Chang, Pei-Chun Yen, and Ya-Chang Chou. Effects of duty cycle on the characteristics of a composite surface-emitting organic distributed feedback laser. *J. Opt. Soc. Am. B*, 24(8):1857–1861, 2007.

[79] J. C. Ribierre, G. Tsiminis, S. Richardson, G. A. Turnbull, I. D. W. Samuel, H. S. Barcena, and P. L. Burn. Amplified spontaneous emission and lasing properties of bisfluorene-cored dendrimers. *Appl. Phys. Lett.*, 91:081108, 2007.

[80] A. E. Vasdekis, S. A. Moore, A. Ruseckas, T. F. Krauss, I. D. W. Samuel, and G. A. Turnbull. Silicon based organic semiconductor laser. *Appl. Phys. Lett.*, 91:051124, 2007.

[81] M. Salerno, G. Gigli, M. Zavelani-Rossi, S. Perissinotto, and G. Lanzani. Effects of morphology and optical contrast in organic distributed feedback lasers. *Appl. Phys. Lett*, 90:111110, 2007.

[82] M. Stroisch, T. Woggon, U. Lemmer, G. Bastian, G. Violakis, and S. Pissadakis. Organic semiconductor distributed feedback laser fabricated by direct laser interference ablation. *Opt. Expr.*, 17(7):3968–3973, 2007.

[83] Naoto Tsutsumi, Makoto Takeuchi, and Wataru Sakai. All-plastic organic dye laser with distributed feedback resonator structure. *Thin Solid Films*, 516:2783–2787, 2008.

[84] Boon Kar Yap, Ruidong Xia, Mariano Campoy-Quiles, Paul N. Stavrinou, and Donal D. C. Bradley. Simultaneous optimization of charge-carrier mobility and optical gain in semiconducting polymer films. *Nat. Mater.*, 7:376–380, 2008.

[85] Y. Yang, G. A. Turnbull, and I. D. W. Samuel. Hybrid optoelectronics: A polymer laser pumped by a nitride light-emitting diode. *Appl. Phys. Lett.*, 92:163306, 2008.

[86] M. Lu, B.T. Cunningham, S.-J. Park, and J.G. Eden. Vertically emitting, dye-doped polymer laser in the green ($\lambda \sim 536$ nm) with a second order distributed feedback grating fabricated by replica molding. *Opt. Commun.*, 281:3159–3162, 2008.

[87] M. Lu, S. S. Choi, U. Irfan, and B. T. Cunningham. Plastic distributed feedback laser biosensor. *Appl. Phys. Lett.*, 93:111113, 2008.

[88] Myoung Hoon Song, Bernard Wenger, and Richard H. Friend. Tuning the wavelength of lasing emission in organic semiconducting laser by the orientation of liquid crystalline conjugated polymer. *J. Appl. Phys.*, 104:033107, 2008.

[89] K. Yamashita, A. Arimatsu, N. Takeuchi, M. Takayama, K. Oe, and H. Yanagi. Multilayered solid-state organic laser for simultaneous multiwavelength oscillations. *Appl. Phys. Lett.*, 93:233303, 2008.

[90] Naoto Tsutsumi and Makoto Takeuchi. Ti-sapphire femtosecond pulse pumped laser emission from all-plastic organic waveguide with distributed feedback resonator. *Opt. Commun.*, 281:2179–2183, 2008.

[91] Wen-Yong Lai, Ruidong Xia, Qi-Yuan He, Peter A. Levermore, Wei Huang, and Donal D. C. Bradley. Enhanced Solid-State Luminescence and Low-Threshold Lasing from Starburst Macromolecular Materials. *Adv. Mater.*, 21:355–360, 2009.

[92] Ju Huang, Quan Liu, Jian-Hua Zou, Xu-Hui Zhu, Ai-Yuan Li, Jun-Wen Li, Sha Wu, Junbiao Peng, Yong Cao, Ruidong Xia, Donal D. C. Bradley, and Jean Roncali. Electroluminescence and Laser Emission of Soluble Pure Red Fluorescent Molecular Glasses Based on Dithienylbenzothiadiazole. *Adv. Funct. Mater.*, 19:2978–2986, 2009.

[93] Ruidong Xia, Wen-Yong Lai, Peter A. Levermore, Wei Huang, and Donal D. C. Bradley. Low-Threshold Distributed-Feedback Lasers Based on Pyrene-Cored Starburst Molecules with 1,3,6,8-Attached Oligo(9,9-Dialkylfluorene) Arms. *Adv. Funct. Mat.*, 19:2844–2850, 2009.

[94] Wuzhou Song, Andreas E. Vasdekis, Zhenyu Li, and Demetri Psaltis. Low-order distributed feedback optofluidic dye laser with reduced threshold. *Appl. Phys. Lett.*, 94:051117, 2009.

[95] M. Stroisch, C. Teiwes-Morin, T. Woggon, M. Gerken, U. Lemmer, K. Forberich, and A. Gombert. Photonic stopband tuning of organic semiconductor distributed feedback lasers by oblique angle deposition of an intermediate high index layer. *Appl. Phys. Lett.*, 95:021112, 2009.

[96] Thomas Woggon, Thomas Kleiner, Martin Punke, and Uli Lemmer. Nanostructuring of organic-inorganic hybrid materials for distributed feedback laser resonators by two-photon polymerization. *Opt. Expr.*, 17(4):2500–2507, 2009.

[97] S. Klinkhammer, T. Woggon, U. Geyer, C. Vannahme, S. Dehm, T. Mappes, and U. Lemmer. A continuously tunable low-threshold organic semiconductor distributed feedback laser fabricated by rotating shadow mask evaporation. *Appl. Phys. B*, 97:787–791, 2009.

[98] Georgios Tsiminis, Yue Wang, Paul E. Shaw, Alexander L. Kanibolotsky, Igor F. Perepichka, Martin D. Dawson, Peter J. Skabara, Graham A. Turnbull, and Ifor D.W. Samuel. Low-threshold organic laser based on an oligofluorene truxene with low optical losses. *Appl. Phys. Lett.*, 94: 243304, 2009.

[99] Michael C. Gwinner, Saghar Khodabakhsh, Myoung Hoon Song, Heinz Schweizer, Harald Giessen, and Henning Sirringhaus. Integration of a Rib Waveguide Distributed Feedback Structure into a Light-Emitting Polymer Field-Effect Transistor. *Adv. Funct. Mater.*, 19:1360–1370, 2009.

[100] Hirofumi Watanabe, Hirotaka So, Yuji Oki, Shigehisa Akine, and Takashige Omatsu. Picosecond-Pulse-Pumped Distributed-Feedback Thick-Film Waveguide Blue Laser Using Fluorescent Brightener 135. *Jpn. J. Appl. Phys.*, 49:072105, 2010.

[101] Victor Navarro-Fuster, Eva M. Calzado, Pedro G. Boj, José A. Quintana, José M. Villalvilla, María A. Díaz-García, Vera Trabadelo, Aritz Juarros, Aritz Retolaza, and Santos Merino. Highly photostable organic distributed feedback laser emitting at 573 nm. *Appl. Phys. Lett.*, 97:171104, 2010.

[102] Ying Yang, Graham A. Turnbull, and Ifor D. W. Samuel. Sensitive Explosive Vapor Detection with Polyfluorene Lasers. *Adv. Funct. Mater.*, 20:2093–2097, 2010.

[103] Kenichi Yamashita, Nobutaka Takeuchi, Kunishige Oe, and Hisao Yanagi. Simultaneous RGB lasing from a single-chip polymer device. *Opt. Lett.*, 35(14):2451–2453, 2010.

[104] Yue Wang, Georgios Tsiminis, Ying Yang, Arvydas Ruseckas, Alexander L. Kanibolotsky, Igor F. Perepichka, Peter J. Skabara, Graham A. Turnbull, and Ifor D.W. Samuel. Broadly tunable deep blue laser based on a star-shaped oligofluorene truxene. *Synth. Met.*, 160:1397–1400, 2010.

[105] V. Trabadelo, A. Juarros, A. Retolaza, S. Merino, M.G. Ramírez, V. Navarro-Fuster, J.M. Villalvilla, P.G. Boj, J.A. Quintana, and M.A. Díaz-García. Highly photostable solid-state organic distributed feedback laser fabricated via thermal nanoimprint lithography. *Microelectronic Engineering*, 87:1428–1430, 2010.

[106] Chun Ge, Meng Lu, Xun Jian, Yafang Tan, and Brian T. Cunningham. Large-area organic distributed feedback laser fabricated by nanoreplica molding and horizontal dipping. *Opt. Expr.*, 18(12):12980–12991, 2010.

[107] M. Stroisch, T. Woggon, C. Teiwes-Morin, S. Klinkhammer, K. Forberich, A. Gombert, M. Gerken, and U. Lemmer. Intermediate high index layer for laser mode tuning in organic semiconductor lasers. *Opt. Expr.*, 18(6):5890–5895, 2010.

[108] Christoph Vannahme, Sönke Klinkhammer, Alexander Kolew, Peter-Jürgen Jakobs, Markus Guttmann, Simone Dehm, Uli Lemmer, and Timo Mappes. Integration of organic semiconductor lasers and single-mode passive waveguides into a PMMA substrate. *Microelectronic Engineering*, 87(5–8):693–695, 2010.

[109] Eva M. Calzado, Jose M. Villalvilla, Pedro G. Boj, Jose A. Quintana, Pablo A. Postigo, and María A. Díaz-García. Blue surface-emitting distributed feedback lasers based on TPD-doped films. *Appl. Opt.*, 49(3):463–470, 2010.

[110] Bodo H. Wallikewitz, Matthias de la Rosa, Jonas H.-W. M. Kremer, Dirk Hertel, and Klaus Meerholz. A Lasing Organic Light-Emitting Diode. *Adv. Mat.*, 22:531–534, 2010.

[111] Bernard Wenger, Nicolas Tétreault, Mark E. Welland, and Richard H. Friend. Mechanically tunable conjugated polymer distributed feedback lasers. *Appl. Phys. Lett.*, 97:193303, 2010.

[112] T. N. Smirnova, O. V. Sakhno, J. Stumpe, V. Kzianzou, and S. Schrader. Distributed feedback lasing in dye-doped nanocomposite holographic transmission gratings. *J. Opt.*, 13:035709, 2011.

[113] Chun Ge, Meng Lu, Yafang Tan, and Brian T. Cunningham. Enhancement of pump efficiency of a visible wavelength organic distributed feedback laser by resonant optical pumping. *Opt. Express*, 19(6):5086–5092, 2011.

[114] Yue Wang, Neil B. McKeown, Kadhum J. Msayib, Graham A. Turnbull, and Ifor D. W. Samuel. Laser Chemosensor with Rapid Responsivity and Inherent Memory Based on a Polymer of Intrinsic Microporosity. *Sensors*, 11:2478–2487, 2011.

[115] Christoph Vannahme, Sönke Klinkhammer, Uli Lemmer, and Timo Mappes. Plastic lab-on-a-chip for fluorescence excitation with integrated organic semiconductor lasers. *Opt. Express*, 19(9): 8179–8186, 2011.

[116] Tianrui Zhai, Xinping Zhang, and Zhaoguang Pang. Polymer laser based on active waveguide grating structures. *Opt. Express*, 19(7):6487–6492, 2011.

[117] Marcus Lehnhardt, Thomas Riedl, Ullrich Scherf, Torsten Rabe, and Wolfgang Kowalsky. Spectrally separated optical gain and triplet absorption: Towards continuous wave lasing in organic thin film lasers. *Organic Electronics*, 12:1346–1351, 2011.

[118] O.V. Sakhno, J. Stumpe, and T.N. Smirnova. Distributed feedback dye laser holographically induced in improved organic-inorganic photocurable nanocomposites. *Appl. Phys. B*, 103:907–916, 2011.

[119] N. Tsutsumi and M. Shinobu. All organic DFB laser enhanced by intermediate high refractive index polymer layer. *Appl. Phys. B*, 105:839–845, 2011.

[120] Lujian Chen, Fengyu Gao, Chun Liu, Qiong Zhou, Sensen Li, Yikun Bu, and Zhiping Cai. Distributed feedback leaky laser emission from dye doped gel-glass dispersed liquid crystal thin film patterned by soft lithography. *Opt. Mater.*, 34:189–193, 2011.

[121] Lujian Chen, Fengyu Gao, Yikun Bu, Fuqiang Jia, Chun Liu, and Zhiping Cai. Tunable distributed feedback lasing from leaky waveguides based on gel-glass dispersed liquid crystal thin films. *Mater. Lett.*, 65:3476–3478, 2011.

[122] Yifan Zhang and Stephen R. Forrest. Existence of continuous-wave threshold for organic semiconductor lasers. *Phys. Rev. B*, 84:241301, 2011.

[123] Manuel G. Ramirez, Pedro G. Boj, Victor Navarro-Fuster, Igor Vragovic, José M. Villalvilla, Ibon Alonso, Vera Trabadelo, Santos Merino, and María A. Díaz-García. Efficient organic distributed feedback lasers with imprinted active films. *Opt. Express*, 19(23):22443–22454, 2011.

[124] Hong-Hua Fang, Ran Ding, Shi-Yang Lu, Jie Yang, Xu-Lin Zhang, Rui Yang, Jing Feng, Qi-Dai Chen, Jun-Feng Song, and Hong-Bo Sun. Distributed Feedback Lasers Based on Thiophene/Phenylene Co-Oligomer Single Crystals. *Adv. Funct. Mater.*, 22:33–38, 2012.

[125] Hiroaki Yoshioka, Yu Yang, Hirofumi Watanabe, and Yuji Oki. Fundamental characteristics of degradation-recoverable solid-state DFB polymer laser. *Opt. Express*, 20(4):4690–4696, 2012.

[126] Leonid M. Goldenberg, Victor Lisinetskii, Yuri Gritsai, Joachim Stumpe, and Sigurd Schrader. Second order DFB lasing using reusable grating inscribed in azobenzene-containing material. *Opt. Mater. Express*, 2(1):11–19, 2012.

[127] M. Berggren, A. Dodabalapur, R. E. Slusher, and Z. Bao. Light amplification in organic thin films using cascade energy transfer. *Nature*, 389:466–469, 1997.

[128] M. Meier, A. Mekis, A. Dodabalapur, A. Timko, R. E. Slusher, J. D. Joannopoulos, and O. Nalamasu. Laser action from two-dimensional distributed feedback in photonic crystals. *Appl. Phys. Lett.*, 74(1):7–9, 1999.

[129] S. Riechel, C. Kallinger, U. Lemmer, J. Feldmann, A. Gombert, V. Wittwer, and U. Scherf. A nearly diffraction limited surface emitting conjugated polymer laser utilizing a two-dimensional photonic band structure. *Appl. Phys. Lett.*, 77(15):2310–2312, 2000.

[130] G. A. Turnbull, P. Andrew, W. L. Barnes, and I. D. W. Samuel. Operating characteristics of a semiconducting polymer laser pumped by a microchip laser. *Appl. Phys. Lett.*, 82(3):313–315, 2003.

[131] G. A. Turnbull, P. Andrew, W. L. Barnes, and I. D. W. Samuel. Photonic mode dispersion of a two-dimensional distributed feedback polymer laser. *Phys. Rev. B*, 67:165107, 2003.

[132] G. Langer, A. Pogantsch, K. F. Iskra, T. Neger, and W. Kern. Laser Action in Optically Written Two-Dimensional DFB Gratings. *Synth. Met.*, 137:997–998, 2003.

[133] G. Heliotis, R. Xia, D. D. C. Bradley, G. A. Turnbull, I. D. W. Samuel, P. Andrew, and W. L. Barnes. Two-dimensional distributed feedback lasers using a broadband, red polyfluorene gain medium. *J. Appl. Phys.*, 96(12):6959–6965, 2004.

[134] A. E. Vasdekis, G. A. Turnbull, and I. D. W. Samuel. Low threshold edge emitting polymer distributed feedback laser based on a square lattice. *Appl. Phys. Lett.*, 86:161102, 2005.

[135] Rachel Jakubiak, Vincent P. Tondiglia, Lalgudi V. Natarajan, Richard L. Sutherland, Pamela Lloyd, Timothy J. Bunning, and Richard A. Vaia. Dynamic Lasing from All-Organic Two-Dimensional Photonic Crystals. *Adv. Mater.*, 17:2807–2811, 2005.

[136] Rik Harbers, John A. Hoffnagle, William D. Hinsberg, Rainer F. Mahrt, Nikolaj Moll, Daniel Erni, and Werner Bächtold. Lasing in interferometrically structured organic materials. *Appl. Phys. Lett.*, 87:241124, 2005.

[137] Naoya Nakai, Makoto Fukuda, and Keiichi Mito. Dual-Beam Distributed Feedback Solid-State Dye Laser with Photoresist Grating. *Jpn. J. Appl. Phys*, 45(21):L543–L545, 2006.

[138] K. Forberich, A. Gombert, S. Pereira, J. Crewett, U. Lemmer, M. Diem, and K. Busch. Lasing mechanisms in organic photonic crystal lasers with two-dimensional distributed feedback. *J. Appl. Pys.*, 100:023110, 2006.

[139] S. Richardson, O. P. M. Gaudin, G. A. Turnbull, and I. D. W. Samuel. Improved operational lifetime of semiconducting polymer lasers by encapsulation. *Appl. Phys. Lett.*, 91:261104, 2007.

[140] Christian Karnutsch, Marc Stroisch, Martin Punke, Uli Lemmer, Jing Wang, and Thomas Weimann. Laser Diode-Pumped Organic Semiconductor Lasers Utilizing Two-Dimensional Photonic Crystal Resonators. *IEEE Photon. Technol. Lett.*, 19(10):741–743, 2007.

[141] Ying Dong, Junfeng Song, Chuanhui Cheng, Wenhai Jiang, Shukun Yu, Guotong Du, and Xu Wang. Emission characterisics of near-ultraviolet two-dimensional organic photonic crystal lasers. *Microwave Opt. Technol. Lett.*, 50:382–385, 2008.

[142] Georgios Tsiminis, Arvydas Ruseckas, Ifor D. W. Samuel, and Graham A. Turnbull. A two-photon pumped polyfluorene laser. *Appl. Phys. Lett.*, 94:253304, 2009.

[143] Sönke Klinkhammer, Xin Liu, Klaus Huska, Yuxin Shen, Sylvia Vanderheiden, Sebastian Valouch, Christoph Vannahme, Stefan Bräse, Timo Mappes, and Uli Lemmer. Continuously tunable solution-processed organic semiconductor DFB lasers pumped by laser diode. *Opt. Express*, 20(6): 6357–6364, 2012.

[144] Christian Bauer, Harald Giessen, Bernd Schnabel, Ernst-Bernhard Kley, Christopher Schmitt, Ullrich Scherf, and Rainer F. Mahrt. A Surface-Emitting Circular Grating Polymer Laser. *Adv. Mater.*, 13(15):1161–1164, 2001.

[145] Asma Jebali, Rainer F. Mahrt, Nikolaj Moll, Daniel Erni, Christian Bauer, Gian-Luca Bona, and Werner Bächtold. Lasing in organic circular grating structures. *J. Appl. Phys.*, 96(6):3043–3049, 2004.

[146] Yan Chen, Zhenyu Li, Zhaoyu Zhang, Demetri Psaltis, and Axel Scherer. Nanoimprinted circular grating distributed feedback dye laser. *Appl. Phys. Lett.*, 91:051109, 2007.

[147] Vincent Dumarcher, Licinio Rocha, Christine Denis, Céline Fiorini, Jean-Michel Nunzi, Frank Sobel, Bouchta Sahraoui, and Denis Gindre. Polymer thin-film distributed feedback tunable lasers. *J. Opt. A: Pure Appl. Opt.*, 2:279–283, 2000.

[148] Takanori Kemanai, Satoshi Tanaka, Seiichiro Hayakawa, and Heihachi Sato. Effect of Photo-Induced Periodic Gain Structure on Oscillation Power and Tunability in Polymer Dye Laser. *Opt. Rev.*, 7(1):18–21, 2000.

[149] G. Kranzelbinder, E. Toussaere, D. Josse, and J. Zyss. Progress in erasable and permanent polymer based DFB-structures with multicolour tunable laser emission. *Synth. Met.*, 121:1617–1620, 2001.

[150] G. Kranzelbinder, E. Toussaere, J. Zyss, A. Pogantsch, E. W. J. List, H. Tillmann, and H.-H. Hörhold. Optically written solid-state lasers with broadly tunable mode emission based on improved poly (2,5-dialkoxy-phenylene-vinylene). *Appl. Phys. Lett.*, 80(5):716–718, 2002.

[151] V. G. Balenko, A. G. Vitukhnovskii, A. I. Drobysh, A. V. Kovtun, A. M. Leontovich, V. M. Mizin, and A. F. Shalin. A compact sol-gel laser with dynamic distributed feedback. *Journal of Russian Laser Research*, 24(5):399–401, 2003.

[152] F. Sobel, D. Gindre, J.-M. Nunzi, C. Denis, V. Dumarcher, C. Fiorini-Debuisschert, K.P. Kretsch, and L. Rocha. Multimode distributed feedback laser emission in a dye-doped optically pumped polymer thin-film. *Opt. Mater.*, 27:199–201, 2004.

[153] Naoto Tsutsumi and Arata Fujihara. Tunable distributed feedback lasing with narrowed emission using holographic dynamic gratings in a polymeric waveguide. *Appl. Phys. Lett.*, 86:061101, 2005.

[154] Naoto Tsutsumi and Masaki Yamamoto. Threshold reduction of a tunable organic laser using effective energy transfer. *J. Opt. Soc. Am. B*, 23(5):842–845, 2006.

[155] Naoto Tsutsumi, Arata Fujihara, and Daisuke Hayashi. Tunable distributed feedback lasing with a threshold in the nanojoule range in an organic guest-host polymeric waveguide. *Appl. Opt.*, 45 (22):5748–5751, 2006.

[156] D. C. Oliveira, Y. Messaddeq, K. Dahmouche, S. J. L. Ribeiro, R. R. Gonçalves, A. Vesperini, D. Gindre, and J.-M. Nunzi. Distributed feedback multipeak laser emission in Rhodamine 6G doped organic-inorganic hybrids. *J. Sol-Gel Sci. Techn.*, 40:359–363, 2006.

[157] H. Sakata, H. Takeuchi, K. Natsume, and S. Suzuki. Vertical-cavity organic lasers with distributedfeedback structures based on active Bragg reflectors. *Opt. Expr.*, 14(24):11681–11686, 2006.

[158] H. Sakata, K. Yamashita, H. Takeuchi, and M. Tomiki. Diode-pumped distributed-feedback dye laser with an organic-inorganic microcavity. *Appl. Phys. B*, 92:243–246, 2008.

[159] Francesco Scotognella, Angelo Monguzzi, Francesco Meinardi, and Riccardo Tubino. DFB laser action in a flexible fully plastic multilayer. *Phys. Chem. Chem. Phys.*, 12:337–340, 2010.

[160] V. I. Kopp, B. Fan, H. K. M. Vithana, and A. Z. Genack. Low-threshold lasing at the edge of a photonic stop band in cholesteric liquid crystals. *Opt. Lett.*, 23(21):1707–1709, 1998.

[161] Heino Finkelmann, Sung Tae Kim, Antonio Muñoz, Peter Palffy-Muhoray, and Bahman Taheri. Tunable Mirrorless Lasing in Cholesteric Liquid Crystalline Elastomers. *Adv. Mater.*, 13(14): 1069–1072, 2001.

[162] Tatsunosuke Matsui, Ryotaro Ozaki, Kazuhiro Funamoto, Masanori Ozaki, and Katsumi Yoshino. Flexible mirrorless laser based on a free-standing film of photopolymerized cholesteric liquid crystal. *Appl. Phys. Lett.*, 81(20):3741–3743, 2002.

[163] D. Wright, E. Brasselet, J. Zyss, G. Langer, A. Pogantsch, K. F. Iskra, T. Neger, and W. Kern. All-optical tunability of holographically multiplexed organic distributed feedback lasers. *Opt. Expr.*, 12(2):325–330, 2004.

[164] Rachel Jakubiak, Lalgudi V. Natarajan, Vincent Tondiglia, Guang S. He, Paras N. Prasad, Timothy J. Bunning, and Richard A. Vaia. Electrically switchable lasing from pyrromethene 597 embedded holographic-polymer dispersed liquid crystals. *Appl. Phys. Lett.*, 85(25):6095–6097, 2004.

[165] Giuseppe Strangi, Valentin Barna, Roberto Caputo, Antonio De Luca, Carlo Versace, Nicola Scaramuzza, Cesare Umeton, and Roberto Bartolino. Color-Tunable Organic Microcavity Laser Array Using Distributed Feedback. *Phys. Rev. Lett.*, 94:063903, 2005.

[166] Valentin Barna, Roberto Caputo, Antonio De Luca, Nicola Scaramuzza, Giuseppe Strangi, Carlo Versace, Cesare Umeton, and Roberto Bartolino. Distributed feedback micro-laser array: helixed liquid crystals embedded in holographically sculptured polymeric microcavities. *Opt. Expr.*, 14 (7):2695–2705, 2006.

[167] Yuhua Huang, Ying Zhou, and Shin-Tson Wu. Spatially tunable laser emission in dye-doped photonic liquid crystals. *Appl. Phys. Lett.*, 88:011107, 2006.

[168] Stephen M. Morris, Philip J. W. Hands, Sonja Findeisen-Tandel, Robert H. Cole, Timothy D. Wilkinson, and Harry J. Coles. Polychromatic liquid crystal laser arrays towards display applications. *Opt. Express*, 16(23):18827–18837, 2008.

[169] Philip J. W. Hands, Stephen M. Morris, Timothy D. Wilkinson, and Harry J. Coles. Two-dimensional liquid crystal laser array. *Opt. Lett.*, 33(5):515–517, 2008.

[170] Simon K. H. Wei, Shaw H. Chen, Ksenia Dolgaleva, Svetlana G. Lukishova, and Robert W. Boyd. Robust organic lasers comprising glassy-cholesteric pentafluorene doped with a red-emitting oligofluorene. *Appl. Phys. Lett.*, 94:041111, 2009.

[171] L. Criante, D. E. Lucchetta, F. Vita, R. Castagna, and F. Simoni. Distributed feedback all-organic microlaser based on holographic polymer dispersed liquid crystals. *Appl. Phys. Lett.*, 94:111114, 2009.

[172] Huai-Pei Tong, Yu-Ren Li, Jia-De Lin, and Chia-Rong Lee. All-optically controllable distributed feedback laser in a dye-doped holographic polymerdispersed liquid crystal grating with a photoisomerizable dye. *Opt. Expr.*, 18(3):2613–2620, 2010.

[173] Jürgen Schmidtke and Eugene M. Terentjev. Polydimethylsiloxane-enclosed liquid crystal lasers for lab-on-chip applications. *Appl. Phys. Lett.*, 96:151111, 2010.

[174] Damian J. Gardiner, Stephen M. Morris, Philip J. W. Hands, Carrie Mowatt, Rupert Rutledge, Timothy D. Wilkinson, and Harry J. Coles. Paintable band-edge liquid crystal lasers. *Opt. Express*, 19(3):2432–2439, 2011.

[175] Deepak N. Kumar, Jayant D. Bhawalkar, and Paras N. Prasad. Solid-state cavity lasing from poly(p-phenylene vinylene)-silica nanocomposite bulk. *Appl. Opt.*, 37(3):510–513, 1998.

[176] E. Yarif and R. Reisfeld. Laser properties of pyrromethene dyes in sol-gel glasses. *Opt. Mater.*, 13:49–54, 1999.

[177] Eli Yarif, Silke Schultheiss, Tsiala Saraidarov, and Renata Reisfeld. Efficiency and photostability of dye-doped solid-state lasers in different hosts. *Opt. Mater.*, 16:29–38, 2001.

[178] Silke Schultheiss, Eli Yariv, Renata Reisfeld, and Hans Dieter Breuer. Solid state dye lasers: Rhodamines in silica-zirconia materials. *Photochem. Photobiol. Sci.*, 1:320–323, 2002.

[179] R. Reisfeld, A. Weiss, T. Saraidarov, E. Yariv, and A. A. Ishchenko. Solid-state lasers based on inorganic-organic hybrid materials obtained by combined sol-gel polymer technology. *Polym. Adv. Technol.*, 15:291–301, 2004.

[180] K. Yamashita, A. Kitanobou, M. Ito, E. Fukuzawa, and K. Oe. Solid-state organic laser using self-written active waveguide with in-line Fabry-Pérot cavity. *Appl. Phys. Lett.*, 92:143305, 2008.

[181] S. S. Anufrik, M. F. Koldunov, A. A. Manenkov, and V. V. Tarkovskii. Lasing Efficiency of Dyes incorporated into a Nanoporous Glass-Polymer Composite. *J. Appl. Spectrosc.*, 75(5):714–722, 2008.

[182] Kenichi Yamashita, Masahiro Ito, Eshin Fukuzawa, Hiroyuki Okada, and Kunishige Oe. Device Parameter Analyses of Solid-State Organic Laser Made by Self-Written Active Waveguide Technique. *J. Lightwave Technol.*, 27(20):4570–4574, 2009.

[183] Kenichi Yamashita, Masahiro Ito, Shuhei Sugimoto, Takashi Morishita, and Kunishige Oe. Optically end-pumped plastic waveguide laser with in-line Fabry-Pérot resonator. *Opt. Express*, 18 (23):24092–24100, 2010.

[184] A. Costela, I. García-Moreno, C. Gómez, O. García, and R. Sastre. New organic-inorganic hybrid matrices doped with rhodamine 6G as solid-state dye lasers. *Appl. Phys. B*, 75:827–833, 2002.

[185] Angel Costela, Inmaculada García-Moreno, Clara Gómez, Olga Garía, and Roberto Sastre. Enhancement of laser properties of pyrromethene 567 dye incorporated into new organic-inorganic hybrid materials. *Chem. Phys. Lett.*, 369:656–661, 2003.

[186] A. Costela, I. García-Moreno, C. Gómez, O. García, and R. Sastre. Environment effects on the lasing photostability of Rhodamine 6G incorporated into organic-inorganic hybrid materials. *Appl. Phys. B*, 78:629–634, 2004.

[187] Angel Costela, Inmaculada García-Moreno, Clara Gómez, Olga García, Leoncio Garrido, and Roberto Sastre. Highly efficient and stable doped hybrid organic-inorganic materials for solid-state dye lasers. *Chem. Phys. Lett.*, 387:496–501, 2004.

[188] A. Costela, I. García-Moreno, D. del Agua, O. García, and R. Sastre. Silicon-containing organic matrices as hosts for highly photostable solid-state dye lasers. *Appl. Phys. Lett.*, 85(12), 2004.

[189] A. Costela, I. García Moreno, C. Gómez, O. García, R. Sastre, A. Roig, and E. Molins. Polymer-Filled Nanoporous Silica Aerogels as Hosts for Highly Stable Solid-State Dye Lasers. *J. Phys. Chem. B*, 109:4475–4480, 2005.

[190] A. Costela, I. García-Moreno, O. García, D. Del Agua, and R. Sastre. Structural influence of the inorganic network in the laser performance of dye-doped hybrid materials. *Appl. Phys. B*, 80: 749–755, 2005.

[191] I. García-Moreno, A. Costela, A. Cuesta, O. García, D. del Agua, and R. Sastre. Synthesis, structure, and physical properties of hybrid nanocomposites for solid-state dye lasers. *J. Phys. Chem. B*, 109:21618–21626, 2005.

[192] Inmaculada García-Moreno, Francisco Amat-Guerri, Marta Liras, Angel Costela, Lourdes Infantes, Roberto Sastre, Fernando López Arbeloa, Jorge Bañuelos Prieto, and Íñigo López Arbeloa. Structural Changes in the BODIPY Dye PM567 Enhancing the Laser Action in Liquid and Solid Media. *Adv. Funct. Mater.*, 17:3088–3098, 2007.

[193] A. Costela, I. García-Moreno, D. del Agua, O. García, and R. Sastre. Highly photostable solid-state dye lasers based on silicon-modified organic matrices. *J. Appl. Phys.*, 101:073110, 2007.

[194] Roberto Sastre, Virginia Martín, Leoncio Garrido, José Luis Chiara, Beatriz Trastoy, Olga García, Angel Costela, and Inmaculada García-Moreno. Dye-Doped Polyhedral Oligomeric Silsesquioxane (POSS)-Modified Polymeric Matrices for Highly Efficient and Photostable Solid-State Lasers. *Adv. Funct. Mater.*, 19:3307–3316, 2009.

[195] V. Bulović, V. G. Kozlov, V. B. Khalfin, and S. R. Forrest. Transform-Limited, Narrow-Linewidth Lasing Action in Organic Semiconductor Microcavities. *Science*, 279:553–555, 1998.

[196] Luana Persano, Andrea Camposeo, Pompilio Del Carro, Elisa Mele, Roberto Cingolani, and Dario Pisignano. Very high-quality distributed Bragg reflectors for organic lasing applications by reactive electron-beam deposition. *Opt. Express*, 14(5):1951–1956, 2006.

[197] H. Matsuura, M. Fukuda, and H. Sakata. Threshold reduction induced by silica nanoparticledispersed active layer in diode-pumped microcavity dye laser. *Laser Phys. Lett.*, 6(3):194–197, 2009.

[198] Qinghai Song, Liying Liu, Lei Xu, Yonggang Wu, and Zhanshan Wang. Electrical tunable random laser emission from a liquid-crystal infiltrated disordered planar microcavity. *Opt. Lett.*, 34(3): 298–300, 2009.

[199] Luana Persano, Andrea Camposeo, Pompilio Del Carro, Pierpaolo Solaro, Roberto Cingolani, Patrizia Boffi, and Dario Pisignano. Rapid prototyping encapsulation for polymer light-emitting lasers. *Appl. Phys. Lett.*, 94:123305, 2009.

[200] Guilin Mao, James Andrews, Michael Crescimanno, Kenneth D. Singer, Eric Baer, Anne Hiltner, Hyunmin Song, and Bijayandra Shakya. Co-extruded mechanically tunable multilayer elastomer laser. *Opt. Mat. Express*, 1(1):108–114, 2011.

[201] Hadi Rabbani-Haghighi, Sébastien Forget, Sébastien Chénais, and Alain Siove. Highly efficient, diffraction-limited laser emission from a vertical external-cavity surface-emitting organic laser. *Opt. Lett.*, 35(12):1968–1970, 2010.

[202] A. E. Vasdekis, G. Tsiminis, J.-C. Ribierre, Liam O' Faolain, T. F. Krauss, G. A. Turnbull, and I. D. W. Samuel. Diode pumped distributed Bragg reflector lasers based on a dye-to-polymer energy transfer blend. *Opt. Express*, 14(20):9211–9216, 2006.

[203] V. G. Kozlov, V. Bulović, P. E. Burrows, and S. R. Forrest. Laser action in organic semiconductor waveguide and double-heterostructure devices. *Nature*, 389:362–364, 1997.

[204] V. G. Kozlov and S. R. Forrest. Lasing action in organic semiconductor thin films. *Curr. Opin. Solid St. M.*, 4:203–208, 1999.

[205] George Heliotis, Donal D. C. Bradley, Graham A. Turnbull, and Ifor D. W. Samuel. Light amplification and gain in polyfluorene waveguides. *Appl. Phys. Lett.*, 81(3):415–417, 2002.

[206] Takeyuki Kobayashi, Jean-Baptiste Savatier, Grace Jordan, Werner J. Blau, Yasuhiro Suzuki, and Toshikuni Kaino. Near-infrared laser emission from luminescent plastic waveguides. *Appl. Phys. Lett.*, 85(2):185–187, 2004.

[207] Musubu Ichikawa, Kiyoshi Nakamura, Masamitsu Inoue, Hiromi Mishima, Takeshi Haritani, Ryota Hibino, Toshiki Koyama, and Yoshio Taniguchi. Photopumped laser oscillation and charge-injected luminescence from organic semiconductor single crystals of a thiophene/phenylene co-oligomer. *Appl. Phys. Lett.*, 87:221113, 2005.

[208] Shun Yuyama, Takahiro Nakajima, Kenichi Yamashita, and Kunishige Oe. Solid state organic laser emission at 970 nm from dye-doped fluorinated-polyimide planar waveguides. *Appl. Phys. Lett.*, 93:023306, 2008.

[209] T. Kobayashi and W.J. Blau. Laser emission from conjugated polymer in fibre waveguide structure. *Electron. Lett.*, 38(2):67–68, 2002.

[210] Takeyuki Kobayashi, Werner J. Blau, Hartwig Tillmann, and Hans-Heinrich Hörhold. Light Amplification and Lasing in a Stilbenoid Compound-Doped Glass-Clad Polymer Optical Fiber. *IEEE J. Quant. Electron.*, 39(5):664–672, 2004.

[211] Alexander Argyros, Martijn A. van Eijkelenborg, Stuart D. Jackson, and Richard P. Mildren. Microstructured polymer fiber laser. *Opt. Lett.*, 29(16):1882–1884, 2004.

[212] G. Wegmann, H. Giessen, D. Hertel, and R. F. Mahrt. Blue-green laser emission from a solid conjugated polymer. *Solid State Commun.*, 104(12):759–762, 1997.

[213] I. García-Moreno, A. Costela, M. Pintado-Sierra, V. Martín, and R. Sastre. Enhanced laser action of Perylene-Red doped polymeric materials. *Opt. Express*, 17(15):12777–12784, 2009.

[214] T. N. Kopylova, G. V. Maier, E. N. Telminov, V. A. Svetlichnyi, and K. M. Degtyarenko. A double-frequency solid-state laser on organic compounds. *Russ. Phys. J.*, 52(7):655–660, 2009.

[215] Magnus Berggren, Ananth Dodabalapur, Zhenan Bao, and Richart E. Slusher. Solid-state Droplet Laser Made from an Organic Blend with a Conjugated Polymer Emitter. *Adv. Mater.*, 9(12): 968–971, 1997.

[216] S. V. Frolov, M. Shkunov, Z. V. Vardeny, and K. Yoshino. Ring microlasers from conducting polymers. *Phys. Rev. B*, 56(8):R4363–R4366, 1997.

[217] Makoto Fukuda and Keiichi Mito. Laser oscillation of energy transfer solid-state dye laser with a thin-film ring resonator. *Jpn. J. Appl. Phys.*, 39(6A):3470–3471, 2000.

[218] Makoto Fukuda, Kunihiko Kodama, Hiroshi Yamamoto, and Keiichi Mito. Evaluation of new organic pigments as laser-active media for a solid-state dye laser. *Dyes and Pigments*, 63:115–125, 2004.

[219] Juhee Yang, Sang-Bum Lee, Jeong-Bo Shim, Songky Moon, Soo-Young Lee, Sang Wook Kim, Jai-Hyung Lee, and Kyungwon An. Enhanced nonresonant optical pumping based on turnstile transport in a chaotic microcavity laser. *Appl. Phys. Lett.*, 93:061101, 2008.

[220] Xiang Wu, Hao Li, Liying Liu, and Lei Xu. High Quality Direct Photo-Patterned Microdisk Lasers With Organic-Inorganic Hybrid Materials. *IEEE J. Quantum. Electron.*, 44(1):75–80, 2008.

[221] Lei Shang, Liying Liu, and Lei Xu. Single-frequency coupled asymmetric microcavity laser. *Opt. Lett.*, 33(10):1150–1152, 2008.

[222] Xiang Wu, Hao Li, Liying Liu, and Lei Xu. Unidirectional single-frequency lasing from a ring-spiral coupled microcavity laser. *Appl. Phys. Lett.*, 93:081105, 2008.

[223] N. Djellali, I. Gozhyk, D. Owens, S. Lozenko, M. Lebental, J. Lautru, C. Ulysse, B. Kippelen, and J. Zyss. Controlling the directional emission of holey organic microlasers. *Appl. Phys. Lett.*, page 101108, 2009.

[224] Sönke Klinkhammer, Tobias Großmann, Karl Lüll, Mario Hauser, Christoph Vannahme, Timo Mappes, Heinz Kalt, and Uli Lemmer. Diode-Pumped Organic Semiconductor Microcone Laser. *IEEE Photon. Technol. Lett.*, 23(8):489–491, 2011.

[225] Jin-Feng Ku, Qi-Dai Chen, Ran Zhang, and Hong-Bo Sun. Whispering-gallery-mode microdisk lasers produced by femtosecond laser direct writing. *Opt. Lett.*, 36(15):2871–2873, 2011.

[226] Van Duong Ta, Rui Chen, and Han Dong Sun. Self-Assembled Flexible Microlasers. *Adv. Mater.*, 24:OP60–OP64, 2012.

[227] R. M. Balachandran, D. P. Pacheco, and N. M. Lawandy. Laser action in polymeric gain media containing scattering particles. *Appl. Opt.*, 35(4):640–643, 1996.

[228] Giannis Zacharakis, George Heliotis, George Filippidis, Demetrios Anglos, and Theodore G. Papazoglou. Investigation of the laserlike behavior of polymeric scattering gain media under subpicosecond laser excitation. *Appl. Opt.*, 38(28):6087–6092, 1999.

[229] S. V. Frolov, Z. V. Vardeny, K. Yoshino, A. Zakhidov, and R. H. Baughman. Stimulated emission in high-gain organic media. *Phys. Rev. B*, 59(8):R5284–R5287, 1999.

[230] Randy C. Polson, Arkadi Chipouline, and Z. Valy Vardeny. Random Lasing in π-Conjugated Films and Infiltrated Opals. *Adv. Mater.*, 13:760–764, 2001.

[231] R. C. Polson, M. E. Raikh, and Z. V. Vardeny. Random lasing from weakly scattering media; spectrum universality in DOO-PPV polymer films. *Physica E*, 13:1240–1242, 2002.

[232] Shiyoshi Yokoyama and Shinro Mashiko. Tuning of Laser Frequency in Random Media of Dye-Doped Polymer and Glass-Particle Hybrid. *Jpn. J. Appl. Phys.*, 42(8A):L970–L973, 2003.

[233] Stéphane Klein, Olivier Crégut, Denis Gindre, Alex Boeglin, and Kokou D. Dorkenoo. Random laser action in organic film during the photopolymerization process. *Opt. Express*, 13(14):5387–5392, 2005.

[234] F. Quochi, F. Cordella, A. Mura, G. Bongiovanni, F. Balzer, and H.-G. Rubahn. Gain amplification and lasing properties of individual organic nanofibers. *Appl. Phys. Lett.*, 88:041106, 2006.

[235] Christiano J. S. de Matos, Leonardo de S. Menezes, Antônio M. Brito-Silva, M. A. Martinez Gámez, Anderson S. L. Gomes, and Cid B. de Araújo. Random Fiber Laser. *Phys. Rev. Lett.*, 99: 153903, 2007.

[236] Vassilis M. Papadakis, Andreas Stassinopoulos, Demetrios Anglos, Spiros H. Anastasiadis, Emmanuel P. Giannelis, and Dimitris G. Papazoglou. Single-shot temporal coherence measurements of random lasing media. *J. Opt. Soc. Am. B*, 24(1):31–36, 2007.

[237] Sara García-Revilla, Joaqun Fernández, Maria Asunción Illarramendi, Begoña García-Ramiro, Rolíndes Balda, Hongtao Cui, Marcos Zayat, and David Levy. Ultrafast random laser emission in a dye-doped silica gel powder. *Opt. Express*, 16(16):12251–12263, 2008.

[238] Xiangeng Meng, Koji Fujita, Yanhua Zong, Shunsuke Murai, and Katsuhisa Tanaka. Random lasers with coherent feedback from highly transparent polymer films embedded with silver nanoparticles. *Appl. Phys. Lett.*, 92:201112, 2008.

[239] Xiangeng Meng, Koji Fujita, Shunsuke Murai, and Katsuhisa Tanaka. Coherent random lasers in weakly scattering polymer films containing silver nanoparticles. *Phys. Rev. A*, 79:053817, 2009.

[240] Angel Costela, Inmaculada García-Moreno, Luis Cerdan, Virginia Martin, Olga García, and Roberto Sastre. Dye-Doped POSS Solutions: Random Nanomaterials for Laser Emission. *Adv. Mater.*, 21:1–4, 2009.

[241] Sara García-Revilla, Marcos Zayat, Rolindes Balda, Mohammad Al-Saleh, David Levy, and Joaquín Fernández. 1Low threshold random lasing in dye-doped silica nano powders. *Opt. Express*, 17(15):13202–13215, 2009.

[242] P. D. García, M. Ibisate, R. Sapienza, D. S. Wiersma, and C. López. Mie resonances to tailor random lasers. *Phys. Rev. A*, 80:013833, 2009.

[243] Edison Pecoraro, Sara García-Revilla, Rute A. S. Ferreira, Rolindes Balda, Luís D. Carlos, and Joaqun Fernández. Real time random laser properties of Rhodamine-doped di-ureasil hybrids. *Opt. Express*, 18(7):7470–7478, 2010.

[244] L. Cerdán, A. Costela, I. García-Moreno, O. García, and R. Sastre. Laser emission from mirrorless waveguides based on photosensitized polymers incorporating POSS. *Opt. Express*, 18(10):10247–10256, 2010.

[245] M. Anni. A flexible organic random laser based on poly(9,9-dioctylfluorene) deposited on a surface corrugated poly-phthalate-carbonate substrate. *Appl. Phys. Lett.*, 98:253304, 2011.

[246] S. Kéna-Cohen, P. N. Stavrinou, D. D. C. Bradley, and S. A. Maier. Random lasing in low molecular weight organic thin films. *Appl. Phys. Lett.*, 99:041114, 2011.

[247] Yue Wang. *Low threshold organic semiconductor lasers and their applications as explosive sensors.* PhD thesis, University of St. Andrews, UK, 2012.

[248] P. P. Sorokin, J. R. Lankard, V. L. Moruzzi, and E. C. Hammond. Flashlamp-Pumped Organic-Dye Lasers. *J. Chem. Phys.*, 48(10):4726–4741, 1968.

[249] R. Bornemann, U. Lemmer, and E. Thiel. Continuous-wave solid-state dye laser. *Opt. Lett.*, 31 (11):1669–1671, 2006.

[250] R. Bornemann, E. Thiel, and P. Haring Bolívar. High-power solid-state cw dye laser. *Opt. Express*, 19(27):26382–26393, 2011.

[251] Kenichi Yamashita, Kengo Hase, Hisao Yanagi, and Kunishige Oe. Optical Amplification in Organic Dye-doped Polymeric Channel Waveguide under CW Optical Pumping. *Jpn. J. Appl. Phys.*, 46(28):L688–L690, 2007.

[252] W. Helfrich and W. G. Schneider. Recombination radiation in anthracene crystals. *Phys. Rev. Lett.*, 14(7):229–231, 1965.

[253] C. W. Tang and S. A. VanSlyke. Organic electroluminescent diodes. *Appl. Phys. Lett.*, 51(12): 913–915, 1987.

[254] J. H. Burroughes, D. D. C. Bradley, A. R. Brown, R. N. Marks, K. Mackay, R. H. Friend, P. L. Burns, and A. B. Holmes. Light-emitting diodes based on conjugated polymers. *Nature*, 347: 539–541, 1990.

[255] J. H. Schön, Ch. Kloc, A. Dodabalapur, and B. Batlogg. An Organic Solid State Injection Laser. *Science*, 289:599–601, 2000. Retracted in 2002.

[256] Zhenan Bao, Bertram Batlogg, Steffen Berg, Ananth Dodabalapur, Robert C. Haddon, Harold Hwang, Christian Kloc, Hong Meng, and J. Hendrik Schön. Retraction. *Science*, 298:961, 2002.

[257] F. J. Duarte. Coherent electrically excited organic semiconductors: coherent or laser emission? *Appl. Phys. B*, 90:101–108, 2008.

[258] Xingyuan Liu, Huibin Li, Chunyan Song, Yaqin Liao, and Miaomiao Tian. Microcavity organic laser device under electrical pumping. *Opt. Lett.*, 34(4):503–505, 2009.

[259] Ifor D.W. Samuel, Ebinazar B. Namdas, and Graham A. Turnbull. How to Recognise Lasing. *Nature Photonics*, 3:546–549, 2009.

[260] S. N. Mohammad and H. Morkoç. Progress and prospects of group-III nitride semiconductors. *Prog. Quant. Electron.*, 20(5/6):361–525, 1996.

[261] Jongwoon Park. Speedup of dynamic response of organic light-emitting diodes. *J. Lightwave Technol.*, 28(19):2873–2880, 2010.

[262] Iain A. Barlow, Theo Kreouzis, and David G. Lidzey. High-speed electroluminescence modulation of a conjugated-polymer light emitting diode. *Appl. Phys. Lett.*, 94:243301, 2009.

[263] M. Wohlgenannt and Z. V. Vardeny. Spin-dependent exciton formation rates in π-conjugated materials. *J. Phys.: Condens. Matter*, 15:R83–R107, 2003.

Part II

Results

Chapter 3

Material Properties

The previous chapter gave a general introduction to light emitting polymers (LEPs), their basic physics and their performance as optical gain media. Here, detailed properties of the specific materials used during this work are presented. This chapter consists of two major parts. Section 3.1 lists the various materials and illustrates their basic properties. The second part, consisting of sections 3.2 and 3.3, concentrates on optical gain and in particular random laser action (RL). Section 3.2 gives a general introduction to the topic and summarises experimental results. A priori, RL was not expected from many of the samples discussed here. However, the data and analysis presented in this chapter indicate that RL can be seen as a material property of high optical gain media. A theoretical analysis of the RL phenomenon which is included here in section 3.3 has been published in the IEEE Journal of Quantum Electronics [1].

3.1 Materials used in this Work

Three types of solution-processible chromophores were used in this study: A blue-emitting star-shaped oligomer, a green-emitting conjugated polymer and inorganic colloidal quantum dots (CQDs). Toluene was used as solvent for solution processing of organic films unless specified otherwise. Other possibilities exist, the most important of which are illustrated in figure 3.1. Generally, a higher boiling point of the solvent will result in better uniformity of solution-cast films [2]. Furthermore, some optically passive organic media were utilised for the creation of functional structures. These are briefly presented in section 3.1.4.

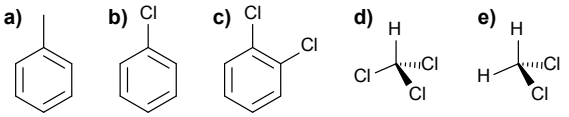

FIGURE 3.1: Solvents for processing of LEPs: *a)* toluene, *b)* chlorobenzene, *c)* o-dichlorobenzene, *d)* chloroform and *e)* dichloromethane (DCM).

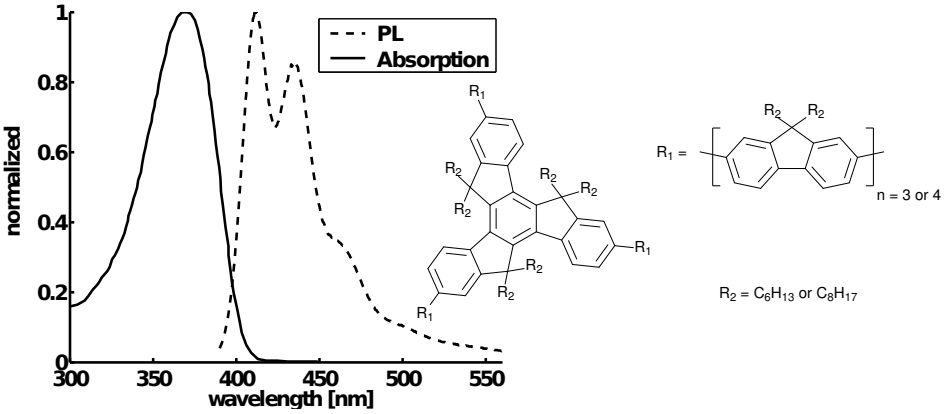

FIGURE 3.2: Absorption, PL (in toluene solution) and chemical structure of oligofluorene truxene. The absorption and emission curves shown here were taken from T3 hexyl.

3.1.1 Blue-emitting Oligofluorene Truxenes

As pointed out in section 2.1.2.4, oligomers are a material class offering a high degree of controllability of the molecular properties. In particular, fluorene-based oligomers have seen considerable interested in the past couple of years. Fluorenes are an important and popular platform for studying fundamental physics of organic semiconductors because they can be synthesised at a high degree of purity [3] and monodisperse oligofluorene-boronic acid chains can be synthesised by repetitive Suzuki-coupling [4], allowing for a wealth of possible fluorene-based structures. It is possible to attach such oligofluorene chains in a star-shaped geometry to a suitable core molecule. This core can simply be a benzene ring (figure 2.6a in the previous chapter). In our case, the oligofluorenes are attached to a truxene core.

The chemical structure, photoluminescence (PL) and absorption spectra of the truxene materials are shown in figure 3.2. For this work, materials with either three (T3) or four (T4) fluorene units per arm were available. The side groups R_2 of the fluorene units can be either hexyl or octyl chains which determine the solubility properties. All measurements presented in this thesis were done on hexyl materials unless specified otherwise. The spectra plotted in figure 3.2 were taken from T3 hexyl, although differences in between T3/T4 with hexyl/octyl side chains are only a few nanometres in the wavelengths of the vibronic peaks and are usually overridden by other experimental factors such as

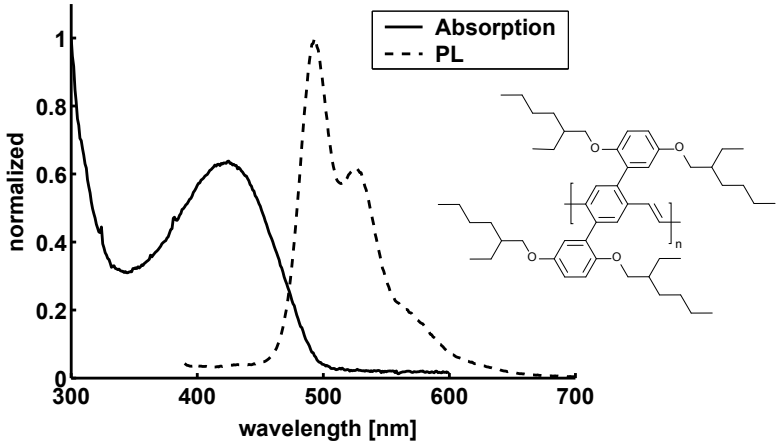

FIGURE 3.3: Absorption, PL (in toluene solution) and chemical structure of BBEHP-PPV.

the surrounding solvent/polymer matrix or self absorption of waveguided emission. See also [4] for a rigorous study of truxene oligofluorenes with different arm length.

3.1.2 Green-emitting Poly-phenylene-vinylene

While the oligofluorene truxenes represent a novel material class, they are not ideally suitable for LED-pumping at high intensity. This is because their absorption peaks in the near UV at around 375 nm and therefore can only be excited by UV LEDs that are not capable of delivering the same output powers as highly efficient blue LEDs (c.f. figure 1.1). A promising material with low laser threshold and an absorption peak in the blue is the green emitting polymer Poly[2,5-bis(2',5'-bis(2"-ethylhexyloxy)phenyl)-p-phenylene-vinylene] (BBEHP-PPV). Its chemical structure, absorption and luminescence spectra are shown in figure 3.3. BBEHP-PPV is soluble in toluene, chloroform and chlorobenzene, all of which were used for spin-coating of this material onto suitable substrates. Originally, this molecule was synthesised by Swager's group at the Massachusetts Institute of Technology for the particular purpose of chemosensing of explosives, as described in the introduction (section 1.2.1) [5].

In contrast to the oligofluorene molecules, the synthesis product here is a highly multidisperse mixture of molecules, not all of which have favourable optical properties. Purified material batches can be extracted from the synthesis product using solvents. In a first step, low molecular weight (MW) material ($\sim$25000 u – where 1 u is the atomic mass unit – giving poor film quality when spin-coating) is extracted with methanol and acetone. Then, high MW material (several 100000 u) is extracted in one or several extraction steps with dichloromethane (DCM) [6]. In this chapter, several material batches of BBEHP-PPV are compared. They are denoted by a leading "AK*xyz*", specifying the synthesis

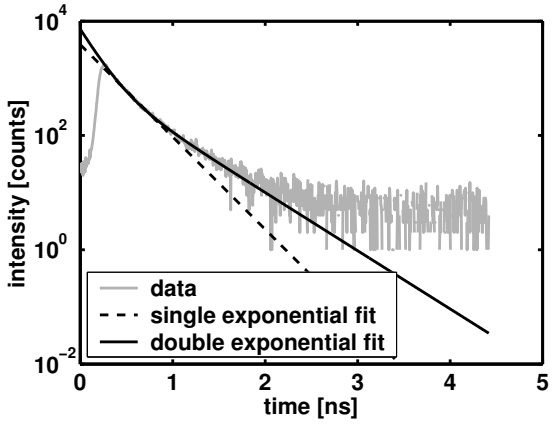

FIGURE 3.4: Time resolved fluorescence of BBEHP-PPV at 530 nm demonstrating the necessity for double-exponential fitting.

batch, and a trailing "DCMn" which specifies the extraction step. The main difference between the batches is the dispersity of polymer chain length. Batch AK391DCM2 has the highest monodispersity, followed by AK391DCM1. Batches AK350DCM and AK408DCM have roughly the same degree of dispersity and are slightly more polydisperse than AK391DCM1 (see also table 3.2 below). While all material batches have a similar photoluminescence quantum yield of around 80 % [7], they do behave differently when operating above threshold for optical gain. These differences are discussed below in section 3.2.3.2 and have also been confirmed by our project partners at the University of St. Andrews [7, 8].

3.1.2.1 Radiative Lifetime

The luminescence dynamics of BBEHP-PPV (AK350DCM) films on glass were studied with a streak camera[1]. The data was fitted by single or double exponential decay functions as described in appendix A.5. As can be seen in figure 3.4, a double-exponential fit yields much better results than assuming a single exponential decay. The two lifetime components are about $\tau_1 \approx 0.43$ ns, $\tau_2 \approx 0.16$ ns and the ratio of the two amplitudes does not depend on the emission wavelength. The overall fluorescence lifetime of 0.4 ns is slightly shorter than that of 0.6 ns reported by Rose *et al.* [5].

3.1.3 Cadmium Selenide Colloidal Quantum Dots

A highly interesting achievement of inorganic semiconductor crystal fabrication is the possibility to create nanometre-sized structures in which charge carriers are confined

[1]The University of Southampton is acknowledged for enabling us to use their streak camera equipment.

due to changes of the (conduction- and/or valence-) band-edge along the boundary of the structure. Due to the small feature size, the discrete nature of quantum-confined states along the direction of confinement dominates the physical properties. Quantum confinement can be achieved along one ("quantum well", QW), two ("nanowire", NW) or three ("quantum dot", QD) directions. QWs are a widespread technology in optical semiconductor devices such as LEDs or laser diodes. The GaN LEDs used in chapters 5 and 6 utilise QWs. NWs and their close relative, the quantum point contact are studied extensively for their electrical properties. From a photonics point of view, NWs are often used as host for QDs. QDs have a discrete set of energy states similar to atomic states and can therefore be viewed as artificial atoms, the properties of which can be designed by choice of material and geometry. Therefore, QDs are the subject of great attention in the optical community.

3.1.3.1 Synthesis

QDs can be created by a wealth of epitaxial (thin-film deposition) procedures, but nanometre-sized semiconductor crystals can also be synthesised chemically by injecting suitable metalorganic precursors into an organic reaction agent (usually trioctylphosphine oxide, TOPO) at a certain temperature around 300°C under vigorous stirring [9, 10]. This is illustrated in figure 3.5. Initially, nucleation will relax the oversaturated mixture within less than a minute. The size distribution of these initial semiconductor nuclei is largely determined by how evenly the onset of nucleation occurs within the reaction vessel [10]. Once the concentration of metalorganics has dropped below the nucleation threshold, the existing nuclei will grow more slowly on a time-scale of minutes to hours, allowing good control of the nanocrystal size which is typically in the diameter range 1-10 nm, corresponding to several hundred to a few thousand atoms [9, 10]. It is possible to resume growth on the surface of existing nuclei but with different precursors, allowing for the creation of core-shell structures with a (wider-bandgap) outer layer. These core-shell CQDs have improved properties due to reduced effects of surface states [10–12]. After growth, the TOPO molecules are attached to the surface of the CQDs as so-called ligands. Ligands can be exchanged allowing one to tailor solubility properties as well as CQD spacing in close-packed films [10].

3.1.3.2 Optical Properties

Due to the conduction- and valence band offsets in CdSe/ZnS CQDs there exists a discrete set of bound states within the CdSe core for both electrons and holes as illustrated in figure 3.6a. A fairly good understanding of the nature of these states can be obtained

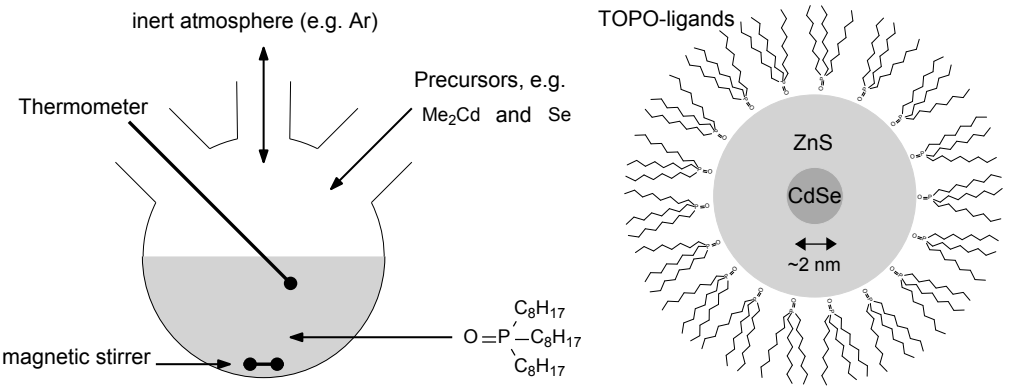

FIGURE 3.5: Schematic illustrating the synthesis of CQDs. The right hand side illustrates a CdSe/ZnS core-shell CQD with TOPO-ligands.

in the Bloch-picture (i.e. the wavefunction is the product of a carrier- and an envelope-function, where the carrier has the same periodicity as the semiconductor crystal) with spherical confinement.

The Bloch carrier functions for the conduction band in CdSe are s-type orbitals and therefore the spin-degenerate bound conduction band states can be labelled by the envelope function radial quantum number n_e and angular momentum L_e [13].

Valence band states are more complicated, because their carrier functions are p-type orbitals, and therefore sixfold degenerate (including spin), and the confinement leads to band-mixing due to interaction of carrier- and envelope angular momenta. If J_h is the total carrier function angular momentum (including spin), then conserved quantum numbers are the total angular momentum $F_h := J_h + L_h$ (L_h being the envelope function angular momentum) and the envelope function radial quantum number n_h. Furthermore, exactly two spherical harmonics of the envelope function are mixed in each state, namely $L_h = \mathscr{L}$ and $L_h = \mathscr{L} + 2$, $\mathscr{L} = s, p, d, \ldots$ [13].

Commonly, bound exciton states in CQDs are hence labelled as $n_e L_e - n_h \mathscr{L}_{F_h}$ [13]. This scheme, illustrated in figure 3.6, is sufficient to understand the absorption and luminescence features of CQDs.

Excited CQDs quickly relax into the $1S_e - 1S_{3/2}$ state which gives rise to a single Gaussian luminescence peak. This luminescence peak is redshifted compared to the $1S_e - 1S_{3/2}$ absorption feature (see figure 3.6c). Contrary to organics, this Stokes-shift is not associated with a structural configuration change of the emitter. It is most pronounced for small CQDs and disappears in the bulk-limit [15]. To understand it, we have to extend the above scheme by the spin configuration of the exciton. In fact, the lowest lying substate of $1S_e - 1S_{3/2}$ (which is mainly contributing to the luminescence) is a spin triplet state and therefore has a negligible absorption cross section (sometimes it is referred to as "dark exciton") whereas the $1S_e - 1S_{3/2}$ absorption feature is due to the singlet state which has a slightly higher energy [15].

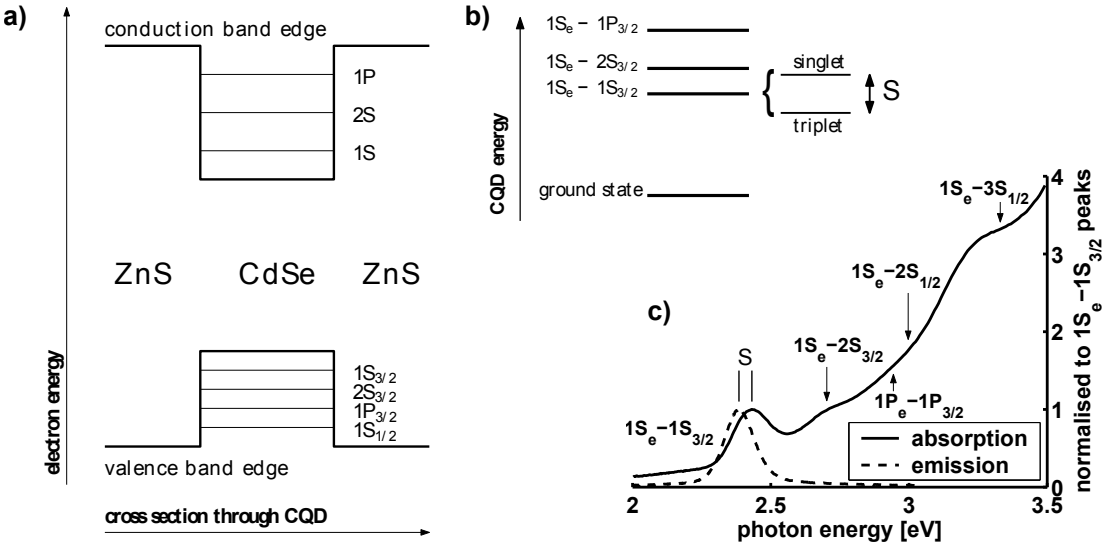

FIGURE 3.6: *a)* Illustration of bound electron and hole states in CdSe/ZnS core-shell quantum dots. *b)* Excitonic energy states of a CQD including illustration of the origin of the Stokes shift S. *c)* Room-temperature absorption and emission spectra of CdSe/ZnS core-shell CQDs in an epoxy matrix (more data including other sizes of dots can be found in [14]). The Stokes shift S is highlighted and approximate positions of dominant higher-lying excitonic transitions according to [13] are indicated.

For our research, CdSe/ZnS core-shell CQDs from Evident Technologies were used with PL peak wavelengths at 522, 564, 596 and 617 nm, respectively.

The radiation dynamics of yellow (564 nm) CQDs have been studied with a streak camera and double-exponential fitting as described in appendix A.5 was used to analyse the data. As can be seen in figure 3.7a), two lifetime components have to be taken into account with decay times $\tau_1 = 7.2$ ns and $\tau_2 = 1.8$ ns. The amplitudes of each lifetime component are plotted in figure 3.7b). Apparently the short lifetime component is only important at the blue end of the QD emission. A possible explanation is energy transfer from smaller dots to larger dots.

3.1.4 Inert Materials

The usage of transparent polymer materials in conjunction with organic light emitters has a long-standing tradition. Dyes need to be spatially separated in order to prevent emission quenching and this can be achieved by embedding them in either a molecular solid or in a chemically inert transparent polymer matrix. The first OSLs reported were in this latter format [16, 17] and to date there is a continuous flow of publications based on this technology. Also, photocurable polymers can be used to create structures by various lithographic methods - e.g. UV-embossing - and inert host matrices or overlayers may reduce effects of photodegradation. For example, an effective encapsulation of an

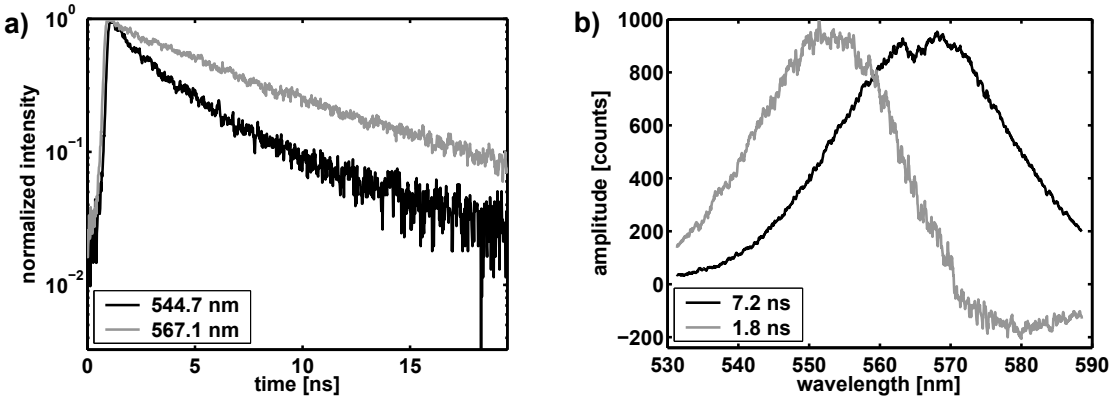

FIGURE 3.7: Time resolved CQD luminescence of CQDs with PL peak at 564 nm: *a)* Traces at two different wavelengths show that at the red end of the CQD emission spectrum, a single exponential decay may be suitable, but at shorter wavelengths a shorter lifetime component is clearly visible. *b)* Amplitudes of the two lifetime components as a function of wavelength. Note that the absolute values for the amplitudes are meaningless because the time origin of the fit was left arbitrary.

OSL was achieved by glass plates sealed with an epoxy [18]. A selection of polymers used in this context is illustrated in figure 3.8. PMMA and SU8 are popular host matrices for dyes and CQDs, and PMMA is the foremost organic material for optical waveguiding. PSS doped with conjugated polymers is commonly used in OLEDs (in particular PEDOT:PSS for p-type contacts) and has been employed for OSLs as well.

During this PhD, our work concentrated largely on CHDV and CHDG which both offer high transmittance in the near UV [19–21] and therefore do not absorb much of the pump light. A transmission spectrum of CHDV is shown in the next chapter in figure 4.2. Polymerisation is initiated with a photo-acid generator (PAG), in our case 4-octyloxy diphenyliodonium hexafluoroantimonite. This is a salt consisting of a negatively charged SbF_6^- ion and a positively charged iodonium ion. The latter is attached to conjugated phenyl groups enabling efficient UV light absorption. Upon photon absorption, complex processes occur usually in interaction with surrounding solvents/matrices (RH group in figure 3.8) though most importantly they result in release of the SbF_6^- ion, along with a proton, which in turn breaks up and connects the double bonds/rings of vinyl ether/epoxy ether functional groups [19].

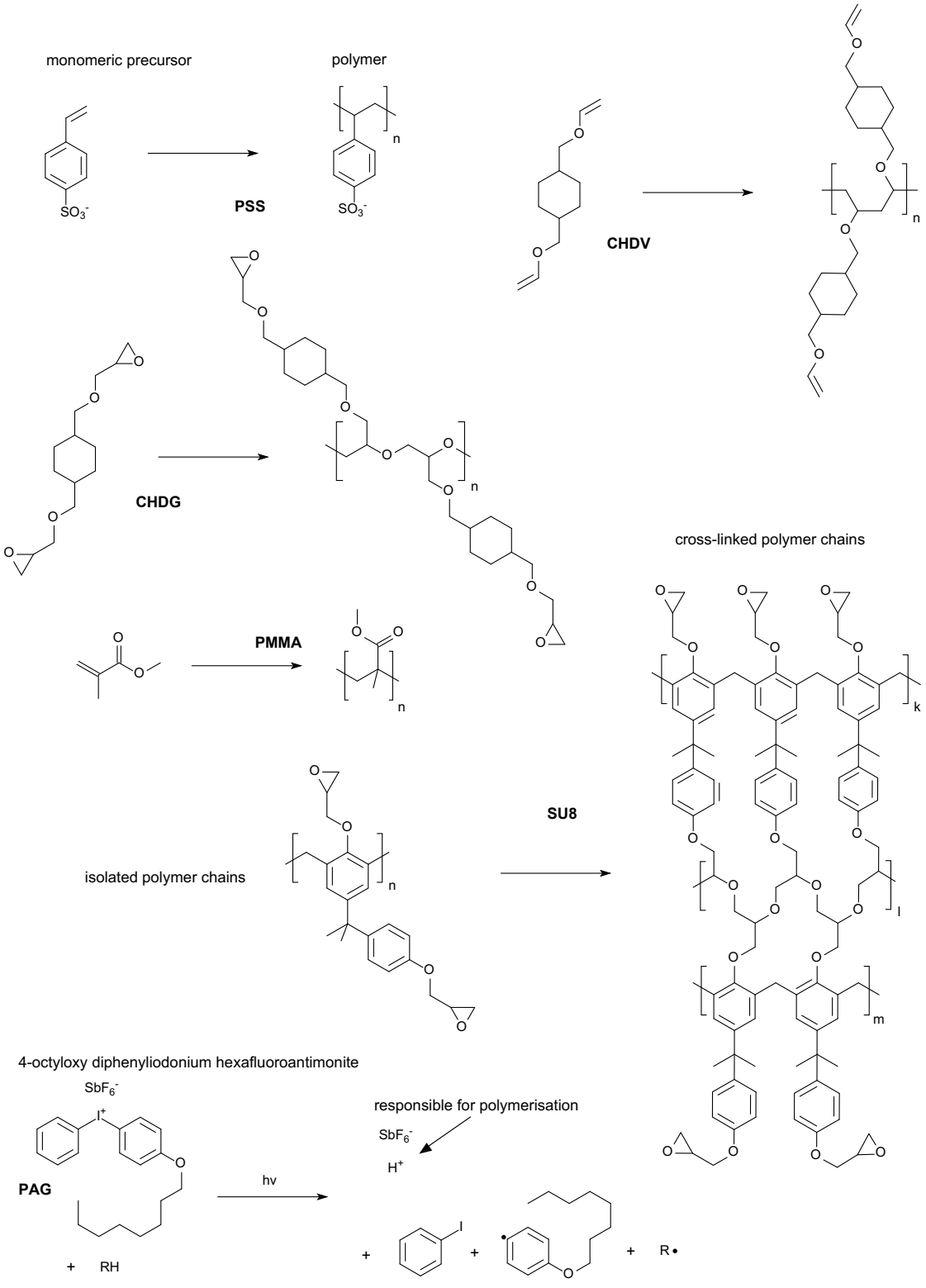

FIGURE 3.8: Some chemically inert polymer matrices used in conjunction with LEPs and CQDs: polymethyl methacrylate (PMMA), polystyrene sulfonate (PSS), 1,4-cyclohexanedimethanol diglycidyl ether (CHDG), 1,4-cyclohexyldimethanol divinyl ether (CHDV) and SU8-photoresist. Also shown is a photo-acid generator (PAG) used to initiate polymerisation.

3.2 Observation of Random Laser Action in Stripe Excitation

Before building a laser cavity from an organic material, it is customary to first assess the material's properties by photo-pumping a neat, unstructured film, usually in stripe-geometry. A good indication for the suitability of the material for laser applications is the observation of amplified spontaneous emission (ASE) in such experiments. ASE is characterised by a "threshold" in the power-transfer function and a modest spectral line-narrowing (to a typical ASE linewidth of 4-10 nm in the case of organic semiconductors) above this threshold. Intriguingly, we did not observe normal, spectrally smooth ASE in any organic neat film fabricated during the course of this work, but instead the observed characteristics are those of a random laser (RL). This section describes the observed RL properties in detail, and below in section 3.3 a simple theoretical model is presented that may explain why RL appears to be so common in high-gain organics.

In this thesis, we will concentrate on RL in neat films where any scatterers were unintentional. However, it can be easier to gain a physical understanding of the relevant processes if the shape, size and optical properties of the scatterers are known. Therefore, deliberately adding scatterers into an LEP film is a fruitful method for fundamental studies. Our work on RL in LEPs doped with glass nano-particles has been published [22] and the interested reader can find a detailed discussion in Yujie Chen's PhD thesis [23].

3.2.1 What is Random Lasing and Why is it Important?

The common understanding of what a laser is, is greatly dominated by those devices that have demonstrated practical applications. Upon hearing the word "laser", one normally assumes a three- or four-level optical gain medium in an engineered optical cavity, with the latter dominating most of the properties of the laser output. Hence, the acronym "light amplification by stimulated emission of radiation" does not cover all aspects that are usually associated with laser devices. One typically expects 1^{st} and 2^{nd} order coherent narrow-linewidth emission in a well-defined beam and very often a definite polarisation state of the laser output. Furthermore, lasers are expected to need a population inversion in between ground- and excited state energy levels and a clear pump threshold is expected in the power transfer function. This limited view has naturally led to a number of (what are regarded as) peculiarities such as lasers without inversion [24], thresholdless lasers [25] and mirrorless lasers [26]. One such peculiarity is the random laser. It lacks some of the above mentioned properties and therefore is subject to divergent views from laser scientists.

	PL	ASE	RL	Conventional Laser
Linewidth	400 meV	30 meV	0.5 meV (highly multimode)	≤1 meV
1^{st} order coherent	normally not	partially	yes (partially)	yes
2^{nd} order coherent	no	normally not	yes	yes
Emission profile	usually divergent	usually divergent	usually divergent	usually a beam
Pump threshold	no	yes	yes	yes
Polarisation	usually none	may or may not be polarised	may or may not be polarised	often polarised
Stable, geometrically defined resonances	no	no	yes	yes

TABLE 3.1: Comparison of key properties of PL, ASE, RL and conventional lasers.

In the case of organic emitters, four emission regimes are of particular importance: PL, ASE, RL and conventional laser action. Table 3.1 gives an overview on how these types of emission typically behave. The use of qualifying words such as "usually" or "normally" indicates that there are barely any hard and fast rules. A photonic crystal structure, for example, can have quite a strong impact on the PL properties, an aspect that is exploited in chapter 5. It can be seen from the table that RL is a form of emission that is generally fairly similar to ASE but has some properties, in particular second order coherence and narrow-linewidth spectral spikes, that would normally only be associated with regular lasers.

3.2.1.1 Coherence

In general, coherence is the property of a radiation field at two or more different points in space or time to interfere with each other. A coherence effect is said to be of n^{th} order if $2n$ components of the field are required to see the effect (while coherence could in principle be defined for an odd number of field components [27], this has so far not seen any practical relevance). The n^{th} order coherence function is measured as:

$$g^{(n)}(\vec{x}_i, \tau_i, j(i)) = \frac{\left\langle \prod_{i=1}^{n} E^*_{j(i)}(\vec{x}_i, t+\tau_i) \prod_{i=n+1}^{2n} E_{j(i)}(\vec{x}_i, t+\tau_i) \right\rangle}{\prod_{i=1}^{2n} \sqrt{\left\langle |E_{j(i)}(\vec{x}_i, t+\tau_i)|^2 \right\rangle}} \tag{3.1}$$

where $E(\vec{x}, t)$ is an m-complex valued field (normally $m = 1$ or $m = 3$), $(\vec{x}, t)$ is a point in space-time, $j(i)$ denotes the field component and $\langle \cdot \rangle$ denotes ensemble averaging (though in practice often time-averaging is used).

If the E_j are classical fields, i.e. complex-valued functions of x and t, then a field whose component j_0 at point x_0 fluctuates randomly around a constant value will obey the

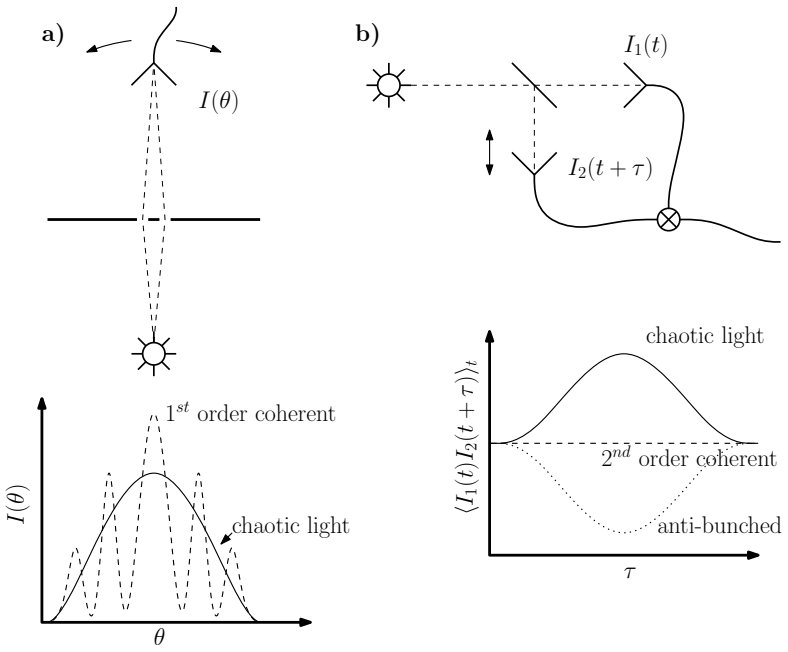

FIGURE 3.9: Illustration of important experiments to determine first and second order coherence. *a)* Young double-slit experiment, *b)* Hanbury-Brown and Twiss setup.

following relations:

$$|g^{(n)}(x_i \equiv x_0, \tau_i \equiv \tau_0, j \equiv j_0)| \geq 1 \tag{3.2a}$$

$$|g^{(n)}(x_i \equiv x_0, \tau_i \equiv \tau_0, j \equiv j_0)| \geq |g^{(n)}(x_i \equiv x_0, \text{various } \tau_i, j \equiv j_0)| \tag{3.2b}$$

The first relation can be proven for any finite ensemble by complete induction and the second relation is a consequence of the Cauchy-Schwartz inequality. More generally though, the E_j are quantum mechanical operators and relations (3.2) may be broken for systems that cannot be described by classical fields.

For $n = 1$ a simple interpretation is possible: light is fully coherent if $g^{(1)} = 1$. In reality, there is normally a time-scale τ_c, the coherence time, for which $|\tau_1|, |\tau_2| < \tau_c \Rightarrow g^{(1)}(\vec{x}, \vec{x}, \tau_1, \tau_2) \approx 1$. In this case of temporal coherence, $g^{(1)}$ reflects the monochromaticity of the light. The narrower the linewidth of the light source, the longer the coherence time. The prototype experiment to probe for first order coherence is the Young double-slit setup, see figure 3.9.

Second order coherence $g^{(2)}$ is in practice normally measured as temporal intensity correlation between two separate photodetectors:

$$g^{(2)}(\tau) = \frac{\langle E^*(\vec{x}_1, t)E^*(\vec{x}_2, t+\tau)E(\vec{x}_1, t)E(\vec{x}_2, t+\tau)\rangle}{\sqrt{\langle |E(\vec{x}_1, t)|^2\rangle^2 \langle |E(\vec{x}_2, t+\tau)|^2\rangle^2}} = \frac{\langle I(\vec{x}_1, t)I(\vec{x}_2, t+\tau)\rangle}{\langle I(\vec{x}_1, t)\rangle \langle I(\vec{x}_2, t+\tau)\rangle} \tag{3.3}$$

Where $\vec{x}_1, \vec{x}_2$ are the positions of the two detectors. Interpretation is not straightforward here. For example, $g^{(2)}(0)$ can be 0 and for chaotic light $g^{(2)}(\infty) \neq 0$. For an ideal laser, $g^{(2)}(\tau)$ is constant, whereas for PL and ASE normally $g^{(2)}(0) > g^{(2)}(\tau > 0)$ (so-called "photon-bunching", see figure 3.9 for illustration). If we speak of "second order coherence" then this refers to the suppression of photon bunching. RL emission has been shown to be second-order coherent [28]. The prototype experiment to determine second order coherence is the Hanbury-Brown and Twiss setup (figure 3.9).

3.2.1.2 Spectral Features

Among the unique characteristics of random lasers, the easiest to observe is the spiky spectrum composed of very narrow-linewidth peaks. Not every random laser shows these spectral features and it was recently discovered that there is a phase transition from spiky to non-spiky spectra depending on the pump geometry [29]. When pumping organic films in a narrow stripe, we consistently observe highly multimode laser emission consisting of narrow linewidth (< 1 meV) peaks. These peaks are not regularly spaced as is normally the case for regular structures such as Fabry-Perot or whispering gallery mode cavities.

3.2.1.3 Motivation

RL was first reported and discussed by Lethokov *et al.* [30, 31] in the mid 1960s in an exploration of the limits of classical laser layouts. Interest was limited, though, until prominent enhancement of stimulated emission and unexpected spectral features were reported from polycrystalline semiconductors [32] and particle-doped dye-based gain materials [33] in the 1990s. It was soon found that the area is rich in fundamental physics including localisation of light [34], complex interference phenomena [35–37] and phase transitions [29]. Numerous experimental observations of RL were reported including some from samples, particularly organic semiconductor films, where any scatterers were entirely unintentional [38]. RL can thus be seen as a material property and this is the point of view this thesis takes on the subject. Obtaining a deep understanding of the material's gain properties will always be beneficial towards developing practical devices and therefore the RL behaviour of organic films deserves study. The findings and theoretical discussion in the remainder of this section suggest that RL may commonly be observed in organic semiconductors as a consequence of their high optical gain, even if there are only few and weak scatterers. Of course, it is also interesting to investigate if disorder effects can be exploited directly towards an application. Suggestions include unique tagging using the RL spectrum as an optical fingerprint [33] and sensing by

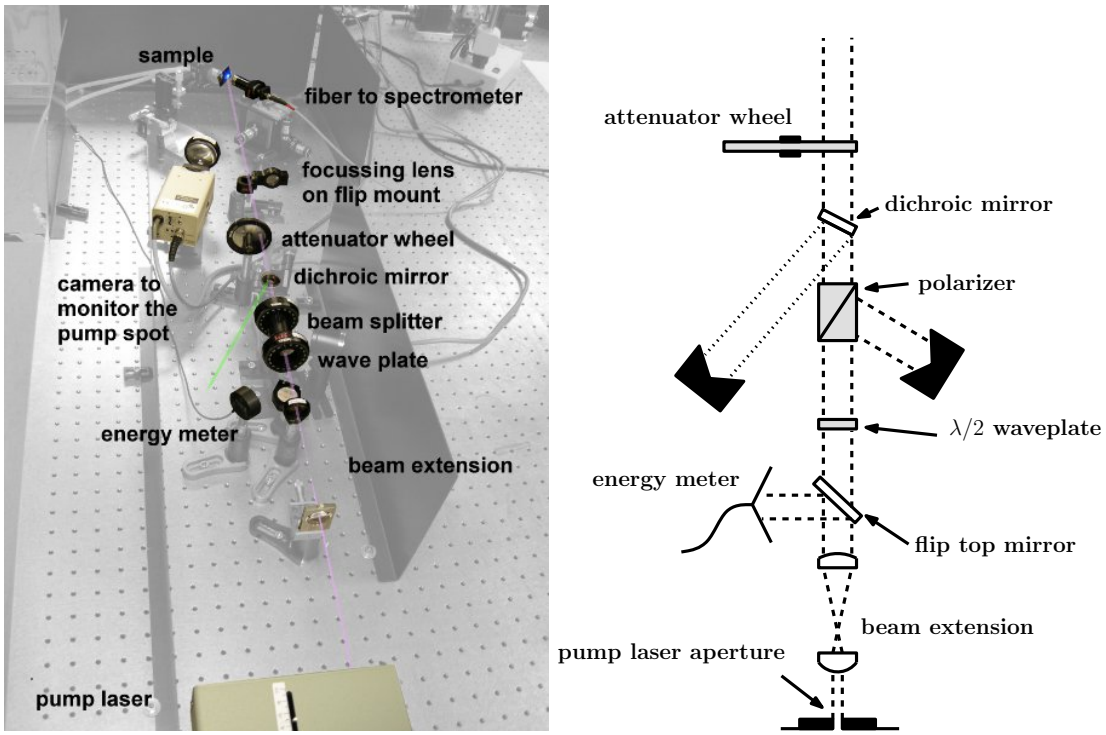

FIGURE 3.10: Photographic image and schematic of the setup used for optical pumping of organic RLs and distributed feedback (DFB) lasers.

change of RL mode pattern due to molecules docking to the surface of the RL device [37].

3.2.2 Experimental Setup

The pump source for stripe-excitation experiments was a flashlamp-pumped frequency-tripled Q-switched Nd:YAG laser, emitting linearly polarised 5 ns optical pulses at 355 nm with 1–15 Hz repetition rate. Control of the pump pulse energy over a wide range (6 nJ–3 mJ) was achieved by a quarter-wavelength plate followed by a polariser and a neutral density filter wheel. The setup is shown in figure 3.10. A dichroic mirror was used to filter any remaining green (frequency-doubled, 532 nm) components out of the laser emission. More details on the control of the pump pulse energy are given in appendix A.4.

Various combinations of cylindrical or spherical lenses were used to shape the pump spot according to the specific experiment. The pump spot sizes were determined by knife-edge measurements as described in the appendix, A.3 and A.4.5. All measurements presented in this chapter were done with a stripe of 3 mm length and ∼300 μm width unless specified otherwise.

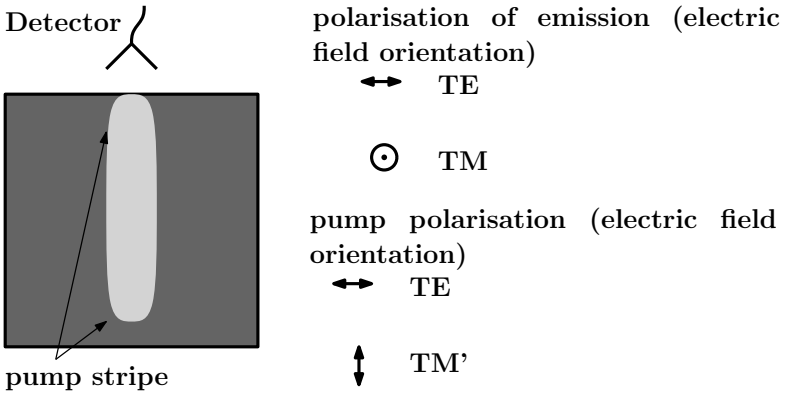

FIGURE 3.11: Schematic top view of a stripe excitation experiment on an organic thin film, illustrating the notation for the different possible polarisation states, TE, TM and TM'.

The pump light is linearly polarised and different directions of pump polarisation were investigated. Polarisation of the ASE/RL emission was examined as well. Figure 3.11 serves to clarify the notation of the different polarisation states in the case of stripe excitation of an unstructured LEP film.

Emission from the polymer film was collected with a silica optical fibre (50 μm core) which in turn was connected to a CCD spectrometer. The spectrometer had several channels with, respectively, 2.4 nm, 0.4 nm and 0.13 nm resolution.

3.2.3 Random Laser Action in Neat Organic Films

This section presents experimental observations on neat films of oligofluorene-truxenes and BBEHP-PPV that were spin-coated at 1500 RPM (truxene materials) and 2000 RPM (BBEHP-PPV) from toluene solution (20 mg/ml) onto glass substrates, yielding uniform films of ∼100 nm thickness. A BBEHP-PPV film spun from chloroform solution and chlorobenzene solution (the latter was done by Y. Wang *et al.* [8]) showed similar RL behaviour as well. The glass substrates were cleaned in an ultrasonic bath with acetone and methanol (in that order) and afterwards rinsed with deionised water.

Under stripe-excitation, some common properties have been observed in all cases:

- With sufficiently high resolution (better than 0.5 nm) spectrometers, RL modes are typically resolved.
  - RL spike positions are temporally stable (see figure 3.12).
- The RL emission from the edge of the stripe is clearly directional. This can be seen in figure 3.13.

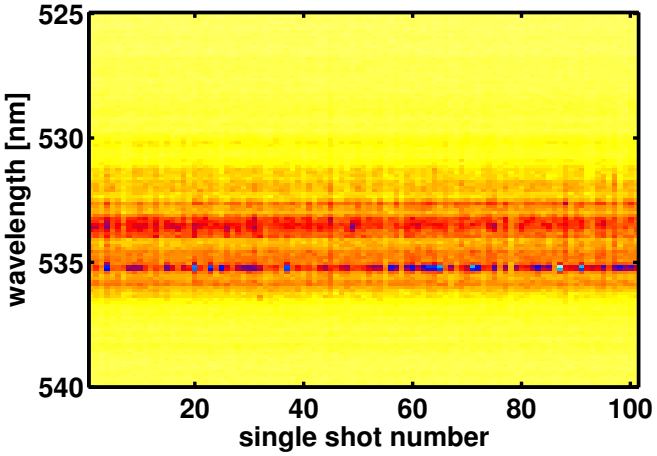

FIGURE 3.12: Single-pulse RL spectra from a BBEHP-PPV film (AK391DCM1) pumped in stripe-geometry at 62 μJ/cm^2, 12.4 kW/cm^2, 15× threshold.

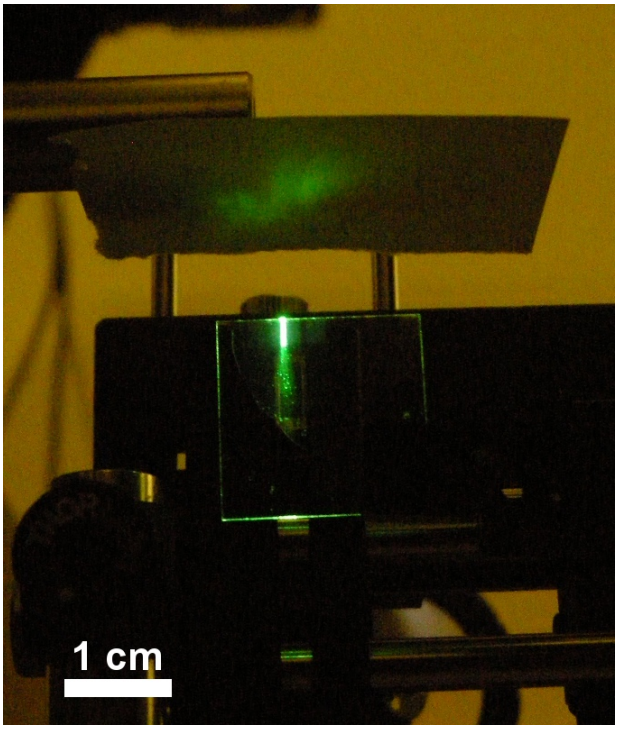

FIGURE 3.13: Photographic image of RL from a BBEHP-PPV film under stripe excitation. On top of the film, a piece of paper is used to screen the emission, showing pronounced directionality.

The following sections point out differences observed in the RL behaviour of different materials and material batches. These are particularly pronounced in the polarisation characteristics.

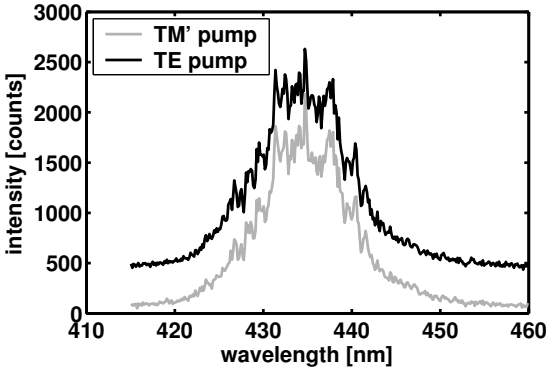

FIGURE 3.14: High (0.13 nm) resolution spectra resolving RL modes from T3 octyl at 580 μJ/cm^2 (116 kW/cm^2).

3.2.3.1 Oligofluorene-Truxenes

RL behaviour as described above has been observed from T3 hexyl, T4 hexyl and T3 octyl with typical RL thresholds around 40 μJ/cm^2 (8 kW/cm^2). The only obvious difference between these materials was the better photostability of hexyl-truxenes. Polarisation characteristics of the RL from truxenes are as follows:

- ASE/RL emission is strongly TE polarised.
  - This is independent of the pump polarisation.
- The power transfer function does not depend strongly on the pump polarisation.

Typical RL spectra are plotted in figure 3.14. The polarisation of RL emission and threshold measurements depending on the pump polarisation are given in figure 3.15. A high degree of polarisation is observed and may be an indicator that the T3/T4 molecules are aligned with the oligofluorene arms in-plane.

3.2.3.2 BBEHP-PPV

RL has been observed in all batches of BBEHP-PPV except for those that did not show gain at all (i.e. the low molecular weight material extracted by acetone). Some data for illustration is shown in figure 3.16. The data presented here is from films spun onto glass substrates, but we point out that RL has also been observed from BBEHP-PPV spun onto an (unpatterned) CHDV film on an acetate substrate and free standing membranes of BBEHP-PPV-doped CHDV. Observed polarisation characteristics are as follows:

- ASE/RL emission may be TE-polarised to some extent with a typical intensity ratio of TE and TM emission of 2:1.

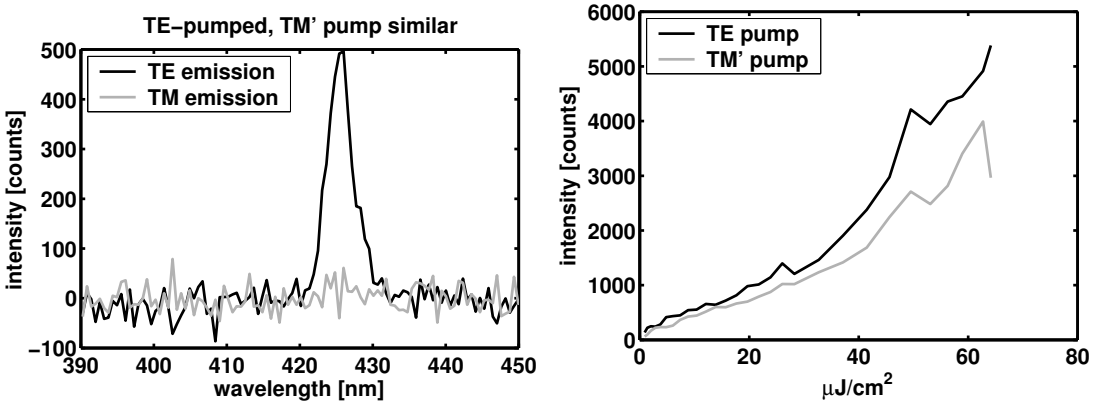

FIGURE 3.15: Left: low (2.4 nm) resolution spectrum (RL modes not resolved) demonstrating strong TE polarisation of T3 hexyl RL emission, Right: threshold measurements of T3 hexyl ASE/RL with different pump polarisations.

- ASE/RL emission intensity may depend strongly on pump polarisation.
  - How much this is the case varies between material batches. The strongest impact of pump polarisation was found for AK391DCM2.
  - It is not clear if there is a difference in threshold.
  - The pump polarisation only affects the emission properties above threshold.

Below threshold, the luminescence was unpolarised which is consistent with the polymer chains being disordered. Partial polarisation of the RL emission can be explained by a better spatial overlap of the TE_0 mode with the gain region in comparison to the TM modes.

ASE/RL thresholds for the different BBEHP-PPV batches pumped in the above conditions vary from 4 μJ/cm^2, 0.8 kW/cm^2 to 20 μJ/cm^2, 4 kW/cm^2. Interestingly, the batch with the lowest degree of polydispersity of polymer chain length, AK391DCM2 which has a polydispersity index (PDI) of 2.1, is not the one giving the lowest threshold. An overview of the properties of the various BBEHP-PPV batches including laser threshold under various conditions is given in table 3.2. There may be a correlation of threshold with both, molecular weight (MW) and PDI, and the DFB laser thresholds in particular suggest that a low PDI is not beneficial for device performance.

A possible explanation can be Förster resonant energy transfer (FRET) between molecules. In a polydisperse mixture of polymer chains, pump light will be absorbed by all types of molecules but excited shorter chains may efficiently transfer energy to longer chains via FRET rather than radiate. The observed reduction in threshold can then be attributed to reduced self-absorption due to the short-chain molecules having a slightly blue-shifted absorption compared to long-chain molecules.

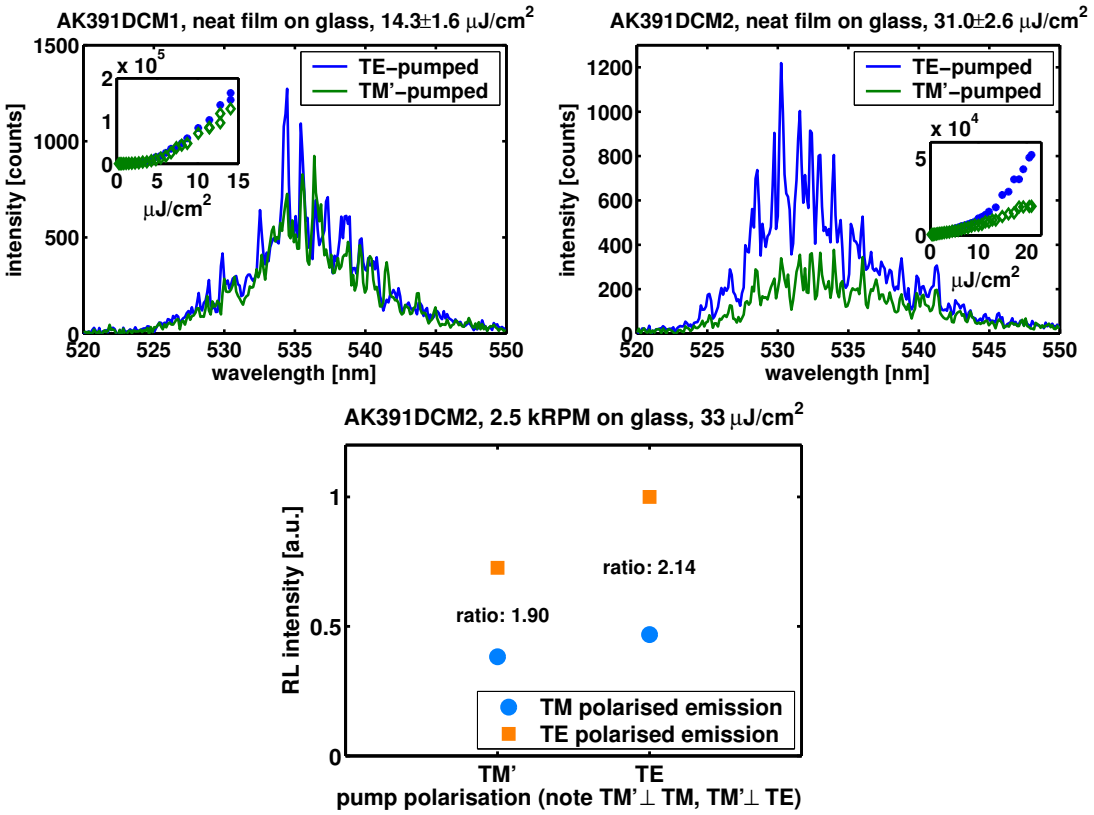

FIGURE 3.16: Top: RL spectra of different BBEHP-PPV batches, Insets: threshold measurements at different pump polarisations. bottom: polarisation of RL emission from BBEHP-PPV

Batch	MW [u]	PDI	threshold[a] [W/cm²]	threshold[b] [kW/cm²]	threshold[c] [W/cm²]	threshold[d] [kW/cm²]
AK342, non-purified	583000	10.6	120		302	
AK408DCM	543000	6.8	93		277	
AK350DCM	455000	5.0	102		270	
AK391DCM1	341000	4.6	253	1.6	167	0.8
AK391DCM2	205000	2.1		20	216	4

[a] DFB laser on silica grating, 4 ns pump pulses at 450 nm, circular pump spot
[b] DFB laser on CHDV grating, 5 ns pump pulses at 355 nm, stripe-shaped pump spot
[c] ASE/RL on silica substrate, 4 ns pump pulses at 450 nm
[d] ASE/RL on silica substrate, 5 ns pump pulses at 355 nm

TABLE 3.2: Properties of different BBEHP-PPV batches. The data in columns [a] and [c] was obtained by Y. Wang [7].

This picture is also consistent with the observed response to pump polarisation. In a mono-disperse mixture of polymer chains, FRET will occur at a reduced rate compared a poly-disperse mixture, i.e. a large fraction of the molecules that contribute to gain are those that have absorbed a pump-photon. Since polarised pump photons preferably excite polymer chains that are aligned in a particular direction, an increase in threshold/laser efficiency is expected if the pump polarisation is parallel to the propagation direction of the laser light (i.e. TM'). This matches the observation on AK391DCM2 shown in figure 3.16. On the other hand, in case of a polydisperse material much of the absorbed TM' pump energy can efficiently be transferred via FRET to molecules that are aligned well for emission into the laser mode. This can be an explanation for the insensitivity of the AK391DMC1 material to the pump polarisation. Further investigation will be needed to clarify the roles of MW and FRET processes for the laser threshold.

3.2.3.3 Photo-Degradation

All experiments were carried out in ambient atmosphere which means that the films were subject to photo-oxidation. In some cases the temporal evolution of RL emission over a large number of pump pulses was recorded. Figure 3.17 shows data obtained from BBEHP-PPV. During degradation, the emission intensity drops rapidly in the first phase to then assume a steady exponential decrease. The degradation dosage is $F_{deg} = 20.7$ J/cm^2, $F_{deg}/F_{th} = 5 \times 10^6$ in total and $F_{deg} = 1.17$ J/cm^2, $F_{deg}/F_{th} = 2.8 \times 10^5$ for the fast component only. RL modes appear to be at fixed spectral positions throughout the process, though their relative intensity changes due to a redshift of the overall emission. Very sudden changes from one RL mode pattern to another may be observed. In the case presented here some new RL modes suddenly appeared/vanished after about 65000 pulses while others are visible before the sudden transition and continue to lase throughout. This transition occurred without any trace in the overall emission intensity.

In neat truxene (T3 hexyl and T3 octyl) films, no redshift of the emission was observed and the overall emission intensity decrease has been observed to be exponential throughout the entire observation period of 18000 pulses. The degradation dosages are $F_{deg} = 7$ J/cm^2, $F_{deg}/F_{th} = 1.75 \times 10^5$ for T3 hexyl and $F_{deg} = 4.6$ J/cm^2, $F_{deg}/F_{th} = 4.6 \times 10^4$ for T3 octyl. Figure 3.18 shows the spectral evolution of T3 octyl RL emission during degradation. Again, the RL modes remain at stable spectral positions.

Given the rarity of reports of OSL lifetimes with organic semiconductors as gain medium (see figure 2.19) it is hard to make a fair comparison with other OSLs. However we can note that unencapsulated OSLs have not been reported to have F_{deg}/F_{th} values above

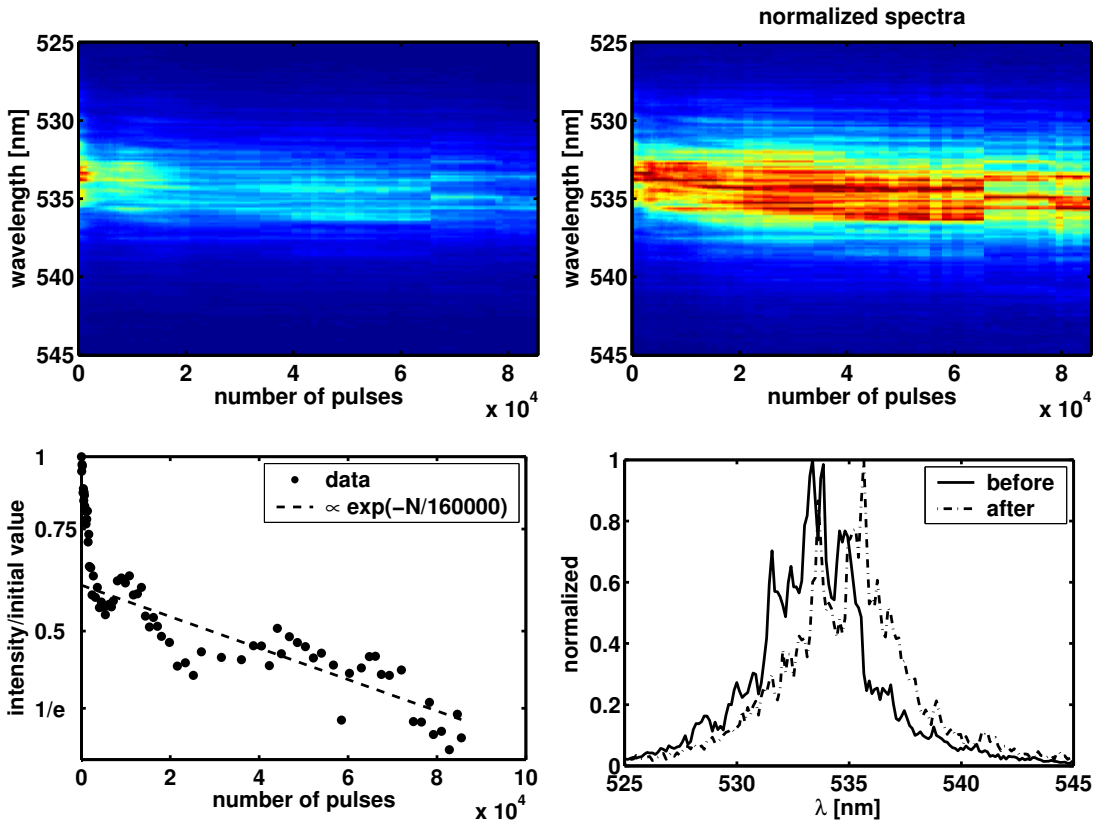

FIGURE 3.17: Top left: spectral evolution of RL emission from BBEHP-PPV (batch AK391DCM1) as a function of incident pump pulses at 260 μJ/cm^2, 63× threshold,15 Hz repetition rate. Top right: the same data but with each spectrum normalised. Bottom left: evolution of the overall RL intensity. Bottom right: comparison of RL spectra from this film before and after degradation by 85500 pulses.

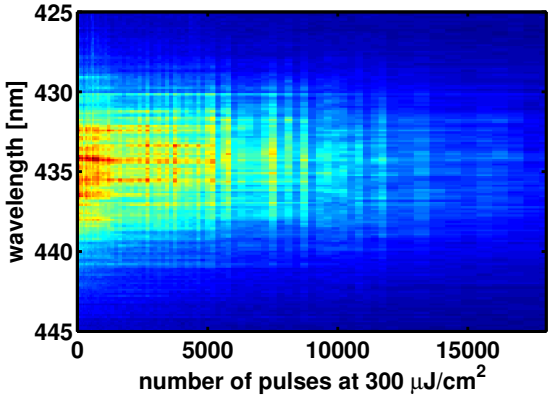

FIGURE 3.18: Spectral evolution of T3 octyl RL as a function of the number of incident pump pulses at 300 μJ/cm^2, 10 Hz repetition rate.

10^6 and there is only one report ([18], using a very small pump spot of only 20 μm diameter) of an unencapsulated OSL with F_{deg} larger than 10 J/cm^2.

3.2.4 Random Laser Action in CQDs

Optical gain in CQDs was first achieved in 2002 [39]. It was then noticed, that the gain was redshifted compared to the photoluminescence. This is related to two aspects, the first being higher self absorption at shorter wavelengths. More importantly, however, gain requires such a high density of excited CQDs, that at the time when transparency is reached a significant number of them are in a biexcitonic state which in turn is slightly redshifted compared to single excitons [40]. Due to the need of such a high exciton density, gain thresholds for CQD lasers are generally high. More recently, structural design modifications such as formation of a type II semiconductor junction (i.e. the holes are not confined to the core) in between core and shell have been undertaken to reduce the gain threshold [41].

During this work, CQDs were drop-coated onto glass substrates that were prepared by scratching grooves with a diamond pen. This procedure was used because the grooves aided agglomeration of CQDs which on a smooth substrate would only form poor quality films that were not suitable for optical waveguiding and amplification. From these CQD-filled grooves, RL emission was consistently observed with the RL peak being slightly redshifted compared to the photoluminescence peak [42]. Figure 3.19 shows RL spectra from CdSe/ZnS CQDs with a PL peak wavelength at 596 nm. In this case RL emission centred around 606 nm was observed above a threshold around 25 mJ/cm^2 (5 MW/cm^2) when exciting with a 0.05×3 mm^2 stripe along one of the grooves. It can clearly be seen that, similar to the LEP-results above, the RL peaks remain at stable spectral positions. RL centred at 630 nm has also been seen from CQDs with a PL peak at 617 nm. However CQDs with PL wavelengths of 564 nm or shorter suffered mechanical damage before reaching gain.

Follow-up work on the above results in collaboration with Nanyang Technological University is summarised in appendix C.

3.3 A Simple Theory of Random laser Action in Stripe Excitation

Photo-excitation of a luminescent film by a stripe-shaped pump spot is a widely applied method for characterisation of the film's optical properties. A very popular experiment

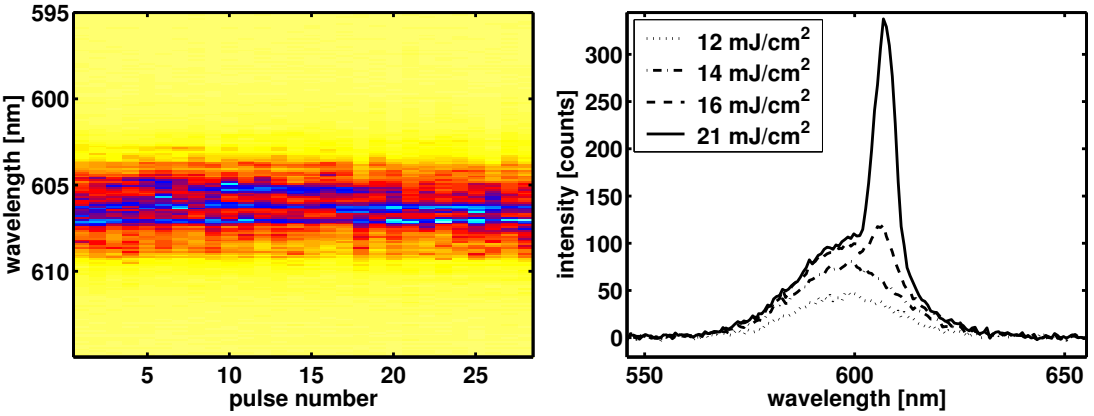

FIGURE 3.19: *Left:* RL spectra from CdSe/ZnS CQDs for a number of successive pump pulses at 53 mJ/cm^2, compare also figure 3.12 for a similar experiment on an LEP. *Right:* low (2.4 nm) resolution (RL modes not resolved) spectra of CQD emission around threshold showing the emergence of the RL emission with increasing pump energy.

is the variable stripe length (VSL) method which was first proposed by Shaklee and Leheny [43] in 1971 as a simple way to measure the optical gain for light waveguided along the stripe. To a first approximation, the intensity emitted from the edge of the stripe follows an exponential law as a function of stripe length, thus allowing quick evaluation of the modal gain. The VSL technique was mainly applied to inorganic semiconductor crystals of high quality and optimised analysis methods were developed [44]. Yet some shortcomings of the strongly simplified initial approach were encountered and researchers have investigated the influence of gain saturation [45–48], pump light diffraction [46], coupling into the detector [46] and carrier depletion [49]. In recent years, VSL measurements have been employed in the rapidly evolving field of organic solid state gain media [47, 48, 50–54]. In contrast to their inorganic counterparts with high crystalline order, these solution-processed active films have exhibited a striking feature: they may show random laser action when excited in stripe geometry [5, 38, 55, 56]. The previous experimental section underlines that RL can commonly be seen in truxene-oligofluorene and BBEHP-PPV films. At first glance, this seems to be a further complication to the applicability of VSL-type analysis because of mode competition and alteration of propagation paths due to scattering. Whilst a quantitative analysis may indeed be problematic, we find however that the VSL approach gives valuable insight into the fundamental principles underlying the formation of RL.

Up to now, theoretical understanding of the RL phenomenon is mostly based on diffusive models [31, 57–62] or finite difference time domain calculations of the full electric and magnetic fields [35, 63, 64]. The former approach yields an analytic handle, though it is limited to systems with a large number of scatterers within the excited volume. The latter approach has been successful in modelling random laser effects in media

with just a few scatterers [35] but is computationally very demanding. We show that the restriction to stripe geometry allows a simple ansatz that has potential to study concepts underlying the occurrence of RL in weakly scattering media. In particular, localised lossy or reflective perturbations are examined and it is found that they lead to spatial and/or spectral redistribution of intensity along the stripe. Our results indicate that RL may be a common material property in high gain media and may only require slight disorder.

3.3.1 VSL Model under Inclusion of Gain Saturation

An important aspect of many laser devices is the saturation of gain, i.e. the rate of emission into an optical mode (which is proportional to the number of excited molecules) will be quenched due to stimulated emission into other optical modes. Given a strong intensity signal I, the stimulated emission rate Γ_{se} and the spontaneous emission rate Γ_{sp} are both quenched according to [65]:

$$\Gamma_{se} = \frac{\gamma_0 I}{1 + I/I_{sat}} \tag{3.4a}$$

$$\Gamma_{sp} = \frac{\Gamma_{sp,0}}{1 + I/I_{sat}} \tag{3.4b}$$

where I_{sat} is the saturation intensity, γ_0 corresponds to the unsaturated optical gain and $\Gamma_{sp,0}$ is proportional to the spontaneous emission rate per excited molecule. If we excite the gain medium with a narrow stripe of length l (in the z-direction, see figure 3.20) then the change of intensity $I_{\rightarrow}$ in positive z direction will be given by the emission rates (similar to equations (3.4)) into the corresponding optical mode(s):

$$\left.\frac{\mathrm{d}I_{\rightarrow}}{\mathrm{d}z}\right|_{sp} = \frac{\eta Y_p}{1 + I_{tot}/I_{sat}} \tag{3.5a}$$

$$\left.\frac{\mathrm{d}I_{\rightarrow}}{\mathrm{d}z}\right|_{se} = \alpha \cdot I_{\rightarrow} \left(\frac{Y_p}{1 + I_{tot}/I_{sat}} - 1 \right) \tag{3.5b}$$

Here I_{tot} is the sum of all signals giving rise to quenching by stimulated emission and a number of convenient parameters are introduced:

$$\begin{aligned} Y_p &:= R_p/R_{th} \quad \text{pump parameter} \\ R_p &\quad \text{pump rate} \\ R_{th} &\quad \text{threshold pump rate, at which transparency is reached} \\ \eta &\quad \text{spontaneous emission rate at transparency} \\ \alpha &\quad \text{waveguide losses when unpumped} \end{aligned} \tag{3.6}$$

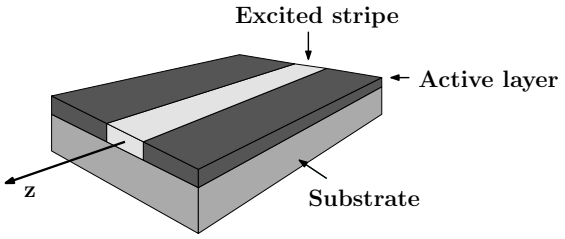

FIGURE 3.20: Schematic of a typical stripe excitation experiment on organic gain media. Typical active layer thicknesses are 100-400 nm, stripe widths 10-500 μm and stripe lengths 1-10 mm.

The maximum intensity that can be supported by the gain medium is $I_{tot,max} = I_{sat}(Y_p - 1)$. We speak of a "high gain" medium if this intensity is reached along the stripe and of a "low gain" medium if the intensity stays significantly below this value.

In the narrow stripe geometry there are two intensity contributions, $I_{\rightarrow}$ evolving in the positive and $I_{\leftarrow}$ evolving in the negative z-direction. From equations (3.5) we thus get a set of two coupled differential equations:

$$\frac{\mathrm{d}I_{\rightarrow}}{\mathrm{d}z} = \frac{\eta Y_p}{1 + (I_{\leftarrow} + I_{\rightarrow})/I_{sat}} + \alpha \cdot I_{\rightarrow} \left(\frac{Y_p}{1 + (I_{\leftarrow} + I_{\rightarrow})/I_{sat}} - 1 \right) \tag{3.7a}$$

$$\frac{\mathrm{d}I_{\leftarrow}}{\mathrm{d}z} = -\frac{\eta Y_p}{1 + (I_{\leftarrow} + I_{\rightarrow})/I_{sat}} - \alpha \cdot I_{\leftarrow} \left(\frac{Y_p}{1 + (I_{\leftarrow} + I_{\rightarrow})/I_{sat}} - 1 \right) \tag{3.7b}$$

Boundary conditions in a real experiment are $I_{\rightarrow}(0) = 0, I_{\leftarrow}(l) = 0$ (assuming the stripe position is from 0 to l). At this point, we do not consider the temporal evolution of the system. This is justified by the fact that propagation times along mm long stripes are on the order of a few ps while the time of positive gain in a typical nanosecond pump experiment will be limited by slower processes such as pump pulse duration, radiative lifetime and singlet-triplet crossing rate, all of which usually exceed several 100 ps [3, 66]. For the sake of simplicity we assume uniform pumping, $Y_p(z) \equiv Y_p$.

Equations (3.7) can be integrated numerically using a standard ordinary differential equation solver. The boundary conditions can be fulfilled by integrating from 0 to l with $I_{\rightarrow}(0) = 0$ and $I_{\leftarrow}(0) = I_{\leftarrow,0}$, where $I_{\leftarrow,0}$ is optimised (using the Matlab$^{\mathrm{TM}}$ `fzero` routine, in our case) such that after integration we obtain $I_{\leftarrow}(l) = 0$. In the numerical results presented in the sections below, the stripe length has been normalised to $l = 1$.

3.3.1.1 Propagation in a Saturated Environment

In high gain media such as organics, the emission will saturate along a propagation length of a few mm. We therefore have to examine how the opposing signals affect each other. In the limit of an infinitely long stripe, one might a priori expect the two signals

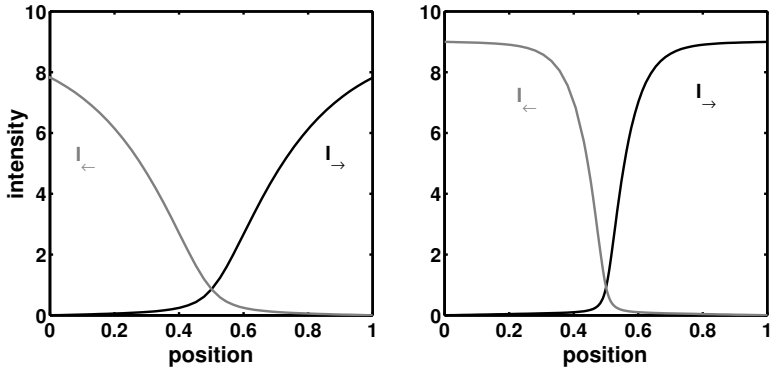

FIGURE 3.21: Numerical solution of equations (3.7) in an intermediate (left, $\eta = 0.2, \alpha = 5, Y_p = 10, I_{sat} = 1$) and high (right, $\eta = 0.2, \alpha = 20, Y_p = 10, I_{sat} = 1$) gain medium.

to be of identical intensity, given by the saturation behaviour of the gain medium. This is indeed the only steady state solution of (3.7) for which $\frac{\mathrm{d}I_{\rightarrow}}{\mathrm{d}z} = \frac{\mathrm{d}I_{\leftarrow}}{\mathrm{d}z} = 0$:

$$\begin{aligned} I_{\rightarrow,steady} &= I_{\leftarrow,steady} \\ &= I_{sat}\left(\frac{Y_p - 1}{4} + \sqrt{\frac{\eta}{2\alpha I_{sat}} Y_p + \frac{(Y_p-1)^2}{16}}\right) \\ &= I_0 \end{aligned} \tag{3.8}$$

However, there are also other, quasi-steady, solutions with a very strong signal in the positive (or negative, respectively) z-direction, close to the maximum allowed by saturation:

$$I_{\rightarrow\,(\leftarrow)} \approx I_{sat}(Y_p - 1) \gg I_{\leftarrow\,(\rightarrow)} \tag{3.9a}$$

$$\frac{\mathrm{d}I_{\rightarrow\,(\leftarrow)}}{\mathrm{d}z} \approx -\frac{\mathrm{d}I_{\leftarrow\,(\rightarrow)}}{\mathrm{d}z} \approx (-)\,\eta \tag{3.9b}$$

Over length scales l where $\eta l \ll I_{sat}(Y_p - 1)$ these are small changes compared to $I_{\rightarrow}$, i.e. the situation is quasi-steady over such a length. Numerical solutions of equations (3.7) shown in figure 3.21 demonstrate that in high gain media the quasi-steady state (3.9) exists in considerable portions of the stripe. Furthermore even in intermediate gain media (i.e. an intensity of $I_{sat}(Y_p - 1)$ is not quite reached) the local field is dominated by only one signal for most of the stripe. This indicates that in the presence of gain-saturation the quasi-steady scenario (3.9) is the physical solution rather than having two signals of equal strength as in equation (3.8).

3.3.1.2 Influence of Disorder

A key point of our work is to include inhomogenities in the film structure. In particular, we look at three types of defects:

- Inhomogeneous additional losses, e.g. due to scatterers
- A 'vacancy', i.e. a non-emissive region
- A localised reflection

Real random scattering will probably have contributions of all these effects. In section 3.3.2.1 we will examine the effect of these defects if they have a wavelength dependence.

Additional losses are modelled by adding a constant loss, α_{add}, within a certain region $z_1 < z < z_2$:

$$\left.\frac{\mathrm{d}I_{\rightarrow}}{\mathrm{d}z}\right|_{z_1<z<z_2} = \left.\frac{\mathrm{d}I_{\rightarrow}}{\mathrm{d}z}\right|_{neat\ film} - \alpha_{add} I_{\rightarrow} \tag{3.10a}$$

$$\left.\frac{\mathrm{d}I_{\leftarrow}}{\mathrm{d}z}\right|_{z_1<z<z_2} = \left.\frac{\mathrm{d}I_{\leftarrow}}{\mathrm{d}z}\right|_{neat\ film} + \alpha_{add} I_{\leftarrow} \tag{3.10b}$$

In case of a vacancy, the derivative is replaced by constant waveguiding losses:

$$\left.\frac{\mathrm{d}I_{\rightarrow}}{\mathrm{d}z}\right|_{z_1<z<z_2} = -\alpha_{wg} I_{\rightarrow} \tag{3.11a}$$

$$\left.\frac{\mathrm{d}I_{\leftarrow}}{\mathrm{d}z}\right|_{z_1<z<z_2} = \alpha_{wg} I_{\leftarrow} \tag{3.11b}$$

$$\alpha_{wg} \geq 0$$

Finally, reflections are modeled by a localised region where the counter-propagating modes are reflected into each other:

$$\left.\frac{\mathrm{d}I_{\rightarrow}}{\mathrm{d}z}\right|_{z_1<z<z_2} = \left.\frac{\mathrm{d}I_{\rightarrow}}{\mathrm{d}z}\right|_{neat\ film} - RI_{\rightarrow} + RI_{\leftarrow} \tag{3.12a}$$

$$\left.\frac{\mathrm{d}I_{\leftarrow}}{\mathrm{d}z}\right|_{z_1<z<z_2} = \left.\frac{\mathrm{d}I_{\leftarrow}}{\mathrm{d}z}\right|_{neat\ film} + RI_{\leftarrow} - RI_{\rightarrow} \tag{3.12b}$$

Numerical solutions of systems with perturbations according to equations (3.10), (3.11) and (3.12) are plotted in figure 3.22. The gain material properties are the same as in the unperturbed system shown in figure 3.21. Parameter values for each simulation are indicated in each figure. Note that the values chosen for additional losses and reflectivity ($\alpha_{add} = 1$, $R = 0.5$) are small compared to the waveguide losses α and the unsaturated

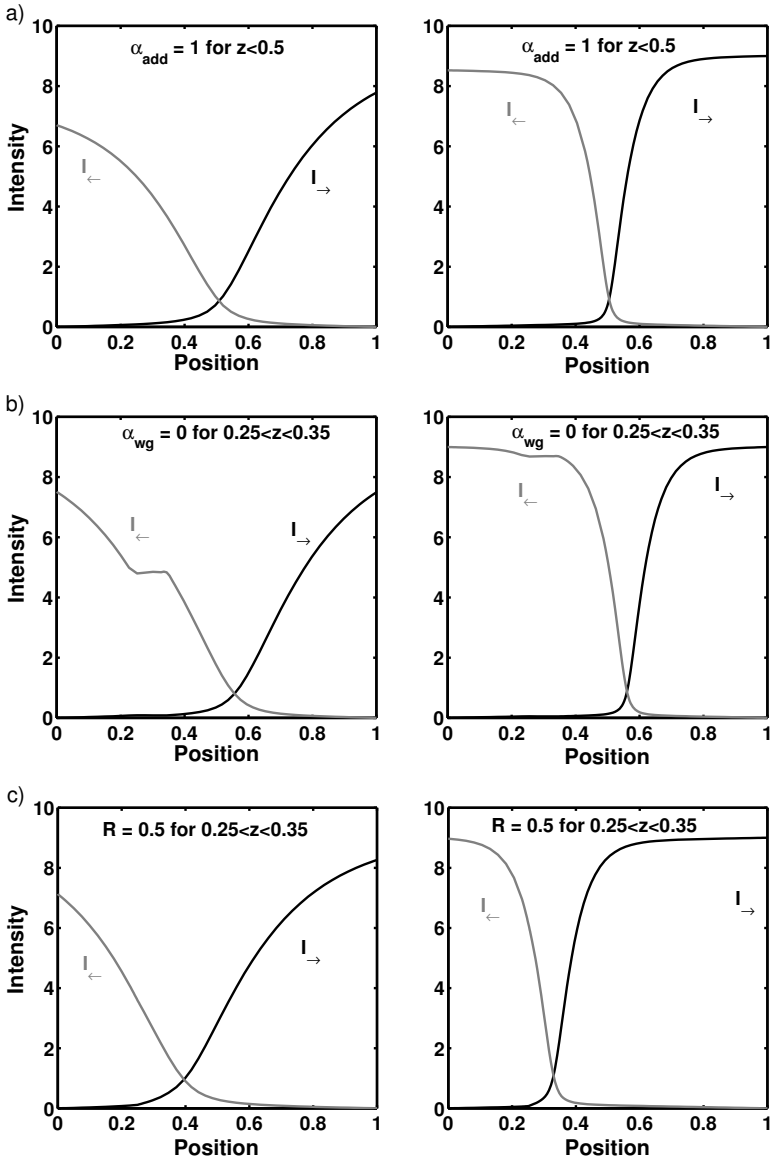

FIGURE 3.22: Numerical solution of equations (3.7) with various types of disorder. As in figure 3.21, the left hand figures show an intermediate gain medium ($\eta = 0.2, \alpha = 5, Y_p = 10, I_{sat} = 1$) and the right hand figures show a high gain medium ($\eta = 0.2, \alpha = 20, Y_p = 10, I_{sat} = 1$). The parameters for the distortions are given in each plot. Figures a) show the effect of a localised loss according to equations (3.10), figures b) a non-emissive region (equations (3.11)) and figures c) a reflective region (equations (3.12)).

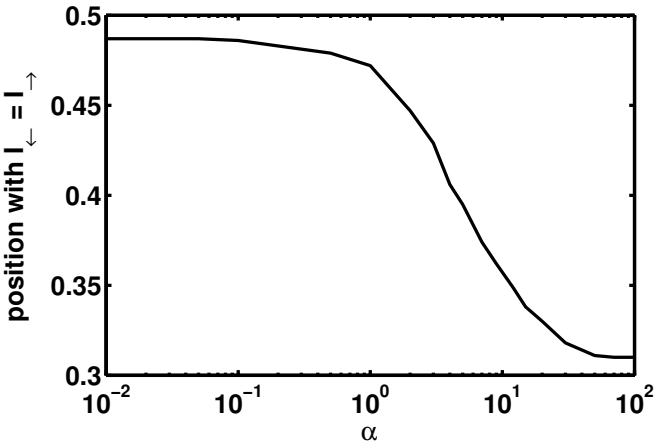

FIGURE 3.23: Assuming a reflective perturbation according to equation (3.12), the position where $I_\leftarrow = I_\rightarrow$ is plotted as a function of α. Parameters are $\eta = 0.2, Y_p = 10, I_{sat} = 1, R_{0.25<z<0.35} = 0.5$, as in figure 3.22c.

gain $(Y_p - 1)\alpha$, i.e. they represent a case of weak scattering. Also the range for reflections and vacancies, $z_1 = 0.25, z_2 = 0.35$, is small compared to the overall stripe length. In general, we note that these types of disorder may alter the intensity distribution along the stripe and the position with $I_\leftarrow = I_\rightarrow$ shifts away from the center of the stripe. This is in particular the case for reflection (figure 3.22c) but to a lesser extent also for a non-emissive region (figure 3.22b). Localised losses appear to only have an effect of intensity reduction but seem not to significantly alter the spatial coverage of the left and right traveling signals (figure 3.22a).

Taking a close look at figure 3.22c, we see that in the case of a reflective perturbation the position where the two signals, $I_\leftarrow$ and $I_\rightarrow$, have the same magnitude is not the same for an intermediate and a high gain medium. The full dependence of this position on α is plotted in figure 3.23. We see that for low gain media it is roughly at the middle of the stripe while for high gain media it shifts towards the position of the perturbation. The conclusion is that, in high gain media, one is much more likely to encounter spatial redistribution of the emission due to disorder effects than in low gain media.

3.3.2 Spectral Effects

The VSL method was employed to obtain gain spectra [51] which means that the wavelength dependence of the parameters enter as a further complication. One well understood effect encountered in this case is spectral narrowing in amplifying media, which was extensively discussed by Casperson and Yariv [67]. Here we extend the model to gain understanding of the influence of distortions.

In order to make a useful analysis, we have to aquire some knowledge about the properties of the gain medium. Spectral tuning experiments with distributed feedback cavities have demonstrated that organic semiconductors can have gain bandwidths of ∼300 meV [53]. Such a broad gain is possible due to the homogeneous splitting of the luminescence into several vibronic transitions, i.e. an excited molecule may relax radiatively into a number of vibronic excitations of the electronic ground state. Amplified spontaneous emission (ASE) or RL typically occurs with a much narrower linewidth of ∼30 meV. Table 3.3 gives an overview of different luminescence broadening mechanisms in organic semiconductors (the notes a-f indicate how the width of each contribution was estimated). For reference, the typical spacing between major vibronic features of a polymer film is 100-150 meV, each of which has a width of 75-150 meV at room temperature. The gain bandwidth is narrower than the spectral width over which the vibronic transitions spread because of self-absorption at the first vibronic transition [66]. It can be seen from table 3.3 that for either narrow ($\leq$ 10 meV) or wide ($>$ 100 meV) spectral ranges, homogeneous mechanisms are dominant, while ranges of a few 10 meV will be dominated by inhomogeneous mechanisms. The effect of having different contributions will be looked at below in section 3.3.2.2 on the basis of experimental data. Here, we ignore inhomogeneous broadening effects and describe spectral quenching effects in a homogeneous fashion, i.e. equations (3.4) become:

$$\Gamma_{se}(\omega) = \frac{\gamma_0(\omega) I(\omega)}{1 + \int_0^\infty \mathrm{d}\omega'\, I_{tot}(\omega')/I_{sat}(\omega')} \tag{3.13a}$$

$$\Gamma_{sp}(\omega) = \frac{\Gamma_{sp,0}(\omega)}{1 + \int_0^\infty \mathrm{d}\omega'\, I_{tot}(\omega')/I_{sat}(\omega')} \tag{3.13b}$$

where the frequency ω relates to the wavelength λ via the dispersion relation $\omega = \frac{2\pi c}{\lambda}$. In this case, equations (3.7) have to be replaced by:

$$\frac{\mathrm{d}I_{\rightarrow}}{\mathrm{d}z}(z,\omega) = \frac{\eta(\omega) Y_p(\omega)}{1+X} + \alpha(\omega) \cdot I_{\rightarrow}(z,\omega) \left(\frac{Y_p(\omega)}{1+X} - 1 \right) \tag{3.14a}$$

$$\frac{\mathrm{d}I_{\leftarrow}}{\mathrm{d}z}(z,\omega) = -\frac{\eta(\omega) Y_p(\omega)}{1+X} - \alpha(\omega) \cdot I_{\leftarrow}(z,\omega) \left(\frac{Y_p(\omega)}{1+X} - 1 \right) \tag{3.14b}$$

$$X := \int_0^\infty \mathrm{d}\omega' \, \frac{I_{\leftarrow}(z,\omega') + I_{\rightarrow}(z,\omega')}{I_{sat}(\omega')}$$

Equations (3.14) raise the following concerns about the recording of gain spectra:

- There are four continuous parameters $\eta(\omega)$, $\alpha(\omega)$, $Y_p(\omega)$, $I_{sat}(\omega)$. Some simplification can be achieved by experimentally measuring the losses $\alpha(\omega)$ and also by taking advantage of the fact that due to the Einstein relation between spontaneous and stimulated emission, the spectral lineshapes of $\eta(\omega)$ and $I_{sat}(\omega)$ should be inverse proportional to each other [65].

Mechanism	**Type**	**Typical width** [meV]
(ensemble of vibronic transitions)	homogeneous	(400) [a]
conjugation length variation	inhomogeneous	5 [b]
ambient temperature	inhomogeneous	30-80 [c]
lifetime broadening	homogeneous	0.6 [d]
intermolecule energy transfer	inhomogeneous	30 [e]
intrinsic linewidth of vibronic transitions	homogeneous	13 [f]

[a] Dominant in all spectra, also observed from isolated MelPPP polymer chains at 5 K [68]. Put in brackets because it is an effect of splitting into spaced transitions rather than classical broadening. The 400 meV "line-width" refers to the spectral region across which these transitions are typically spread.
[b] Comparison of spectra of an isolated MelPPP polymer chain and an ensemble at 5 K [68].
[c] Comparison of polyfluorene spectra at 5 K and 300 K [69] and systematic study of temperature dependent broadening in various PPV derivatives [70]. Heating by the pump is not considered.
[d] Theoretical value for 1 ns lifetime.
[e] Suggested from detailed dynamics investigations on PPV and PPPV [71].
[f] Obtained from isolated MelPPP polymer chain spectrum at 5 K [68].

TABLE 3.3: Luminescence broadening mechanisms in organic semiconductor films. The tablenotes indicate how each contribution was assessed.

- The pump parameter will be different for various wavelengths. In particular, it can no longer be determined by a simple threshold measurement.
- A continuous set of differential equations has to be solved, which is likely to be a time-consuming task with little prospect for useful results.

For these reasons it will be very difficult to extract accurate gain spectra from VSL type measurements in the presence of gain saturation.

It is, though, possible to learn a general concept from equations (3.14). In organic semiconductor thin films, the ASE/RL emission is typically confined to a wavelength range of 4-7 nm. Within these boundaries it is reasonable to assume constant parameters, $\eta(\omega) \simeq \eta$, $\alpha(\omega) \simeq \alpha$, $Y_p(\omega) \simeq Y_p$, $I_{sat}(\omega) \simeq I_{sat}$. Further, we take advantage of the observation that the counter-propagating modes are spatially separated. Thus we simplify to an expression where only spectral components travelling in one direction contribute to saturation:

$$\frac{\mathrm{d}I}{\mathrm{d}z}(z,\omega) = \frac{\eta Y_p}{1+\int_0^\infty \mathrm{d}\omega'\, I(z,\omega')/I_{sat}} + \alpha \cdot I(z,\omega)\left(\frac{Y_p}{1+\int_0^\infty \mathrm{d}\omega'\, I(z,\omega')/I_{sat}} - 1\right) \quad (3.15)$$

Now assume that at some point, z_0, one wavelength component is dominant:

$$I_0 := \int_{\omega_0-\delta}^{\omega_0+\delta} \mathrm{d}\omega'\, I(\omega') \gg_{z=z_0} \int_{rest} \mathrm{d}\omega'\, I(\omega') =: I_{rest} \tag{3.16}$$

Such an imbalance of the wavelength components could be caused by the randomness of the spontaneous emission seed or interference effects at random scatterers. We have then:

$$\frac{\mathrm{d}I_{0,rest}}{\mathrm{d}z} \approx_{z=z_0} \frac{\eta Y_p}{1+I_0/I_{sat}} + \alpha \cdot I_{0,rest}\left(\frac{Y_p}{1+I_0/I_{sat}} - 1\right) \tag{3.17}$$

From equations (3.16) and (3.17) it follows (assuming that I_0 does not exceed the maximum sustainable value, i.e. $I_0 < I_{sat}(Y_p - 1)$) that:

$$\frac{\mathrm{d}I_0}{\mathrm{d}z} > \frac{\mathrm{d}I_{rest}}{\mathrm{d}z} \tag{3.18}$$

which means that the imbalance will only get stronger. We believe that this is the mechanism that causes the spiky nature of RL spectra from organic thin films. It is interesting to note that the above argument does not rely on strong optical confinement within systems that could be described as random cavities, which is in good agreement with reports observing that random lasing can occur even in weakly scattering systems [35, 36, 72]. The assumed spectral imbalance can be triggered by Fabry-Perot [35] or Mie [73] type resonances at scatterers of micron or sub-micron size, but also by interference effects in an ensemble of randomly distributed weak scatterers each of which does not have pronounced resonances [36].

3.3.2.1 Spectral Quenching due to Disorder

Even though it appears very difficult to solve the continuous set of equations (3.14), we can still qualitatively study spectral quenching effects with a reduced set of equations. Let us assume there are only two spectral components, ω_1 and ω_2. Equations (3.14) can then be rewritten as:

$$\frac{\mathrm{d}I_{\rightarrow}(\omega_1)}{\mathrm{d}z} = \frac{\eta Y_p}{1+I_{tot}/I_{sat}} + \alpha \cdot I_{\rightarrow}(\omega_1)\left(\frac{Y_p}{1+I_{tot}/I_{sat}} - 1\right) \tag{3.19a}$$

$$\frac{\mathrm{d}I_{\leftarrow}(\omega_1)}{\mathrm{d}z} = -\frac{\eta Y_p}{1+I_{tot}/I_{sat}} - \alpha \cdot I_{\leftarrow}(\omega_1)\left(\frac{Y_p}{1+I_{tot}/I_{sat}} - 1\right) \tag{3.19b}$$

$$\frac{\mathrm{d}I_{\rightarrow}(\omega_2)}{\mathrm{d}z} = \frac{\eta Y_p}{1+I_{tot}/I_{sat}} + \alpha \cdot I_{\rightarrow}(\omega_2)\left(\frac{Y_p}{1+I_{tot}/I_{sat}} - 1\right) \tag{3.19c}$$

$$\frac{\mathrm{d}I_{\leftarrow}(\omega_2)}{\mathrm{d}z} = -\frac{\eta Y_p}{1+I_{tot}/I_{sat}} - \alpha \cdot I_{\leftarrow}(\omega_2)\left(\frac{Y_p}{1+I_{tot}/I_{sat}} - 1\right) \tag{3.19d}$$

$$I_{tot} = I_{\leftarrow}(\omega_1) + I_{\rightarrow}(\omega_1) + I_{\leftarrow}(\omega_2) + I_{\rightarrow}(\omega_2)$$

Boundary conditions are:

$$I_{\rightarrow}(\omega_1, z = 0) = I_{\rightarrow}(\omega_2, z = 0) = 0$$
$$I_{\leftarrow}(\omega_1, z = l) = I_{\leftarrow}(\omega_2, z = l) = 0$$

For simplicity, we have assumed here that the two wavelength components are sufficiently close to each other that threshold, losses and spontaneous emission rates are the same for both components. Inhomogenities are modelled according to equations (3.10), (3.11) and (3.12) in section 3.3.1.2, just that the parameters may depend on the wavelength.

$$\begin{aligned} \alpha_{add} &\rightarrow \alpha_{add}(\omega_1), \alpha_{add}(\omega_2) \\ \alpha_{wg} &\rightarrow \alpha_{wg}(\omega_1), \alpha_{wg}(\omega_2) \\ R &\rightarrow R(\omega_1), R(\omega_2) \end{aligned}$$

Figure 3.24 shows numerical solutions of perturbed two-wavelength systems (it is the two-wavelength equivalent of figure 3.22 in section 3.3.1.2). Parameter values are indicated in the figures, using the same material properties as in previous sections and comparable values for the perturbations as those used in section 3.3.1.2. Again, α_{add} and R are chosen small compared to waveguiding losses and unsaturated gain, i.e. they represent weak scattering. While a vacancy with wavelength-dependent waveguiding losses does not appear to alter the relative signal strength noticably (figure 3.24b), we clearly see spectral quenching due to either wavelength-dependent localised losses (figure 3.24a) or wavelength-dependent localised reflections (figure 3.24c). We summarise our observations:

- (Weak) localised losses do not alter the spatial distribution of the emission significantly but, they can lead to suppression of certain wavelengths.
- Non-emissive regions may slightly alter the spatial distribution of emission, but do not appear to have a significant impact on the spectrum.
- (Weak) localised reflections may have strong impact on the spatial and spectral properties of the emission, particularly in high gain media.

The effects considered above are centred around the idea that the spikyness of RL spectra is governed by inhomogenities and is not a result of the randomness of the spontaneous emission seed. This idea is justified by the fact that RL spectra from a solid target do not change significantly for a large number of successive pulses. Corresponding data from a BBEHP-PPV film was shown above in figure 3.12. It can be seen from this figure that the spectral positions of the individual RL spikes do do not change at all

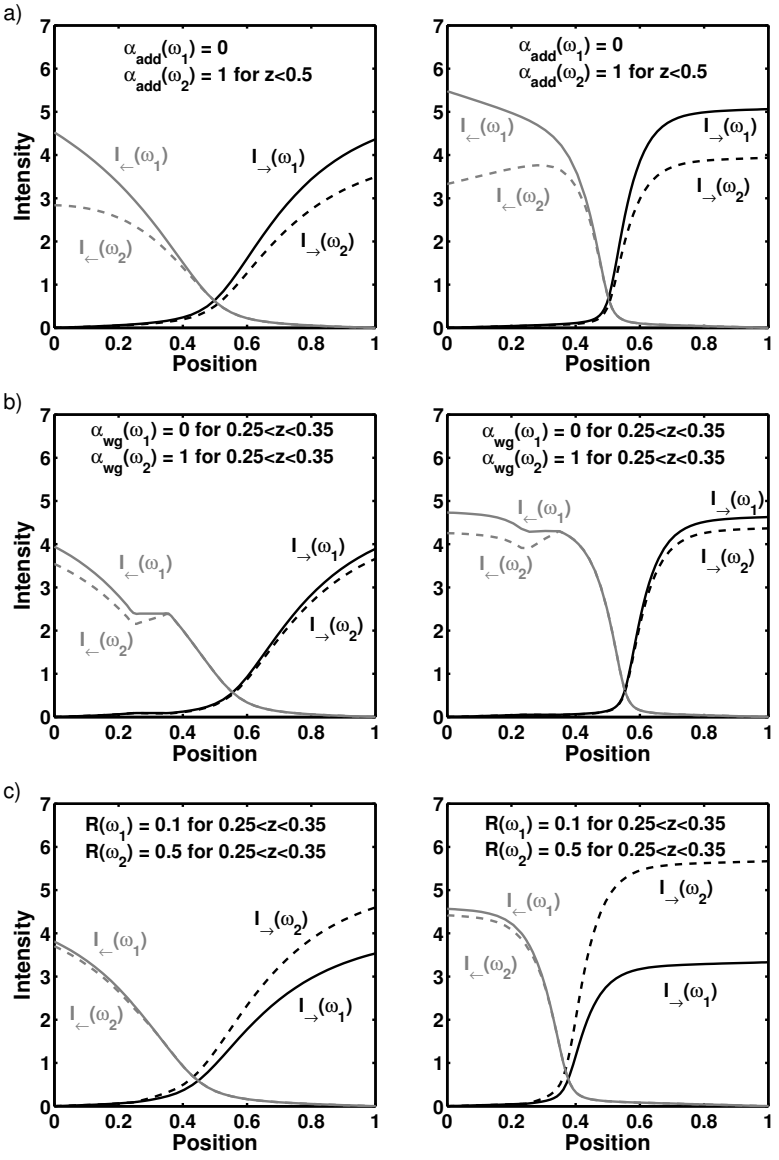

FIGURE 3.24: Numerical solution of equations (3.19) with various types of disorder. As in figures 3.21 and 3.22, the left hand figures show an intermediate gain medium ($\eta = 0.2, \alpha = 5, Y_p = 10, I_{sat} = 1$) and the right hand figures show a high gain medium ($\eta = 0.2, \alpha = 20, Y_p = 10, I_{sat} = 1$). The parameters for the distortions are given in each plot. Figures a) show the effect of a localised loss according to equations (3.10), figures b) a non-emissive region (equations (3.11)) and figures c) a reflective region (equations (3.12)).

from pulse to pulse and their intensities fluctuate around a fixed value. This proves that events which are random for each pulse (such as noise of the spontaneous emission) are not responsible for the observed behaviour.

3.3.2.2 Spectral Quenching in Real Organic Media

We have seen in section 3.3.2 that in conjugated polymers both homogeneous and inhomogeneous broadening mechanisms exist. In particular, for spectral ranges below 10 meV homogeneous broadening is dominant and we expect spectral quenching in stripe excitation due to perturbations as discussed above. An indication that this is indeed the case is obtained by looking at the first order self-correlation of a random laser spectrum:

$$\gamma(\hbar \cdot \delta\omega) := \frac{\langle I(\hbar\omega) \cdot I(\hbar\omega + \hbar \cdot \delta\omega)\rangle}{\sqrt{\langle |I(\hbar\omega)|^2\rangle \langle |I(\hbar\omega + \hbar \cdot \delta\omega)|^2\rangle}} \tag{3.20}$$

where $I(\hbar\omega)$ is the experimentally recorded spectral intensity and $\langle\cdot\rangle$ denotes averaging over ω. Figure 3.25 shows a typical RL spectrum and its self correlation of BBEHP-PPV in stripe excitation (experimental details are described in section 3.2.2). The self correlation drops very rapidly initially to a local anti-correlation at $\hbar \cdot \delta\omega \approx 5$ meV. Above ∼9 meV the self correlation drops off at a normal rate as would be expected for a smooth ASE peak. A spectrum consisting of entirely randomly positioned spikes at high density would more closely resemble the correlation function of a smooth peak. The observation of a 5-meV-anti-correlation is in good agreement with the expectation to see spectral quenching due to homogeneous broadening. The random laser spikes still spread over several 10 meV, owing to the inhomogeneous broadening at work over such a range. Spikes with a spectral separation of ∼10-80 meV are not strongly correlated to each other because they are not linked by a homogeneous mechanism.

3.3.3 Implications for Experimental Analysis

We have seen that the left and right travelling signals are spatially separated when saturation effects occur. One can therefore expect that VSL data will fit reasonably to an ansatz that only considers one signal:

$$\frac{\mathrm{d}I}{\mathrm{d}z} = \frac{\eta Y_p}{1 + I/I_{sat}} + \alpha \cdot I \left(\frac{Y_p}{1 + I/I_{sat}} - 1 \right) \tag{3.21}$$

Equation (3.21) has been used before [45–48] and it has been shown that it can explain 'soft threshold' behaviour [74], i.e. a gradual rather than a sharp threshold transition due to coupling of spontaneous emission into the laser mode which has been observed

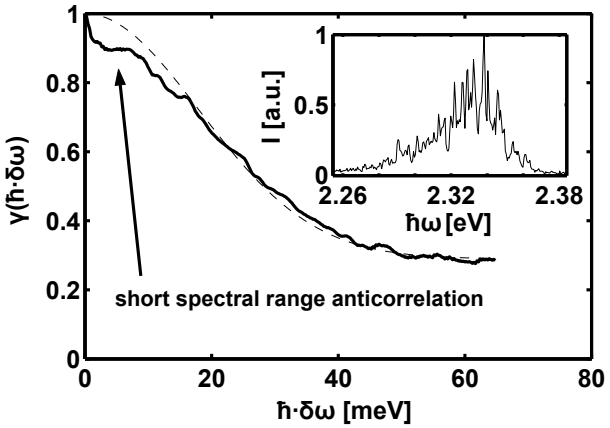

FIGURE 3.25: Self correlation of a random laser spectrum obtained in stripe geometry (31 μJ/cm^2, 6 kW/cm^2, 3× threshold). The spectrum itself is shown in the inset and has a spectral resolution of 0.5 meV. The typical line-width of individual random laser spikes is not resolved. The dashed line represents the theoretical self-correlation of a smooth Gaussian ASE peak with 30 meV width on top of a flat photoluminescence background.

in organic distributed feedback lasers, see section 4.1.2.1 below for more details. Experimental data indeed fits very well with equation (3.21) as is shown in figure 3.26, confirming this assumption. The data has been taken from BBEHP-PPV (AK391DCM2) film which was prepared and characterised as described in sections 3.2.2 and 3.2.3.2.

Despite good fitting of the individual curves, the parameters η, α, I_{sat} seem to vary considerably with the pump level Y_p (figure 3.27), even when ignoring the last data point. A fit of the overall data with η, α, I_{sat} forced to be independent of Y_p did not lead to a satisfying fit result. We also have to point out that equation (3.21) assumes that the signal evolves along the full length of the stripe, though figure 3.21 shows that it is significantly less than that, leading to a general systematic error in the parameters obtained. Therefore, the same data was also fitted with the more accurate set of equations (3.7), yielding similar order of magnitude values for the fit parameters as in figure 3.27 but also considerable variations. This indicates that the exact values found by those fits are not trustworthy. In the light of the above discussion, it may be an effect of disorder but other effects such as ground state bleaching could be held responsible as well. To accomodate for such effects, further parameters would need to be introduced. Given that equation (3.21) already reproduces experimental data fairly well, the use of additional parameters should be backed up by independent measurements. In combination with the concerns of other researchers [46, 49], it has to be concluded that *in high gain media the VSL technique should only be used for order-of-magnitude estimation of the material parameters.*

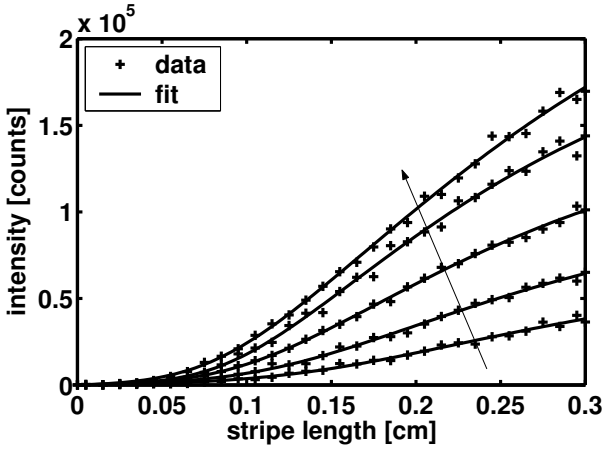

FIGURE 3.26: Fit of experimental data at different pump levels Y_p = 2.95, 4.28, 6.05, 7.89, 8.86 with equation (3.21). The arrow indicates the evolution of the VSL curve with increasing pump level. The threshold was 6.5 μJ/cm^2, 1.3 kW/cm^2.

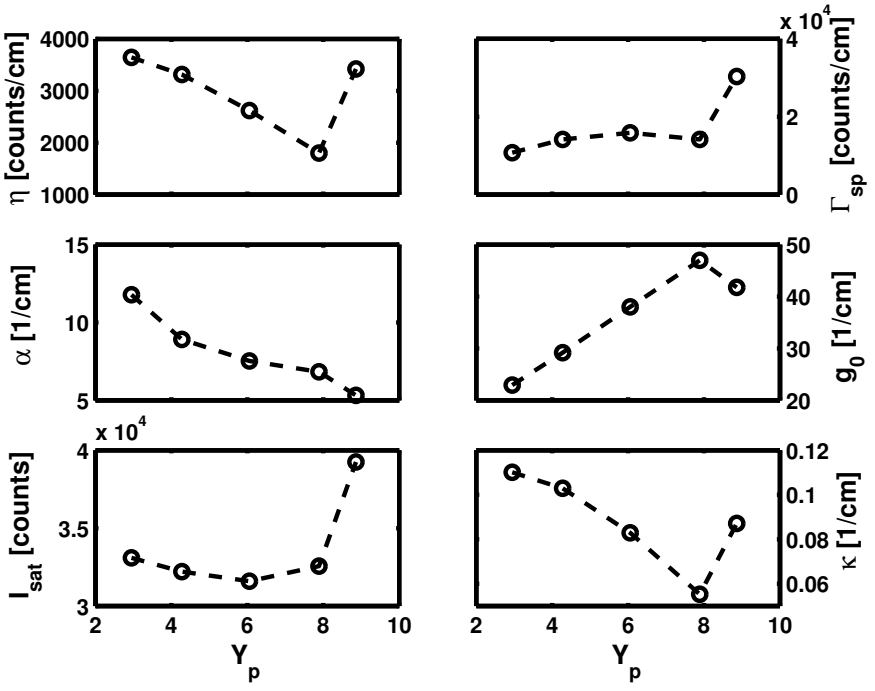

FIGURE 3.27: Parameters from the fits shown in figure 3.26. For reference, the right hand side plots show the spontaneous emission rate $\Gamma_{sp} = \eta Y_p$, the unsaturated optical gain $g_0 = \alpha(Y_p - 1)$ and the spontaneous emission coupling $\kappa = \eta / I_{sat}$.

3.4 Conclusion

The properties of blue-emitting oligofluorene-truxenes, green-emitting BBEHP-PPV and CdSe/ZnS CQDs (various wavelengths) were discussed. Under stripe excitation with a pulsed (5 ns) 355 nm pump we observe RL from all of these materials (deposited onto glass substrates) above typical thresholds of 40 μJ/cm^2 (8 kW/cm^2), 4–20 μJ/cm^2 (0.8–4 kW/cm^2) and 25 mJ/cm^2 (5 MW/cm^2), respectively. RL centre wavelengths were 435 nm, 535 nm and 606–630 nm, respectively. Due to photo-oxidation of the organic chromophores, the RL intensity from the LEPs faded with degradation dosages of the order of a few J/cm^2, yielding approximately 10^5 useful pulses.

To our understanding, the consistent occurence of RL in the stripe-excitation experiments described in this chapter is related to the high gain delivered by the gain media leading to gain saturation along the pump stripe. This understanding is based on a set of equations, (3.14) with, or (3.7) without, paying respect to wavelength dependence, which describes the counter-propagating signals under the inclusion of gain saturation. It has been shown that in high gain media (where the intensity reaches the maximum value allowed by saturation) left and right travelling signals along the stripe are spatially separated. The influence of inhomogenities has been studied. It was found that small reflective perturbations result in significant spectral and spatial redistribution of the emission and localised losses can cause spectral quenching. Local non-emissive regions may lead to a slight alteration of the spatial distribution but seem not to have a strong spectral effect. Spectral quenching due to perturbations is expected to occur over spectral ranges where homogeneous broadening mechanisms dominate. The experimental observation of a 5-meV-anti-correlation in a polymer random laser spectrum supports this idea. We think that such effects can explain the RL behaviour of high gain media in stripe excitation. In particular, our arguments suggest that RL may be a common material property of such media. The described VSL approach could be a relatively simple ansatz to gain insight into some fundamental aspects of random laser action.

Furthermore, our results suggest that gain spectra cannot practically be extracted from VSL type measurements if there is gain saturation. In general, VSL analysis of experimental data should be treated with caution and rather as a rough estimate. For this latter purpose, data may be fitted with equation (3.21).

Among the materials discussed in this chapter, BBEHP-PPV is the most promising candidate as gain material for LED-pumped lasers, because of its low ASE/RL threshold and because its absorption is well suited for highly efficient 450 nm GaN LEDs.

References

[1] Johannes Herrnsdorf, Yujie Chen, Benoit Guilhabert, Nicolas Laurand, and Martin D. Dawson. Stripe Excitation of High Gain Media With Disorder. *IEEE J. Quantum Electron.*, 48(9):1184–1192, 2012.

[2] John McGurk, Diego Andersen, Colin Belton, Paul Stavrinou, Gareth Parry, and Donal Bradley. Private communication, 2009–2012.

[3] Andy Monkman, Carsten Rothe, Simon King, and Fernando Dias. Polyfluorene Photophysics. *Adv. Polym. Sci.*, 212:187–225, 2008.

[4] Alexander L. Kanibolotsky, Rory Berridge, Peter J. Skabara, Igor F. Perepichka, Donald D. C. Bradley, and Mattijs Koeberg. Synthesis and Properties of Monodisperse Oligofluorene-Functionalized Truxenes: Highly Fluorescent Star-Shaped Architectures. *J. Am. Chem. Soc.*, 126: 13695–13702, 2004.

[5] Aimée Rose, Zhengguo Zhu, Conor F. Madigan, Timothy M. Swager, and Vladimir Bulović. Sensitivity gains in chemosensing by lasing action in organic polymers. *Nature*, 434:876–879, 2005.

[6] Alexander L. Kanibolotsky and Peter J. Skabara. Private communication, 2011.

[7] Yue Wang. *Low threshold organic semiconductor lasers and their applications as explosive sensors.* PhD thesis, University of St. Andrews, UK, 2012.

[8] Yue Wang, Georgios Tsiminis, Graham Turnbull, and Ifor Samuel. Private communication, 2010–2012.

[9] C. B. Murray, D. J. Norris, and M. G. Bawendi. Synthesis and characterization of nearly monodisperse CdE (E = sulfur, selenium, tellurium) semiconductor nanocrystallites. *J. Am. Chem. Soc.*, 115(19):8706–8715, 1993.

[10] C.B. Murray, C.R. Kagan, and M.G. Bawendi. Synthesis and Characterization of Monodisperse Nanocrystals and Close-Packed Nanocrystal Assemblies. *Annu. Rev. Mater. Sci.*, 30:545–610, 2000.

[11] Margaret A. Hines and Philippe Guyot-Sionnest. Synthesis and Characterization of Strongly Luminescing ZnS-Capped CdSe Nanocrystals. *J. Phys. Chem.*, 100:468–471, 1996.

[12] B. O. Dabbousi, J. Rodriguez-Viejo, F. V. Mikulec, J. R. Heine, H. Mattoussi, R. Ober, K. F. Jensen, and M. G. Bawendi. (CdSe)ZnS Core-Shell Quantum Dots: Synthesis and Characterization of a Size Series of Highly Luminescent Nanocrystallites. *J. Phys. Chem. B*, 101:9463–9475, 1997.

[13] D. J. Norris and M. G. Bawendi. Measurement and assignment of the size-dependent optical spectrum in CdSe quantum dots. *Phys. Rev. B*, 53(24):16338–16346, 1996.

[14] B. Guilhabert, D. Elfström, A. J. C. Kuehne, D. Massoubre, H. X. Zhang, S. R. Jin, A. R. Mackintosh, E. Gu, R. A. Pethrick, and M. D. Dawson. Integration by self-aligned writing of nanocrystal/epoxy composites on InGaN micropixelated light-emitting diodes. *Opt. Express*, 16(23):18933–18941, 2008.

[15] D. O. Demchenko and Lin-Wang Wang. Optical transitions and nature of Stokes shift in spherical CdS quantum dots. *Phys. Rev. B*, 73:155326, 2006.

[16] H. Kogelnik and C. V. Shank. Stimulated Emission in a Periodic Structure. *Appl. Phys. Lett.*, 18 (4):152–154, 1971.

[17] I. P. Kaminow, H. P. Weber, and E. A. Chandross. Poly(Methyl Methacrylate) Dye Laser with Internal Diffraction Grating Resonator. *Appl. Phys. Lett.*, 18(11):497–499, 1971.

[18] S. Richardson, O. P. M. Gaudin, G. A. Turnbull, and I. D. W. Samuel. Improved operational lifetime of semiconducting polymer lasers by encapsulation. *Appl. Phys. Lett.*, 91:261104, 2007.

[19] Alexander J. C. Kühne. *UV Transparent and Light Emitting Photo-Polymers for Optoelectronic Applications*. PhD thesis, University of Strathclyde, Glasgow, UK, 2008.

[20] A. R. Mackintosh, A. J. C. Kuehne, R. A. Pethrick, B. Guilhabert, E. Gu, C. L. Lee, M. D. Dawson., G. Heliotis, and D. D. C. Bradley. Novel polymer systems for deep UV microlens arrays. *J. Appl. Phys. D*, 41:094007, 2008.

[21] Alexander J. C. Kuehne, David Elfström, Allan R. Mackintosh, Alexander L. Kanibolotsky, Benoit Guilhabert, Erdan Gu, Igor F. Perepichka, Peter J. Skabara, Martin D. Dawson, and Richard A. Pethrick. Direct Laser Writing of Nanosized Oligofluorene Truxenes in UV-Transparent Photoresist Microstructures. *Adv. Mat.*, 21:781–785, 2009.

[22] Yujie Chen, Johannes Herrnsdorf, Benoit Guilhabert, Yanfeng Zhang, Alexander L. Kanibolotsky, Peter J. Skabara, Erdan Gu, Nicolas Laurand, and Martin D. Dawson. Modification of emission wavelength in organic random lasers based on photonic glass. *Org. Electron.*, 13:1129–1135, 2012.

[23] Yujie Chen. *Laser Action in Solution-Processed Gain Media*. PhD thesis, University of Strathclyde, Glasgow, UK, 2012.

[24] Marian O. Scully and Michael Fleischhauer. Lasers without inversion. *Science*, 263:337–338, 1994.

[25] F. De Martini and G. R. Jacobovitz. Anomalous spontaneous-stimulated-decay phase transition and zero-threshold laser action in a microscopic cavity. *Phys. Rev. Lett.*, 60(17):1711–1714, 1988.

[26] Lee W. Casperson. Threshold characteristics of mirrorless lasers. *J. Appl. Phys.*, 48(1):256–262, 1977.

[27] L. Mandel and E. Wolf. Coherence properties of optical fields. *Rev. Mod. Phys.*, 37(2):231–287, 1965.

[28] Randall C. Polson, Mikhail E. Raikh, and Z. Valy Vardeny. Universal Properties of Random Lasers. *IEEE J. Sel. Top. Quant. Electron.*, 9(1):120–123, 2003.

[29] Marco Leonetti, Claudio Conti, and Cefe Lopez. The mode-locking transition of random lasers. *Nature Photonics*, 5:615–617, 2011.

[30] R. V. Ambartsumyan, N. G. Basov, P. G. Kryukov, and V. S. Letokhov. A Laser with a Nonresonant Feedback. *IEEE J. Quant. Electron.*, QE-2(9):442–446, 1966.

[31] V. S. Letokhov. Stimulated emission of an ensemble of scattering particles with negative absorption. *JETP Lett.*, 5:212–215, 1967.

[32] H. Cao, Y. G. Zhao, H. C. Ong, S. T. Ho, J. Y. Dai, J. Y. Wu, and R. P. H. Chang. Ultraviolet lasing in resonators formed by scattering in semiconductor polycrystalline films. *Appl. Phys. Lett.*, 73(25):3656–3658, 1998.

[33] R. M. Balachandran, D. P. Pacheco, and N. M. Lawandy. Laser action in polymeric gain media containing scattering particles. *Appl. Opt.*, 35(4):640–643, 1996.

[34] Diederik S. Wiersma, Paolo Bartolini, Ad Lagendijk, and Roberto Righini. Localization of light in a disordered medium. *Nature*, 390:671–673, 1997.

[35] X. Wu, W. Fang, A. Yamilov, A. A. Chabanov, A. A. Asatryan, L. C. Botten, and H. Cao. Random lasing in weakly scattering systems. *Phys. Rev. A*, 74:053812, 2006.

[36] C. Vanneste, P. Sebbah, and H. Cao. Lasing with Resonant Feedback in Weakly Scattering Random Systems. *Phys. Rev. Lett.*, 98:143902, 2007.

[37] Seung Ho Choi and Young L. Kim. Random lasing mode alterations by single-nanoparticle perturbations. *Appl. Phys. Lett.*, 100:041101, 2012.

[38] S. V. Frolov, Z. V. Vardeny, K. Yoshino, A. Zakhidov, and R. H. Baughman. Stimulated emission in high-gain organic media. *Phys. Rev. B*, 59(8):R5284–R5287, 1999.

[39] A.V. Malko, A.A. Mikhailovsky, M.A. Petruska, J.A. Hollingsworth, H. Htoon, M.G. Bawendi, and V.I. Klimov. From amplified spontaneous emission to microring lasing using nanocrystal quantum dot solids. *Appl. Phys. Lett.*, 81(7):1303–1305, 2002.

[40] A.A. Mikhailovsky, A.V. Malko, J.A. Hollingsworth, M.G. Bawendi, and V.I. Klimov. Multiparticle interactions and stimulated emission in chemically synthesized quantum dots. *Appl. Phys. Lett.*, 80 (13):2380–2382, 2002.

[41] Victor I. Klimov, Sergei A. Ivanov, Jagjit Nanda, Marc Achermann, Ilya Bezel, John A. McGuire, and Andrei Piryatinski. Single-exciton optical gain in semiconductor nanocrystals. *Nature*, 447: 441–446, 2007.

[42] Yujie Chen, Johannes Herrnsdorf, Benoit Guilhabert, Yanfeng Zhang, Ian M. Watson, Erdan Gu, Nicolas Laurand, and Martin D. Dawson. Colloidal quantum dot random laser. *Opt. Express*, 19 (4):2996, 2011.

[43] K.L. Shaklee and R.F. Leheny. Direct determination of optical gain in semiconductor crystals. *Appl. Phys. Lett.*, 18(11):475–477, 1971.

[44] C. Lange, M. Schwalm, S. Chatterjee, W.W. Rühle, N.C. Gerhardt, S.R. Johnson, J.-B. Wang, and Y.-H. Zhang. The variable stripe-length method revisited: Improved analysis. *Appl. Phys. Lett.*, 91:191107, 2007.

[45] G.J. Pert. Output characteristics of amplified-stimulated-emission lasers. *J. Opt. Soc. Am. B*, 11 (8):1425–1435, 1994.

[46] L. Dal Negro, P. Bettotti, M. Cazzanelli, D. Pacifici, and L. Pavesi. Applicability conditions and experimental analysis of the variable stripe length method for gain measurements. *Opt. Commun.*, 229:337–348, 2004.

[47] A. Costela, O. García, L. Cerdán, I. García-Moreno, and R. Sastre. Amplified spontaneous emission and optical gain measurements from pyrromethene 567 - doped polymer waveguides and quasi-waveguides. *Opt. Express*, 16(10):7023–7036, 2008.

[48] A. Costela, O. García, L. Cerdán, I. García-Moreno, and R. Sastre. Amplified spontaneous emission and optical gain measurements from pyrromethene 567 - doped polymer waveguides and quasi-waveguides: erratum. *Opt. Express*, 16(10):7587, 2008.

[49] C. Lange, M. Schwalm, B. Metzger, and S. Chatterjee. Carrier-depletion in the stripe-length method: Consequences for gain measurement. *J. Appl. Phys.*, 108:103119, 2010.

[50] George Heliotis, Donal D. C. Bradley, Graham A. Turnbull, and Ifor D. W. Samuel. Light amplification and gain in polyfluorene waveguides. *Appl. Phys. Lett.*, 81(3):415–417, 2002.

[51] Takeyuki Kobayashi, Michael Flämmich, Grace Jordan, Rebekah D'Arcy, Manuel Rüther, Werner J. Blau, Yasuhiro Suzuki, and Toshikuni Kaino. Blue-green small-signal gain and saturation in a luminescent polymer gain medium. *Appl. Phys. Lett.*, 89:131119, 2006.

[52] Georgios Tsiminis, Yue Wang, Paul E. Shaw, Alexander L. Kanibolotsky, Igor F. Perepichka, Martin D. Dawson, Peter J. Skabara, Graham A. Turnbull, and Ifor D.W. Samuel. Low-threshold organic laser based on an oligofluorene truxene with low optical losses. *Appl. Phys. Lett.*, 94: 243304, 2009.

[53] Yue Wang, Georgios Tsiminis, Ying Yang, Arvydas Ruseckas, Alexander L. Kanibolotsky, Igor F. Perepichka, Peter J. Skabara, Graham A. Turnbull, and Ifor D.W. Samuel. Broadly tunable deep blue laser based on a star-shaped oligofluorene truxene. *Synth. Met.*, 160:1397–1400, 2010.

[54] Yujie Chen, Johannes Herrnsdorf, Benoit Guilhabert, Alexander L. Kanibolotsky, Allan R. Mackintosh, Yue Wang, Richard A. Pethrick, Erdan Gu, Graham A. Turnbull, Peter J. Skabara, Ifor D.W. Samuel, Nicolas Laurand, and Martin D. Dawson. Laser action in a surface-structured free-standing membrane based on a π-conjugated polymer-composite. *Org. Electron.*, 12:62–69, 2011.

[55] Giannis Zacharakis, George Heliotis, George Filippidis, Demetrios Anglos, and Theodore G. Papazoglou. Investigation of the laserlike behavior of polymeric scattering gain media under subpicosecond laser excitation. *Appl. Opt.*, 38(28):6087–6092, 1999.

[56] R. C. Polson, M. E. Raikh, and Z. V. Vardeny. Random lasing from weakly scattering media; spectrum universality in DOO-PPV polymer films. *Physica E*, 13:1240–1242, 2002.

[57] Diederik S. Wiersma and Ad Lagendijk. Light diffusion with gain and random lasers. *Phys. Rev. E*, 54(4):4256–4265, 1996.

[58] Sajeev John and Gendi Pang. Theory of lasing in a multiple-scattering medium. *Phys. Rev. A*, 54 (4):3642–3652, 1996.

[59] R. M. Balachandran, N. M. Lawandy, and J. A. Moon. Theory of laser action in scattering gain media. *Opt. Lett.*, 22(5):319–321, 1997.

[60] G. A. Berger, M. Kempe, and A. Z. Genack. Dynamics of stimulated emission from random media. *Phys. Rev. E*, 56(5):6118–6122, 1997.

[61] A. Lubatsch, J. Kroha, and K. Busch. Theory of light diffusion in disordered media with linear absorption or gain. *Phys. Rev. B*, 71:184201, 2005.

[62] Pierre Barthelemy, Jacopo Bertolotti, and Diederik S. Wiersma. A Lévy flight for light. *Nature*, 453:495–498, 2008.

[63] Xunya Jiang and C. M. Soukoulis. Time Dependent Theory for Random Lasers. *Phys. Rev. Lett.*, 85(1):70–73, 2000.

[64] C. Conti, M. Leonetti, A. Fratalocchi, L. Angelani, and G. Ruocco. Condensation in Disordered Lasers: Theory, 3D + 1 Simulations, and Experiments. *Phys. Rev. Lett.*, 101:143901, 2008.

[65] Bahaa E.A. Saleh and Malvin Carl Teich. *Fundamentals of Photonics.* John Wiley & Sons, Inc., 1991.

[66] G. Wegmann, B. Schweitzer, D. Hertel, H. Giessen, M. Oestreich, U. Scherf, K. Müllen, and R.F. Mahrt. The dynamics of gain-narrowing in a ladder-type π-conjugated polymer. *Chem. Phys. Lett.*, 312:376–384, 1999.

[67] Lee. W. Casperson and Amnon Yariv. Spectral Narrowing in High-Gain Lasers. *IEEE J. Quant. Electron.*, QE-8(2):80–85, 1972.

[68] J. G. Müller, M. Anni, U. Scherf, M. Lupton, and J. Feldmann. Vibrational fluorescence spectroscopy of single conjugated polymer molecules. *Phys. Rev. B*, 70:035205, 2004.

[69] Kohei Asada, Takashi Kobayashi, and Hiroyoshi Naito. Temperature dependence of photoluminescence in polyfluorene thin films–Huang-Rhys factors of as-coated, annealed and crystallized thin films. *Thin Solid Films*, 499:192–195, 2006.

[70] Sebastian T. Hoffmann, Heinz Bässler, and Anna Köhler. What Determines Inhomogeneous Broadening of Electronic Transitions in Conjugated Polymers? *J. Phys. Chem. B*, 114:17037–17048, 2010.

[71] B. Mollay, U. Lemmer, R. Kersting, R. F. Mahrt, H. Kurz, H. F. Kauffmann, and H. Bässler. Dynamics of singlet excitations in conjugated polymers: Poly(phenylenevinylene) and poly(phenylphenylenevinylene). *Phys. Rev. B*, 50(15):10769–10779, 1994.

[72] Diederick S. Wiersma. The physics and applications of random lasers. *Nature Physics*, 4:359–367, 2008.

[73] Stefano Gottardo, Riccardo Sapienza, Pedro D. Garzía, Alvaro Blanco, Diederik S. Wiersma, and Cefe López. Resonance-driven random lasing. *Nature Photonics*, 2:429–432, 2008.

[74] J. Herrnsdorf, B. Guilhabert, Y. Chen, A. L. Kanibolotsky, A. R. Mackintosh, R. A. Pethrick, P. J. Skabara, E. Gu, N. Laurand, and M. D. Dawson. Flexible blue-emitting encapsulated organic semiconductor DFB laser. *Opt. Express*, 18(25):25535–25545, 2010.

Chapter 4

Flexible Distributed Feedback Lasers

In recent years, much effort has been put into the development of solid-state organic light emitters. In particular, the success of organic light emitting diodes combined with advances in polymeric waveguides has been accompanied by increased interest in organic semiconductor lasers (OSL). Such devices have a number of benefits compared to their inorganic counterparts, including simplified production methods and the avoidance of highly toxic materials [1]. Another attractive property of organics is their compatibility with a large range of different materials thus allowing for example the usage of mechanically flexible substrates [2–6]. A thorough review of OSLs was provided in chapter 2. To put the content of this chapter into context more clearly, the most relevant findings are reiterated in the remainder of this introduction.

One of the key challenges in the development of these lasers is their susceptibility to photo-induced oxidation which limits their useful lifetime. To date, the majority of organic film laser demonstrations required the laser structure to be pumped in vacuum or in a protective inert gas atmosphere [7]. For example the first flexible OSL reported [2] was characterised in vacuum. In general, only limited information on quantitative analysis of OSL degradation, both in vacuum and aerobic operating conditions, has been published (see figure 2.19). One possible approach to address the issue of photo-degradation is to create a multilayer structure where the active medium is enclosed in between layers of a transparent polymer that serves as an oxygen and water barrier. Encouraging results by Richardson *et al.* [7, 8] on red-emitting MEH-PPV are based on such an encapsulation technique including inorganic layers.

A commonly used resonator layout for organic thin-film lasers is based on distributed feedback (DFB), where the optical feedback and out-coupling are provided by Bragg reflections of different order, from a grating within the film [1]. In section 2.2.1 it was shown that DFB resonators are the most promising candidates for LED-pumped OSLs due to their low threshold. DFB gratings are typically custom made by electron beam lithography, two-beam interference or deep-ultraviolet photo-lithography. These methods can be quite complicated and expensive thus counteracting organic semiconductors' important potential for low-cost production. In order to simplify matters, soft-lithographic imprint methods to replicate a master grating have been developed [9–11]. The approach presented below is based on soft lithography using commercially available holographic reflective gratings as a master. Commercially available gratings have been used before by Song, Wenger and Friend [12] for the fabrication of unencapsulated devices on glass substrates. DFB resonators are particularly suitable for building flexible lasers and a number of reports on such devices have been published. However, all reported flexible devices, with the exception of the LPPP-based work by Scherf *et al.* [2, 4], are based on dye-doped polymers with thresholds ranging from 16 μJ/cm^2 [5] to 800 μJ/cm^2 [6].

In the first section, the fabrication and optical characterisation (including photo-stability) of blue-emitting devices is shown, followed by two sections on green-emitting devices and investigations on the pump geometry and polarisation. The key findings presented in this chapter have been published in Optics Express [13].

4.1 Blue-emitting Truxene Lasers

The lasers described in this section are based on T3 hexyl oligofluorene-truxenes which were introduced in section 3.1.1. These materials were shown to have a high photoluminescence quantum yield and to form low-loss film onto a hard substrate when deposited from solution [14, 15]. Consequently, low threshold for optical gain and laser oscillation as reported for such non-flexible devices [15, 16]. However, no data on the operating lifetime was given. This section describes mechanically flexible lasers that use encapsulated T3 nanochromophores as the active region and operate at deep-blue wavelengths from 425 to 442 nm. Furthermore, it is shown that even without encapsulation the truxenes have better photo-stability properties than other star-shaped molecules.

4.1.1 Fabrication

An important feature of the lasers presented here is their simple production. The grating structure is copied from the master grating into a UV-transparent polymer that is

obtained by photo-curing 1,4-cyclohexyldimethanol divinyl ether (CHDV) with added photo-acid generator (PAG, see figure 3.8 for chemical structures of CHDV and PAG). As PAG we use 4-octyloxy diphenyliodonium hexafluoroantimonite which is dissolved in the CHDV at a weight ratio of 0.2 %. The solution is then mixed in an ultrasonic bath for at least 5 min and degassed. It is in principle possible to incorporate the T3 molecules directly into the CHDV matrix, resulting in a nanocomposite that is capable of providing optical gain [17] though this chapter will focus on stacked structures where the undoped CHDV grating is overcoated by a layer of pure T3. A schematic of the structure is shown in figures 4.1a and 4.1b.

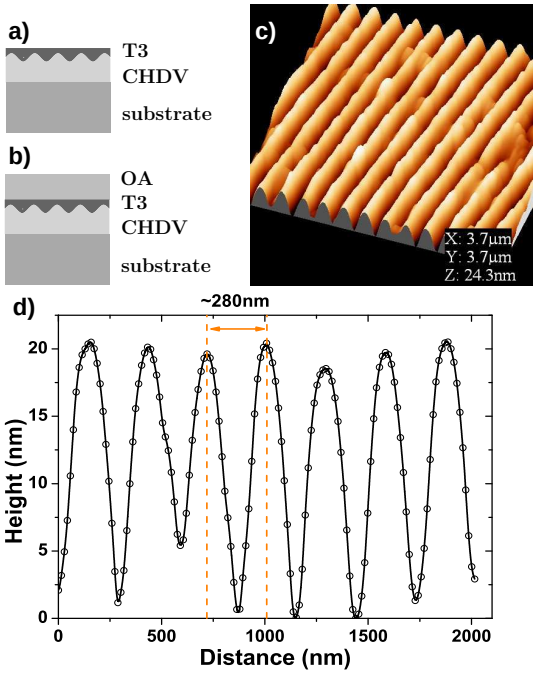

FIGURE 4.1: On the left, schematics of the device structure are shown: *a)* unencapsulated and *b)* encapsulated by an optical adhesive (OA). On the right side is *c)* an AFM image of the reproduced grating and at the bottom *d)* a plot of the surface profile perpendicular to the grating.

After preparation, the PAG/CHDV solution is drop-coated onto the substrate. As a substrate we use commercially available acetate sheets of 0.1 mm thickness, made for ink-jet printed transparencies.

The substrate with the film on it is pressed onto the master grating. We use a commercially available holographic reflection grating with 3600 lines/mm, i.e. a period of 278 nm. The grating surface is a polymer overcoated with aluminum. The photoresist is cured by flooding with UV light at an exposure dose of 30.5 J/cm^2 through the substrate while in contact with the master grating. Finally, the grating structure is peeled off from the master. An approximate area of 1 cm^2 with a high quality grating can be obtained by this method, which is suitable to produce several devices at a time. Analysis by AFM

(a scan profile is shown in figures 4.1c and 4.1d) reveals that the resulting grating has an average modulation depth of 21 nm in a scanned area of 3.7×3.7 μm^2. The thickness of the CHDV layer has been measured with a caliper and a value of 30 μm was found. The refractive index of this material is $n_{CHDV} = 1.472$ (Sigma-Aldrich, Inc.).

The T3 molecules are spin-coated from 20 mg/ml toluene solution onto the grating at a spinning speed of 2700 to 3200 RPM, resulting in films of different thickness (100 nm - 150 nm) which impacts the laser emission wavelength as discussed below in section 4.1.3. Further overcoating with optical adhesives provides protection of the chromophores against oxygen and moisture. We present devices that are encapsulated with Norland optical adhesive (NOA) 88 by drop-coating a 1 mm thick top layer of refractive index $n_{NOA} = 1.56$ (Norland Products, Inc.). The transmission spectra of acetate and CHDV are shown in figure 4.2 and PL and absorption spectra of the chromophores were shown in the previous chapter in figure 3.2. Detailed analysis of the truxene PL and absorption has been done by Kanibolotsky *et al.* [14] and the refractive index of the active material is $n_{T3} = 1.77$ [16].

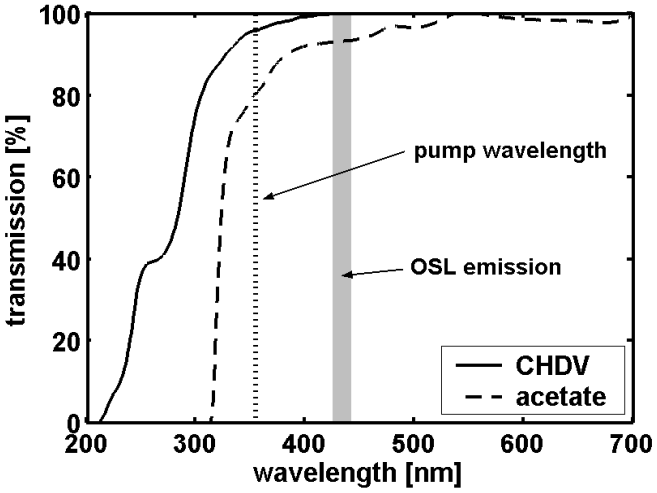

FIGURE 4.2: Transmission spectra of an 0.1 mm thick acetate sheet and an 11 μm thick film of CHDV (taken from [18]).

4.1.2 Optical Characterisation

The organic DFB lasers were optically pumped with 355 nm wavelength pulses (5 ns pulse duration) at 10 Hz repetition rate, as described in section 3.2.2. A full width half maximum (FWHM) of 2.9 mm across the beam has been measured at 6 cm and 40 cm distance from the attenuator wheel (see figure 4.3), i.e. the beam divergence is negligible within the length scales used in the setup. The samples were placed at a 45° angle with respect to the beam axis resulting in an elliptical pump spot of 2.9 mm × 4.1 mm

FWHM. Energy densities given in the text and figures are peak values assuming a Gaussian shaped beam cross section. The vertical emission from the sample surface was monitored by a 50-μm-core optical fibre which was connected to a CCD-spectrometer with a maximum spectral resolution of 0.13 nm. The detection angle is controllably variable, which enables mapping of the beam profile with an angular resolution of 0.45° (7.8 mrad). During measurements, the samples are exposed to normal ambient air at room temperature. No vacuum or inert gases are used to protect the active material. A schematic of the setup is shown in figure 4.3 and a more detailed description was given earlier in section 3.2.2. It is possible to focus the pump spot using a 75 mm spherical lens. In this case, an upper boundary of the pump area of 0.0014 cm^2 has been measured (area with intensity higher than half the peak value) by monitoring the pump spot luminescence with a CCD camera (see appendix A.3.1 for issues with this method).

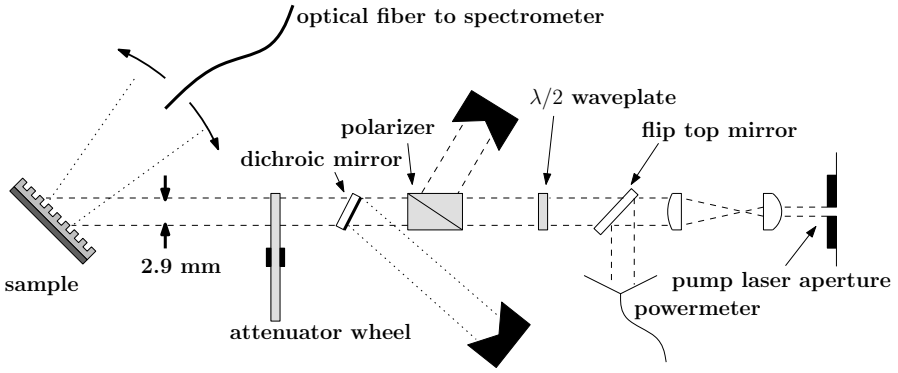

FIGURE 4.3: Schematic of the setup for optical characterisation. See also figure 3.10 in section 3.2.2.

Upon appropriate pulsed UV excitation, laser action is observed with a soft threshold behaviour that is discussed in the next section. Above threshold, a fan-shaped beam is visible which is the typical mode profile of one-dimensional DFB grating lasers.

4.1.2.1 Threshold crossing

When pumping close to threshold for optical gain, we observe a gradual steepening of the laser emission intensity from the initial photo-luminescence (PL) slope towards the final laser slope, rather than a well defined sharp threshold. Theoretical work by Stéphan [19] and Boucher *et al.* [20, 21] suggests that such a soft threshold can be expected to be fairly typical for microresonator lasers in general and DFB lasers in particular. The origin of this behaviour is the significant contribution of ASE and hence unsaturated gain when close to threshold.

It is possible to understand soft threshold behaviour as a property of ASE using a variation of the variable stripe length equation that includes saturation, as has been

discussed before by Pert [22], Dal Negro *et al.* [23] and Costela *et al.* [24, 25]:

$$\frac{\mathrm{d}I_{ASE}}{\mathrm{d}x} = \frac{aF_p}{1 + I_{ASE}/I_{sat}} + bI_{ASE}\left(\frac{F_p/F_{th}}{1 + I_{ASE}/I_{sat}} - 1\right) \tag{4.1}$$

where F_p is the pump fluence, $x \in [0, 1]$ is the position along an optical path normalised to the path length, F_{th} is the pump threshold for optical gain, I_{sat} the saturation intensity, a the spontaneous emission rate and b the scattering and absorption losses. Note that in the previous chapter (section 3.3) a similar ansatz was used to investigate random laser action. Equation (4.1) can be integrated numerically from $x = 0, I_{ASE}(0) = 0$ to $x = 1$. It is assumed that $I_{ASE}(1)$ is directly proportional to the detected intensity. This model has four parameters, F_{th}, I_{sat}, a and b, that have to be optimised when fitting experimental data. Boucher and Féron [21] suggested that a three-parameter model may be suitable for microresonators:

$$I_{laser} = \frac{I_{sat}\kappa F_p/F_{th}}{1 + I_{laser}/I_{sat} - F_p/F_{th}} \tag{4.2}$$

The dimensionless parameter κ basically accounts for the coupling of spontaneous emission into the laser mode. Here again, it is the contribution of unsaturated stimulated emission that is responsible for the softness of the threshold.

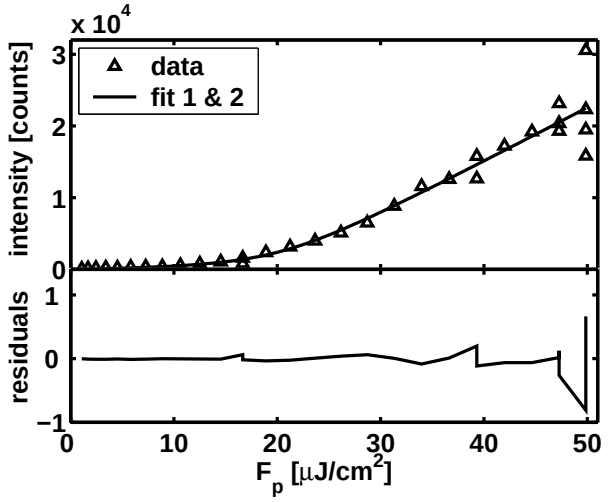

FIGURE 4.4: Threshold measurement of an unencapsulated device fitted with equation (4.1) (fit 1) and (4.2) (fit 2). The curves given by the two models are not distinguishable at the scale of this plot. Fitting parameters are given in table 4.1.

Fit	F_{th} [μJ $\times$ cm^{-2}]	I_{sat} [counts]	a [counts/ (μJ $\times$ cm^{-2})]	b	κ
fit 1	21.69	1.655×10^4	540	20.3	-
fit 2	21.67	1.653×10^4	-	-	3.46×10^{-2}

TABLE 4.1: Fitting parameters used in figure 4.4.

For fitting experimental data, the saturation intensity I_{sat} is treated as a linear parameter and solved for by linear regression while the other parameters are optimised using the `fminsearch` function from Matlab (details on this function can be found in the Matlab documentation [26] and a description of the Matlab functions for soft threshold fitting is given in appendix A.2). Both models fit experimental measurements quite well as shown in figure 4.4. In the example given in figure 4.4, the two models agree with each other extremely closely, both in curve shape and in the values for threshold and saturation intensity (table 4.1). More generally we observe that both models rarely deviate from each other by more than 10 %. In conclusion the three-parameter model, Equation (4.2), should be preferred for fitting microresonator thresholds because it has one numerical variable less, needs significantly less computation time and yields similar results to the ASE based model.

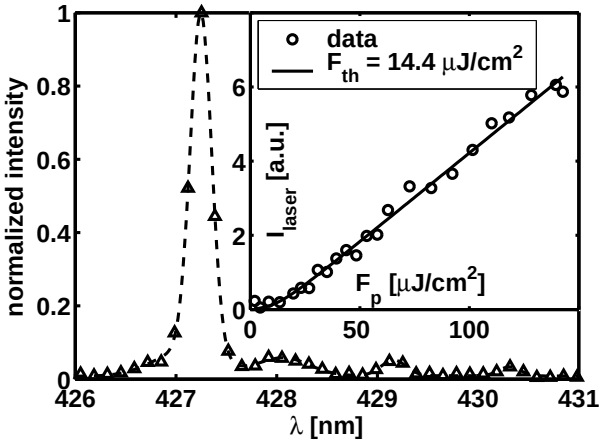

FIGURE 4.5: Laser spectrum fitted by Gaussian decomposition. The unencapsulated sample has been pumped with the unfocussed (2.9 mm diameter) beam and satellite peaks are visible. The dominant peak has a linewidth of 0.25 nm full width half maximum. *Inset:* Threshold measurement fitted with equation (4.2).

The power transfer function of the lasers was extracted from the spectra at different pump fluences. In figure 4.5 we see that a typical laser spectrum consists of a dominant peak and a couple of smaller satellite peaks. The individual laser emission peaks have a spectral width of 0.25 nm or less. If we integrate the intensity over the spectral range of the dominant peak, we get the slope measurement shown in the inset of figure 4.5. For the best sample, a threshold pump fluence of 14.4 μJ/cm^2 (2.7 kW/cm^2) has been found by fitting model (4.2) with the spontaneous emission coupling coefficient being $\kappa = 0.13$. This value is just below the ASE threshold of a neat truxene film on a hard silica substrate (16 μJ/cm^2, 4 kW/cm^2) but higher than the lowest truxene DFB laser threshold on a corrugated silica substrate (2.7 μJ/cm^2, 270 W/cm^2) measured by Tsiminis *et al.* [15]. Both of these earlier reported values were achieved using protection of the sample by vacuum. The higher threshold in our devices can be explained by

slightly lower grating quality and poorer confinement of the transverse optical mode to the active layer because of reduced refractive index contrast between the layers. An early laser demonstration with a different type of star-shaped oligomers by Xia *et al.* [27] revealed an even lower threshold of $0.16 - 0.28$ μJ/cm^2 ($38 - 65$ W/cm^2) though we will show in section 4.1.4 that the pyrene-cored molecules in that report are less stable than truxene-cored oligofluorenes.

A sample encapsulated by drop-coating had a higher threshold of 63 μJ/cm^2 (12.2 kW/cm^2). The main factors contributing to the increase of threshold are believed to be a lensing effect due to the curvature of the of the encapsulation surface, reduced overlap of the transverse optical mode with the active layer and pump absorption in the optical adhesive.

Precise measurements of the threshold of high-quality devices pumped with the focussed (≤ 0.0014 cm^2) pump spot were not possible because limits of the setup were reached, especially in terms of detector sensitivity. It is clear however, that the lowest threshold pump energies in this configuration are slightly below 30 nJ (≥ 21 μJ/cm^2, 4 kW/cm^2). This indicates that for pump spot sizes ranging from 0.0014 cm^2 to 0.093 cm^2 (1:1.4 elliptical pump spot shape) the threshold pump fluence may not vary strongly.

4.1.3 Properties of the laser beam

Above threshold, a fan-shaped laser beam was observed on a white screen placed parallel to the surface of the sample. Photographic images of the operating sample and the laser beam are shown in figures 4.6a and 4.6b, respectively. Figure 4.6c shows a photo of the sample under illumination from a UV lamp. The set of graphics in figure 4.7 shows polarisation-resolved spectral maps across the beam waist. In these measurements, the effect of the grating yields an X-shaped structure. The wavelength of the crossing point of this structure is the position of the stop band [28]. Laser oscillation occurs at that wavelength if the material is able to provide optical gain. The position of the stop-band can be controlled by the spin-coating parameters thus allowing tuning of the laser wavelength between 425 nm and 442 nm, corresponding to an in-plane effective refractive index in between $n_{eff} = 1.529$ and $n_{eff} = 1.590$. In general, an increase of the spinning speed will blue-shift the stop-band, because the film thickness and thus the effective refractive index decrease. The effective refractive index can also be estimated from the waveguide materials' refractive indices given in section 4.1.1 by solving the boundary conditions of the fundamental TE_0 mode at the top and bottom surfaces of the active layer for a given layer thickness. The above values are consistent with the thickness of the T3 layer ranging from 100 nm to 150 nm. Encapsulation with NOA

88 raised the effective index to 1.592 (442.5 nm laser wavelength of the encapsulated device, corresponding to a 110 nm thick T3 layer) which is higher than the index of the cladding material. Optical confinement is therefore still provided in this configuration.

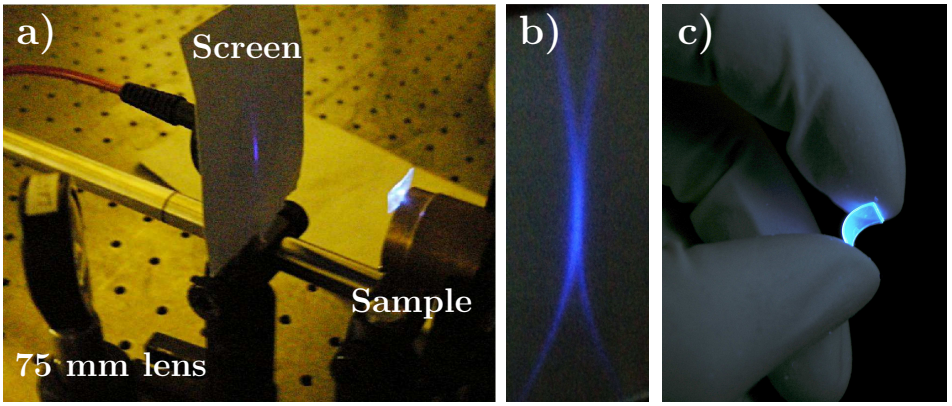

FIGURE 4.6: *a)* Photo of the operating sample, pumped with a focussed pump spot. *b)* Image of the beam profile that is visible on the screen. The spectral maps in figure 4.7 are recorded from left to right across the waist of the fan-shaped beam. *c)* Photography of a laser demonstrating mechanical flexibility. UV illumination is used to show the devices fluorescence.

The spectral maps plotted in figure 4.7a show that the output has a low angular divergence of 1° (17.5 mrad) and is TE polarised, i.e. the electric field is polarised parallel to the grating. This is consistent with the laser operating in the TE_0 mode. In some cases, an unpolarised isotropic ASE background is observed. It is likely that in these cases the ASE originates from regions of poor grating quality that lie within the large area of the unfocussed pump spot. When the pump beam is focussed by a spherical 75-mm lens, we observe that satellite peaks in the spectrum are reduced and the angular beam divergence is improved to (or below) the resolution of our setup of 0.45° (7.8 mrad) as can be seen in figure 4.7b. This effect is probably due to reduced influence of inhomogenities in the sample structure.

4.1.4 Operational Lifetime

A crucial aspect of organic solid-state light emitters is their susceptibility to photo-induced oxidation which ultimately limits the device lifetime. The ASE intensity of an unencapsulated T3 layer that is directly exposed to air follows an exponential decrease with the number of absorbed pump pulses as shown in figure 4.8 for a film of T3 on silica pumped at 0.5 mJ/cm^2. During the $1/e$ lifetime, the sample was exposed to a total pump energy of $F_{deg} = 7$ J/cm^2. This is substantially better than the result by Xia *et al.* [27] on pyrene-cored oligomers which is $F_{deg} = 176$ mJ/cm^2 within the time during which the laser output decreased to half the initial value.

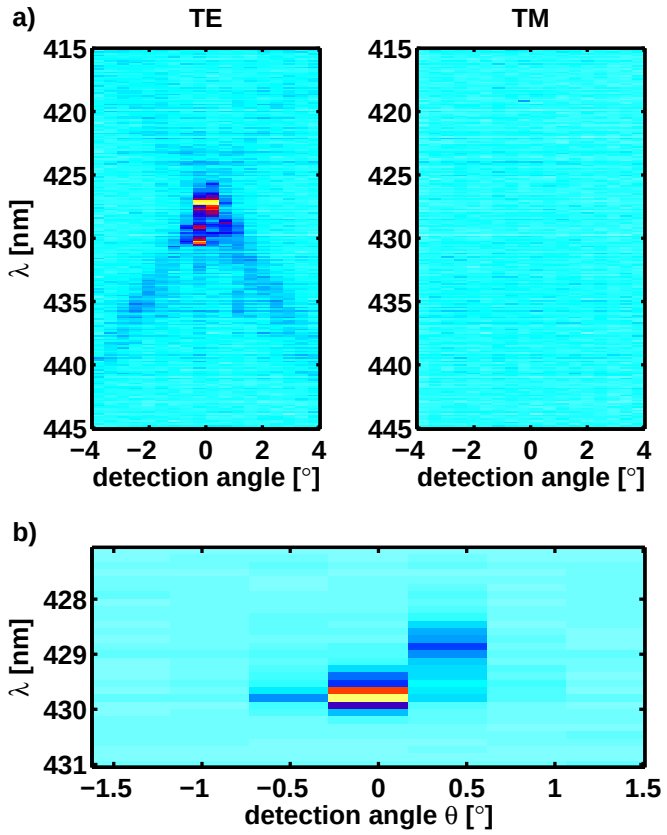

FIGURE 4.7: Spectral map across the laser beam. *a)* Pumped with the unfocussed 2.9 mm diameter beam at 4× threshold. A polariser has been used to distinguish the electrical field components polarised parallel (TE) and perpendicular (TM) to the grating. *b)* The same sample pumped with a focussed pump spot (≤ 0.0014 cm^2) at 5.5× threshold. Only a TE polarised signal has been detected.

Possible figures of merit for the characterisation and comparison of laser operational lifetimes are the already-introduced degradation energy dosage, F_{deg}, that the sample has been exposed to during its lifetime and the ratio of this degradation dosage to the threshold pump fluence F_{deg}/F_{th}. In case of the pyrenes this value is $F_{deg}/F_{th} = 6.4 \times 10^5 - 1.1 \times 10^6$. To our knowledge, only two flexible laser reports include measurements of the lifetime: for Alq_3:DCM based lasers $F_{deg} = 1.6 - 16$ J/cm^2 and $F_{deg}/F_{th} = 10^5 - 10^6$ were found [5], although it was not specified how the lifetime was determined, and a recent experiment on Coumarin540-doped NOA88 [6] revealed a degradation energy dosage of only $F_{deg} = 0.8$ J/cm^2 at $F_{deg}/F_{th} = 1.14 \times 10^3$, where the lifetime was defined as the time during which the laser output decayed to 10% of its initial value. The best performance for non-flexible devices so far has been reported by Richardson *et al.* [8] where the MEH-PPV laser structure was sandwiched between two glass plates that were glued together by NOA68. Within the lifetime during which the laser output dropped to half the initial intensity, a degradation energy dosage of 1.27 MJ/cm^2 was achieved with a high threshold of 8 mJ/cm^2 and thus $F_{deg}/F_{th} = 1.6 \times 10^8$.

4.1.4.1 Lifetime of truxene lasers

Unencapsulated lasers had a $1/e$ degradation dosage of 11.5 ± 5.8 J/cm^2 ($F_{deg}/F_{th} = (8.0 \pm 4.0) \times 10^5$) which is slightly higher than that of T3 on silica. The large variance is possibly related to partial incorporation of the T3 molecules into the CHDV matrix. A sample encapsulated by drop-coated optical adhesive yielded $F_{deg} = 53$ J/cm^2 and $F_{deg}/F_{th} = 8.4 \times 10^5$. This indicates that encapsulation by optical adhesives can indeed enhance device lifetime. The lifetime measurements that yielded these results are plotted in figure 4.8 for comparison. The pump fluence was kept constant at 0.5 mJ/cm^2 per pulse for all samples, though investigations by Richardson *et al.* [7, 8] on MEH-PPV suggest that the degradation dosage remains the same for various pump levels. Remarkably, there is an initial phase where the laser output is stable and at some point the intensity suddenly starts to drop exponentially. The reason for this behaviour is currently under investigation. During the degradation process, a redshift of the laser emission wavelength by about 1.5 nm is observed. A degradation-induced wavelength shift of DFB laser emission has been reported before for MEH-PPV based devices [8] and was attributed to a change in refractive index of the active layer, though in that case a blue-shift was observed.

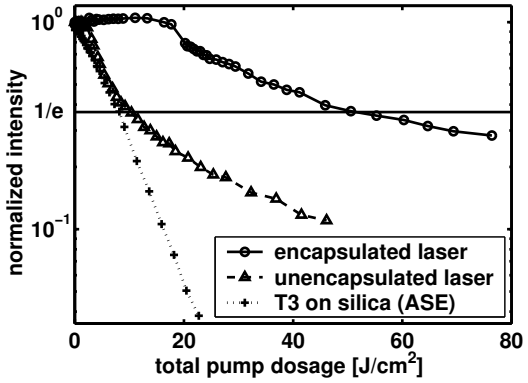

FIGURE 4.8: The operational lifetime of the devices is examined by monitoring the laser intensity as a function of the total pump dosage the samples have been exposed to.

4.1.5 Laser Arrays

The fabrication process described in section 4.1.1 can be altered in order to produce arrays of separated mesas with a grating structure, each of which works as an individual laser. The fabrication process is illustrated in figure 4.9a). In fact, only one additional step is needed here, which is defining the mesa edges on the master grating with a photoresist (PR) mask. Instead of CHDV, NOA65 is used as transparent polymer because it has better flexibility and less issues of sticking to the master grating during the peel-off

process. However, the refractive index contrast to the LEP is poorer ($n_{NOA65} = 1.53$) and it has stronger absorption of UV and violet light than CHDV. Photographic images of the mesas with gratings in the NOA65 film are shown in figure 4.9b). The master grating used here was defined by electron beam lithography, had a period of 276 nm and a modulation depth of 50 nm. T3 was used as gain material for the demonstration of laser operation above a threshold of 70 $\mu J/cm^2$ (14 kW/cm^2) when pumping with a 370 μm diameter pump spot [29]. This approach enables closely spaced but physically separated DFB lasers that can be individually addressed. Furthermore, it allows studies of size- and shape-effects of the mesa on the laser properties.

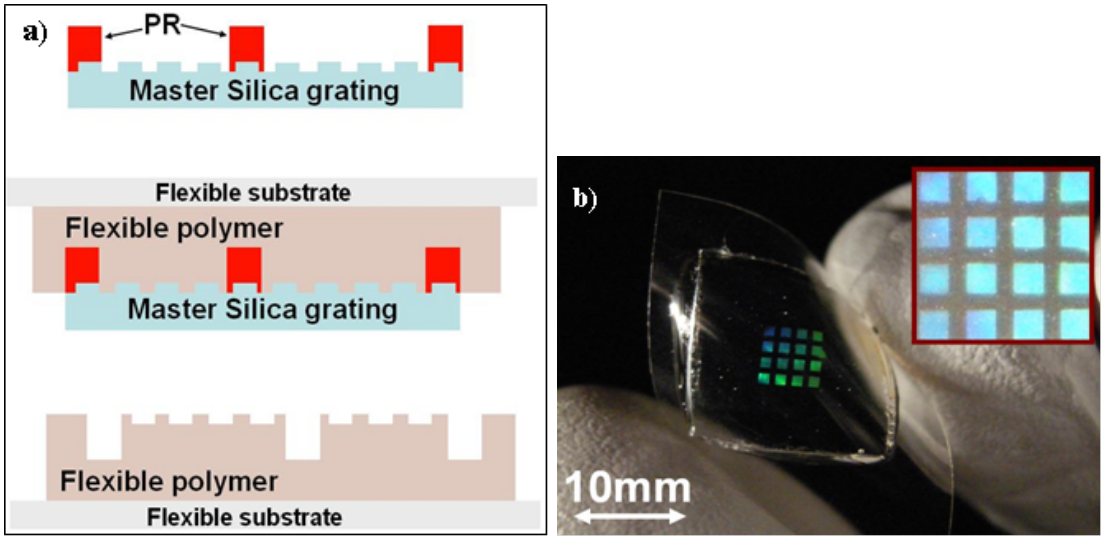

FIGURE 4.9: OSL array: *a)* Schematic of the fabrication of separated DFB mesas. *b)* Photograph of the grating array in a transparent polymer film.

4.2 Green-emitting BBEHP-PPV Lasers

Flexible DFB laser structures have been fabricated by the same method, but with BBEHP-PPV (AK391DCM1) as the gain material. In this case the master grating with 340 nm period and 50 nm modulation depth was created by electron beam lithography. Green laser emission with a wavelength of about 535 nm was observed above a threshold of 11.7 $\mu J/cm^2$ (2.34 kW/cm^2) using the 3×4.5 mm^2 pump spot. A degradation dosage of 1.35 J/cm^2 ($F_{deg}/F_{th} = 1.15 \times 10^5$) was measured when pumping at 47.9 $\mu J/cm^2$ ($4.1 \times F_{th}$).

The photonic crystal properties that these devices show below threshold have been studied as well. Results are discussed in detail in chapter 5.

4.2.1 Pump Polarisation and Geometry

Since the laser emission is linearly polarised, it may be expected that the pump polarisation as well as the pump spot geometry have an impact on the laser threshold. For that purpose, BBEHP-PPV based lasers were excited with a 0.3×3 mm^2 pump stripe and the linearly polarised UV light from the pump frequency-tripled Nd:YAG laser could be rotated by a $\lambda/2$-waveplate. Figure 4.10 illustrates the possible stripe alignment and polarisation.

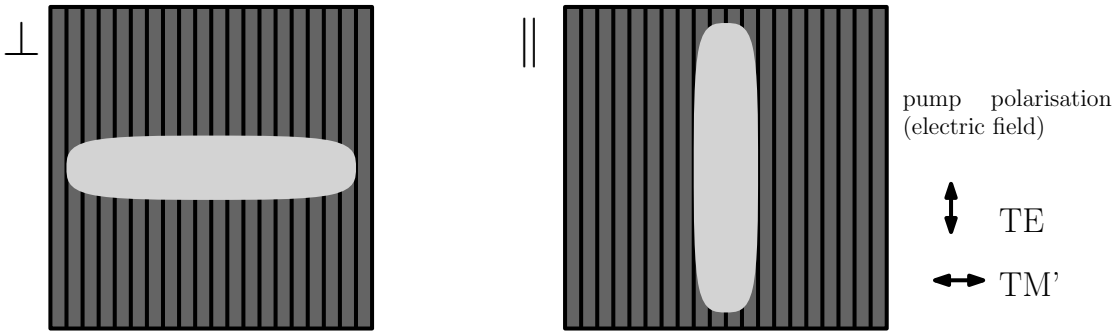

FIGURE 4.10: Schematic illustrating the notation of pump geometry (|| and ⊥) and pump polarisation (TE and TM') when pumping one-dimensional DFB lasers in a stripe geometry.

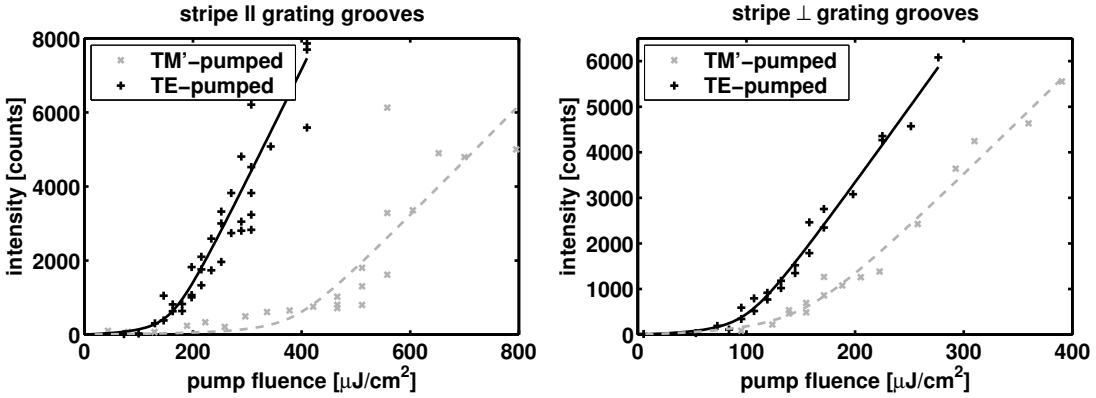

FIGURE 4.11: DFB laser transfer functions using the different pump configurations illustrated in figure 4.10.

Results are shown in figure 4.11. It can generally be seen, that pumping in the ⊥ geometry has a lower threshold than pumping in || direction. This can readily be explained by the fact that the laser mode propagates in ⊥-direction and thus is supplied with gain over a longer propagation length when pumped in ⊥ geometry. Also, gain-guiding may help optical confinement to the laser mode. This latter aspect is supported by the observation that laser thresholds are slightly lower when pumped 0.3 mm broad stripe than when pumped with the 3×4.5 mm^2 pump spot. For example, the BBEHP-PPV laser presented above in section 4.2 that had a threshold of 11.7 $\mu J/\text{cm}^2$ in the latter

geometry, had a lower threshold of 7.9 $\mu J/cm^2$ (1.58 kW/cm^2) when pumped with a stripe.

In terms of pump polarisation, it can be seen from figure 4.11 that both threshold and slope efficiency are superior when the pump is TE-polarised compared to the TM' case. The interpretation is that linearly polarised pump light preferentially excites molecules that are aligned in a certain direction such that their dipole moment is parallel to the pump electric field vector. These molecules will give a stronger contribution to the gain of the laser mode if this dipole moment is also parallel to the laser mode polarisation. This is the case for TE pumping but not for TM' pumping.

4.3 Red-emitting Colloidal Quantum Dot DFB Lasers

Grating patterned flexible substrates fabricated in a similar way as described in section 4.1.1 have been overcoated with a neat colloidal quantum dot (CQD) film by drop-coating, similar to the random laser experiments mentioned in section 3.2.4. The grating period was 740 nm and provided 4^{th} order distributed feedback for the TE-polarised laser emission at wavelengths from 610 nm to 638 nm, depending on the size of the dots used. A typical spectrum and power transfer function are shown in figure 4.12. Several spectral modes are visible, which is probably a result of film non-uniformity. The best performing devices had a laser threshold near 4 mJ/cm^2 (800 kW/cm^2). During the first 10000 pump pulses at 6 mJ/cm^2 degradation was observed and attributed to damage to the ligands, but after this initial performance reduction the laser output remained stable and no further degradation was observed until the measurement was interrupted after 30000 pulses. This gives a lower limit for the degradation dosage of $F_{deg} > 180$ J/cm^2, $F_{deg}/F_{th} > 4.5 \times 10^4$ [30]. Collaborative work on CQD DFB lasers with Nanyang Technological University is undertaken and initial results are given in appendix C.

4.4 Conclusion

The promising category of organic lasers based on monodisperse star-shaped oligofluorenes has been assessed in mechanically flexible and encapsulated format. As a further feature of the work, the distributed feedback structures in these lasers were obtained by soft lithographic templating from a commercially available master grating. It has been shown that the fabrication process can easily be modified so that an array of separated DFB lasers can be produced. Encapsulation increases the $1/e$ degradation energy dosage in ambient from 11.5 J/cm^2 to $F_{deg} = 53$ J/cm^2. Measured relative to the threshold of the encapsulated device, this latter value corresponds to $F_{deg}/F_{th} = 8.4 \times 10^5$.

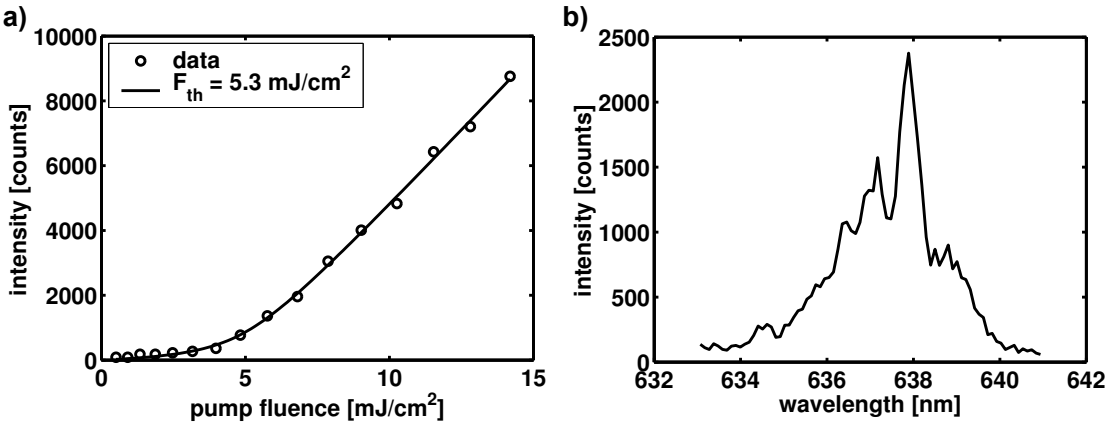

FIGURE 4.12: *a)* Power transfer function and *b)* optical spectrum of a red-emitting DFB laser employing CdSe/ZnS core-shell CQDs as gain medium.

Similar devices based on BBEHP-PPV were examined as well, yielding thresholds of $F_{th} = 11.7\ \mu J/\text{cm}^2$ and degradation characteristics of 1.35 J/cm^2, $F_{deg}/F_{th} = 1.15 \times 10^5$. In this case it was found that stripe-excitation perpendicular to the grating grooves with a TE-polarised pump was beneficial for the power transfer characteristics and in particular the pump threshold of the device.

CQDs were used as well as gain medium for DFB lasers. Despite good photo-stability, they are, at this stage, not as promising candidates for LED-pumped lasers as the organic compounds because of high, 4 mJ/cm^2, thresholds when pumped with 5 ns pulses.

References

[1] I.D.W. Samuel and G.A. Turnbull. Organic Semiconductor Lasers. *Chem. Rev.*, 107:1272–1295, 2007.

[2] Christian Kallinger, Martin Hilmer, Andreas Haugeneder, Martin Perner, Wolfgang Spirkl, Uli Lemmer, Jochen Feldmann, Ullrich Scherf, Klaus Müllen, Andreas Gombert, and Volker Wittwer. A Flexible Conjugated Polymer Laser. *Adv. Mat.*, 10(12):920–923, 1998.

[3] M. Berggren, A. Dodabalapur, R. E. Slusher A. Timko, and O. Nalamasu. Organic solid-state lasers with imprinted gratings on plastic substrates. *Appl. Phys. Lett.*, 72(4):410–411, 1998.

[4] S. Riechel, C. Kallinger, U. Lemmer, J. Feldmann, A. Gombert, V. Wittwer, and U. Scherf. A nearly diffraction limited surface emitting conjugated polymer laser utilizing a two-dimensional photonic band structure. *Appl. Phys. Lett.*, 77(15):2310–2312, 2000.

[5] S. Riechel, U. Lemmer, J. Feldmann, S. Berleb, A. G. Mückl, W. Brütting, A. Gombert, and V. Wittwer. Very compact tunable solid-state laser utilizing a thin-film organic semiconductor. *Opt. Lett.*, 26(9):593–595, 2001.

[6] M. Lu, B.T. Cunningham, S.-J. Park, and J.G. Eden. Vertically emitting, dye-doped polymer laser in the green ($\lambda \sim 536$ nm) with a second order distributed feedback grating fabricated by replica molding. *Opt. Commun.*, 281:3159–3162, 2008.

[7] Scott Richardson. *The Fabrication and Lithography of Conjugated Polymer Distributed Feedback Lasers and Development of their Applications.* PhD thesis, University of St. Andrews, School of Physics and Astronomy, 2007.

[8] S. Richardson, O. P. M. Gaudin, G. A. Turnbull, and I. D. W. Samuel. Improved operational lifetime of semiconducting polymer lasers by encapsulation. *Appl. Phys. Lett.*, 91:261104, 2007.

[9] Dario Pisignano, Luana Persano, Paolo Visconti, Roberto Cingolani, Giuseppe Gigli, Giovanna Barbarella, and Laura Favaretto. Oligomer-based organic distributed feedback lasers by room-temperature nanoimprint lithography. *Appl. Phys. Lett.*, 83(13):2545–2547, 2003.

[10] Justin R. Lawrence, Graham A. Turnbull, and Ifor D. W. Samuel. Polymer laser fabricated by a simple micromolding process. *Appl. Phys. Lett.*, 82(23):4023–4025, 2003.

[11] Musubu Ichikawa, Yuji Tanaka, Naotoshi Suganuma, Toshiki Koyama, and Yoshio Taniguchi. Low-Threshold Photopumped Distributed Feedback Plastic Laser Made by Replica Molding. *Jpn. J. Appl. Phys.*, 42(9A):5590–5593, 2003.

[12] Myoung Hoon Song, Bernard Wenger, and Richard H. Friend. Tuning the wavelength of lasing emission in organic semiconducting laser by the orientation of liquid crystalline conjugated polymer. *J. Appl. Phys.*, 104:033107, 2008.

[13] J. Herrnsdorf, B. Guilhabert, Y. Chen, A. L. Kanibolotsky, A. R. Mackintosh, R. A. Pethrick, P. J. Skabara, E. Gu, N. Laurand, and M. D. Dawson. Flexible blue-emitting encapsulated organic semiconductor DFB laser. *Opt. Express*, 18(25):25535–25545, 2010.

[14] Alexander L. Kanibolotsky, Rory Berridge, Peter J. Skabara, Igor F. Perepichka, Donald D. C. Bradley, and Mattijs Koeberg. Synthesis and Properties of Monodisperse Oligofluorene-Functionalized Truxenes: Highly Fluorescent Star-Shaped Architectures. *J. Am. Chem. Soc.*, 126: 13695–13702, 2004.

[15] Georgios Tsiminis, Yue Wang, Paul E. Shaw, Alexander L. Kanibolotsky, Igor F. Perepichka, Martin D. Dawson, Peter J. Skabara, Graham A. Turnbull, and Ifor D.W. Samuel. Low-threshold organic laser based on an oligofluorene truxene with low optical losses. *Appl. Phys. Lett.*, 94: 243304, 2009.

[16] Yue Wang, Georgios Tsiminis, Ying Yang, Arvydas Ruseckas, Alexander L. Kanibolotsky, Igor F. Perepichka, Peter J. Skabara, Graham A. Turnbull, and Ifor D.W. Samuel. Broadly tunable deep blue laser based on a star-shaped oligofluorene truxene. *Synth. Met.*, 160:1397–1400, 2010.

[17] Benoit Guilhabert, Nicolas Laurand, Johannes Herrnsdorf, Yujie Chen, Allan R. Mackintosh, Alexander L. Kanibolotsky, Erdan Gu, Peter J. Skabara, R. A. Pethrick, and Martin D. Dawson. Amplified spontaneous emission in free-standing membranes incorporating star-shaped monodisperse π-conjugated truxene oligomers. *J. Opt.*, 12:035503, 2010.

[18] Alexander J. C. Kuehne, David Elfström, Allan R. Mackintosh, Alexander L. Kanibolotsky, Benoit Guilhabert, Erdan Gu, Igor F. Perepichka, Peter J. Skabara, Martin D. Dawson, and Richard A. Pethrick. Direct Laser Writing of Nanosized Oligofluorene Truxenes in UV-Transparent Photoresist Microstructures. *Adv. Mat.*, 21:781–785, 2009.

[19] G.M. Stéphan. Semiclassical study of the laser transition. *Phys. Rev. A*, 55(2):1371–1384, 1997.

[20] Y. Boucher, A.G. Deryagin, V.I. Kuchinskii, and G.S. Sokolovskii. Near-threshold spectral and modal characteristics of a curved-grating quantum-well distributed-feedback laser. *Nanotechnology*, 14:615–618, 2003.

[21] Y.G. Boucher and P. Féron. Generalized transfer function: A simple model applied to active single-mode microring resonators. *Opt. Commun.*, 282:3940–3947, 2009.

[22] G.J. Pert. Output characteristics of amplified-stimulated-emission lasers. *J. Opt. Soc. Am. B*, 11 (8):1425–1435, 1994.

[23] L. Dal Negro, P. Bettotti, M. Cazzanelli, D. Pacifici, and L. Pavesi. Applicability conditions and experimental analysis of the variable stripe length method for gain measurements. *Opt. Commun.*, 229:337–348, 2004.

[24] A. Costela, O. García, L. Cerdán, I. García-Moreno, and R. Sastre. Amplified spontaneous emission and optical gain measurements from pyrromethene 567 - doped polymer waveguides and quasi-waveguides. *Opt. Express*, 16(10):7023–7036, 2008.

[25] A. Costela, O. García, L. Cerdán, I. García-Moreno, and R. Sastre. Amplified spontaneous emission and optical gain measurements from pyrromethene 567 - doped polymer waveguides and quasi-waveguides: erratum. *Opt. Express*, 16(10):7587, 2008.

[26] *Matlab Documentation*. The Mathworks. Available online at http://www.mathworks.com/.

[27] Ruidong Xia, Wen-Yong Lai, Peter A. Levermore, Wei Huang, and Donal D. C. Bradley. Low-Threshold Distributed-Feedback Lasers Based on Pyrene-Cored Starburst Molecules with 1,3,6,8-Attached Oligo(9,9-Dialkylfluorene) Arms. *Adv. Funct. Mat.*, 19:2844–2850, 2009.

[28] G. A. Turnbull, P. Andrew, M. J. Jory, W. L. Barnes, and I. D. W. Samuel. Relationship between photonic band structure and emission characteristics of a polymer distributed feedback laser. *Phys. Rev. B*, 64:125122, 2001.

[29] B. Guilhabert, N. Laurand, J. Herrnsdorf, Y. Chen, A. L. Kanibolotsky, C. Orofino, P. J. Skabara, and M. D. Dawson. Mechanically Flexible Organic Semiconductor Laser Array. *IEEE Photon. J.*, 4(3):684–690, 2012.

[30] Yujie Chen, Benoit Guilhabert, Johannes Herrnsdorf, Yanfeng Zhang, Allan R. Mackintosh, Richard A. Pethrick, Erdan Gu, Nicolas Laurand, and Martin D. Dawson. Flexible distributed-feedback colloidal quantum dot laser. *Appl. Phys. Lett.*, 99:241103, 2011.

Chapter 5

Hybrid Organic/Inorganic Photonic Crystal LED

One of the many recent advances in light-emitting diode (LED) technology is the development of photonic crystal (PhC) LEDs [1]. In these devices, the active layer interacts with a periodic refractive index pattern whose photonic bandstructure modifies the emission properties [1]. Most of the PhC LED research to date is dedicated to enhancement of the light extraction efficiency in monolithic structures, usually involving hard materials such as III-V semiconductors, including GaN-based alloys. It is important to note, however, that PhCs allow control of the spatial, spectral and polarisation properties of the emission. For example, in the case of GaN PhC LEDs, confinement of the emission to a narrow beam [2] and polarised output [3] have been reported. Directional, spectrally narrow and/or polarised emission is beneficial for some applications, e.g. visible light communications (VLC), or sources for imaging or spectroscopy. In the case of VLC for example, highly directional green light is optimal for coupling into polymer optical fibres (POF) [4, 5]. Typically, the PhC is created by etching the PhC pattern into the LED structure. The etch mask can be defined by electron-beam lithography, nanoimprint lithography, two-beam interference or self-assembly [1]. Modification of emission by PhCs has also been observed in organic films [6], as well as colloidal quantum dot (CQD) doped films [7], and organic PhC LEDs have been demonstrated [8, 9]. Enhanced colour conversion efficiency has been reported for a GaN PhC LED where the etch-holes of the PhC structure were filled with CQDs [10].

Here, we take the above investigations further, by reporting hybrid GaN/organic polymer LEDs where the PhC is not etched into the inorganic part of the device but implemented in a light-emitting polymer overlayer. These hybrid devices permit soft lithographic methods to be utilised in defining the PhC structure, thus simplifying and de-coupling

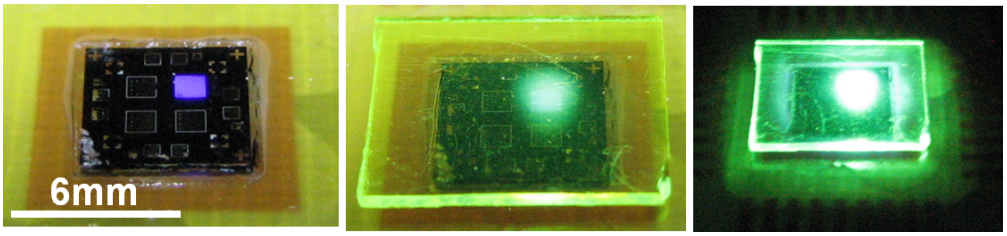

FIGURE 5.1: Photographic images of the device. *Left:* bare 405 nm LED, *middle and right:* with organic PhC overlayer.

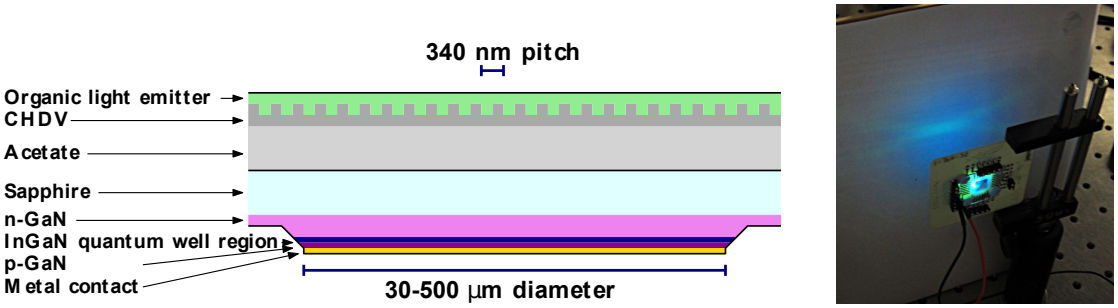

FIGURE 5.2: *Left:* Schematic of the device structure. *Right:* Photographic image of a PhC LED in front of a white screen on which fan-shaped emission is visible.

the LED and PhC fabrication processes. Importantly, however, they also permit efficient colour-conversion of high performance blue LED emission into the so-called "green (spectral) gap" (c.f. figure 1.1), facilitate control of the emission pattern and polarisation and retain the fast modulation characteristics [11] suitable for such applications as VLC. This latter aspect exploits the short radiative lifetimes of light emitting polymers, typically on the order of 1 ns, which is 5-10× shorter than CQDs and several orders of magnitude shorter than phosphorescent emitters often used for organic LEDs and conventional colour converters. Electrically driven organic devices additionally suffer from low carrier mobilities [12] and therefore the hybrid approach may be favourable for any application that requires fast modulation or switching.

The hybrid PhC LED work reported here has been published in Applied Physics Letters [13].

5.1 Device Fabrication

As organic colour-converter we use BBEHP-PPV, which absorbs light efficiently with wavelengths below 470 nm and is therefore suitable for integration onto highly efficient blue-emitting GaN LEDs. Details of this material are described above in section 3.1.2. A particular benefit of this material regarding the suitability for VLC is its short, 0.62 ns, radiative lifetime [14] which is key for fast data transmission (see also section

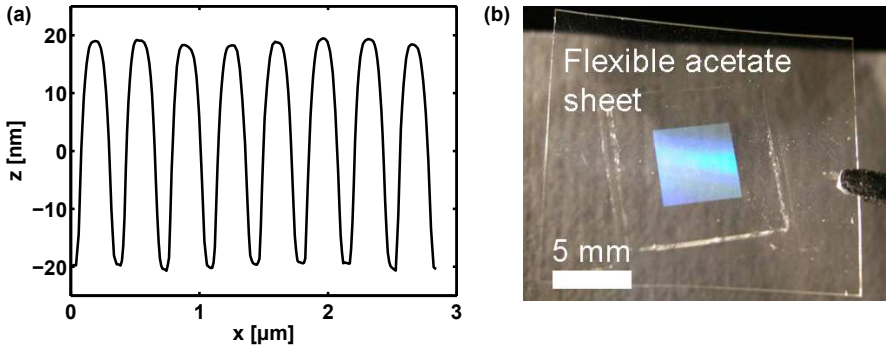

FIGURE 5.3: *a)* AFM of the imprinted grating in CHDV. *b)* Photographic image of the imprinted grating. The grating area is visible due to diffration of the room light.

3.1.2.1). The active material is spin-coated from a 20 mg/ml solution in toluene at 1500–2750 RPM onto a structured film of CHDV on a flexible acetate substrate. The PhC structure in the CHDV film was created by a simple soft-lithography method that has been described in the previous chapter, section 4.1.1. As master for the soft-lithography step we use a one-dimensional grating in silica with a pitch of 340 nm and 50 nm modulation depth which was defined by electron-beam lithography. The result is a second-order grating for the green BBEHP-PPV emission, meaning that Bragg scattering of the first order will couple light out vertically while Bragg scattering of second order will cause an in-plane photonic stop-band (see figure 2.14 for illustration). The organic film was then mechanically contacted onto the polished upper sapphire window of flip-chip GaN LEDs emitting at 405 nm or 450 nm with diameters in the range $30 - 500\ \mu m$ (see [11] for VLC characteristics). A schematic of the whole device is given in figure 5.2, which shows the layout of the multi-layer structure. Photographic images of hybrid PhC LEDs are shown in figure 5.1. Note that after overcoating with BBEHP-PPV the grating is not visible by eye or in photographic images. Before the overcoating step, the grating area can be recognized by diffraction of the room light as can be seen in figure 5.3b. Good quality of the imprinted gratings in the CHDV film was confirmed by atomic force microscopy (AFM). An example of an AFM scan of the grating in the CHDV film is shown in figure 5.3 alongside a photographic image showing a high quality grating with an area of 5 mm × 5 mm.

5.2 Characterisation

5.2.1 Photonic Crystal Effect

Spectra were recorded with an optical fibre (50 μm core diameter) connected to a CCD-spectrometer. The fibre tip could be placed at well-defined angles with respect to the

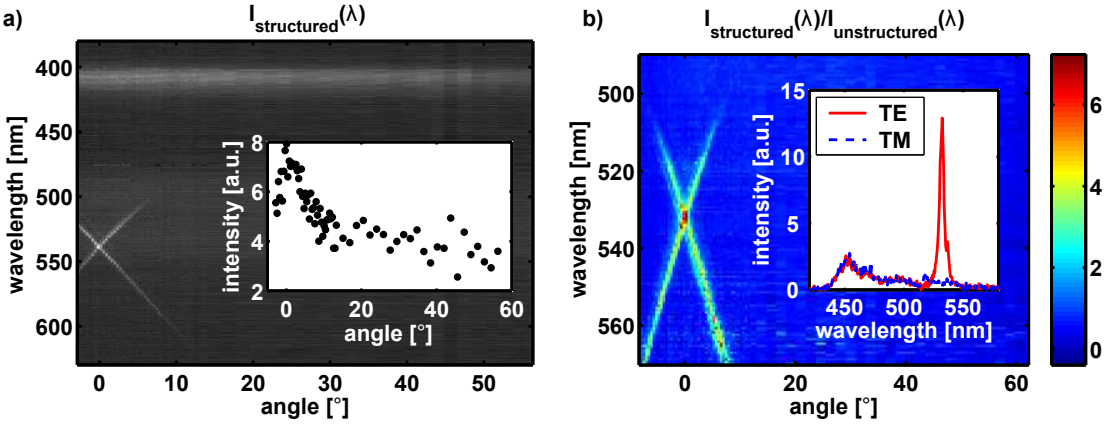

FIGURE 5.4: *a)* Angle resolved spectral intensity map of a device based on a GaN micro-LED emitting at 405 nm. In the inset, the profile of the overall of colour-converted (wavelength >490 nm) emission intensity is plotted. *b)* Map of the wavelength- and angle- dependent enhancement of the converted light from a device based on a micro-LED emitting at 450 nm. The inset demonstrates TE polarisation of the emission from this device.

sample surface, thus allowing one to map out the angular dependence of the emission spectrum. Figure 5.4a shows the angle resolved spectral intensity of such a PhC LED. The PhC effect yields a prominent X-shaped feature in this plot. This PhC-enhanced emission gives rise to directional colour-converted emission with a divergence of only 7° in air, appearing as a fan-shaped beam when screening the emission pattern. In figure 5.4b, the emission intensity enhancement is plotted. This enhancement is defined as the ratio of the spectral intensity from a device with patterned film compared to an identical one without a PhC pattern. In the direction vertical to the sample surface a 7× enhancement of the emission at 535 nm was found. Furthermore, the PhC coupled emission is TE-polarised, i.e. the electric field is aligned parallel to the grating.

5.2.2 Conversion Efficiency

The overall conversion efficiency (ratio of colour-converted light intensity to bare GaN LED intensity) was measured with an integrating sphere in 2π-configuration (see section 6.2.2.2) and results are shown in figure 5.5a. A value of about 20 % was achieved which is similar to the one reported for a CQD based device relying on non-radiative energy transfer [10]. For an unpatterned but otherwise identical film, the conversion efficiency was 15 %, proving a clear enhancement of the conversion efficiency due to the PhC pattern confirming earlier reports [6]. Similar enhancement of polymer emission was also seen when butt-coupling into POF. Polymer spectra from a device based on a 405 nm LED butt-coupled to PMMA fibre (1 mm core diameter) are shown in figure 5.6a and the enhancement is clearly visible. At a drive current of 10 mA, the transmitted polymer

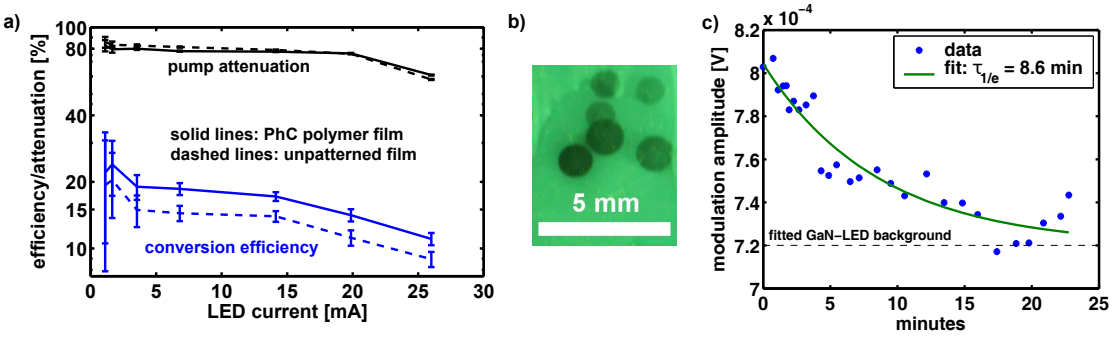

FIGURE 5.5: *a)* Conversion efficiency and pump attenuation of patterned and unpatterned films integrated onto a 500×500 μm^2 LED emitting at 405 nm. *b)* Photographic image of a polymer film under UV illumination showing bleached spots that were exposed to intense LED light. *c)* Temporal decrease of the modulation amplitude of a hybrid device due to photo-degradation. Here, the organic film was in contact with the sapphire window of a 34 μm diameter pixel modulated at 200 Mb/s at an average current of 10 mA.

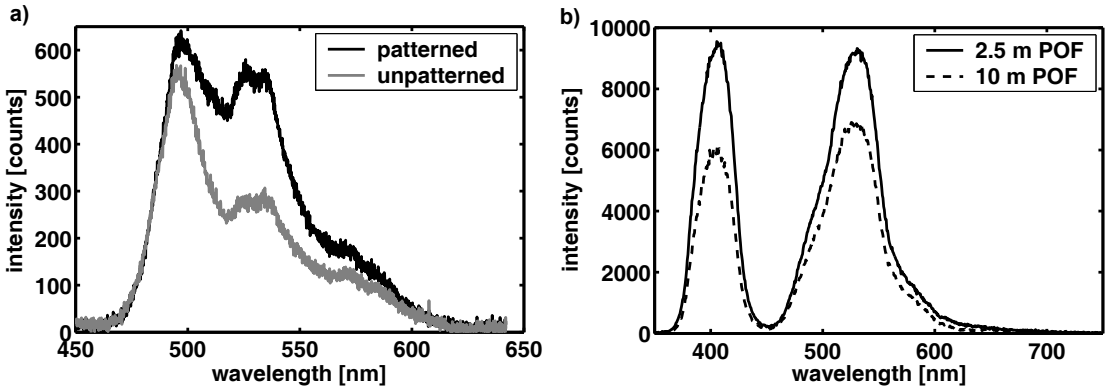

FIGURE 5.6: *a)* Spectra (0.4 nm resolution) of polymer emission from patterned and unpatterned films transmitted through 10 m of PMMA step-index fibre. The fibre was in direct contact with the organic film. *b)* Spectra (20 nm resolution) of PhC LED emission transmitted through PMMA fibres of different length. There was a separation of 2.2 cm between the fibre tip and organic film.

emission power was 4 μW. If comparing LED and LEP emission intensities transmitted through POF of different length (figure 5.6b) there is a general trend that the 405 nm LED emission is attenuated more strongly than the 530 nm LEP emission. This is due to the LEP emission being at the attenuation minimum of PMMA fibre. However, for fibre lengths ranging from 1–10 m the effect was not sufficiently pronounced to clearly distinguish it from coupling effects at the fibre ends.

Photobleaching occured during the measurement and the drop in conversion efficiency above 15 mA may be an effect of photodegradation rather than chromophore saturation. Using a device based on a 450 nm LED, the polymer emission degraded with a half time of 6 min at a 10 mA current (data shown in figure 5.5c) leading to bleached spots

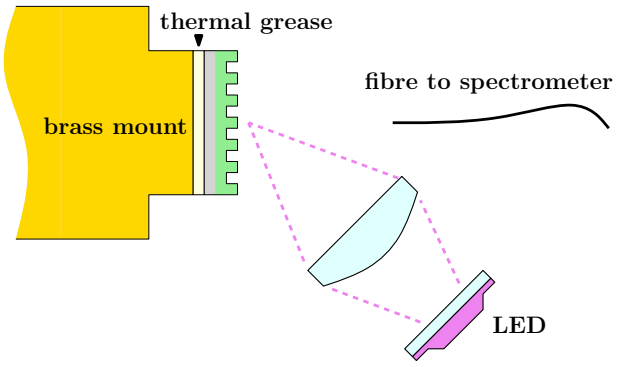

FIGURE 5.7: Schematic of the setup for measurement of temperature effects on the PhC emission

on the organic film as shown in figure 5.5b. It should be possible to employ similar encapsulation as developed for organic LEDs to overcome this issue.

5.2.3 Temperature Stability

Temperature effects on the PhC-coupled organic emission were studied, by attaching organic films with thermal grease to a temperature-controlled brass mount. The organic film was excited by LED light that was focussed by a lens and the vertical emission spectrum was monitored with an optical fibre as illustrated in figure 5.7. Figure 5.8a shows that the grating coupled emission peak blue-shifts reversibly at a rate of 0.15 nm/K. This means that the effect of grating period increase by thermal expansion is overridden by a reduction of the in-plane effective refractive index. Assuming that thermal expansion is negligible, we find effective refractive indices of $n_{eff}(15°C) = 1.549$ and $n_{eff}(80°C) = 1.519$. We also observe reversible temperature-induced reduction of the pump absorption and overall polymer emission intensity which is in agreement with earlier reports [15–17] and is probably due to reduction of effective conjugation length [17]. The corresponding data is shown in figure 5.8b. The decrease in emission intensity was measured directly whereas the reduced absorption manifests in an increase of pump light intensity scattered by the thermal grease (i.e. this light passed through the sample without being absorbed). Furthermore, both intensities returned to their orginal values after cooling down, showing that the effect is indeed reversible. Blue-shift and reduction of absorption will cause a decrease of the refractive index of the active material at the design wavelength which leads to the observed shift of the PhC stop-band.

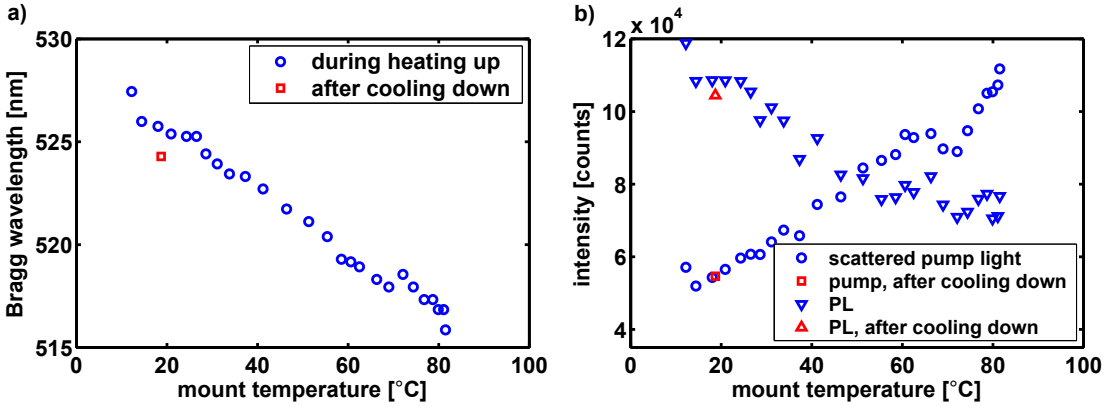

FIGURE 5.8: *a)* Temperature dependence of the photonic stopband wavelength of the PhC. *b)* Intensities of the LED pump light (430-470 nm) scattered by the thermal grease underneath the organic substrate and the organic photoluminescence (530-600 nm) as a function of temperature. The wavelength boundaries were chosen to avoid effects of spectral overlap.

5.2.3.1 Temperature Dependence of the Refractive Index

The refractive index of conjugated polymers at their emission wavelength is strongly influenced by the dominant 0-0 absorption peak, which in case of BBEHP-PPV is located at 430 nm. To get a simplified picture, we model this peak as a Lorentzian resonance in the complex susceptibility, $\chi = \chi' + i\chi''$:

$$\chi''(\omega, T) = -\frac{A(T)}{(\omega - \omega_0(T))^2 + (\Delta(T)/2)^2}$$

Note that the strength A of the transition, its centre frequency ω_0 and its linewidth Δ will depend on the temperature T. We will ignore the temperature dependence of the linewidth $\Delta(T) \equiv \Delta$. Due to the Kramers-Kronig relations, the real part of the susceptibility is:

$$\chi'(\omega, T) = -2\frac{\omega - \omega_0(T)}{\Delta} \cdot \frac{A(T)}{(\omega - \omega_0(T))^2 + (\Delta/2)^2}$$

As a consequence, the refractive index will have a maximum at a slightly longer wavelength than the resonance and then drop back at a rate of $1/(\omega - \omega_0)$. Due to the large Stokes shift in organic semiconductors they emit at a wavelength where the refractive index is already dropping with increasing wavelength. Above in figure 5.8b and in references [15–17] it is shown that:

$$\begin{aligned} T_2 > T_1 \quad \Rightarrow \quad & A(T_2) < A(T_1) \\ & \omega_0(T_2) > \omega_0(T_1) \end{aligned}$$

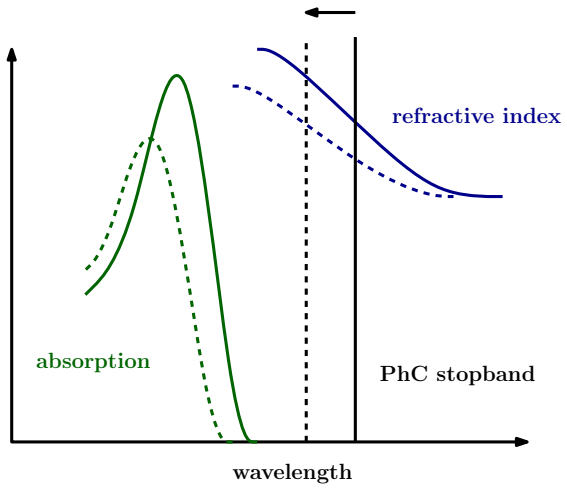

FIGURE 5.9: Illustration of temperature effects on the absorption and refractive index of organic semiconductors, causing a blue-shift of the PhC stop-band of a grating with fixed period. Solid lines represent a temperature T_1 and dashed lines a higher temperature $T_2 > T_1$.

For the refractive index at a given PhC stopband frequency, ω_{PhC}, this has two consequences:

1. The magnitude of both, χ' and χ'' at temperature T_2 is lower than at temperature T_1
2. The refractive index drops as $\frac{1}{\omega_{PhC}-\omega_0(T_2)}$, and note that in particular we have $\frac{1}{\omega_{PhC,fixed}-\omega_0(T_2)} < \frac{1}{\omega_{PhC,fixed}-\omega_0(T_1)}$

Both mean that at a fixed frequency, $\omega_{PhC,fixed}$, the refractive index is $n(\omega_{PhC,fixed}, T_2) < n(\omega_{PhC,fixed}, T_1)$. Therefore, the PhC stopband is forced to blue-shift, $\omega_{PhC}(T_2) > \omega_{PhC}(T_1)$. This is schematically illustrated in figure 5.9.

For analysis of the effective refractive index, we model the system as a slab waveguide where the effective refractive index is given by:

$$n_{eff} = n_{core} \cos\theta$$

For the TE_0 waveguided mode, the angle θ is found by solving:

$$\begin{aligned} \tan\left(\frac{4\pi d n_{core}}{\lambda_0}\sin\theta\right) &= \frac{\tan\phi_1 + \tan\phi_2}{1 - \tan\phi_1 \tan\phi_2} \\ \tan\phi_1 &= \sqrt{\frac{1 - n_{sub}^2/n_{core}^2}{\sin^2\theta} - 1} \\ \tan\phi_2 &= \sqrt{\frac{1 - n_{sup}^2/n_{core}^2}{\sin^2\theta} - 1} \end{aligned}$$

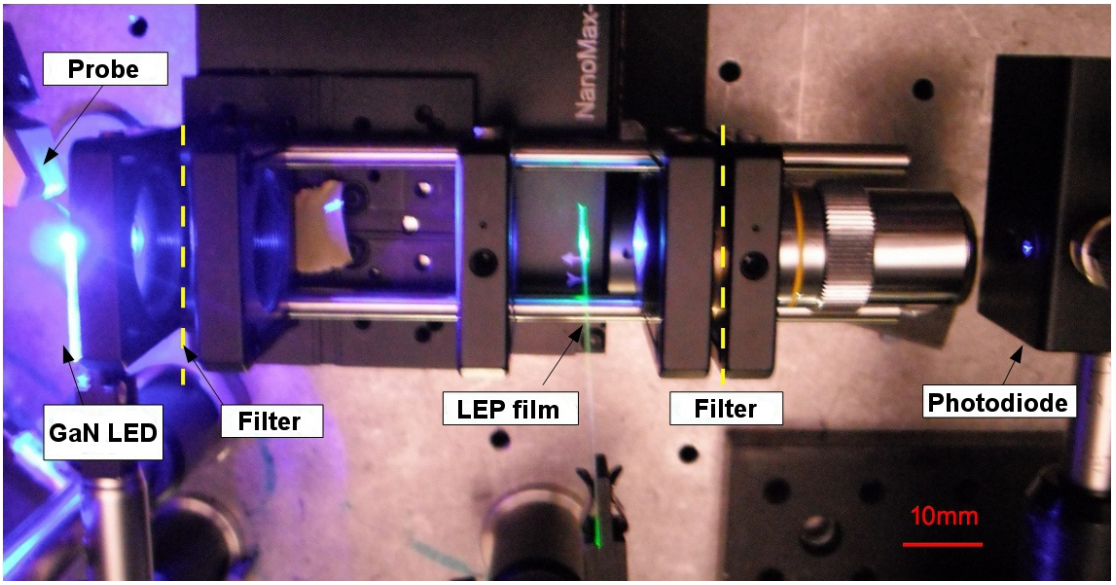

FIGURE 5.10: Photographic plan view image of the setup used for modulation bandwidth measurements of LED-pumped organics.

where d is the thickness of the active layer, λ_0 is the vacuum wavelength and n_{core}, n_{sub}, n_{sup} are the refractive indices of the active film, substrate (CHDV, $n_{sub} = 1.472$ [18]) and superstrate (air, $n_{sup} = 1$). Assuming that at 15°C we have $n_{core}(15°C) = 1.7$ [14], yields an active film thickness of $d = 147$ nm. Assuming a fixed film thickness, the required refractive index at 80°C to get an effective refractive index of $n_{eff}(80°C) = 1.519$ is then $n_{core}(80°C) = 1.584$. This means that the refractive index of BBEHP-PPV changes with temperature at a rate of -1.8×10^{-3} K^{-1}.

5.2.4 Suitability for Data Transmission

The frequency response of the LED-pumped PhC was measured by a network analyser whose output was used to modulate the LED current via a bias-tee. The network analyser's input was connected to a fast photodiode [11] that picked up the colour-converted optical signal. A short-pass filter in between LED and organic structure was used to remove any green emission of the LED. Furthermore a long-pass filter in between PhC and detector was used to ensure that only the polymer emission was detected. An image of the setup is shown in figure 5.10. At an LED current of 1.26 kA/cm^2 (70 mA) an optical -3 dB bandwidth of 168 MHz was measured which compares very well to 155 MHz for green inorganic resonant cavity LEDs [5]. Due to the short radiative lifetime of the polymer, this value is mainly limited by the GaN LED bandwidth which under these conditions is 204 MHz. Bandwidths for several LED currents are plotted in figure 5.11 and the corresponding eye diagrams suggest that data transmission at several hundred Mb/s is feasible. Data transmission demonstrations of unencapsulated

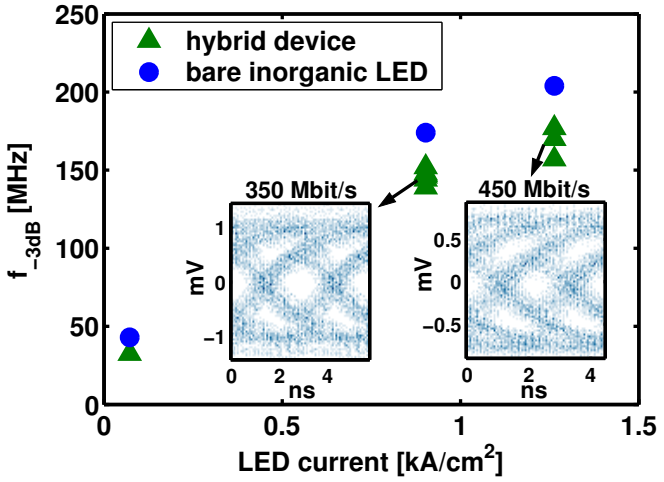

FIGURE 5.11: Optical -3 dB bandwidth of the green emission from LED pumped polymer compared to bare LED at different LED currents. The insets show corresponding eye diagrams at 350 Mb/s, 0.9 kA/cm^2 (50 mA) and 450 Mb/s, 1.26 kA/cm^2 (70 mA), respectively.

devices were not possible due to the short operational lifetime of only several minutes. In the current non-flexible format, efficient encapsulation can be achieved on the basis of inorganic oxygen barriers.

5.3 Conclusion

In summary, we have demonstrated modification of the colour-converted light of a hybrid organic/inorganic LED by a nano-pattern in the organic layer. The devices sustain temperatures up to 80°C without suffering damage and tuning of the emission characteristics by temperature control is possible. This versatile technology could meet a range of demands in terms of wavelength across the visible spectrum, divergence and polarisation of the emission. An application area of particular interest is VLC, for which hybrid organic/inorganic PhC LEDs offer favourable properties such as high modulation bandwidth and directional emission in the green spectral region.

References

[1] Christopher Wiesmann, Krister Bergenek, Norbert Linder, and Ulrich T. Schwarz. Photonic crystal LEDs - designing light extraction. *Laser Photon. Rev.*, 3(3):262–286, 2009.

[2] Chun-Feng Lai, Chia-Hsin Chao, and Wen-Yung Yeh. Optimized Microcavity and Photonic Crystal Parameters of GaN-Based Ultrathin-Film Light-Emitting Diodes for Highly Directional Beam Profiles. *IEEE Photon. Technol. Lett.*, 22(21):1547–1549, 2010.

[3] Elison Matioli, Stuart Brinkley, Kathryn M. Kelchner, Shuji Nakamura, Steven DenBaars, James Speck, and Claude Weisbuch. Polarized light extraction in m-plane GaN light-emitting diodes by embedded photonic-crystals. *Appl. Phys. Lett.*, 98:251112, 2011.

[4] T. Matsuoka, T. Ito, and T. Kaino. First plastic optical fibre transmission experiment using 520nm LEDs with intensity modulation/direct detection. *Electron. Lett.*, 36(22):1836–1837, 2000.

[5] Shih-Yung Huang, Ray-Hua Horng, Jin-Wei Shi, Hao-Chung Kuo, and Dong-Sing Wuu. High-Performance InGaN-Based Green Resonant-Cavity Light-Emitting Diodes for Plastic Optical Fiber Applications. *J. Lightwave Technol.*, 27(18):4084–4090, 2009.

[6] A. N. Safonov, M. Jory, B. J. Matterson, J. M. Lupton, M. G. Salt, J. A. E. Wasey, W.L. Barnes, and I. D. W. Samuel. Modification of polymer light emission by lateral microstructure. *Synth. Met.*, 116:145–148, 2001.

[7] Fuchyi Yang and Brian T. Cunningham. Enhanced quantum dot optical down-conversion using asymmetric 2D photonic crystals. *Opt. Express*, 19(5):3908–3918, 2011.

[8] Yong-Jae Lee, Se-Heon Kim, Joon Huh, Guk-Hyun Kim, Yong-Hee Lee, Sang-Hwan Cho, Yoon-Chang Kim, and Young Rag Do. A high-extraction-efficiency nanopatterned organic light-emitting diode. *Appl. Phys. Lett.*, 82(21):3779–3781, 2003.

[9] Ziyao Wang, Julian Hauss, Christoph Vannahme, Uwe Bog, Sönke Klinkhammer, Dong Zhao, Martina Gerken, Timo Mappes, and Uli Lemmer. Nanograting transfer for light extraction in organic light-emitting devices. *Appl. Phys. Lett.*, 98:143105, 2011.

[10] Soontorn Chanyawadee, Pavlos G. Lagoudakis, Richard T. Harley, Martin D. B. Charlton, Dmitri V. Talapin, Hong Wen Huang, and Chung-Hsiang Lin. Increased Color-Conversion Efficiency in Hybrid Light-Emitting Diodes utilizing Non-Radiative Energy Transfer. *Adv. Mater.*, 22:602–606, 2010.

[11] Jonathan McKendry, Richard P. Green, A. E. Kelly, Zheng Gong, Benoit Guilhabert, David Massoubre, Erdan Gu, and Martin D. Dawson. High-Speed Visible Light Communications Using Individual Pixels in a Micro Light-Emitting Diode Array. *IEEE Photon. Technol. Lett.*, 22(18): 1346–1348, 2010.

[12] Jongwoon Park. Speedup of dynamic response of organic light-emitting diodes. *J. Lightwave Technol.*, 28(19):2873–2880, 2010.

[13] J. Herrnsdorf, B. Guilhabert, J. J. D. McKendry, Z. Gong, David Massoubre, S. Zhang, S. Watson, A. E. Kelly, E. Gu, N. Laurand, and M. D. Dawson. Hybrid organic/GaN photonic crystal light-emitting diode. *Appl. Phys. Lett.*, 101:141122, 2012.

[14] Aimée Rose, Zhengguo Zhu, Conor F. Madigan, Timothy M. Swager, and Vladimir Bulović. Sensitivity gains in chemosensing by lasing action in organic polymers. *Nature*, 434:876–879, 2005.

[15] T. W. Hagler, K. Pakbaz, K. F. Voss, and A. J. Heeger. Enhanced order and electronic delocalization in conjugated polymers oriented by gel processing in polyethylene. *Phys. Rev. B*, 44(16):8652–8666, 1991.

[16] A.K. Sheridan, J.M. Lupton, I.D.W. Samuel, and D.D.C. Bradley. Temperature dependence of the spectral line narrowing and photoluminescence of MEH-PPV. *Synth. Met.*, 111–112:531–534, 2000.

[17] Katsuichi Kanemoto, Ichiro Akai, Mitsuru Sugisaki, Hideki Hashimoto, Tsutomu Karasawa, Nobukazu Negishi, and Yoshio Aso. Temperature effects on quasi-isolated conjugated polymers as revealed by temperature-dependent optical spectra of 16-mer oligothiophene diluted in a sold matrix. *J. Chem. Phys.*, 130:234909, 2009.

[18] J. Herrnsdorf, B. Guilhabert, Y. Chen, A. L. Kanibolotsky, A. R. Mackintosh, R. A. Pethrick, P. J. Skabara, E. Gu, N. Laurand, and M. D. Dawson. Flexible blue-emitting encapsulated organic semiconductor DFB laser. *Opt. Express*, 18(25):25535–25545, 2010.

Chapter 6

Micro-LED Pumped Organic Laser

Organic semiconductors are a highly promising category of gain media for visible wavelength lasers, due to their potential for simple and low cost device fabrication. However, most work to date was based on solid-state or gas lasers as pump sources, which counteracts some of the benefits of organics. Therefore simpler and more compact pump sources have been investigated, as was reviewed in section 2.2.1.5. In particular, gallium nitride based laser diodes (LDs) [1, 2] and light emitting diodes (LEDs) [3, 4] are a promising category of pump sources for organic semiconductor lasers (OSLs) in practical scenarios.

This chapter explores the "early stage" feasibility of micron-scale flip-chip GaN LEDs as pump sources for OSLs. Micro-LEDs in this format allow bump-bonding to sophisticated complementary metal oxide semiconductor (CMOS) control electronics which in turn enable a broad range of functionality such as electronic control of the pump spot shape, or on-chip detection schemes which can enable feedback mechanisms or ultra-compact sensing devices. A more detailed vision of possible applications for CMOS-controlled micro-LEDs is given above in chapter 1.

For OSL pumping, it is important that the pump source can deliver nanosecond pulses (see sections 2.1.5 and 2.2.3) and the main focus of this chapter is on the assessment of micro-LED performance in pulsed operation. Developments made during the course of this work enabled demonstration of micro-LED pumped OSLs which are briefly presented in section 6.3.

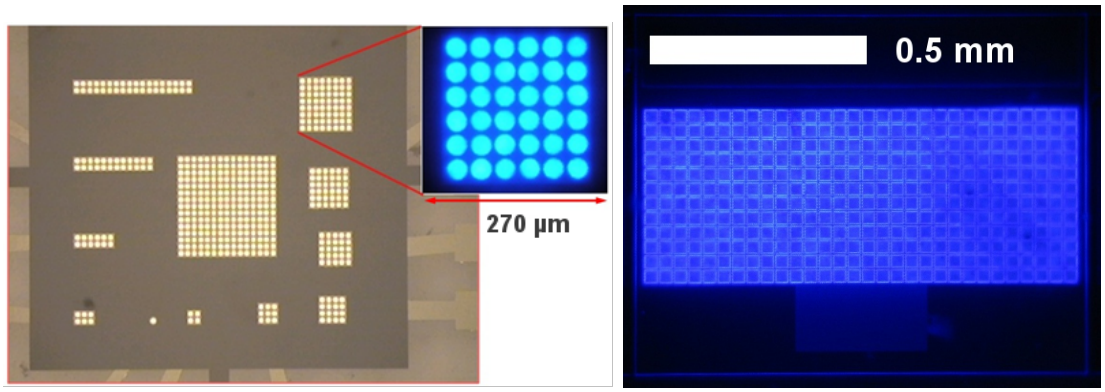

FIGURE 6.1: Plan view micrographs of micro-LED arrays for OSL pumping. *Left:* circular pixels with 30 μm diameter and 35 μm pitch and *right:* square pixels with 30 μm edge length at a 33 μm pitch.

6.1 Micro-LED Arrays for Laser Pumping

Commercially available LEDs are normally fabricated in broad-area format, being roughly square-shaped with the order of 1 mm^2 emissive area. When comparing to the pump spot geometries used for OSLs which were reviewed in section 2.2.1.4, we see that this is in general suitable, though smaller pump spots and stripe geometries were used as well.

Individual micro-LEDs are (by definition) no larger than 100×100 μm^2 and typically smaller than that. This is not only smaller than the preferred pump spot dimensions (see sections 2.2.1.4 and 6.3.1) but as will be shown below in this section there is also a problem of divergence of LED light while propagating through the sapphire window in flip-chip format. Therefore, multiple micro-LEDs have to be arranged in array-format allowing one to shape the pump spot to the desired dimensions. Early devices for this purpose used clusters of circular pixels of 30 μm diameter at a 35 μm pitch. In order to enhance the fill factor from 0.58 to 0.83, later devices used square pixels of 30 μm edge length at 33 μm pitch. In the remainder of this chapter these two formats will be referred to as "circular pixels" and "square pixels", respectively. Pixel size and spacing were chosen to allow reliable fabrication of high-quality devices limited by the precision of mask-alignment during photolithographic fabrication steps. Both geometries are shown in figure 6.1. Normally, the LED chip is glued onto the backside of a drilled hole in a printed circuit board (PCB) and wire bonds from the LED chip to the metal tracks on the PCB allow contacting. A schematic (including optional heat sinking) is shown further below in figure 6.15.

6.1.1 Epitaxial Structure

The micro-LEDs were fabricated from commercially available wafers grown on patterned sapphire substrates (PSS). On the PSS, a ∼3.4 μm thick buffer layer of undoped GaN is grown, followed by 2.6 μm of n-GaN. On top of the n-GaN, an InGaN/GaN multi quantum well structure (typically 11 quantum wells) is grown. The final epitaxial layer is 190 nm of p-GaN. Micro-LED mesas about 1 μm high (with a side-wall angle of about 40°) are created by etching. The p-GaN backplane is then overcoated with a current spreading layer of NiAu alloy. Typical PSS thicknesses are around 350 μm and can be as thick as 430 μm. It is possible to thin the sapphire layer down to 150 μm without having to change the micro-LED fabrication process.

6.1.2 Actual Pump Spot Dimensions

The micro-LED arrays used for OSL pumping were in flip-chip format, i.e. they emit through the sapphire substrate on which the epitaxial structure was grown. Typical PSS thicknesses of 350 μm are considerably larger than the diameter of individual micro-LEDs and therefore the divergence of LED emission upon propagation through the PSS is important. To study this, a Monte-Carlo ray-tracing model was employed, the details of which are described in appendix B. Ab-initio calculations of the full LED structure are computationally expensive, and quantitatively trustworthy results require simple and well-controlled conditions [5, 6]. To obtain reliable results in the complex situation of a micro-LED array, only the propagation through the sapphire was modelled based on three simplifying assumptions:

1. Since the n-GaN and GaN buffer layers are relatively thin, it was assumed that the spatial emission profile at the GaN/sapphire interface is identical to the mesa-profile of the micro-LED array.
2. Each point at the GaN/sapphire interface has the same angular emission profile.
3. Multiple reflections between the sapphire/air and sapphire/GaN surfaces can be neglected. To properly account even for one back-reflection would be very time-consuming owing to the patterned nature of the GaN/sapphire interface.

Below in section 6.2.2.1 it will be shown that the far-field LED emission profile is roughly Lambertian. On the basis of the above assumptions it is possible to recreate from Fresnel equations the angular emission profile within the sapphire for all emission within the acceptance cone. Then, a large number of point emitters at the GaN/sapphire interface are positioned randomly within the emissive area. They all have the same angular

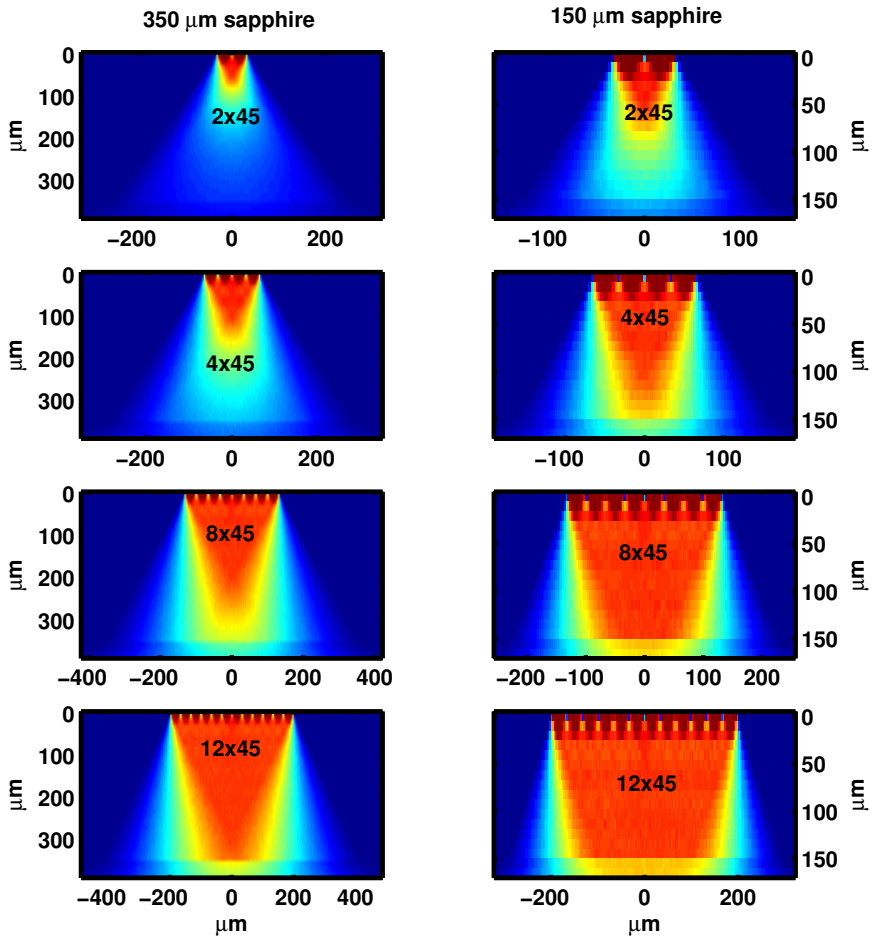

FIGURE 6.2: Calculated intensity of LED light as it diverges while propagating through the sapphire window of flip-chip micro-LED arrays (square pixels). Only emission within the escape cone has been accounted for.

emission profile and the propagation of their emission is traced, yielding the desired spatial emission profile at the sapphire/air surface.

Figure 6.2 shows calculated intensity cross sections through the sapphire along the short axis of micro-LEDs arranged in stripe-format. It is clearly visible how, particularly in the case of thin stripes, the LED emission diverges strongly before reaching the sapphire/air surface. The available pump spots after passing through the sapphire/air interface are plotted in figure 6.3. From both figures it becomes clear that (in the case of square pixels) one needs at least 12 pixel wide stripes to fully mitigate the effects of divergence through 350 μm of sapphire and 8 pixels in the case of 150 μm thick sapphire. A summary of calculated stripe widths is given in table 6.1. Calculated pump spot dimensions in the case of other micro-LED array geometries are included in table 6.2 and further below in table 6.5.

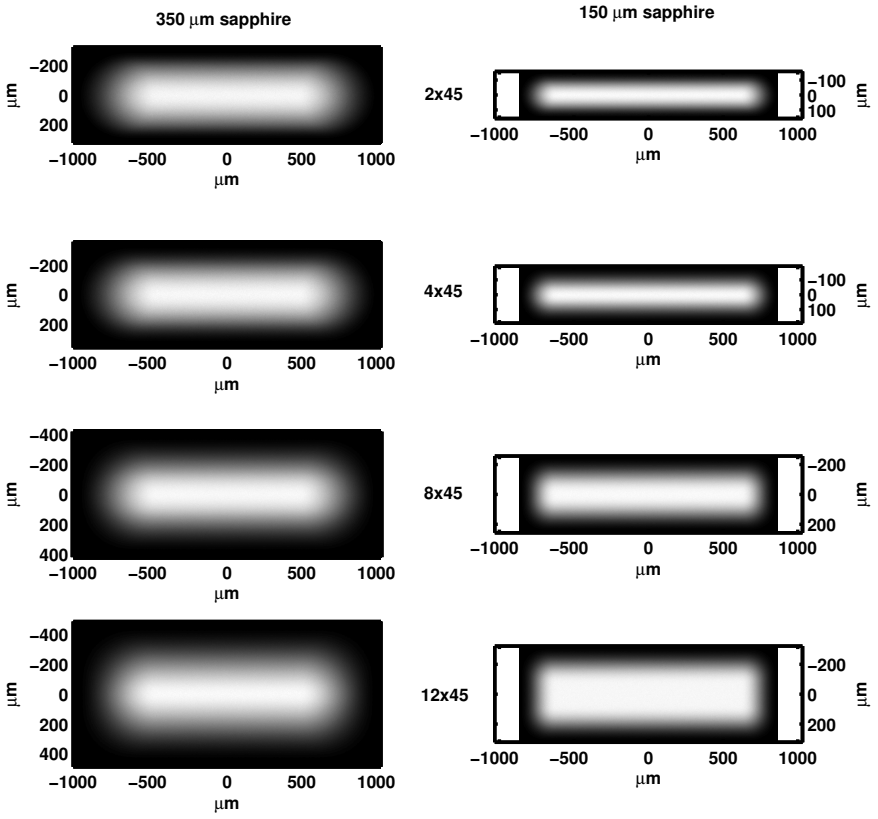

FIGURE 6.3: Calculated intensity profiles at the sapphire surface of stripe-shaped micro-LED clusters (square pixels).

array	stripe width (active region)	sapphire thickness	stripe width (sapphire surface)
	μm	μm	μm
2×n	66	350	350
4×n	132	350	344
8×n	264	350	365
12×n	396	350	420
2×n	66	150	150
4×n	132	150	168
8×n	264	150	267
12×n	396	150	400

TABLE 6.1: Calculated stripe widths of stripe-shaped micro-LED arrays consisting of square pixels.

array	active area	pump spot size	pump spot area
	cm^2	μm	cm^2
8×8	5.8×10^{-4}	367	1.06×10^{-3}
16×16	2.3×10^{-3}	514	2.6×10^{-3}
30×30	8.1×10^{-3}	982	9.6×10^{-3}

TABLE 6.2: Dimensions of square pixel arrays including calculated pump spot area at the sapphire surface assuming a 350 μm thick sapphire substrate.

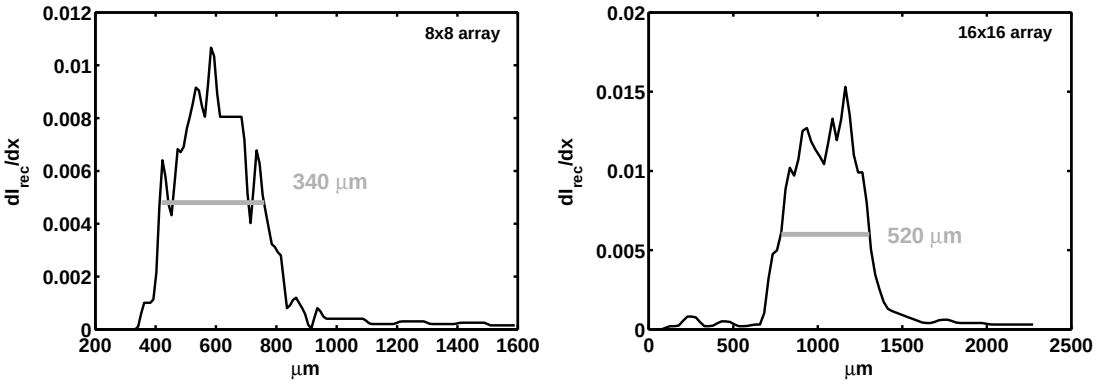

FIGURE 6.4: Derivative of the recorded intensity of knife-edge measurements of the pump spot on the sapphire surface of micro-LEDs with 350 μm thick sapphire. Theoretically predicted pump spot diameters are 367 μm (8×8 array) and 514 μm (16×16 array).

In order to confirm the numerical results, the pump spot width at the sapphire surface was assessed with a knife-edge measurement. For this purpose, a metal step-edge on a glass cover-slide was brought in contact with the sapphire surface and moved across a lit up micro-LED array. The derivative of the recorded intensity I_{rec} then yields the intensity cross section of the pump spot, see also appendix A.3. Results are shown in figure 6.4 and good agreement with the ray-tracing model was found.

6.2 Pulsed Performance of Micro-LEDs

In chapter 2, it was explained how important nanosecond-pulsed excitation is in order to achieve laser action from an organic medium. In this section it is examined how closely these requirements can currently be matched using micro-LEDs.

6.2.1 Pulsed Operation

The results presented in this chapter are obtained by operating the micro-LEDs with a LD driver. A simplified schematic of the LD driver circuit is shown in figure 6.5. As long as the switch (a metal oxide semiconductor field effect transistor, MOSFET) is open and a positive voltage is applied to the high voltage input, a capacitor will be charged through an on-board diode. Upon closing of the switch, this capacitor will discharge through the LED giving rise to a short current pulse. As will be shown below, pulses obtained this way are several 10s of nanoseconds long. Sub-nanosecond pulses were demonstrated by MOSFET-switching of a constant supply voltage [7] but at much lower peak power. Up to now, using an LD driver yielded the highest peak power from LEDs. An optional inductor can be installed in parallel to the LED in order to reduce

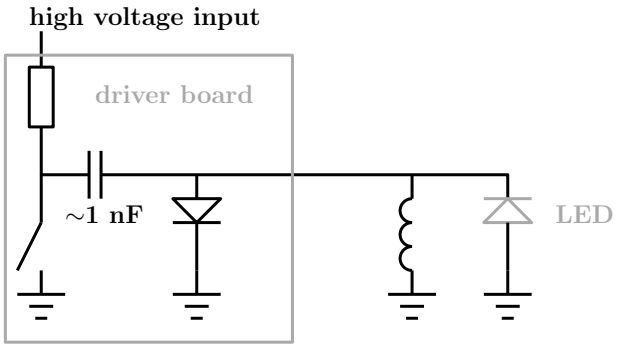

FIGURE 6.5: Schematic of the driver circuit used for pulsed driving of micro-LEDs.

unwanted current oscillations. In this setup, the pulse duration, pulse shape and peak power generally depend on the voltage supplied to the high voltage input, the capacitance that is discharged, the inductance in parallel to the LED, the switching characteristics of the MOSFET, the electrical characteristics of the LED and the external quantum efficiency (EQE) of the LED.

Three drivers, Directed Energy PCO-7110-120-15, PCO-7110-40-4 and PCO-7110-100-7 were used to operate micro-LEDs. The 120-15 driver delivered the highest pulse energies in ∼50 ns optical pulses. The 40-4 driver can deliver 30 ns short pulses, however typically at lower peak intensities than the 120-15 driver. The 100-7 driver is capable of delivering comparable peak intensities as the 120-15 driver in ∼35 ns optical pulses. A typical optical pulse from micro-LEDs obtained using such drivers is shown in figure 6.6. Normally, the pulses are asymmetric with a relatively short rise time and a much longer fall time. According to the gain dynamics modelling in section 2.1.5, these pulses are in a regime where the determining factors for laser threshold condition are the rise time and the peak intensity. Typical rise times are 6–9 ns (40-4 and 100-7 drivers) and 10-15 ns (120-15 driver) and appear to be independent of the peak current density, whereas the fall time tends to increase with increasing current. Optical pulse durations were measured by a photo-multiplier tube (PMT) or a fast photodiode connected to an oscilloscope with 500 MHz bandwidth. Electrical pulses were measured with an oscilloscope current probe.

6.2.2 Measurement of Total Output Power

In contrast to conventional lasers, many light sources and in particular LEDs have a very broad angular spread of emission. Due to this, it is very difficult to record all the emitted light with a powermeter. Methods have to be developed that for a given power detection scheme estimate how the recorded power relates to the total emitted power. In the lighting industry, there are two widely accepted methods for this. These are either

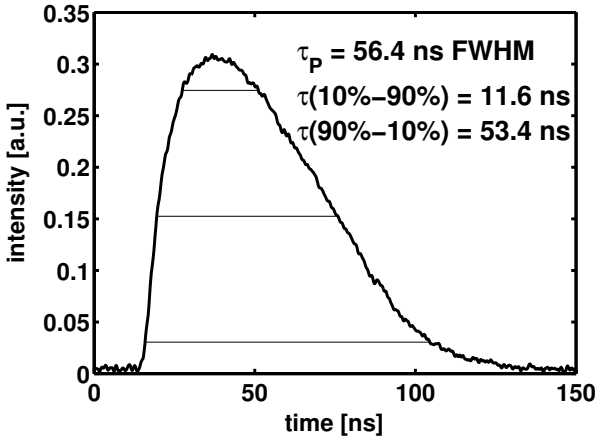

FIGURE 6.6: Typical temporal shape of a micro-LED optical pulse recorded with a PMT when driven by the 120-15 driver.

using a photo-goniometer to determine the angular emission pattern or an integrating sphere which ensures that light emitted at any angle has the same probability of reaching the detector.

6.2.2.1 Photo-Goniometer

Let $I(\theta)$ be the emission pattern of a (micro-) LED where θ is the emission angle with respect to the surface normal. It is assumed that the emission is invariant upon rotation of the sample around the surface normal, i.e. full knowledge of the emission pattern is gained by measuring $I(\theta)$ within a single plane. This hypothesis has been verified for a few of the devices discussed here. For example, the data plotted below in figure 6.9 was taken in two planes orthogonal to each other. For this work a photo-goniometer was available that allowed measuring $I(\theta)$ with a precision of 1°. Examples of micro-LED emission patterns thus recorded are plotted in figure 6.8. In general, emission patterns were reasonably close to a Lambertian emission profile ($I(\theta) \propto \cos(\theta)$) though typically slightly broader. The examples in figure 6.8 represent extreme cases of broad and narrow angular spread of micro-LED emission. It was also verified that the emission patterns in continuous wave (CW, tens of A/cm^2) and pulsed (a few kA/cm^2 peak current density) operation are identical, as is shown in figure 6.9.

The pulsed energy output is measured with a detector that is placed at a distance d from the LED. The detection area has diameter D and typically is situated in a recess of depth r, see figure 6.7 for illustration. Only light within a cone of $\theta \leq \vartheta$ will be detected, where ϑ is given by:

$$\sin(\vartheta) = \frac{D}{\sqrt{D^2 + 4(r+d)^2}} \tag{6.1}$$

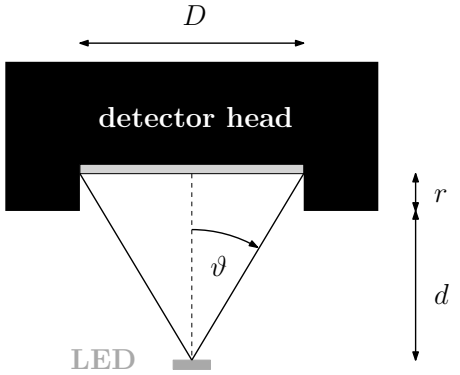

FIGURE 6.7: Illustration of detection geometry.

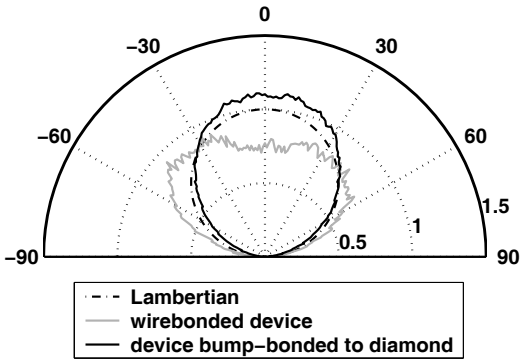

FIGURE 6.8: Polar plots of normalised emission patterns of two LED-arrays in comparison to a Lambertian emission profile. One of the devices was glued to a PCB whereas the other was bump-bonded to a diamond backplane as described in section 6.2.3.1.

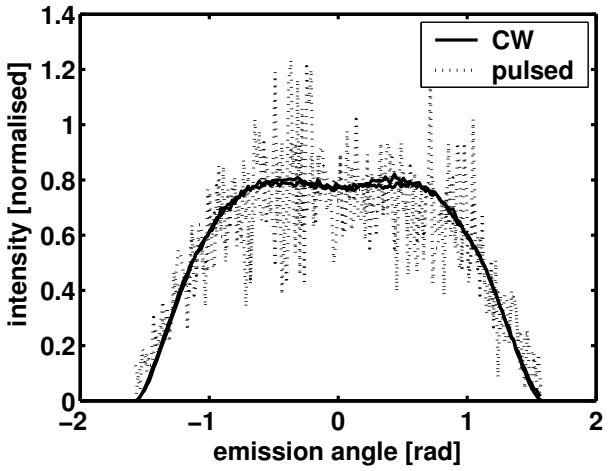

FIGURE 6.9: Comparison of LED emission pattern when operated in CW and pulsed mode.

emission pattern	D [mm]	$r+d$ [mm]	c	c_{exp}
Lambertian	10	3	1.36	
Lambertian	10	5	2	
LED with diamond backplane	10	5	1.8	
Lambertian	10	80	256	
LED with diamond backplane	10	80	220	185
PCB bonded LED	10	80	375	324

TABLE 6.3: Calibration factors calculated from the emission profiles shown in figure 6.8 according to equation (6.3). Experimental values c_{exp} were measured using a powermeter with cosine corrector as described in section 6.2.2.3.

We want to determine the calibration factor c that relates the total emitted pulse energy to the detected pulse energy:

$$E_{LED} =: c \cdot E_{detector} \tag{6.2}$$

This calibration factor is given by:

$$c = \frac{\int_{-\pi/2}^{\pi/2} \mathrm{d}\theta \, |\sin(\theta)| \cdot I(\theta)}{\int_{-\vartheta}^{\vartheta} \mathrm{d}\theta \, |\sin(\theta)| \cdot I(\theta)} \tag{6.3}$$

In the case of a Lambertian profile ($I(\theta) \propto \cos(\theta)$) the integrals can be evaluated analytically:

$$c = 1/\sin^2(\vartheta) = \frac{D^2 + 4(r+d)^2}{D^2} \tag{6.4}$$

For arbitrary (experimental) $I(\theta)$, equation (6.3) has to be evaluated numerically. It was found that due to the $|\sin(\theta)|$ factor in the integral the resolution of 1° was insufficient for simply applying the trapezoidal rule. Good results were achieved by using the Matlab™ `quad` routine and interpolating $I(\theta)$ linearly in between measured points. A short description of Matlab functions that were written for this task is provided in the appendix A.6. Values obtained for typical configurations are listed in table 6.3.

6.2.2.2 Integrating Sphere

An alternative method for total power measurements is to prevent any direct line-of-sight detection of the emitted light, but to force the light to proceed via multiple diffusive reflections towards the detector such that photons emitted at any angle have the same probability of hitting the detector. This is normally achieved by a sphere, the inside of which is coated with a spectrally neutral diffusive layer. The direct line of sight between detector and source is blocked by a baffle which is coated as well. Integrating spheres can be set up either in so called "2π" or "4π" configuration depending on whether all

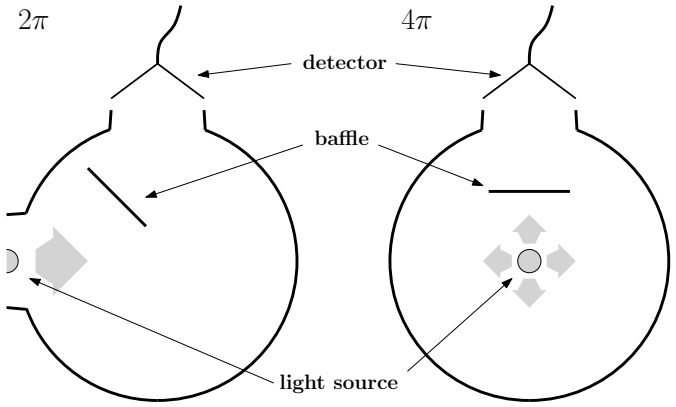

FIGURE 6.10: Illustration of 2π and 4π integrating spheres.

emission or only emission into the top hemisphere is considered. These configurations are illustrated in figure 6.10. Generally, integrating sphere measurements suffer from systematic errors caused by any deviations from the ideal sphere geometry, i.e. in particular due to the baffle, sphere entrances, wiring, the source itself and the detector. These errors are smaller the larger the sphere diameter is in relation to the distortions. For industrial purposes, a minimum sphere diameter of 25 cm is recommended [8]. However, the larger the sphere, the smaller will be the fraction of light that reaches the detector. Hence, there is a trade-off in between accuracy and sensitivity which is in particular important in the case of micro-LEDs.

6.2.2.3 Close-Proximity Measurements

A quick and convenient method of measuring the output power of an LED is to just put the LED in as close proximity to the detector as possible. While this method allows simple and quick comparison between different LEDs, it has to be kept in mind that the absolute values obtained this way cannot be considered to be exact and only allow an order-of-magnitude estimation. Concerns with close-proximity measurements are:

- Reduced detector response at high angle of incidence[1]
- Electrical noise pickup by the detector, in particular in pulsed mode
- Multiple reflections between detector and emitter surface
- Depending on device and detector geometry there may be a non-negligible separation between detector and device

[1] In the case of a silicon-based energy meter a flat response was found for angles of incidence $\leq 40°$ but at higher angles the response dropped significantly.

Some of these effects can be reduced significantly if a cosine corrector is mounted onto the detector. In sections 6.2.3 and 6.3, some pulsed measurements were done by first placing an energy meter at some distance d to the device and measuring pulsed output and then measuring the calibration factor with the aid of a cosine-corrector equipped power meter. With this powermeter the CW emission was measured both, in close proximity and at the same distance as the energy meter. The ratio of the two readings was taken as the calibration factor. Table 6.3 contains calibration factors obtained this way which are slightly lower than those predicted by photogoniometer measurements.

6.2.2.4 Comparison of Different Methods

In general, pulsed performance can either be measured using an energy meter at low repetition rates (tens of Hz) or a powermeter at high repetition rate (several kHz). When keeping all other experimental details (in particular the separation between LED and detector) the same, good agreement of power-meter and energy-meter measurements was observed for the same high voltage input to the LD driver. Also, the various measurement methods discussed above gave reproducible results when the same method was applied repeatedly under the same conditions. Different methods for estimating the overall emission of LEDs were compared on the basis of a commercial LED (Luxeon Rebel) at 450 nm and 1.3×1.3 mm^2 active area, driven by a Directed Energy PCO-7110-120-15 LD driver (no inductor was used), delivering 50 ns optical pulses at 200 V high voltage input and 54 ns at 260 V. The results obtained by various methods are summarised in table 6.4. Unfortunately, no good agreement is observed at all. An immediate conclusion is that (close-proximity) measurements with the detector closer than a few cm from the sample cannot be trusted unless a cosine corrector is used. Even when ignoring close-proximity data, deviations by a factor up to 1.75 are observed, the reason for which could not be determined. It should be pointed out that the integrating sphere available for this work does not meet recommendations by national institutes for standards and close proximity measurements with a cosine corrector are not a recommended method either.

6.2.3 Results

Conventionally, LEDs are driven by a direct current (DC) source and important characteristics of device performance are the electric current as a function of voltage applied to the LED ("I-V curve") and the optical power (or luminance) as a function of injected current ("L-I curve"). Analogously, in pulsed operation the optical pulse energy and peak intensity are measured as a function of the peak electrical current which in

method[1]	$d + r$ [cm]	calibration factor	peak intensity[2] [W/cm^2]	peak intensity[3] [W/cm^2]
PG	0.3	1.32	284	297[4]
CP	0	-	355	371[4]
CE	7.5	155	381	436
CE	0.3	1.9	407	426[4]
IS	-	85[5]	496	564
PG	7.5	239	589	673
CC	7.5	271	668	763
CC[6]	7.5	271	870	960

[1] CC = calibrated by CW close-proximity measurement with cosine corrector
CE = calibrated by pulsed close-proximity measurement without cosine corrector
CP = close-proximity measurement with powermeter at high repetition rate without cosine corrector
IS = integrating sphere with 9 cm diameter
PG = calibrated by photogoniometer measurement
[2] At 200 V high voltage supply to the LD driver
[3] At 260 V high voltage supply to the LD driver
[4] The energy meter saturated and the peak power was assessed by the PMT signal
[5] Measured using a pulsed 405 nm LD
[6] This measurement was done by Yue Wang (University of St. Andrews) using different, though equivalent equipment

TABLE 6.4: Comparison of different pulsed power measurement methods on the basis of a commercial 450 nm broad area LED.

turn depends on the high voltage supplied to the LD driver. Representative data of a micro-LED array in pulsed mode is shown in figure 6.11.

In DC operation it was found that single micro-LED pixels of a few tens of μm diameter can sustain much higher current densities than broad area LEDs with a few hundred μm diameter, which was attributed to the improved thermal properties of small pixels [9]. A similar effect is observed in pulsed operation. Table 6.5 lists measured performances of a large variety of array sizes from 1×1 to 15×15 based on circular pixels. If normalised to the active area, it can be seen that the 1×1 and 2×n arrays typically outperform larger clusters by a factor 2–4. However this does not take into account the divergence of the emission through the sapphire window of flip-chip devices as discussed above in section 6.1.2. In fact, the highest fluences at the sapphire/air interface which are actually available for laser pumping were obtained with the largest arrays tested.

To mitigate the effects of divergence through the sapphire the fill factor was increased by moving from circular to square pixels (see section 6.1) and some devices used a thinned sapphire substrate of only 150 μm thickness. However, reliable and repeatable

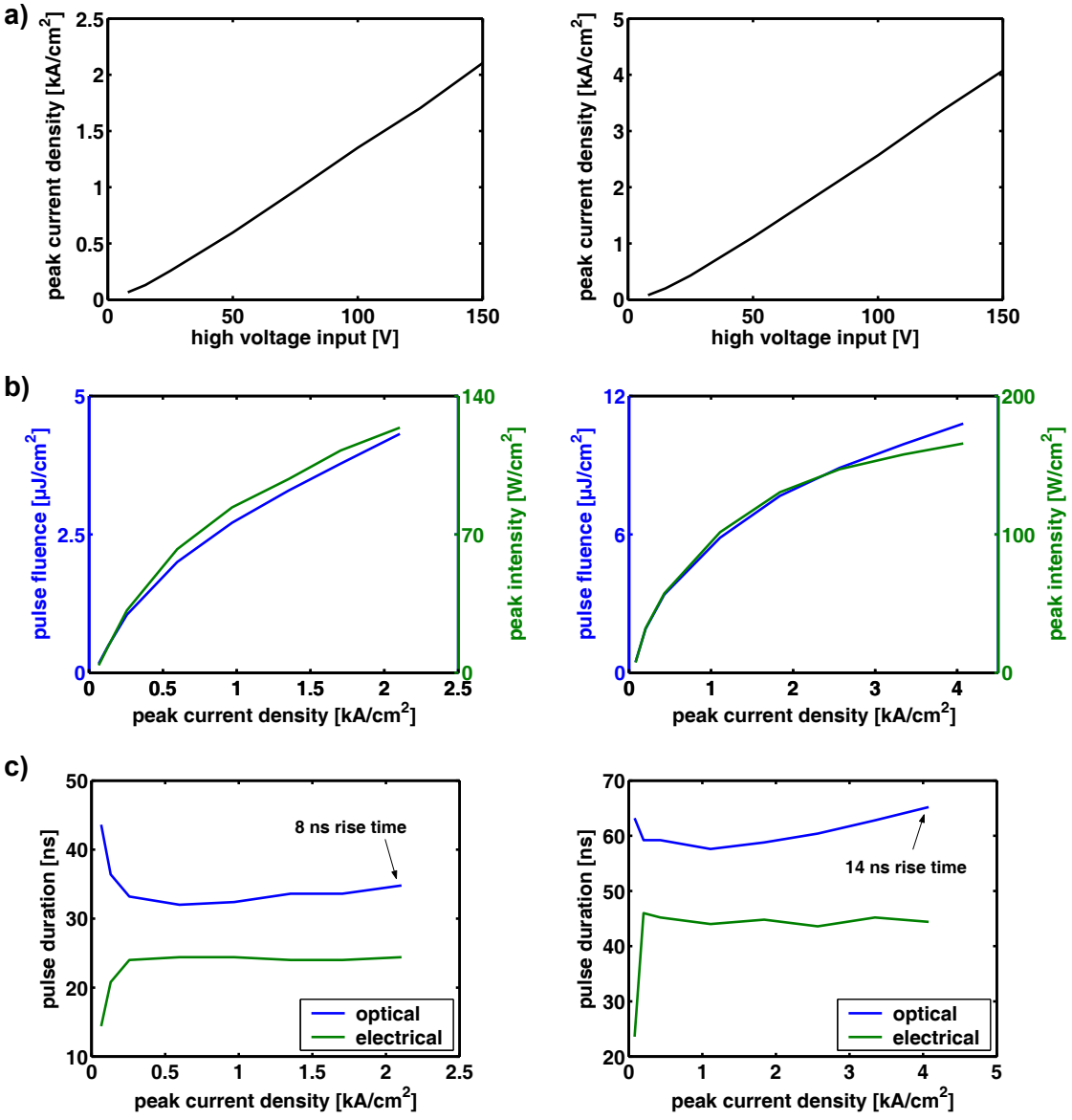

FIGURE 6.11: *a)* Pulse I-V curve, *b)* pulsed L-I characteristics and *c)* optical and electrical pulse durations of a 12×30 array of square pixels emitting at 450 nm driven by an LD driver. Graphs to the *left* are for driving with a PCO-7110-40-4 driver and results with a PCO-7110-120-15 are shown on the *right*. In both cases, a 10 μH inductor was put in parallel to the LED array. The optical fluences and intensities in graphs *b)* are on the sapphire surface, assuming a sapphire thickness of 350 μm.

array	active area cm^2	pumpspot size μm	pumpspot area[a] cm^2	power density W/cm^2 [b]	W/cm^2 [c]
1×1	7.1×10^{-6}	379	1.13×10^{-3}	392[d]	2.45[d]
2×2	2.8×10^{-5}	393	1.21×10^{-3}	195[d]	7.4[d]
2×3	4.2×10^{-6}	393×396	1.56×10^{-3}	352[d]	9.6[d]
2×6	8.5×10^{-6}	375×384	1.44×10^{-3}	353[d]	20.8[d]
2×12	1.7×10^{-4}	354×435	1.54×10^{-3}	224[d]	24.7[d]
2×18	2.54×10^{-4}	330×612	2.02×10^{-3}	272[d]	34.3[d]
3×3	6.4×10^{-5}	391	1.2×10^{-3}	265[d]	13.7[d]
4×4	1.13×10^{-4}	388	1.18×10^{-3}	267[d]	25.6[d]
5×5	1.77×10^{-4}	381	1.14×10^{-3}	254[d]	39.4[d]
5×5	1.77×10^{-4}	381	1.14×10^{-3}	311[d]	48.2[d]
6×6	2.54×10^{-4}	370	1.08×10^{-3}	184[d]	43.6[d]
8×8	4.5×10^{-4}	378	1.12×10^{-3}	175[d]	70.4[d]
15×15	1.59×10^{-3}	487	2.37×10^{-3}	62[d]	41.7[d]
15×15	1.59×10^{-3}	487	2.37×10^{-3}	237[e]	159[e]
15×15	1.59×10^{-3}	487	2.37×10^{-3}	152[e]	102[e]
15×15	1.59×10^{-3}	487	2.37×10^{-3}	96[e]	64[e]

[a] on sapphire surface, 350 μm thick sapphire
[b] with respect to active area
[c] at sapphire surface
[d] close-proximity measurement at 2 kHz repetition rate with powermeter
[e] calibrated by CW close-proximity measurement with cosine corrector

TABLE 6.5: Summary pulsed performance of micro-LED arrays based on circular pixels emitting at 450 nm.

peak intensities beyond 150 W/cm^2 to in excess of 200 W/cm^2 were only possible by improved quality of the commercially available wafers from which the micro-LEDs are fabricated. A number of arrays emitting at 450 nm achieved peak intensities ranging from 180–290 W/cm^2 obtained with either the 120-15 or the 100-7 driver and the best performing arrays were capable of delivering up to 345 W/cm^2. The best performance of an LED array emitting at 405 nm was 123 W/cm^2 in a 55 ns optical pulse driven by the 120-15 driver.

6.2.3.1 Device Damage in Pulsed Operation

When driving an LED with a DC voltage the light intensity will peak at a certain current and stagnate or even drop if the current is further increased. This roll-over is normally reversible if the current was never pushed significantly beyond the roll-over point. In pulsed operation however, no such roll-over was observed and LEDs were damaged irreversibly in a very sudden manner. In a few cases, damage occured at the wire bond pads resulting in detachment of the wire from the pad. It is believed that connecting two or three wires to each pad reduces the risk of this happening. The most common type of

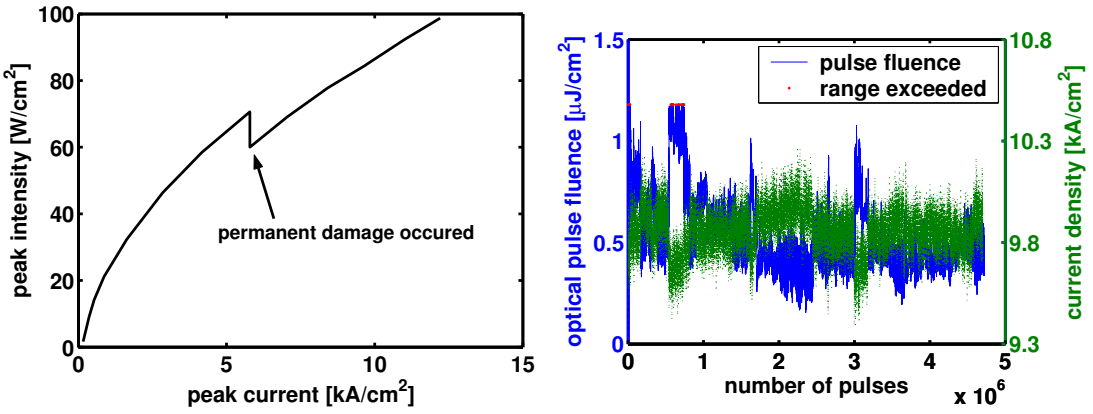

FIGURE 6.12: *Left:* Pulsed L-I curve of an 8×8 array of 450 nm square LEDs, showing a characteristic kink due to typical pulsed damage. The device had a strong leakage current in CW after the measurement see figure 6.13. *Right:* Pulse energy and peak current density monitored over a huge number of successive pulses under the same driving conditions (2×18 array of circular 405 nm LEDs, PCO-7110-40-4 driver with 72 V high voltage input, 0.47 μH inductor yielding 19 ns electrical pulses at 20 Hz repetition rate). The device was shorted after the measurement when operating CW.

damage however is the sudden occurence of a current leak. In pulsed L-I curves, such an event manifests in a sudden drop of pulse energy as is visible in figure 6.12. Once such damage has occured, pulsed device performance remains significantly inferior than prior to the event and a strong leakage current is observed in DC operation. The latter aspect is visible in DC I-V and L-I curves plotted in figure 6.13. It was also observed that no well-defined damage threshold exists. Damage may occur after a large number of pulses has already been applied at constant driving conditions. An experiment where a micro-LED array was driven in pulsed mode under constant conditions for a large number of successive pulses is shown in figure 6.12. Gradual shifts of the recorded pulse energy are fairly small but a series of discontinuous jumps is observed leading to variation of the recorded pulse energy by a factor of two. During the whole measurement, the electrical pulse width remained constant and the peak current density varied by not more than 10 %. Interestingly, the peak current density and the pulse energy are anti-correllated, i.e. at times when a relatively large pulse energy was recorded, the peak current density was slightly lower than at other times. This may be an effect of current leaks that cause a slightly higher peak current but a significantly reduced optical output.

It is known that in the regime of high current densities LEDs tend to suffer from an effect called "current crowding" [10], i.e. the electric current is not spread uniformly across the LED area. Micrographs shown in figure 6.14 show that LED arrays which light up uniformly in DC operation show significant current crowding towards the n-contact when driven in pulsed mode at a few kA/cm^2 peak current density. Figure 6.14 also shows a micrograph of a damaged LED-array where the damaged area can clearly be associated with the area of highest current density. It has to be noted though that in

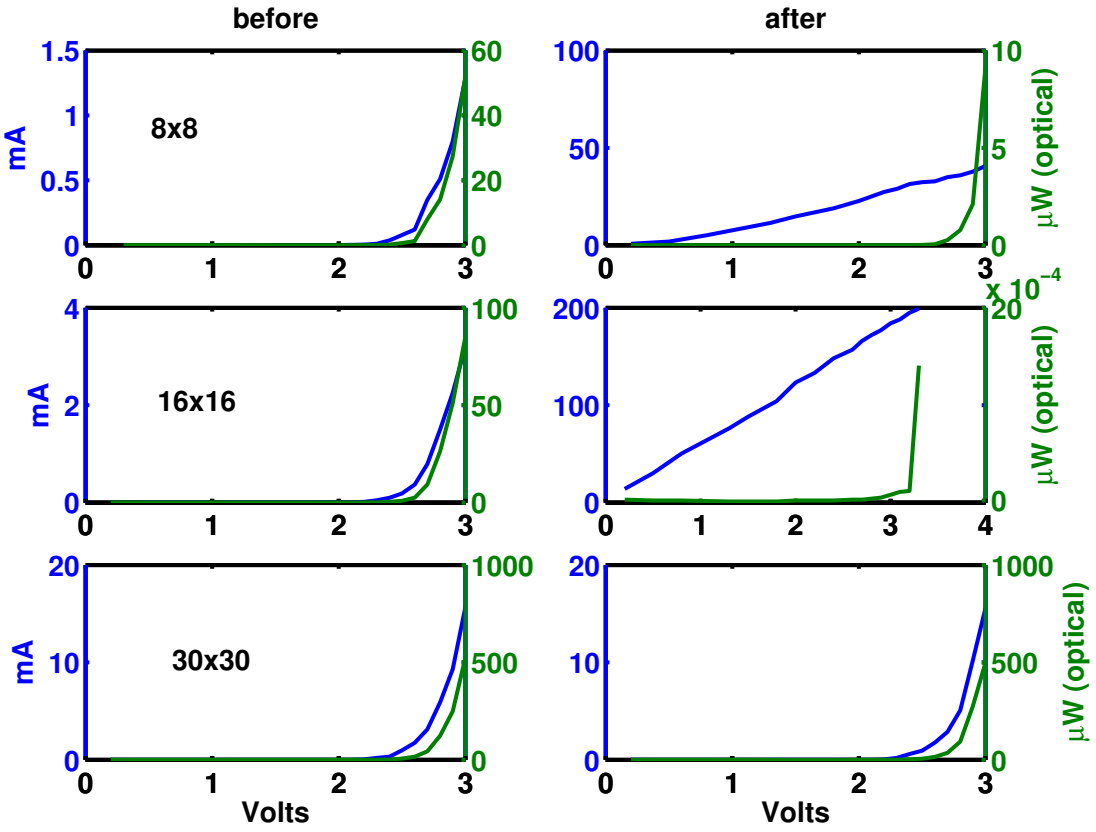

FIGURE 6.13: CW I-V and L-I characteristics of 450 nm LED arrays before and after pulsed operation at a few kA/cm^2. All but the 30×30 array suffered from a sudden loss of pulse energy during pulsed operation as shown in figure 6.12.

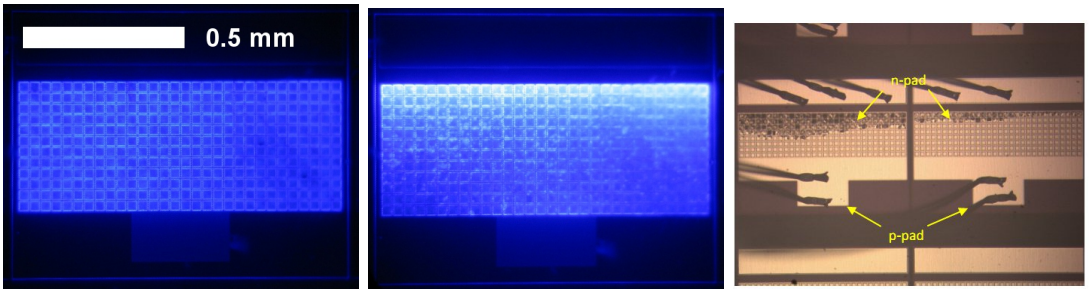

FIGURE 6.14: *Left:* Optical micro-graph of a micro-LED array under CW driving (<10 A/cm^2). *Middle:* The same stripe under pulsed pumping (2 kA/cm^2 peak current in 55 ns pulses). *Right:* Optical micrograph of micro-LED arrays that were damaged during pulsed operation.

most cases the damaged region cannot be clearly identified under a microscope. Effects of current crowing can be reduced by optimised layout of contacts and the use of different materials than NiAu as current spreading layer is under investigation.

It is likely that the occurence of damage to the devices in pulsed operation is related to heating by the high electric current flowing through the device. Therefore, two schemes for improved thermal characteristics were examined. Some devices were bump bonded

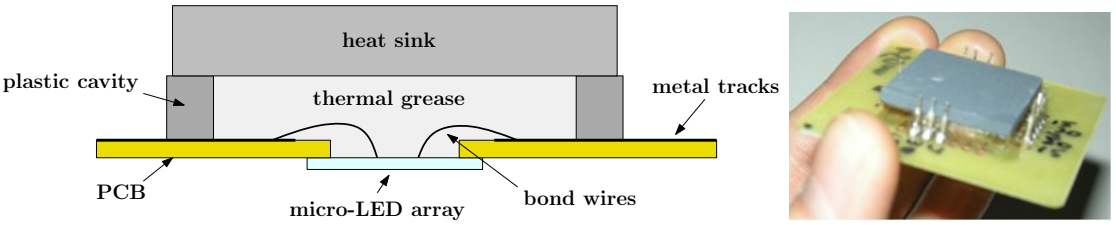

FIGURE 6.15: Schematic and photographic image of a micro-LED array with heat sink.

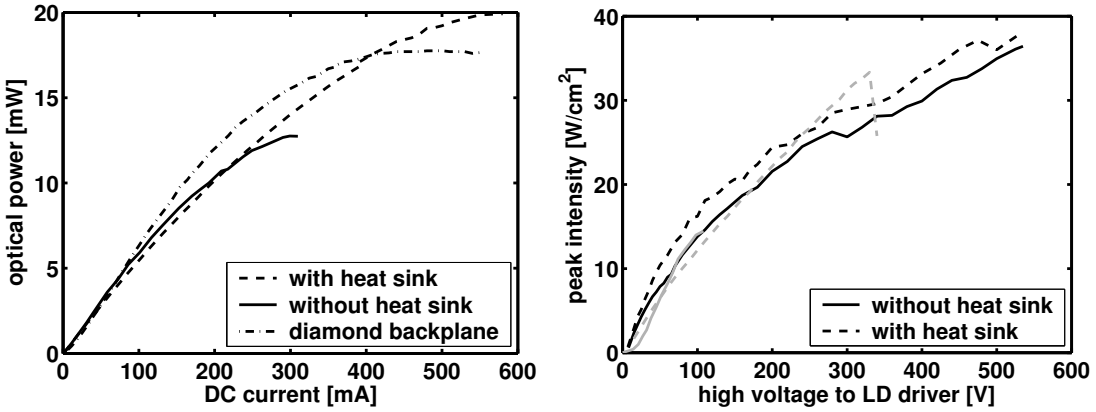

FIGURE 6.16: DC (*left*) and pulsed (*right*) performance of heat sinked micro-LED arrays in comparison to devices without heat sink.

to a diamond-backplane with metal tracks on it. The diamond-chip served as a heat spreader and was mounted in a ceramic package. Alternatively, a wire-bonded LED-chip was thermally contacted to a heat sink with electrically insulating thermal grease. The latter device is shown in figure 6.15. Performances of both types of devices in comparison to devices without heat sink are shown in figure 6.16. While the DC characteristics are significantly improved allowing up to double the optical output, no impact on pulsed performance was seen.

6.3 Micro-LED pumped OSL

Micro-LED pumped organic lasers have been achieved in a collaborative effort between the Universities of Strathclyde and St. Andrews as part of the HYPIX project (Hybrid organic semiconductor/gallium nitride/CMOS smart pixel arrays). This chapter so far focussed on the performance of micro-LEDs as pump sources. In this final section, successful laser pumping is demonstrated and the key properties of the successful devices are briefly described. A detailed discussion of the various lasers can be found in Y. Wang's PhD thesis [4].

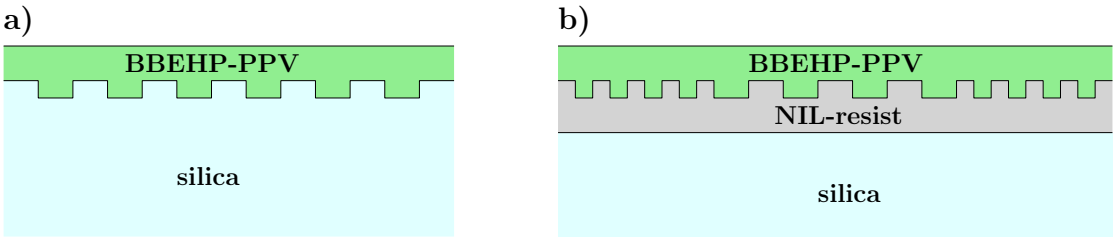

FIGURE 6.17: Schematics of BBEHP-PPV based DFB laser structures that yielded low pump thresholds suitable for LED pumping. *a)* Second order DFB laser on silica, *b)* mixed order NIL grating DFB laser.

6.3.1 DFB Laser Structures

In chapter 4 OSLs were presented that demonstrate the outstanding potential of organics for easy fabrication of mechanically flexible lasers. However, these devices have too high a threshold for pumping with LEDs. In order to lower laser thresholds, hard substrates are used, providing a route to improved structural quality and refractive index contrast between active layer and substrate. Furthermore, more sophisticated types of DFB patterns can help to reduce laser threshold as well. In particular, two types of BBEHP-PPV based DFB lasers were studied for possible micro-LED pumping. The first structure is a normal second order grating (compare also figure 2.14) patterned directly into silica. Alternatively, a mixed order grating with 15 or 30 periods of second order in the centre enclosed by first order gratings was created by nanoimprint lithography (NIL). Both structures are illustrated in figure 6.17.

Laser properties were assessed initially by pumping with an optical parametric oscillator (OPO) delivering 4 ns pulses at 450 nm wavelength. Here, only the most relevant findings for LED-pumping are included and the interested reader is referred to Y. Wang's PhD thesis for more details [4]. Both laser geometries allowed reliable fabrication of OSLs with threshold peak intensities at or below 100 W/cm^2 which is in fact competitive to the most outstanding results reported in literature, compare also section 2.2.1.3. An overview of these achievements in relation to previous results is provided in figure 6.18. Here, "HYPIX" refers to the results from the collaborative programme that funded this work (http://hypix.photonics.ac.uk). A major achievement of this programme was to demonstrate low threshold OSL reproducibility. In case of the second order grating, the influence of the pump geometry was studied. Above in section 4.2.1 it was shown that stripe-excitation perpendicularly to the grating grooves is beneficial for second order DFB laser characteristics. In the case of the devices studied here a threshold reduction by an order of magnitude could be achieved as is shown in figure 6.19. To date, the lowest threshold of a BBEHP-PPV laser is 30 W/cm^2 (0.12 μJ/cm^2) from a second order DFB laser (figure 6.17a) pumped by a 4 mm long and 404 μm wide stripe.

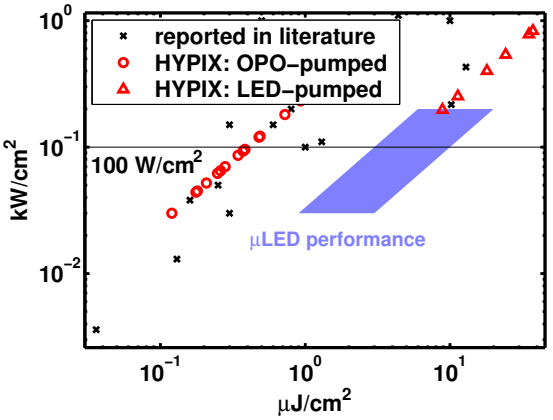

FIGURE 6.18: Thresholds of BBEHP-PPV lasers in the configurations shown in figure 6.17 which were achieved by our project partners in St. Andrews [4]. Similar to figure 2.16 typical micro-LED performance is indicated and values reported in literature are included for comparison.

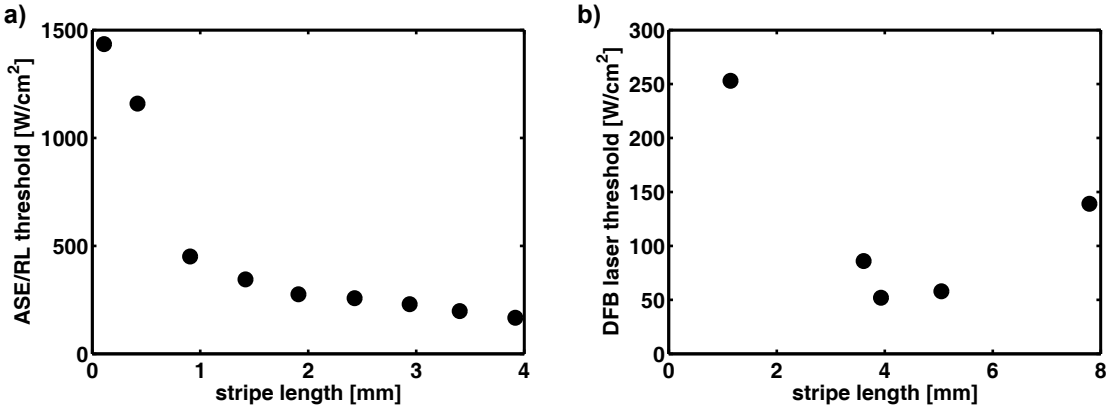

FIGURE 6.19: Pump thresholds of *a)* ASE/RL from a neat film and of *b)* a second order DFB laser on silica as a function of stripe length when pumped by a stripe of 404 μm width.

6.3.2 LED-Pumping

Given that OPO pumped BBEHP-PPV lasers regularly had thresholds at or below 100 W/cm^2 one might a priori expect that these lasers could possibly be pumped with micro-LED arrays even if their maximum (repeatable) pulsed intensity does not, so far, exceed 150 W/cm^2. However, it was already explained in section 2.1.5 that LED-pumping happens in a regime where the pulse duration and in particular the pulse rise time have a significant impact on the threshold. Therefore, the threshold peak intensity of LED-pumped lasers (∼45 ns pump pulse) is typically 3–4 times higher than the in case of OPO-pumping. Examples for illustration are given in table 6.6. Successful pumping of BBEHP-PPV mixed order DFB lasers (figure 6.17b) has, however, been achieved in three cases above pump thresholds of 250, 175 and 300 W/cm^2. One example of

Grating	OPO-threshold [W/cm^2]	LED-threshold [W/cm^2]
2^{nd} order	122	538
mixed order[a]	62	197
mixed order[b]	96	252

[a] 30 second order periods
[b] 15 second order periods

TABLE 6.6: Comparison of BBEHP-PPV laser thresholds when pumped by an OPO (4 ns pulses) or a broad-area LED (45 ns pulses). See figure 6.17 for schematics of the device structures.

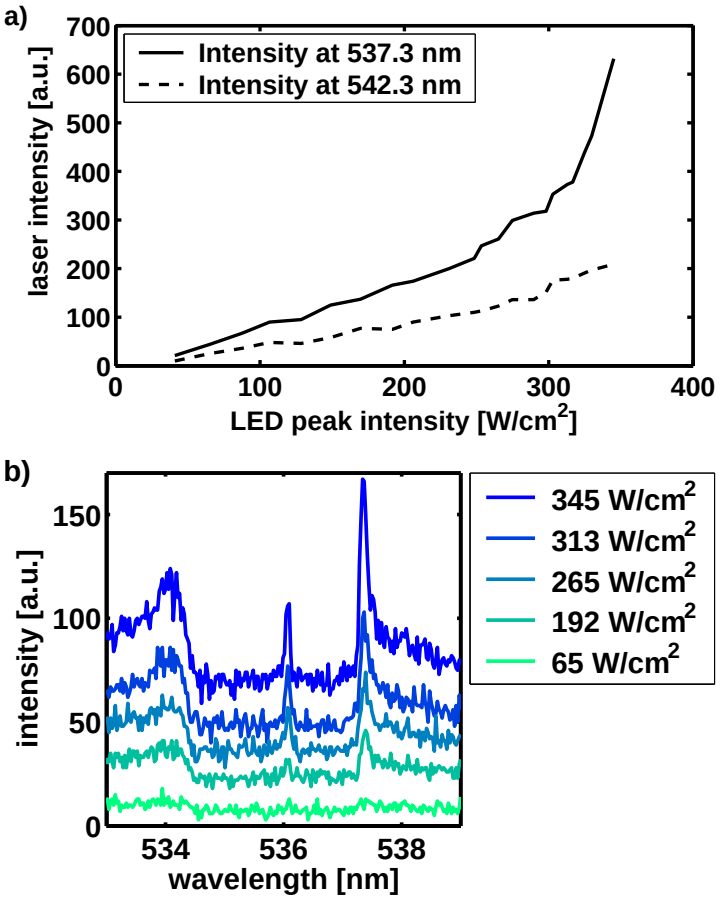

FIGURE 6.20: *a)* Power transfer function of a mixed order BBEHP-PPV DFB laser emitting at 537.3 nm pumped by a micro-LED array (8×90 square pixels). For reference, the power transfer function of the photoluminescence with a wavelength different from the laser line is included as well. *b)* Spectral evolution of the laser emission with increasing pump power.

these is given in figure 6.20. In all three cases, the micro-LED array was driven by a PCO-7110-100-7 driver.

6.4 Conclusion

Micro-LED arrays in flip-chip format for pulsed pumping of OSLs have been developed. In order to reach threshold intensity, the micro-LEDs are driven in a nanosecond pulsed regime by a LD driver close to the limit of their capability. Under these conditions sudden irreversible damage may occur without warning. The damage mechanism is likely related to current crowding and could not be mitigated by heat-sinking. Therefore, crucial factors for demonstration of micro-LED pumped lasers were LED-efficiency, optimisation of LED-geometry and the capability of the LD driver to deliver powerful pulses with a short rise time. In particular, arrays of square-shaped 30×30 μm LEDs at 33 μm pitch yielding a high fill-factor were driven simultaneously. These arrays were stripe-shaped with a few hundred μm width and a few mm length according to optimal threshold condition of DFB lasers and mitigation of LED light divergence while propagating through the sapphire layer. Blue-emitting devices in the above described stripe-geometry were capable of pumping BBEHP-PPV based mixed-order DFB lasers above thresholds on the order of 200 W/cm^2. This is an exciting preliminary demonstration, opening the way to direct CMOS driving of OSLs in future work.

References

[1] T. Riedl, T. Rabe, H.-H. Johannes, W. Kowalsky, J. Wang, T. Weimann, P. Hinze, B. Nehls, T. Farrell, and U. Scherf. Tunable organic thin-film laser pumped by an inorganic violet diode laser. *Appl. Phys. Lett.*, 88:241116, 2006.

[2] A. E. Vasdekis, G. Tsiminis, J.-C. Ribierre, Liam O' Faolain, T. F. Krauss, G. A. Turnbull, and I. D. W. Samuel. Diode pumped distributed Bragg reflector lasers based on a dye-to-polymer energy transfer blend. *Opt. Express*, 14(20):9211–9216, 2006.

[3] Y. Yang, G. A. Turnbull, and I. D. W. Samuel. Hybrid optoelectronics: A polymer laser pumped by a nitride light-emitting diode. *Appl. Phys. Lett.*, 92:163306, 2008.

[4] Yue Wang. *Low threshold organic semiconductor lasers and their applications as explosive sensors.* PhD thesis, University of St. Andrews, UK, 2012.

[5] Fei Hu, Ke-Yuan Qian, and Yi Luo. Far-field pattern simulation of flip-chip bonded power light-emitting diodes by a Monte Carlo photon-tracing method. *Appl. Opt.*, 44(14):2768–2771, 2005.

[6] Elison Matioli and Claude Weisbuch. Direct measurement of internal quantum efficiency in light emitting diodes under electrical injection. *J. Appl. Phys.*, 109:073114, 2011.

[7] Jonathan J. D. McKendry, Bruce R. Rae, Zheng Gong, Keith R. Muir, Benoit Guilhabert, David Massoubre, Erdan Gu, David Renshaw, Martin D. Dawson, and Robert K. Henderson. Individually Addressable AlInGaN Micro-LED Arrays With CMOS Control and Subnanosecond Output Pulses. *IEEE Photon. Technol. Lett.*, 21(12):811–813, 2009.

[8] *The measurement of luminous flux.* Commission Internationale de l'Eclairage, Paris, 1989. CIE 84.

[9] Zheng Gong, Shirong Jin, Yujie Chen, Jonathan McKendry, David Massoubre, Ian M. Watson, Erdan Gu, and Martin D. Dawson. Size-dependent light output, spectral shift, and self-heating of 400 nm InGaN light-emitting diodes. *J. Appl. Phys.*, 107:013103, 2010.

[10] Han-Youl Ryu and Jong-In Shim. Effect of current spreading on the efficiency droop of InGaN light-emitting diodes. *Opt. Express*, 19(4):2886–2894, 2011.

Part III

Conclusion and Outlook

Chapter 7

The Future of Hybrid Organic/Inorganic Optoelectronics

Research in the field of organic and inorganic semiconductor devices covers a broad range of topics. Activities range from fundamental material physics studies such as the random laser action discussed in chapter 3, through device engineering (e.g. lasers in chapter 4 and 6 or light emitting diodes in chapters 5 and 6) to the development of fully functional systems for certain applications (e.g. explosive sensing [1] and visible light communications systems [2]). This thesis has explored light emitting polymer (LEP) films for integration onto GaN light emitting diodes (LEDs) to enable colour conversion and laser operation. Achievements include a better understanding of the physics of LEP emission under intense stripe-excitation (chapter 3), development of mechanically flexible lasers employing very simple fabrication methods (chapter 4), observation of photonic crystal effects in the colour converted emission of a hybrid device (chapter 5), again employing very simple fabrication, and the first micro-LED pumped organic laser (chapter 6).

This chapter ventures a glimpse into the near future based on the most recent developments. Here, the focus is entirely on light emitting devices, though it should be kept in mind that a hybrid approach can also yield benefits for the opposite process in hybrid photodetectors and photovoltaics [3].

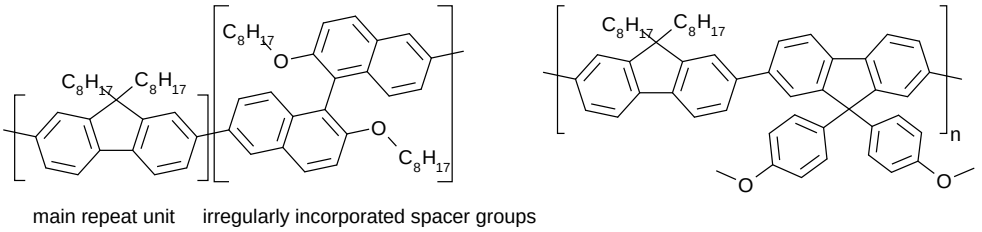

FIGURE 7.1: Examples of fluorene-based co-polymers yielding very low laser thresholds [6, 7].

7.1 Solution Processible Gain-Materials

Being synthesised chemically, solution-processible chromophores offer in general an overwhelming range of possibilities for design of the chemical structure. Starting from the first PPV-based lasers in the 1990s there has been a continuous improvement of the available materials. Key challenges in the process are development of synthesis procedures with reasonably high yields (typically 90 % per synthesis step are desired) and decision-making on the actual design targets as prediction of material properties, on the basis of the chemical structure only, is extremely difficult.

The latter aspect is currently tackled by refining computational models on the basis of model compounds with well-controlled properties such as the oligo-fluorene truxenes [4, 5]. However, current methods do not yet have the maturity to significantly aid the design of new materials. As of now, design targets are chosen empirically. This section gives an overview of current trends with particular focus on the suitability for LED-pumping.

7.1.1 Light Emitting Polymers

OSLs with record low thresholds below 100 W/cm^2 in nano-second pulses have predominantly used fluorene-based systems and in particular co-polymers [6, 7] some of which are shown in figure 7.1. These materials are blue-emitting and therefore not ideally suited for pumping with GaN LEDs whose peak external quantum efficiency is itself in the blue (figure 1.1). However, conjugated molecules with co-polymeric structures are in the focus of current synthetic ambitions [8] and it is likely that a low-threshold material of this type with efficient absorption in the blue wavelength region will emerge eventually.

It has been suggested that an important aspect of these co-polymers is the stabilisation of molecular conformation if the co-polymeric groups are chosen carefully [6]. A different approach to improve structural properties is to attach oligomeric compounds

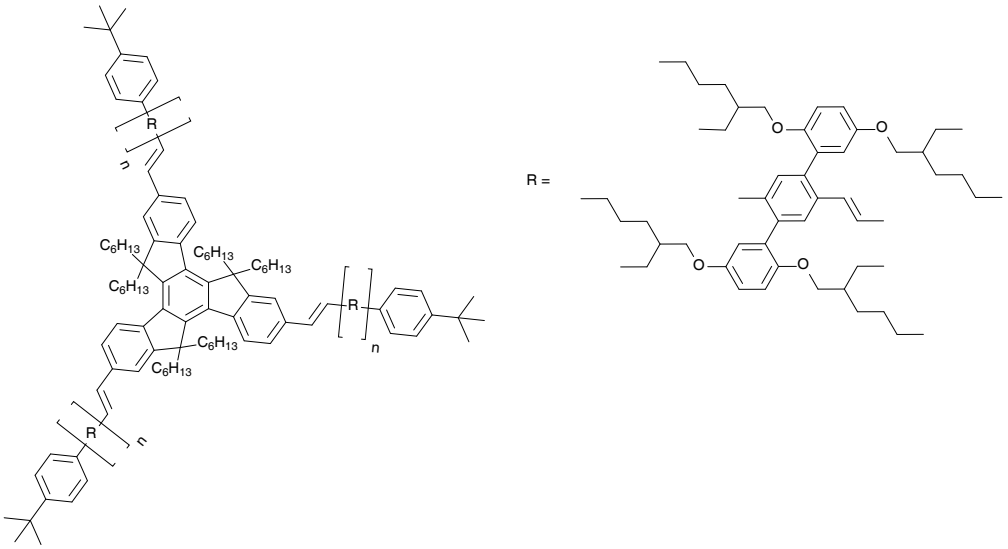

FIGURE 7.2: Chemical structure of an envisaged star-shaped truxene-cored oligo-phenylene-vinylene which could provide a route to combine the reliability and high film quality of truxene-cored oligomers with the LED-pumping capability of BBEHP-PPV.

to a stabilising core. Examples of this are the oligo-fluorene truxenes, which have been investigated for their properties as laser gain medium in chapter 4, and similar molecules are also currently of great interest [5, 9]. The truxene materials were found to give high quality films with very low optical losses (2.3 cm^{-1}, about half of what is typical for organic semiconductors) [10] and very low thresholds of 160 nJ/cm^2 (38 W/cm^2) were found in the case of pyrene-cored materials [9].

Given that BBEHP-PPV neither has copolymeric spacer-groups nor a core that could stabilise the structure, it is quite remarkable that sufficiently low thresholds for micro-LED pumping were achieved with this material. Therefore, interesting synthesis targets may be more complex structures based on the BBEHP-PPV repeat unit. An example of this is the truxene-cored oligomer system envisaged in figure 7.2.

7.1.2 Colloidal Nanocrystals

In this work some fundamental studies on laser action from CdSe/ZnS colloidal quantum dots (CQDs) have also been undertaken. Random laser behaviour was observed and is probably related to high optical gain delivered by the material. Also, a CQD DFB laser fabricated by very simple methods was realised. However, the high pump thresholds of several mJ/cm^2 are prohibitive for using simple pump sources such as LEDs. A fundamental reason for these high thresholds is the requirement for a significant biexciton population because the absorption for generation of a second exciton cancels the gain by

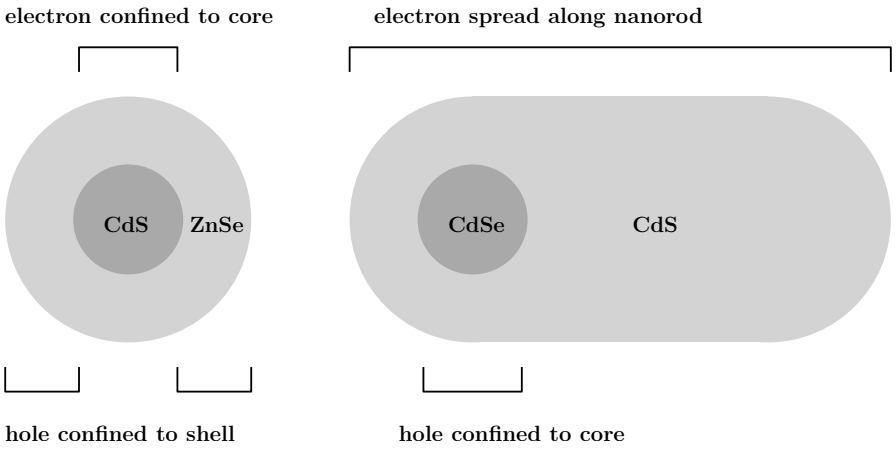

FIGURE 7.3: Examples of core-shell CQDs employing type-II semiconductor junctions leading to spatial separation of electron and hole wave functions [11, 12].

stimulated emission from the single excitons. Structures employing type-II semiconductor junctions between core and shell lead to spatial separation of electron and hole wave functions as illustrated in figure 7.3. The resulting giant exciton-exciton repulsion leads to blue-shift of the absorption for generation of a second exciton thus enabling single exciton gain [11]. Currently, amplified spontaneous emission thresholds are still on the order of 1 mJ/cm^2 but since the fundamental barrier of the biexciton requirement is overcome there is potential for further threshold reduction.

7.2 LED-Pumped Lasers

An important outcome of the work presented here is the first micro-LED pumped organic laser described in section 6.3. In general, BBEHP-PPV based lasers can now routinely be pumped with commercial LEDs using "thin-GaN" technology, delivering up to 1 kW/cm^2 in 45 ns pulses [13, 14]. Therefore, GaN LED and LD pumping of OSLs is a very promising candidate for possible commercialisation of OSL technology. The previous section gave a vision of how the organic part in these devices could develop. Here, the focus will be on the inorganic LEDs.

7.2.1 LED Performance

Currently the best flip-chip micro-LED performance in pulsed operation is about a third of that of the best commercially available broad area LEDs. This may partly be caused by the sapphire window creating an additional interface that the light has to pass through. The sapphire substrate can in principle be removed by laser lift-off which may increase extraction efficiency and allow pumping with narrower stripes (compare section

6.1.2) potentially reducing the overall current needed. On the other hand, laser lift-off may cause complications for the integration process onto CMOS control electronics.

The limiting factors of LEDs in pulsed performance apart from extraction efficiency are not yet fully understood. A dominant mode of failure is the sudden occurence of current leaks, see section 6.2.3.1. These seem not to be caused by accumulative heating. Given that these defects have been observed more often in micro-LEDs than in commercial broad area LEDs, one could examine if there is an effect of the micro-LED side-walls. A proposed set of micro-LED structures for systematic analysis of side-wall effects is given in figure 7.4. These can be characterised in DC and pulsed operation giving insight to how these two operation modes are influenced by the side-walls. A photolithography mask for these devices has already been created.

7.2.2 CMOS-controlled LEDs

An important benefit of micro-LEDs in general is their potential for integration onto a highly functional CMOS backplane. In that case, optical pulses are created by switching of metal oxide semiconductor field effect transistors (MOSFETs) of a supply voltage rather than by a capacitor discharge. These MOSFETs therefore have to sustain the currents needed to drive micro-LED pixels at several kA/cm^2. Furthermore, the CMOS chip should ideally be designed to drive stripe-shaped micro-LED arrays with high fill factor according to section 6.1 simultaneously. A schematic of a CMOS chip layout designed with these considerations in mind is shown in figure 7.5 [15]. At the time of writing, these devices are being fabricated.

7.3 Mechanically Flexible Devices

An interesting aspect of the lasers discussed in chapter 4 is their mechanical flexibility. This property allows for example conformation to uneven and/or non-rigid surfaces such as soft tissue. Flexible photonics remain an important topic of current research in particular towards biological applications. Current challenges in the field include improvement of device longevity and compatibility of inorganic excitation sources with the flexible format.

7.3.1 Operational Lifetime

Dubbed as “plastic-lasers”, concerns about the rapid degradation of OSL performance over time are sometimes answered by the fact that these very compact devices have the

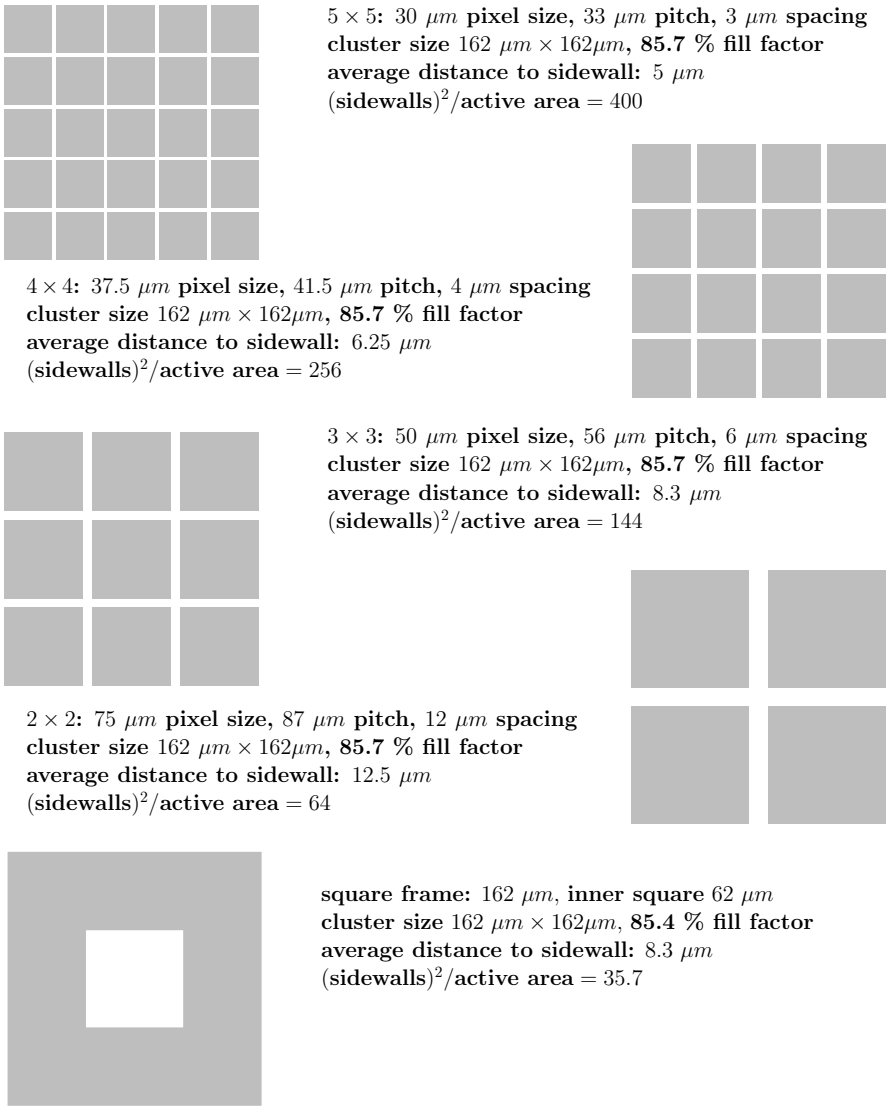

FIGURE 7.4: Proposed design of a series of micro-LEDs for systematic study of sidewall effects. Each device occupies the same area and has the same fill factor and are therefore expected to have similar thermal properties. However, the total length of sidewalls (given as ratio to the active area) is different for each design. For reference, the average distance of an arbitrary point within the active region to the next side-wall is given as well.

potential to be produced at very low-cost and can be regarded as disposable. While this may be acceptable for some applications such as chemo-sensing, it may prove very impractical in others such as data transmission. Looking back at figure 2.19 it becomes apparent that organic semiconductors have not been investigated systematically for their durability in most cases. Part of the reason may be that since the commercialisation of organic LEDs, highly efficient encapsulation of the active layer is in principle available once there is sufficient commercial interest. However, as pointed out earlier existing schemes are not possible in mechanically flexible format. In chapter 4, polymeric overlayers were used to enhance OSL lifetime. These results can only be seen as an initial

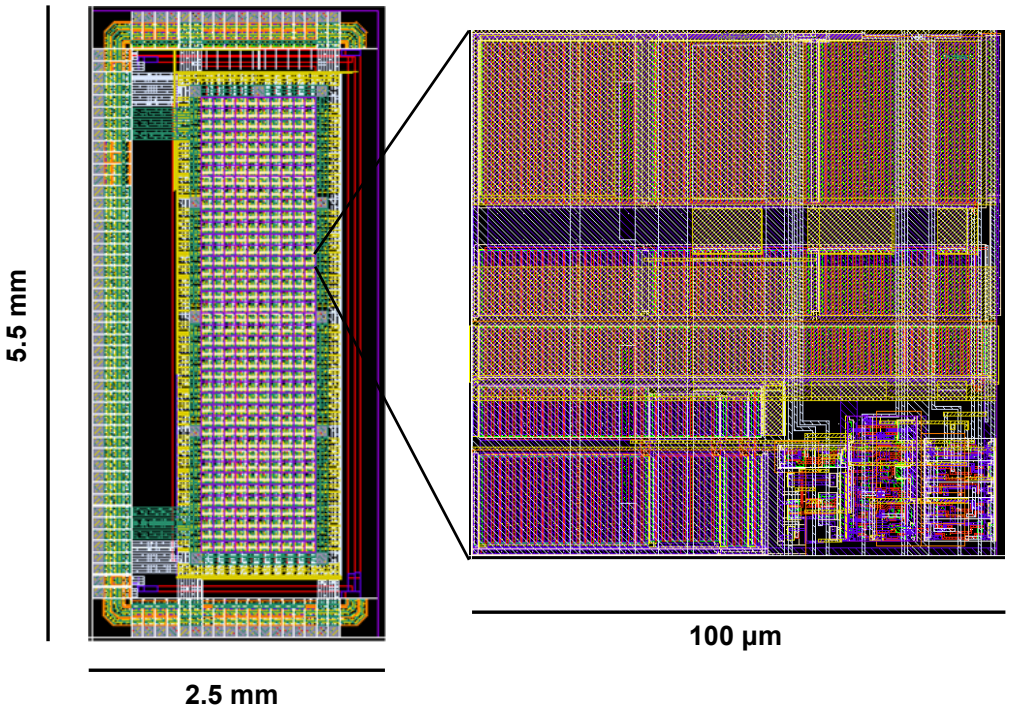

FIGURE 7.5: CMOS electronics designed for pulsed driving a 10×40 LED array at 100 μm pitch. In each pixel, most of the area is occupied by MOSFETs in order to maximise the pulse energy they can deliver. Only the small area in the bottom right of the pixel is used for pixel addressing logics. [15]

step and rigorous systematic studies may be required to understand how device longevity can be achieved. In fact, a comparative study of devices in the same format as those in chapter 4 but with different material compositions has been started [16].

7.3.2 Micro-LEDs for Flexible Photonics

It was briefly mentioned in the introduction chapter 1 that flexible photonics is no longer exclusive to organic materials but has also been created using GaN-LEDs, see figure 7.6. Typically, these were in micro-LED format [17, 18] and normally make use of inert organic materials as substrates. Overcoating/printing of (possibly patterned) colour-converting layers onto these devices using solution-processible materials will preserve the key aspect of mechanical flexibility but can open up additional functionality such as flexible multi-colour displays. In comparison to the alternative all-organic approach the hybrid device would benefit from the electronic properties of inorganic semiconductors and degradation issues of the LEP are less severe because no highly reactive charge states are generated. The possibility of creating the photonic crystal LEDs described in chapter 5 in fully flexible format is planned to be explored.

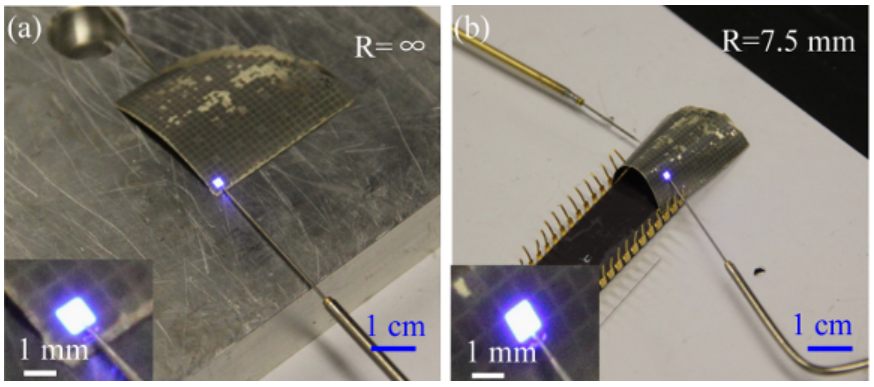

FIGURE 7.6: Mechanically flexible GaN LED *a)* unbent and *b)* bent. [19]

7.4 Towards Applications

LEP based devices can now be fabricated with a reliability that allows research focus to shift from fundamental device physics towards application-oriented engineering. In some areas such as sensing, fairly mature systems have been demonstrated already whereas other fields, e.g. communications, are still in the early stages with some important proof-of-concept demonstrations still to be done.

7.4.1 Sensing Devices

A prominent example of a sensing device based on the hybrid organic/inorganic approach is the explosive detection device that was already discussed in the introduction 1.2.1 [1]. Another field that has evolved fairly recently is the use of organic lasers or photonic crystal films as refractive index sensors [20, 21]. In fact, the DFB lasers presented in chapter 4 have been examined for their suitability as refractive index sensors [22] and A.-M. Haughey *et al.* are currently developing these lasers towards biosensors that allow detection of certain proteins.

7.4.2 Communications

An exciting vision of a device for short-range optical communications is a CMOS-controlled micro-LED array allowing highly parallel multiple input/multiple output (MIMO) data transfer, possibly making use of organic overlayers for colour conversion. Up to now, individual aspects of development towards this goal have been realised. These are in particular high speed modulation of micro-LEDs [23], data transfer via CMOS controlled micro-LEDs [2], micro-LED based dual-channel operation [24] and high modulation bandwidth of colour-converted LEP-emission (included here in chapter 5). Also,

chapter 5 contains preliminary results of coupling PhC modified emission into polymer fibre (POF), indicating an enhancement of transmitted intensity. Important future steps will be demonstration of data transmission via colour-converted light through free-space and POF. Bringing all these elements together to form a highly capable communications device will be an exciting challenge.

7.5 Summary

Hybrid device performance will continue to improve as a result of ongoing synthetic efforts and the increasing standard of available inorganic LEDs. An important, yet unsolved, challenge is the improvement of operational lifetime of mechanically flexible organic devices. With the availability of flexible inorganic devices, it will be interesting to see whether all-organic, hybrid or inorganic devices will prevail in this field. Nanosecond pulsed operation of LEDs will be further examined to gain a better understanding of the physics relevant for organic laser pumping and visible light data transmission. Overall, the technology has reached a level of maturity that fully functional sensing and visible light communications systems will be a reality soon.

References

[1] Yue Wang, Bruce R. Rae, Robert K. Henderson, Zheng Gong, Jonathan Mckendry, Erdan Gu, Martin D. Dawson, Graham A. Turnbull, and Ifor D. W. Samuel. Ultra-portable explosives sensor based on a CMOS fluorescence lifetime analysis micro-system. *AIP Advances*, 1:032115, 2011.

[2] Jonathan J. D. McKendry, David Massoubre, Shuailong Zhang, Bruce R. Rae, Richard P. Green, Erdan Gu, Robert K. Henderson, A. E. Kelly, and Martin D. Dawson. Visible-Light Communications Using a CMOS-Controlled Micro-Light-Emitting-Diode Array. *J. Lightwave Technol.*, 30(1): 61–67, 2012.

[3] Baoquan Sun, Alp T. Findikoglu, Milan Sykora, Donald J. Werder, and Victor I. Klimov. Hybrid Photovoltaics Based on Semiconductor Nanocrystals and Amorphous Silicon. *Nano Lett.*, 9(3): 1235–1241, 2009.

[4] Neil A. Montgomery, Jean-Christophe Denis, Stefan Schumacher, Arvydas Ruseckas, Peter J. Skabara, Alexander Kanibolotsky, Martin J. Paterson, Ian Galbraith, Graham A. Turnbull, and Ifor D. W. Samuel. Optical Excitations in Star-Shaped Fluorene Molecules. *J. Phys. Chem. A*, 115: 2913–2919, 2011.

[5] Alexander L. Kanibolotsky, Igor F. Perepichka, and Peter J. Skabara. Star-shaped π-conjugated oligomers and their applications in organic electronics and photonics. *Chem. Soc. Rev.*, 39:2695–2728, 2010.

[6] C. Karnutsch, C. Gärtner, V. Haug, U. Lemmer, T. Farrell, B. S. Nehls, U. Scherf, J. Wang, T. Weimann, G. Heliotis, C. Pflumm, J. C. deMello, and D. D. C. Bradley. Low threshold blue conjugated polymer lasers with first- and second-order distributed feedback. *Appl. Phys. Lett.*, 89: 201108, 2006.

[7] C. Karnutsch, C. Pflumm, G. Heliotis, J. C. deMello, D. D. C. Bradley, J. Wang, T. Weimann, V. Haug, C. Gärtner, and U. Lemmer. Improved organic semiconductor lasers based on a mixed-order distributed feedback resonator design. *Appl. Phys. Lett.*, 90:131104, 2007.

[8] Alan J. Heeger. Semiconducting polymers: the Third Generation. *Chem. Soc. Rev.*, 39:2354–2371, 2010.

[9] Ruidong Xia, Wen-Yong Lai, Peter A. Levermore, Wei Huang, and Donal D. C. Bradley. Low-Threshold Distributed-Feedback Lasers Based on Pyrene-Cored Starburst Molecules with 1,3,6,8-Attached Oligo(9,9-Dialkylfluorene) Arms. *Adv. Funct. Mat.*, 19:2844–2850, 2009.

[10] Georgios Tsiminis, Yue Wang, Paul E. Shaw, Alexander L. Kanibolotsky, Igor F. Perepichka, Martin D. Dawson, Peter J. Skabara, Graham A. Turnbull, and Ifor D.W. Samuel. Low-threshold

organic laser based on an oligofluorene truxene with low optical losses. *Appl. Phys. Lett.*, 94: 243304, 2009.

[11] Victor I. Klimov, Sergei A. Ivanov, Jagjit Nanda, Marc Achermann, Ilya Bezel, John A. McGuire, and Andrei Piryatinski. Single-exciton optical gain in semiconductor nanocrystals. *Nature*, 447: 441–446, 2007.

[12] J. Müller, J. M. Lupton, P. G. Lagoudakis, F. Schindler, R. Koeppe, A. L. Rogach, J. Feldmann, D. V. Talapin, and H. Weller. Wave Function Engineering in Elongated Semiconductor Nanocrystals with Heterogeneous Carrier Confinement. *Nano Lett.*, 5(10):2044–2049, 2005.

[13] Yue Wang, Georgios Tsiminis, Graham Turnbull, and Ifor Samuel. Private communication, 2010–2012.

[14] Yue Wang. *Low threshold organic semiconductor lasers and their applications as explosive sensors.* PhD thesis, University of St. Andrews, UK, 2012.

[15] Bruce Rae, Edward Fisher, Andrew Cogman, Wafi Zhudi, , David Renshaw, Anthony Walton, Ian Underwood, and Robert Henderson. Private communication, 2009–2012.

[16] C. Foucher, B. Guilhabert, A. Kanibolotsky, P.J. Skabara, N. Laurand, and M. D. Dawson. Flexible Polyimide-based Nanocomposite Laser. EOSAM, 2012.

[17] Sang-Il Park, Yujie Xiong, Rak-Hwan Kim, Paulius Elvikis, Matthew Meitl, Dae-Hyeong Kim, Jian Wu, Jongseung Yoon, Chang-Jae Yu, Zhuangjian Liu, Yonggang Huang, Keh chih Hwang, Placid Ferreira, Xiuling Li, Kent Choquette, and John A. Rogers. Printed Assemblies of Inorganic Light-Emitting Diodes for Deformable and Semitransparent Displays. *Science*, 325:977–981, 2009.

[18] Rak-Hwan Kim, Dae-Hyeong Kim, Jianliang Xiao, Bong Hoon Kim, Sang-Il Park, Bruce Panilaitis, Roozbeh Ghaffari, Jimin Yao, Ming Li, Zhuangjian Liu, Viktor Malyarchuk, Dae Gon Kim, An-Phong Le, Ralph G. Nuzzo, David L. Kaplan, Fiorenzo G. Omenetto, Yonggang Huang, Zhan Kang, and John A. Rogers. Waterproof AlInGaP optoelectronics on stretchable substrates with applications in biomedicine and robotics. *Nature Materials*, 9:929–937, 2010.

[19] P. Tian, E. Xie, Z. Gong, Z. Chen, T. Yu, Y. Sun, S. Qi, Y. Chen, Y. Zhang, S. Calvez, E. Gu, G. Zhang, and M. D. Dawson. Flexible Vertical Structure GaN-Based Light Emitting Diodes on an AuSn Substrate. IEEE Photonics, 2011.

[20] M. Lu, S. S. Choi, U. Irfan, and B. T. Cunningham. Plastic distributed feedback laser biosensor. *Appl. Phys. Lett.*, 93:111113, 2008.

[21] Yafang Tan, Chun Ge, Meng Lu Allen Chu, William Goldshlag, Cheng Sheng Huang, Anusha Pokhriyal, Sherine George, and Brian T. Cunningham. Plastic-Based Distributed Feedback Laser Biosensors in Microplate Format. *IEEE Sensors J.*, 12(5):1174–1180, 2012.

[22] A.-M. Haughey, B. Guilhabert, G. A. Burley, A. Kanibolotsky, P. Skabara, N. Laurand, and M. D. Dawson. Organic distributed feedback biosensor. Photon 12, 2012.

[23] Jonathan McKendry, Richard P. Green, A. E. Kelly, Zheng Gong, Benoit Guilhabert, David Massoubre, Erdan Gu, and Martin D. Dawson. High-Speed Visible Light Communications Using Individual Pixels in a Micro Light-Emitting Diode Array. *IEEE Photon. Technol. Lett.*, 22(18): 1346–1348, 2010.

[24] J. J. D. McKendry, S. Zhang, D. Massoubre, E. Gu, R. K. Henderson, A. E. Kelly, and M. D. Dawson. Data communications with gallium nitride LEDs. UKNC 2012, 2012.

Part IV

Appendix

Appendix A

Matlab Functions

During the course of this work, a number of Matlab functions were created to facilitate workflow. All of them are equipped with a brief description of usage that can be accessed by typing `help <function name>` on the Matlab command line. This appendix highlights a selection of these functions, explains their usage and how they relate to the work presented in the main text.

A.1 Peak Decomposition

The Matlab function `peakdecomposition` is a tool to decompose (e.g.) a spectrum into a superposition of 1 to 6 peaks. This is particularly useful to accurately determine the properties of a single peak on top of a broad luminescence background which can for example be found in the emission of PhC LEDs. If you have this function in your path and type `help peakdecomposition` on the Matlab console you will see the following output:

```
 [x0, fwhm, ymax, peaktype, linbg] = peakdecomposition(x, y, n)

 decompose a spectrum into up to 6 peaks

 input arguments:
-----------------
 x, y: experimentally obtained spectrum
 n: number of peaks, has to be in between 1 and 6

 output arguments:
```

```
x0: [n x 1] vector of peak positions
fwhm: [n x 1] vector of peak full width half maxima
ymax: [n x 1] vector of peak heights
peaktype: n vertically concatenated strings specifying the peak shapes
linbg: [1 x 2] vector of polynomial coefficients specifying the linear
       background (to be used with polyval)
```

Since the numerics need some guidance by the user, the function uses a graphical user interface (GUI).

A.1.1 Fitting Equation

The function that the experimental data is fitted to is the sum of n peaks of selected peak shape and a linear background. This function is shown in equation (A.1) while the possible peak shapes are defined in equation (A.2). There is an independent function, `peakclc.m`, that does the actual peak shape calculation (`peakclc.m` has to be in the Matlab search path for functions for `peakdecomposition.m` to work).

$$y(x) \stackrel{!}{=} y(x; \vec{x}_0, \vec{\Delta}, \vec{y}_{max}, \alpha, \beta) := \sum_{i=1}^{n} P_i(x; x_{0,i}, \Delta_i, y_{max,i}) + \alpha \cdot x + \beta \tag{A.1}$$

$$P(x; x_0, \Delta, y_{max}) := \begin{cases} y_{max} \cdot \exp\left(-4\log(2)\frac{(x-x_0)^2}{\Delta^2}\right) & , \text{ gaussian} \\ y_{max} \cdot \frac{(\Delta/2)^2}{(x-x_0^2)+(\Delta/2)^2} & , \text{ lorentzian} \\ y_{max} \cdot \text{sech}^2\left(2\text{asech}\left(\frac{1}{\sqrt{2}}\right) \cdot \frac{x-x_0}{\Delta}\right) & , \text{ sech}^2 \end{cases} \tag{A.2}$$

Here x, y is the experimentally obtained spectrum, x_0 is the peak position, Δ the full width half maximum (FWHM), y_{max} the peak height and α, β define the linear background. Due to technical reasons the notation in the actual Matlab code is slightly different. A comparison of the notation here and the notation in the code is given table A.1.

The goal of the fit is to minimise the residual function:

$$\varepsilon(\vec{x}_0, \vec{\Delta}, \vec{y}_{max}, \alpha, \beta) := \sum_{j=1}^{m} \Big(y_j - y(x_j; \vec{x}_0, \vec{\Delta}, \vec{y}_{max}, \alpha, \beta)\Big)^2 \tag{A.3}$$

where m is the number of data points $(x_j|y_j)$ and $y(x_j; \vec{x}_0, \vec{\Delta}, \vec{y}_{max}, \alpha, \beta)$ is defined by equation (A.1). We use the built-in Matlab function `fminsearch` to minimise ε (type

variable		Matlab name
peak position	x_0	`x0`
full width half maximum	Δ	`fwhm`
peak height	y_{max}	`ymax`
(e.g. wavelength)	x	`x`
spectral intensity	y	`y`
number of peaks	n	`n`
background slope	α	`linbg(1)`
background offset	β	`linbg(2)`
peak shape	denoted by subscript i	`peaktype(i,:)`

TABLE A.1: Overview of the variables

`doc fminsearch` on the Matlab console for further information). Since `fminsearch` often gets caught on local minima or fails to converge it is advisable to first set a big part of the parameters by hand and subsequently add them to the fit the closer one gets to the best solution.

A.1.2 Manual

The features of the GUI are illustrated on the example of a truxene T3 photoluminescence spectrum which will be fitted with four peaks:

```
>> [x0, fwhm, ymax, peaktype, linbg] =
    peakdecomposition(wavelength, spectrum, 4)
```

This command opens a figure window with a plot of the spectrum shown in figure A.1. One is asked to select two points by mouse clicks to define the spectral range for our fit (only the x values of the selection are important).

In the next step, a similar plot of the cropped spectrum is shown and one has to define the rough positions (this time both, x and y value of the selection are important) by mouse clicks.

Once this is done, the GUI shown in figure A.2 will be opened. On the left hand side there are two plots, one visualising the fit and the other plotting the residuals $\epsilon := y - y(x; \vec{x}_0, \vec{\Delta}, \vec{y}_{max}, \alpha, \beta)$. On the top right hand side there is a number of UI controls that allow us to control the parameters x_0, Δ, y_{max} as well as the peak type for each peak. Tick boxes allow to specify which parameters are to be fitted and which ones remain fixed. Fitting all parameters at the same time is computationally expensive and is likely to not give good results unless the fit is fairly accurate already. On the bottom right hand side are controls that allow fitting (or manual setting) of the linear

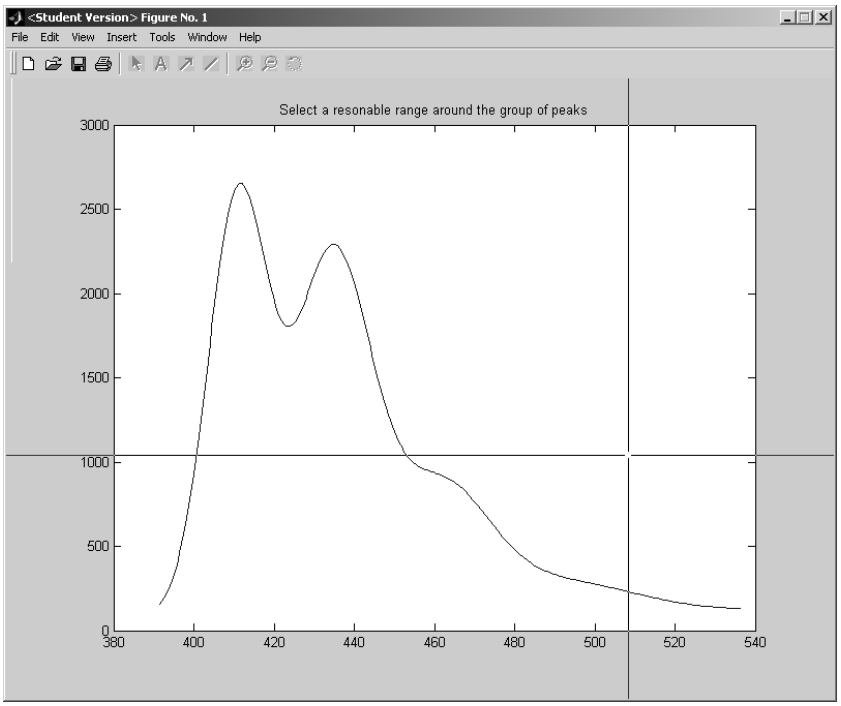

FIGURE A.1: Range selection window of the peak decomposition tool.

background parameters, α, β. Hitting the "Recalculate" button will fit the selected parameters and update the plot with the new fit. Once the fit is satisfactory, one can hit the "Finish" button which will plot the result in a format suitable for printing or saving in a graphics format.

The "avoid overshoots" tick box at the bottom changes how the data points are treated. Normally, each measured point is interpreted as an infinitely sharp spectral selection of the emission:

$$I_{exp}(\lambda) \doteq \int_0^\infty \mathrm{d}\lambda' \, I_{real}(\lambda')\delta(\lambda' - \lambda) \tag{A.4}$$

In reality, the spectral response will be a convolution of the real spectrum with the instrument response $r(lambda, \Delta\lambda)$:

$$I_{exp}(\lambda) = \int_0^\infty \mathrm{d}\lambda' \, I_{real}(\lambda')r(\lambda, \lambda' - \lambda) \tag{A.5}$$

In the case of a CCD spectrometer with a narrow slit and a high quality grating (i.e. the resolution is effectively given by the CCD pixel size) it is possible to approximate equation (A.5) by assuming that the intensity I_n recorded by the n_{th} pixel is the integrated light within a fixed range around the pixel center wavelength λ_n:

$$I_n \doteq \int_{(\lambda_{n-1}+\lambda_n)/2}^{(\lambda_n+\lambda_{n+1})/2} \mathrm{d}\lambda' \, I_{real}(\lambda') \tag{A.6}$$

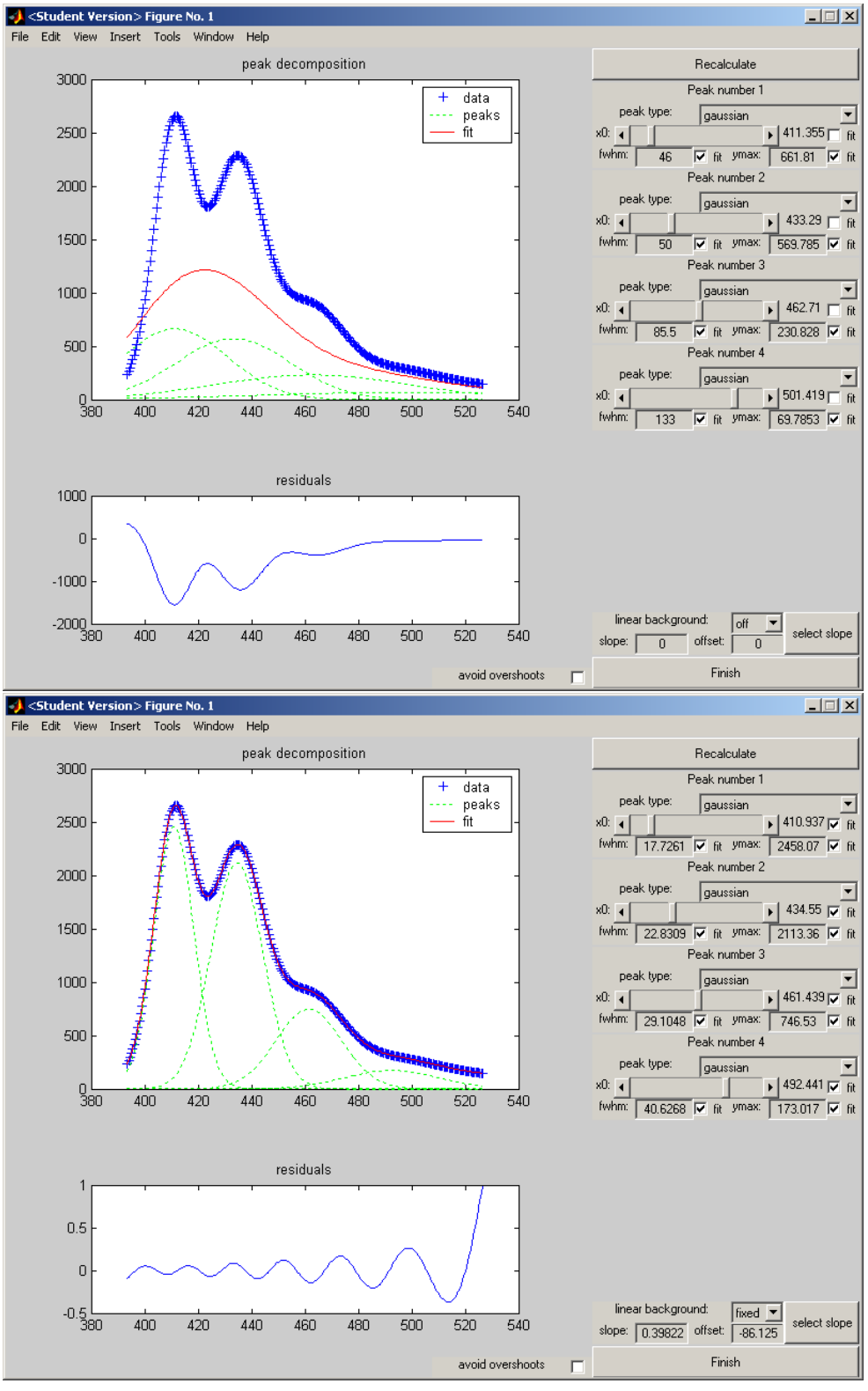

FIGURE A.2: GUI for peak decomposition. *Top:* inital view before optimisation. *Bottom:* after several iterations of optimisation. Each iteration is started by the "Recalculate" button on the top right of the window. Immediately below this button are controls for fitting of the individual peaks. On the bottom right of the window are controls for fitting an additional linear background. The top plot in each window shows the experimental curve, the fit curve and the individual peaks. The bottom plot shows the residuals of the fit.

Ticking "avoid overshoots" forces the optimisation to use (A.6) instead of (A.4). This is numerically much more expensive and in most cases, the difference in between (A.4) and (A.6) is negligible. However, in the case of very narrow peaks that only span two or three pixels the default behaviour (A.4) may cause an unphysical overestimation of the peak intensity. In this case the peak will grossly overshoot the data points and the option "avoid overshoots" has to be selected.

A.2 Threshold Fitting

In section 4.1.2.1 it was shown that organic DFB lasers typically have a soft threshold behaviour that can be fitted with either equation (4.1) or (4.2) which for convenience are reprinted here.

$$\frac{\mathrm{d}I_{ASE}}{\mathrm{d}x} = \frac{aF_p}{1 + I_{ASE}/I_{sat}} + bI_{ASE}\left(\frac{F_p/F_{th}}{1 + I_{ASE}/I_{sat}} - 1\right) \qquad \text{(reprint of (4.1))}$$

$$I_{laser} = \frac{I_{sat}\kappa F_p/F_{th}}{1 + I_{laser}/I_{sat} - F_p/F_{th}} \qquad \text{(reprint of (4.2))}$$

Both fits are done by the same Matlab function, `softthreshold.m`. Its calling syntax for fitting is:

```
[Fth, Isat, kappa] = softthreshold(Fp, I)
[Fth, Isat, a, b] = softthreshold(Fp, I)
```

Whether equation (4.1) or (4.2) is used is determined by the number of output arguments (three or four). By default, the function plots the fitted data and the fit residuals. This can be suppressed by passing the string `'no plot'` as a third argument:

```
[Fth, Isat, kappa] = softthreshold(Fp, I, 'no plot')
[Fth, Isat, a, b] = softthreshold(Fp, I, 'no plot')
```

`softthreshold.m` can also be called with a single output argument. In this case, the theoretical curve for a given set of parameters will be calculated:

```
I = softthreshold(Fp, Fth, Isat, kappa)
I = softthreshold(Fp, Fth, Isat, a, b)
```

Here, the choice in between equation (4.1) or (4.2) is made upon the number of input arguments.

A.3 Knife Edge Fitting

A popular method to determine beam profiles is to to move a thin and sharp edge, e.g. a razor blade, across the beam and record the drop in intensity due to partial blocking of the beam. Given the beam profile $P(x)$ with x being the position of the knife edge, the recorded knife-edge data $I_{rec}(x)$ will obey one of the following expressions:

$$I_{rec}(x) = \int_x^\infty \mathrm{d}x'\, P(x') \tag{A.7}$$

$$I_{rec}(x) = \int_{-\infty}^x \mathrm{d}x'\, P(x') \tag{A.8}$$

Whether (A.7) or (A.8) is appropriate depends on the direction of movement. The Matlab function `knifeedge.m` can fit knife-edge data if the beam profile is one of the shapes supported by `peakclc.m` (see equation (A.2) in section A.1.1). Its calling syntax is:

```
[fwhm, I0, res] = knifeedge(x, Iexp)
[fwhm, I0, res] = knifeedge(x, Iexp, shape)
```

The fitting equation is:

$$I_{exp}(x) \stackrel{!}{=} I_{rec}(x) + I_0 \tag{A.9}$$

It is automatically determined whether $I_{rec}(x)$ is given by (A.7) or (A.8). The optional argument `shape` defines, which sort of profile (`gaussian`, `lorentzian`, `sech2`) is to be fitted. Default is `gaussian`. The output argument `res` is the vector of residuals from the fit.

If the above method does not yield satisfactory results, one can try to calculate $P(x) = \frac{\mathrm{d}I_{rec}}{\mathrm{d}x}$ directly. Results tend to be noisy though due to the numerical differentiation.

A.3.1 Pump Spot Size versus Fluorescent Spot Size

A convenient method to determine pump spot dimensions might be to image the fluorescence of an organic film excited by the pump light. It has been evaluated if this method is viable. For this purpose, a spin coated film of truxene T3 on a glass substrate was partially covered by a black tape whose edge was aligned parallel with a pump stripe obtained by focussing the pump light with a 40 mm cylindrical lens. The tape-edge thus functions as a knife-edge for the pump light while at the same time the fluorescence was imaged onto a CCD camera, allowing simultaneous recording of the actual pump stripe width and the apparent luminescent area. Due to the thickness of the tape and the low

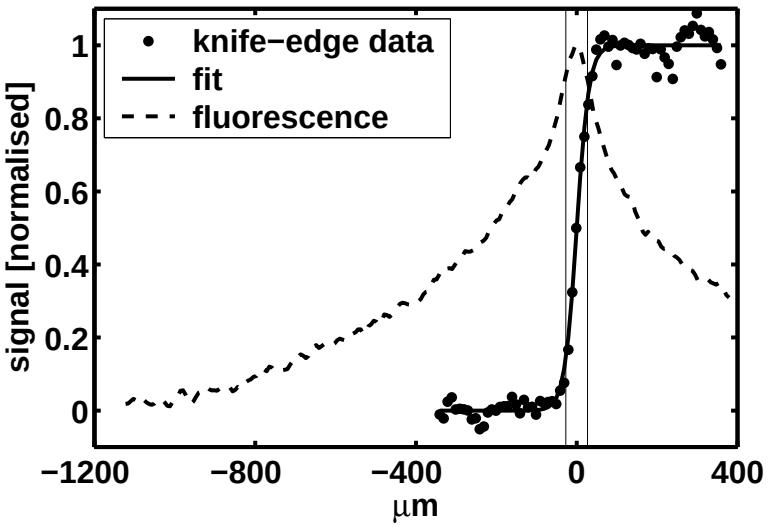

FIGURE A.3: Comparison of knife-edge measurement and fluorescence profile of a pump stripe obtained by focussing the pump light with a 40 mm cylindrical lens onto a film of T3 on glass. The FWHM of 54 μm found by fitting a sech^2 shaped profile to the knifeedge data is indicated by vertical lines.

quality of its edge compared to a razor blade, the knife-edge data obtained this way will not be as accurate as other knife-edge measurements presented in this thesis. However, this proved to be irrelevant for the key findings. Figure A.3 shows the results. Fitting of the knife-edge data yielded an upper boundary for the pump stripe width of 54 μm. It is obvious from the figure that the apparent luminescent area is much broader (by more than a factor of 2) than the actual pump spot size. This is most likely due to scattering of in-plane waveguided PL. It has to be concluded that imaging of fluorescence is not a suitable method for determining pump spot sizes and data obtained this way should always be treated as an upper boundary.

A.4 Calibration of the Pump Laser

Chapters 3 and 4 describe optical excitation of organic samples with a frequency-tripled pulsed Nd:YAG laser. The pump pulse energy and fluence in these experiments can conveniently be calculated using the Matlab function `minilite.m`. As illustrated in figure A.4, the pulse energy E_P and its estimated error ΔE_P depend on four parameters: the waveplate angle α, the attenuator wheel angle β, the reference energy E_1 and its standard deviation ΔE_1. For given parameters, the pump energy can be calculated using the Matlab function `minilite` which is based on the calibration shown below, see section A.4.6.

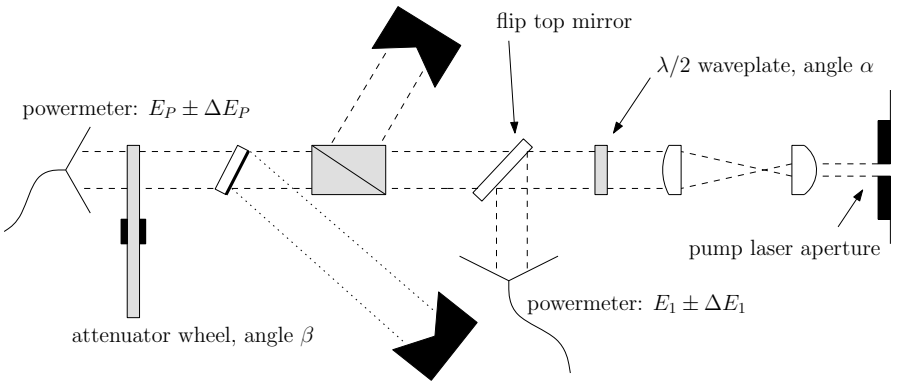

FIGURE A.4: Schematic of the pump energy control.

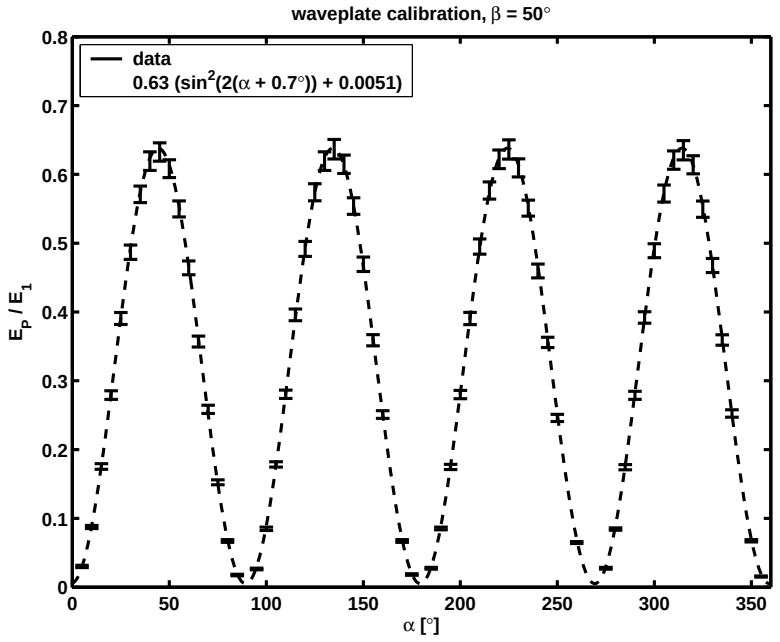

FIGURE A.5: Waveplate calibration.

A.4.1 Waveplate

The waveplate calibration data is fitted with a $\sin^2$ function:

$$\frac{E_P}{E_1} = A[\sin^2(2(\alpha + \phi)) + t_0] \tag{A.10}$$

The fit parameters A, ϕ, t_0 are assumed to only have negligible error. Values are given in table A.2.

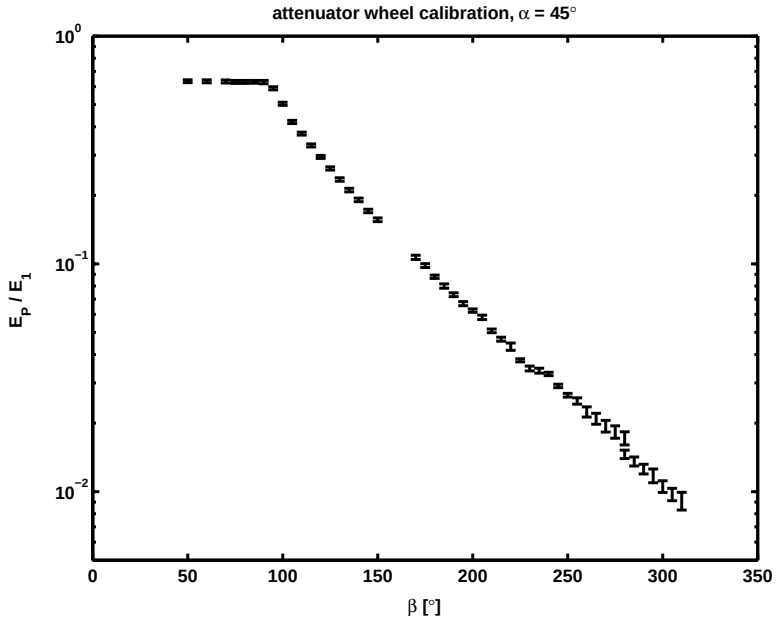

FIGURE A.6: Attenuator wheel calibration.

Parameter	A	ϕ [°]	t_0	B	C	a [1/°]	b [1/°2]	c [1/°]
Value	0.63	0.7	0.0051	2.08	0.16	0.0175	2.1×10^{-5}	0.026

TABLE A.2: Values for parameters of the pump laser calibration according to equations (A.10) and (A.11).

A.4.2 Attenuator Wheel

Figure A.6 shows the attenuator calibration data. For attenuator wheel angles $\beta > 150°$, an exponential law is assumed:

$$\begin{aligned} \frac{E_P}{E_1}(\beta > 150°) &= B \cdot e^{-a\beta} \\ \Delta\frac{E_P}{E_1}(\beta > 150°) &= C \cdot e^{b\beta^2 - c\beta} \end{aligned} \tag{A.11}$$

For $\beta < 50°$ we assume $\frac{E_P}{E_1}(\beta < 50°) \equiv \frac{E_P}{E_1}(\beta = 50°)$ and otherwise the data is linearly interpolated. Wheel positions $\beta < 50°$ or $\beta > 310°$ should be avoided due to the lack of calibration data! Parameter values are given in table A.2.

A.4.3 Consistency and Stability

Figure A.7 shows calculated and measured pulse energies for a random selection of parameters. Good agreement is observed. Also, good temporal stability of the setup has been observed. After a year of operation, all components were removed and put back together. A recalibration of the α, β settings yielded the same results as were found in

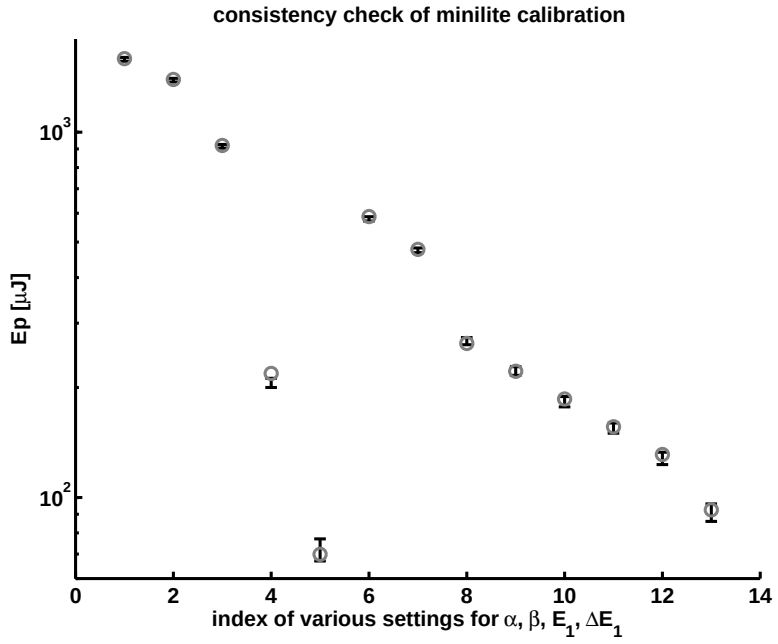

FIGURE A.7: Gray circles: pulse energies calculated from the calibration, Black: measured data

label	`lens`	type	f [mm]	T [%]
-	`mainbeam`	none	-	100
LJ1402L1-A	`cyl40mm`	cylindrical	40	87.7 ± 1.4
300 mm	`sph300mm`	spherical	300	87.2 ± 1.4
LA4725-UV	`sph75mm`	spherical	75	93.6 ± 1.3
	`c40c3_9`	cylindrical‖cylindrical	40, 3.9	51.0 ± 0.9
	`c40_c3_9vert`	cylindrical‖cylindrical	40, 3.9	48.8 ± 0.7

TABLE A.3: Pump transmission of various focussing lenses. The column `lens` specifies the string for the `lens` argument to be used with the `minilite` function, see section A.4.6.

the first place. Changes have been found in the beam dimensions which is probably due to shifts of the non-linear elements for the frequency up-conversion of the pump laser. These can be realigned and the manufacturer recommends to regularly do so. Also, some of the lenses discussed below in section A.4.4 are sensitive to even small displacements and require regular checking.

A.4.4 Transmission of Lenses

In several experiments, lenses were used to shape the pump spot. The pump transmissions of these lenses are given in table A.3.

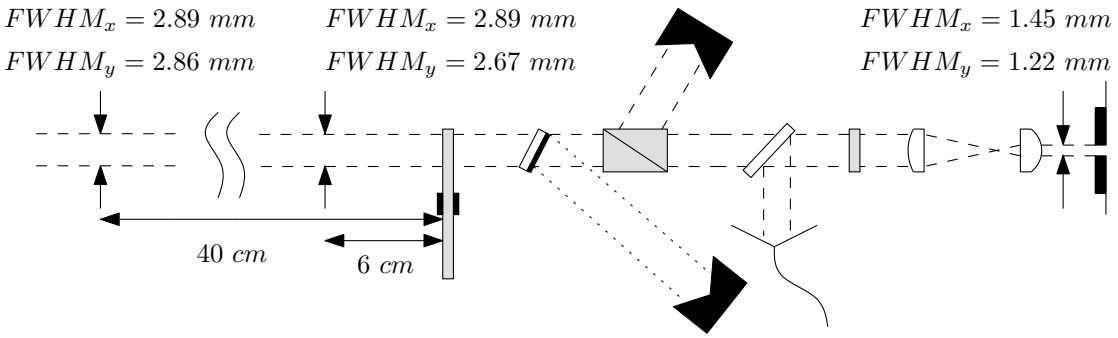

FIGURE A.8: Dimensions of the pump beam before and after the attenuation.

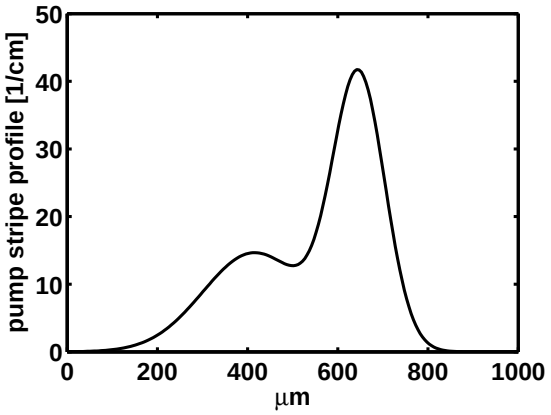

FIGURE A.9: Profile of a stripe obtained by combination of 40 mm and 3.9 mm cylindrical lenses along the short axis of the stripe, obtained by fitting knife-edge data with a double-gaussian profile.

A.4.5 Pump Spot Shape

The pump spot profile was determined with a knife-edge method, compare also section A.3. As shown in figure A.8, the diameter of the main beam (collimated after the setup shown in figure A.4) is approximately 2.9 mm FWHM, though not exactly circular. The according pump fluence is calculated by `minilite.m` using `lens = 'mainbeam'`.

Using a combination of 40 mm and 3.9 mm cylindrical lenses, a stripe-shaped beam relatively insensitive to focal position can be achieved. The 3 mm long stripe had a somewhat irregular profile along the short axis which is shown in figure A.9. Its peak intensity (compared to overall intensity) corresponds to that of a 300 μm broad stripe. If the 40 mm cylindrical lens is used on its own, the precise stripe width could not be determined due to micromachining effects of the knife-edge when close to focus but an upper boundary for the stripe width of 30 μm could be obtained.

A.4.6 Matlab File

The calculation of the pump energy from the parameters $\alpha, \beta, E_1, \Delta E_1$ can be done using the Matlab function `minilite.m`, which can be called in a number of ways depending on the setup used:

```
[Ep, deltaEp] = minilite(alpha, beta, E1, deltaE1)
```

Calculates the pulse energy and an error estimation in the same units as E_1.

```
[Ep, deltaEp] = minilite(alpha, beta, E1, deltaE1, lens)
```

Calculates the pulse energy taking into account the transmission of the lens according to table A.3. The lens is specified by the corresponding string.

```
[Ep, deltaEp, Fp, deltaFp, Wmax, deltaWmax] =
    minilite(alpha, beta, E1, deltaE1, lens)
```

Additionally calculates the fluence F_p and the peak power density W_{max} if the pump spot shape for `lens` is known. The area unit in this case is 1 cm^2.

```
[Ep, deltaEp, Fp, deltaFp, Wmax, deltaWmax] =
    minilite(alpha, beta, E1, deltaE1, lens, angle)
```

Same as above but also handles the case where the sample is tilted with respect to the beam axis (i.e. `angle`$\neq 90°$). `angle` is measured in degrees.

Parameters $\alpha, \beta, E_1, \Delta E_1$ accept both, vector and scalar input. Mixing scalar and vector input is allowed but vectors have to have the same size.

A.5 Single and Double Exponential Decays

In chapter 3 streak camera measurements of photoluminescence are presented, showing the wavelength-resolved decay of the fluorescence. The data can either be fitted with single or double exponential decay curves as described below. For clarity, a summary of the notation is provided in table A.4. Two Matlab functions, `singleexpfit.m` and `doubleexpfit.m` were written for this task.

Variable	Description	Function of
	Experimental variables	
t	time	-
λ	wavelength	-
I	detector signal, background not subtracted	t, λ
$I_{bg,exp}$	measured background	t, λ
$\langle I \rangle_\lambda$	wavelength averaged detector signal	t
$\langle I \rangle_t$	time averaged detector signal	λ
$\Delta\langle I_{bg,exp} \rangle_\lambda$	standard deviation of the wavelength averaged background	-
	Numerical variables	
I_{bg}	fitted background	λ
A	single exponential amplitude	λ
τ	single exponential lifetime	λ
A_1	amplitude 1	λ
τ_1	lifetime 1	-
A_2	amplitude 2	λ
τ_2	lifetime 2	-

TABLE A.4: Overview of the variables used for single and double exponential decay fitting.

A.5.1 Single Exponential Fit

The fitting equation is:

$$I(t) = A \cdot \exp\left(-t/\tau\right) + I_{bg} \tag{A.12}$$

where I is the detected intensity at time t. The fitting parameters are the amplitude A, the $1/e$-lifetime τ and the background level I_{bg}. Ideally, after subtraction of the dark frame we would expect $I_{bg} \equiv 0$ but in some cases this was not exactly true (apparent in plots on a logarithmic scale). Equation (A.12) is fitted individually for each wavelength resulting in vectors $A(\lambda), \tau(\lambda), I_{bg}(\lambda)$ where λ is the wavelength vector. A and I_{bg} are treated as linear parameters and solved for by linear regression on the raw detector signal (background not subtracted) while the lifetime τ is optimised for least squares using the `fminsearch` function from Matlab.

The time range for the fit is selected manually based a plot of the detector signal averaged over all wavelengths.

A.5.2 Double Exponential Fit

The fitting equation is:

$$I(t) = A_1 \cdot \exp\left(-t/\tau_1\right) + A_2 \cdot \exp\left(-t/\tau_2\right) + I_{bg} \tag{A.13}$$

with fitting parameters $A_1, A_2, \tau_1, \tau_2, I_{bg}$. In order to reduce noise effects, not all of them are considered to be wavelength dependent. The lifetimes τ_1, τ_2 are assumed to be the same for all wavelengths, $\tau_1(\lambda) \equiv \tau_1, \tau_2(\lambda) \equiv \tau_2$. The fit thus results in two scalars τ_1, τ_2 and three vectors $A_1(\lambda), A_2(\lambda), I_{bg}(\lambda)$. Again, $A_1(\lambda), A_2(\lambda), I_{bg}(\lambda)$ are found by linear regression and τ_1, τ_2 by optimisation using `fminsearch`. However, the exact procedure is a bit more complicated than in the single exponential case:

1. First, the time range for the fit is selected manually based a plot of the detector signal averaged over all wavelengths, $\langle I \rangle_\lambda$.
2. $\langle I \rangle_\lambda$ is fitted under the assumption of a single exponential decay, i.e. $A_2 \equiv 0, \tau_2 \equiv \infty$
3. If the mean deviation of this single exponential fit from the data is smaller than $3\times$ the standard deviation of the (wavelength-averaged) experimental background $\Delta\langle I_{bg,exp} \rangle_\lambda$, then a single exponential decay is assumed to be accurate, $A_1(\lambda)$ and $I_{bg}(\lambda)$ are determined for each wavelength and the fit is finished.
4. Otherwise, equation (A.13) is fitted to $\langle I \rangle_\lambda$ with non-zero A_2, thus determining two lifetimes τ_1, τ_2.
5. Finally, for each wavelength $A_1(\lambda), A_2(\lambda), I_{bg}(\lambda)$ are calculated.

A.6 Emission Pattern Evaluation

During this work, a photo-goniometer was used to measure the emission patterns of LEDs within a plane in which the goniometer arm moves. Section 6.2.2.1 explains how this data can be used for absolute power measurements under the assumption of symmetrical emission. Two Matlab functions are available to facilitate this work. The first is used for normalisation:

```
pattern = normalised_pattern(angle, signal)
```

Normalises the recorded emission pattern such that (compare equation (6.3)):

$$\int_{-\pi/2}^{\pi/2} \mathrm{d}\theta \, |\sin(\theta)| \cdot I(\theta) = 1$$

The emission pattern plots in chapter 6 are normalised this way.

The second function calculates the calibration factor for absolute power measurements according to equation (6.3):

```
calibration_factor =
    get_calibration_factor(angle, signal, detector_diameter,
                           detector_distance)
```

Both functions require the angle to be specified in radians.

Appendix B

Details of the Ray Tracing Model

This appendix outlines the computational details of the ray tracing model that was used in section 6.1.2 to estimate the available pump spot size for OSL pumping at the sapphire surface of micro-LED arrays. The model was written in C++. Section B.1 simply lists the various C++ classes, section B.2 explains how they are used and the rest of this appendix summarises technical details.

B.1 Class Hierarchy

The class hierarchy is depicted in figure B.1. The basic classes `ray`, `triangle`, `surfaces`, `source`, `target` and `emission_profile` are each declared in the header file of the same name (i.e. `ray.h` etc.). Derived classes are declared in the same `.h` file as their parent class but their methods are implemented in individual `.cpp` files (i.e. `metalmirror_triangle.cpp` etc.). There are two header files that are not associated with classes: `globalsettings.h` and `metalmirror.h`. The former contains some global variables that are initialised in the main function, the latter declares the function

```
void metalmirror(double *RTE,
                 double *rTE,
                 double *RTM,
                 double *rTM,
                 double *phiTE,
                 double *phiTM,
                 double costhetai,
                 double n_diel,
                 std::complex<double> n_met);
```

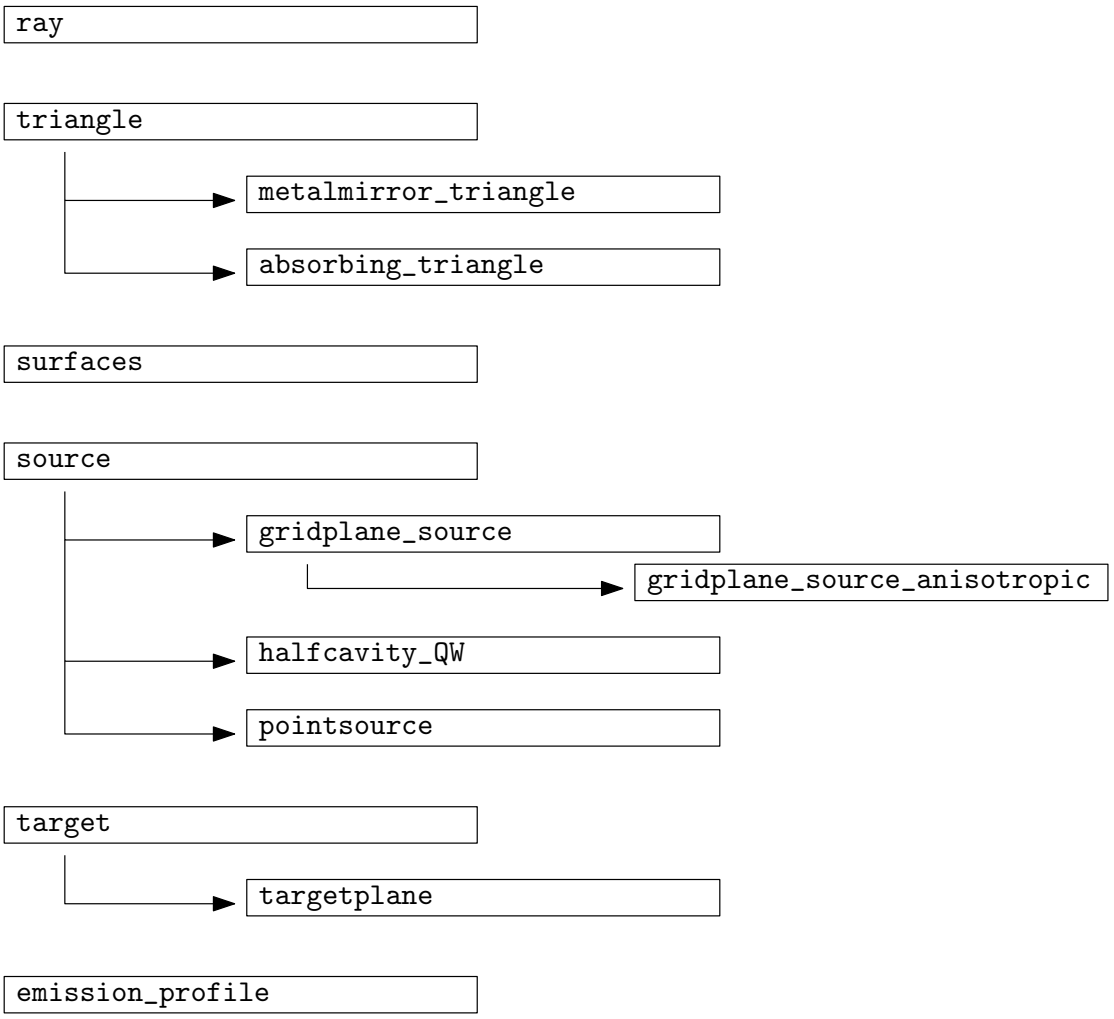

FIGURE B.1: Schematic overview of the C++ classes used in the simulation

which is implemented in `metalmirror.cpp` and calculates complex reflection coefficients. It has been defined outside class bodies because at some point it was used by completely different classes (though I think currently there is only one of them, `metalmirror_triangle`, left).

The class `surfaces` contains and manages objects of types `triangle` and `target`. It is responsible for the propagation and detection of rays coming from the sources. The function that does both of these tasks is:

```
struct raylist * surfaces::propagate_ray(ray incident);
```

The return argument is a dynamic list containing all (reflected and refracted) rays that leave the device:

```
struct raylist{
```

```
        ray element;
        struct raylist *next;
};
```

This list is used for the calculation of the extraction efficiency (maybe a meaningless number, depending on how the program is used) and as input for the class `emission_profile` that records the angular distribution of these outgoing rays by the function:

```
void emission_profile::register_ray(ray incident);
```

B.2 Program flow and Monte Carlo iteration

The program works in three steps:

1. Read in definition files, create sources, surfaces and targets
2. Do the Monte Carlo iteration (actually, this step is interrupted after some iterations to allow estimation of the computation time needed and then resumed)
3. Store the target recordings and the recorded emission profile to the output files

The Monte Carlo iteration works as follows:

1. Create a random ray `source::fire_an_emitter()`
2. propagate this ray `surfaces::propagate_ray(ray)`
3. record emitted rays, e.g. `emission_profile::register_ray(ray)`
4. Create next random ray ...

B.3 Rays

Rays are characterised by the following parameters:

- The origin $\vec{r}_0$
- The direction

$$\vec{e} = \begin{pmatrix} \sin(\theta)\cos(\phi) \\ \sin(\theta)\sin(\phi) \\ \cos(\theta) \end{pmatrix}$$

- The (linear) polarisation $\vec{p}$, the class `ray` is programmed such that $\vec{p} \perp \vec{e}$ is always guaranteed
- The "number of lifes". This is a positive integer number. If it is 0, then the ray will be ignored by targets and not further propagated. On each reflection, one "life" will be subtracted.

B.4 Surfaces

B.4.1 Plane Parametrisation

Any plane is defined by three points, $\vec{P}_1, \vec{P}_2, \vec{P}_3 \in$ plane that are not colinear. This comes in handy because much of the program is based on triangles in which case $\vec{P}_1, \vec{P}_2, \vec{P}_3$ are just the corner points. For convenience, we define two in-plane base vectors $\vec{e}_1 := \vec{P}_2 - \vec{P}_1$ and $\vec{e}_2 := \vec{P}_3 - \vec{P}_1$. The function `planeparametrization` that is declared in `planeparam.h` and implemented in `planeparam.cpp` takes $\vec{P}_1, \vec{e}_1, \vec{e}_2$ as input and calculates the plane parametrisations presented in this section.

Additionally, planes can be assigned to a layer, which is a positive integer number. If the assigned layer is 0, then the plane (or the triangle within the plane) will be probed at any step of the ray propagation. If otherwise the layer is $l > 0$ then the plane will only be probed if the current ray emerges from a plane (or source) of layer $0, l-1, l$ or $l+1$. This is to save computation time in layered structures where this simple integer comparison can save a couple of flops per triangle per ray. Highly complex features still take long computation times and more sophisticated algorithms (by smartly tiling space) than the one implemented here may have to be used.

B.4.1.1 Hesse Form

One very useful plane parametrisation is the Hesse normal form. For each point $\vec{r} \in$ plane an equation of the following form is fulfilled:

$$\vec{n} \cdot \vec{r} = c \tag{B.1}$$

The normal vector is proportional to the vector product of the in-plane base vectors:

$$\vec{n} \propto \vec{e}_1 \wedge \vec{e}_2$$

We normalise $\vec{n}$, though there is still an ambiguity in the definition of $\vec{n}$: both, $\vec{n}$ and $-\vec{n}$ are suitable for the plane parametrisation. In class `triangle` we choose the direction of

$\vec{n}$ such that it points towards the half space with refractive index n_2. The offset c can now easily be calculated:

$$c = \vec{n} \cdot \vec{P}_1$$

B.4.1.2 In-plane Coordinates

For various purposes it is useful to express a point $\vec{x} \in$ plane by coordinates with respect to the in-plane base vectors:

$$\vec{r} =: \vec{P}_1 + \alpha\vec{e}_1 + \beta\vec{e}_2 \tag{B.2}$$

For given $\vec{r}$, the coordinates α, β shall be calculated in a linear fashion:

$$\alpha =: a_0 + \vec{a} \cdot \vec{r} \tag{B.3}$$

$$\beta =: b_0 + \vec{b} \cdot \vec{r} \tag{B.4}$$

The parameters $a_0, \vec{a}, b_0, \vec{b}$ are obtained by linear regression of the overdetermined equation system:

$$\begin{pmatrix} e_{1,x} & e_{2,y} \\ e_{1,y} & e_{2,y} \\ e_{1,z} & e_{2,y} \end{pmatrix} \begin{pmatrix} \alpha \\ \beta \end{pmatrix} = \begin{pmatrix} r_x - P_{1,x} \\ r_y - P_{1,y} \\ r_z - P_{1,z} \end{pmatrix}$$

The regression matrix M is:

$$\begin{aligned} M &= \begin{pmatrix} M_1 & M_2 \\ M_3 & M_4 \end{pmatrix} \\ M_1 &= \vec{e}_1^2 \\ M_2 = M_3 &= \vec{e}_1 \cdot \vec{e}_2 \\ M_4 &= \vec{e}_2^2 \\ \det(M) &= M_1 M_4 - M_2^2 \end{aligned}$$

For optimal numerical condition we distinguish three cases, looking out for the largest of the matrix elements of M:

Case 1, $|M_1| > |M_2|, |M_4|$**:**

$$\begin{aligned} a_0 &= \frac{M_2}{\det(M)}\vec{e}_2 \cdot \vec{P}_1 - \frac{1}{M_1}\left(1 + \frac{M_2^2}{\det(M)}\right)\vec{e}_2 \cdot \vec{P}_1 \\ \vec{a} &= \frac{1}{M_1}\left(1 + \frac{M_2^2}{\det(M)}\right)\vec{e}_1 - \frac{M_2}{\det(M)}\vec{e}_2 \\ b_0 &= \frac{M_2}{\det(M)}\vec{e}_1 \cdot \vec{P}_1 - \frac{M_1}{\det(M)}\vec{e}_2 \cdot \vec{P}_1 \\ \vec{b} &= \frac{M_1}{\det(M)}\vec{e}_2 - \frac{M_2}{\det(M)}\vec{e}_2 \end{aligned}$$

Case 2, $|M_4| > |M_1|, |M_2|$**:**

$$\begin{aligned} a_0 &= \frac{M_2}{\det(M)}\vec{e}_2 \cdot \vec{P}_1 - \frac{M_4}{\det(M)}\vec{e}_1 \cdot \vec{P}_1 \\ \vec{a} &= \frac{M_4}{\det(M)}\vec{e}_1 - \frac{M_2}{\det(M)}\vec{e}_2 \\ b_0 &= \frac{M_2}{\det(M)}\vec{e}_1 \cdot \vec{P}_1 - \frac{1}{M_4}\left(1 + \frac{M_2^2}{\det(M)}\right)\vec{e}_2 \cdot \vec{P}_1 \\ \vec{b} &= \frac{1}{M_4}\left(1 + \frac{M_2^2}{\det(M)}\right)\vec{e}_2 - \frac{M_2}{\det(M)}\vec{e}_1 \end{aligned}$$

Case 3, $|M_2| \geq |M_1|, |M_4|$**:**

$$\begin{aligned} a_0 &= \frac{M_1 M_4}{M_2 \det(M)}\vec{e}_1 \cdot \vec{P}_1 - \left(\frac{1}{M_2} + \frac{M_4}{\det(M)}\right)\vec{e}_2 \cdot \vec{P}_1 \\ \vec{a} &= \left(\frac{1}{M_2} + \frac{M_4}{\det(M)}\right)\vec{e}_2 - \frac{M_1 M_4}{M_2 \det(M)}\vec{e}_1 \\ b_0 &= \frac{M_2}{\det(M)}\vec{e}_1 \cdot \vec{P}_1 - \frac{M_1}{\det(M)}\vec{e}_2 \cdot \vec{P}_1 \\ \vec{b} &= \frac{M_1}{\det(M)}\vec{e}_2 - \frac{M_2}{\det(M)}\vec{e}_1 \end{aligned}$$

B.4.1.3 Incident Ray

If a ray with direction θ_i, ϕ_i (in spherical coordinates) and origin $\vec{r}_0$ is given, the first thing to do is to calculate the distance r that the ray has to travel until it hits the surface. The direction vector of the incident ray is:

$$\vec{e}_i = \begin{pmatrix} \sin(\theta_i)\cos(\phi_i) \\ \sin(\theta_i)\sin(\phi_i) \\ \cos(\theta_i) \end{pmatrix}$$

Then we can calculate r as:

$$r = \frac{c - \vec{n} \cdot \vec{r}_0}{\vec{n} \cdot \vec{e}_i} \tag{B.5}$$

(Note that if $\vec{e}_i \cdot \vec{n} = 0$ then the ray travels parallel to the surface and never hits it)
This calculation is done by the functions `triangle::rayhitstriangle` and `targetplane::tickle`. If $r < 0$ is found, then the ray travels away from the surface and never hits it. The point where the surface is hit is:

$$\vec{r} = \vec{r}_0 + r\vec{e}_i \tag{B.6}$$

The in-plane coordinates α, β of the point of incidence are then calculated by equations B.3 and B.4.
The function `triangle::rayhitstriangle` probes if the conditions

$$\begin{aligned} 0 \leq \quad & \alpha \quad & \leq 1 \\ 0 \leq \quad & \beta \quad & \leq 1 \\ 0 \leq \quad & \alpha + \beta \quad & \leq 1 \end{aligned}$$

are fulfilled. If this is not the case then the triangle is missed and a negative value for r is returned.

B.4.2 Fresnel Diffraction

This section describes the fresnel diffraction on triangles as implemented in the function `triangle::fresnel`. Given is an incident ray with direction $\vec{e}_i$, (linear) polarisation $\vec{p}$ and intensity A_i. This ray hits a surface parametrised as described above in section B.4.1. The refractive index of the incident half space shall be n_i and n_t that of the other half space. We conveniently redefine the surface normal $\vec{n}$ such that it points into the half space with refractive index n_t. Our task is now to calculate the reflected TE and TM rays, $A_{r,TE}, \vec{e}_{r,TE}, \vec{p}_{r,TE}$ and $A_{r,TM}, \vec{e}_{r,TM}, \vec{p}_{r,TM}$, and also the transmitted rays, $A_{t,TE}, \vec{e}_{t,TE}, \vec{p}_{t,TE}$ and $A_{t,TM}, \vec{e}_{t,TM}, \vec{p}_{t,TM}$.

The intensities are calculated from the transmission and reflection coefficients obtained by Fresnel equations:

$$
\begin{aligned}
r_{TE} &= \frac{n_i \cos(\vartheta_i) - n_t \cos(\vartheta_t)}{n_i \cos(\vartheta_i) + n_t \cos(\vartheta_t)} && \text{(B.7)}\\
r_{TM} &= \frac{n_i \cos(\vartheta_t) - n_t \cos(\vartheta_i)}{n_i \cos(\vartheta_t) + n_t \cos(\vartheta_i)} && \text{(B.8)}\\
R_{TE} &= |r_{TE}|^2 && \text{(B.9)}\\
R_{TM} &= |r_{TM}|^2 && \text{(B.10)}\\
T_{TE} &= 1 - R_{TE}\\
T_{TM} &= 1 - R_{TM}\\
A_{r,TE} &= R_{TE} A_{i,TE}\\
A_{r,TM} &= R_{TM} A_{i,TM}\\
A_{t,TE} &= T_{TE} A_{i,TE}\\
A_{t,TM} &= T_{TM} A_{i,TM}\\
\cos(\vartheta_t) &= \sqrt{1 - \sin^2(\vartheta_t)}\\
\sin(\vartheta_t) &= \frac{n_i}{n_t} \sin(\vartheta_i)\\
\sin(\vartheta_i) &= \sqrt{1 - \cos^2(\vartheta_i)}\\
\cos(\vartheta_i) &= \vec{n} \cdot \vec{e}_i
\end{aligned}
$$

B.4.2.1 Incident Ray Polarisation Components

The unit vector in TE direction is:

$$\vec{p}_{i,TE} = \frac{\vec{n} \wedge \vec{e}_i}{|\vec{n} \wedge \vec{e}_i|} \tag{B.11}$$

If $\vec{n} \parallel \vec{e}_i$, we can choose $\vec{p}_{i,TE} := \vec{p}_i$. If $\vec{p}_{i,TE} \cdot \vec{p}_i < 0$ it is convenient to flip the direction of the TE vector $\vec{p}_{i,TE} \rightarrow -\vec{p}_{i,TE}$. The TM vector can then be determined by:

$$\vec{p}_{i,TM} \propto \vec{p}_i - (\vec{p}_{i,TE} \cdot \vec{p}_i)\vec{p}_{i,TE} \tag{B.12}$$

If the incident beam is purely TE polarised, we can conveniently choose $\vec{p}_{i,TM} = \vec{0}$ and conversely, for purely TM polarised light $\vec{p}_{i,TE} = \vec{0}$. The intensities of the polarisation components are:

$$
\begin{aligned}
A_{i,TE} &= (\vec{p}_{i,TE} \cdot \vec{p}_i) A_i\\
A_{i,TM} &= (\vec{p}_{i,TM} \cdot \vec{p}_i) A_i
\end{aligned}
$$

B.4.2.2 Reflected Ray Direction

The reflected ray direction is simply the normal component of the incident direction flipped:

$$\vec{e}_r = \vec{e}_i - 2(\vec{n} \cdot \vec{e}_i)\vec{n} \tag{B.13}$$

B.4.2.3 Reflected Ray Polarisation

The TE vector does not change upon reflection:

$$\vec{p}_{r,TE} = \vec{p}_{i,TE} \tag{B.14}$$

The in-plane component of the TM vector however flips:

$$\vec{p}_{r,TM} = 2(\vec{n} \cdot \vec{p}_{t,TM})\vec{n} - \vec{p}_{i,TM} \tag{B.15}$$

B.4.2.4 Transmitted Ray Direction

Given, at this stage, are incident ray direction $\vec{e}_i$, refractive indices n_i, n_t and a surface normal vector $\vec{n}$ pointing towards the half space with refractive index n_t. Our goal now is to calculate the transmitted ray direction $\vec{e}_t$. Let us define:

$$\begin{aligned}
\vec{e}_{i,\perp} &:= (\vec{n} \cdot \vec{e}_i)\vec{n} \\
\vec{e}_{i,\parallel} &:= \vec{e}_i - \vec{e}_{i,\perp} \\
\vec{e}_{t,\perp} &:= (\vec{n} \cdot \vec{e}_t)\vec{n} \\
\vec{e}_{t,\parallel} &:= \vec{e}_t - \vec{e}_{t,\perp}
\end{aligned}$$

The out-of-plane component $\vec{e}_{t,\perp}$ can be calculated from Snell's law:

$$\begin{aligned}
\vec{e}_{t,\perp} &= \cos(\vartheta_t)\vec{n} \\
\cos(\vartheta_t) &= \sqrt{1 - \sin^2(\vartheta_t)} \\
\sin(\vartheta_t) &= \frac{n_i}{n_t}\sin(\vartheta_i) \\
\sin(\vartheta_i) &= \sqrt{1 - \cos^2(\vartheta_i)} \\
\cos(\vartheta_i) &= \vec{n} \cdot \vec{e}_i
\end{aligned} \tag{B.16}$$

From symmetry considerations we must have $\vec{e}_{t,\parallel} \propto \vec{e}_{i,\parallel}$. The correct factor can be found from normalising $\vec{e}_t$:

$$\vec{e}_{t,\parallel} = \sqrt{\frac{1 - \cos^2(\vartheta_t)}{\vec{e}_{i,\parallel}^2}}\vec{e}_{i,\parallel} \tag{B.17}$$

In the end we have:

$$\vec{e}_t = \vec{e}_{t,\parallel} + \vec{e}_{t,\perp}$$

B.4.2.5 Transmitted Ray Polarisation

The TE vector does not change upon transmission:

$$\vec{p}_{t,TE} = \vec{p}_{i,TE} \tag{B.18}$$

The TM direction can now be calculated from the TE direction and ray direction:

$$\vec{p}_{t,TM} \propto \vec{p}_{t,TM} \wedge \vec{e}_t \tag{B.19}$$

B.4.3 Metal Mirrors

If a surface is covered by a metal, we assume that the transmitted ray can be completely neglected (`metalmirror_triangle::fresnel` calls `ray::kill` for the transmitted rays). The reflection coefficients can still be calculated by equations (B.7, B.8, B.9, B.10), but the complex refractive index n_{metal} (in place of n_t) yields complex values:

$$\begin{aligned} r_{TE} &= \rho_{TE} \exp(i\Phi_{TE}) \\ r_{TM} &= \rho_{TM} \exp(i\Phi_{TM}) \end{aligned}$$

As a result, reflected light may be elliptically or circularly polarised. We can safely ignore this for the ray tracing. The complex phase is important though for interference effects such as the emission pattern change of an emitter close to the metal surface. Calculation of complex reflection coefficients is done by the function `metalmirror` which is declared in `metalmirror.h` and implemented in `metalmirror.cpp`.

B.4.4 Target Planes

A useful tool for analysis are CCD-like detector arrays, just that in our simulation we can let the rays pass through. We define a plane by origin $\vec{P}_1$ and two in-plane base vectors $\vec{e}_1, \vec{e}_2$. The array is defined by two integer numbers, n_1, n_2, that give the number of rows/columns in $\vec{e}_1/\vec{e}_2$-direction (starting from $\vec{P}_1$). If a ray hits the plane, we calculate the coordinates α, β of the hitting point as discussed above (equations (B.2, B.3, B.4))

and convert them into indices:

$$\begin{aligned} i &= \lceil \alpha \rceil \\ j &= \lceil \beta \rceil \end{aligned}$$

If $1 \leq i \leq n_1, 1 \leq j \leq n_2$ then the corresponding pixel count gets increased by the rays amplitude.

B.5 Sources

The base class defines what sources will do:

```
class source{
public:
        virtual ray fire_an_emitter() = 0;
};
```

The function `fire_an_emitter` returns a linearly polarised ray of intensity 1 that starts at a random position, points in a random direction and has random polarisation direction. The derived classes of `source` define how random these parameters really are, e.g. the starting position is chosen randomly only within a certain region of space or a ray is more likely to point into some direction than into some other.

B.6 Compilation

The C++ code comes with a Makefile that is designed for usage with GNU make and GNU C compiler. Simply type `make` (possibly preceded by a `make clean`) in a Unix shell (or Cygwin under Windows). The code is mostly ANSI C++ with one exception: the functions to read in files make use of the GNU library function `getline` (which is defined in `stdlib.h` of the GNU C library) because it is much more convenient to use than the ANSI C functions for this task.

Appendix C

Optical Gain from CdSeZnS Alloy Quantum Dots

Optical gain and distributed feedback (DFB) laser operation based on CdSeZnS alloy colloidal quantum dots (CQDs) has been achieved with laser wavelengths in the regime 625–640 nm. These results were obtained during a three-month intership of the author at the Luminous! Centre for Lighting and Displays, Nanyang Technological University (NTU). This collaborative work aims to combine the expertise of Luminous! in CQD synthesis with the experience of the Institute of Photonics (IOP), University of Strathclyde, on optical gain and laser action using solution-processible gain media. Previous work by the IOP [1, 2] was briefly presented in sections 3.2.4 and 4.3.

C.1 Experimental Methods

C.1.1 Alloy-Core-Shell CQDs

The CQDs used in this work had a CdSe core, a ZnS shell and oleic acid ligands. As opposed to traditional core-shell structures however, the interface in between core and shell is not discrete but the transition from CdSe to ZnS is gradual. This can be achieved by adding the precursors for both, core and shell, either simultaneously or in rapid succession into the reaction vessel. These alloy-CQDs allow simple synthesis of nanophosphors with high photoluminescence quantum yields [3].

Red (PL peak wavelength at about 630 nm) and green-yellow (540 nm) dots were available. CQDs at both wavelengths have also been supplied to the Institute of Photonics. It was attempted to access wavelengths in between based on a recipe provided in [3], however the synthesis result were red-emitting dots.

In a first experiment, CQDs were incorporated into a poly-methyl-methacrylate (PMMA) matrix, see section C.2. For the subsequent experiments, CQDs were drop-coated from solution onto various substrates. Normally, toluene was used as solvent but in some cases, hexane was used as well. With hexane, coffee-staining was reduced resulting in a better film quality. Apart form the improved film homogenity when using hexane, no difference in the behaviour of dots coated from hexane or toluene was observed.

C.1.2 Nanosecond Pulsed Excitation

The CQD samples were photo-pumped at 532 nm with 1 ns pulses at 60 Hz repetition rate. The pump laser delivered a pulse nergy of 100 μJ and pulse energy could be controlled with an attenuator wheel. An energy meter was used to characterise the pump pulse energy as a function of the attenuator wheel angle.

For most measurements (except those described in section C.1.2.3), the beam was - for practical purposes - redirected via several mirrors and lenses. In addition to the inherent losses of these optical elements there were also losses due to aperturing effects owing to the poor beam quality of the pump laser. In each case, an estimation of these losses was made, based on measurements with the energy meter, and pump energy values in this document take account of these effects.

C.1.2.1 Micro-Spot

Some experiments used a micro-photoluminescence (micro-PL) setup where the emission from the sample is collected by a microscope objective and coupled into a CCD-Spectrometer with 0.05 nm resolution. At the same time, the microscope objective can be used to take micrographs of the excited area. This setup was used before for the study of dye-doped polymer whispering gallery (WGM) mode lasers [4]. The pump spot was elliptical and fluences quoted here assume a pump spot size of 500×800 μm^2. Due to the above mentioned losses upon redirection of the pump beam, only about 4 % of the initial pump light reach the sample. Therefore, a maximum pump fluence of 1.25 mJ/cm^2 could be delivered.

C.1.2.2 Stripe-Excitation

Optical gain in films is often assessed by stripe-excitation, collecting the edge-emission from the stripe. The exact stripe dimensions have not been measured but probably

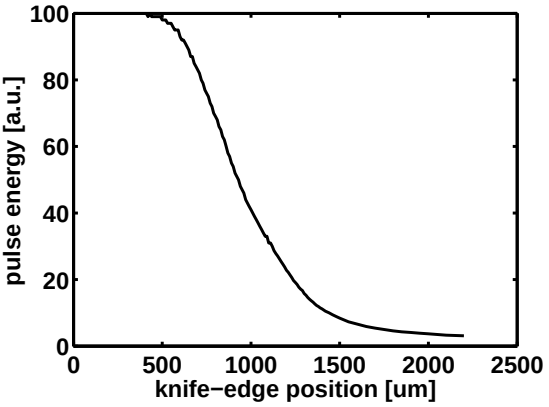

FIGURE C.1: Knife-edge measurement across the pump beam.

not larger than 10×0.3 mm. Edge emission was collected and focussed into a CCD-spectrometer (0.05 nm resolution) by two lenses. Due to the losses upon redirection of the beam, an estimated 57 % of the initial pump light reach the sample.

C.1.2.3 Unfocussed Beam

DFB laser operation as described in section C.4 was not achieved in the above formats, but the sample was placed close (ca 10 cm) to the aperture of the pump laser. In this case portable fibre spectrometers (Ocean Optics USB 2000 and USB 4000) were used to collect the surface emission from the samples. The beam diameter was measured with a knife-edge method. The result shown in figure C.1 yields a pump spot diameter of 600 μm. It should be noted that due to the poor beam quality the curve does not fit well when assuming a Gaussian beam profile.

C.1.3 Femtosecond Excitation

As alternative pump source, a wavelength-tunable system delivering 100 fs pulses at a repetition rate of 1 kHz. Two wavelength-settings were used, one for 450 nm center wavelength and one at 490 nm. The 450 nm setting had an intense pump wavelength-component at 560 nm, see also figure C.9, and pulse energy was up to 2 μJ (could be attenuated with a gradient neutral density filter). At the 490 nm setting, only the fundamental pump-wavelength component was present. Pulse energy was not measured in this case because these experiments were unsuccessful with no gain being achieved below damage threshold, see section C.3.3.

A spherical lens was used to focus the pump beam. Samples were not placed at the exact position of the focus and the pump spot size is unknown (smaller than 1 mm^2). Spectra were recorded using an Ocean Optics USB 2000 spectrometer.

C.2 WGM Laser Emission from Defects in doped PMMA Film

A film of PMMA doped with red-emitting (620 nm) CdSe/ZnS gradient shell colloidal quantum dots (CQDs) at high concentration was spun onto a glass substrate. In general the film quality appeared reasonably good on visual inspection but local defects existed throughout the sample. In the following, I will refer to these defects as "bubbles" but please note that the true nature of the defects has not been confirmed yet. No signs of optical gain were found when pumping a neat area of the film. However, if the pump spot contained a bubble, laser emission was observed in several cases with characteristics consistent with those of a whispering gallery mode (WGM) laser.

The laser characteristics of two exemplary bubbles have been recorded with the micro-PL setup. Two and three laser peaks, respectively, were observed in the wavelength range 625–630 nm which is slightly red-shifted compared to the photoluminescence peak and therefore consistent with earlier observations of laser action in CdSe/ZnS CQDs. Linewidths were 0.35 nm (1 meV) which is an order of magnitude narrower than typical amplified spontaneous emission (ASE, typically 4–5 nm linewidth), strongly suggesting a cavity effect. The observed linewidths correspond to Q-factors in the range 1.7×10^3–2.1×10^3. In the power transfer functions, a laser threshold near 600 $\mu J/cm^2$ can be seen.

Micrographs of the pump region including one of the two bubbles are shown in figure C.2. A spectrum of the laser emission is shown in figure C.3. The spacing in between the two laser modes is 11.01 meV which roughly corresponds to a resonator diameter of 25 μm. The power transfer function of both peaks individually and the sum of them is plotted in figure C.4. The laser threshold is approximately 600 $\mu J/cm^2$. Close to threshold, the short-wavelength resonance is dominant but with increasing pump fluence it is overtaken by the long-wavelength resonance. A possible explanation is the red-shifted gain from biexcitons at high pump fluences. For reference, the other bubble probed (not shown in this sumary) had a laser threshold of approximately 800 $\mu J/cm^2$ and a mode spacing of 5.65 meV which roughly corresponds to a resonator diameter of 50 μm.

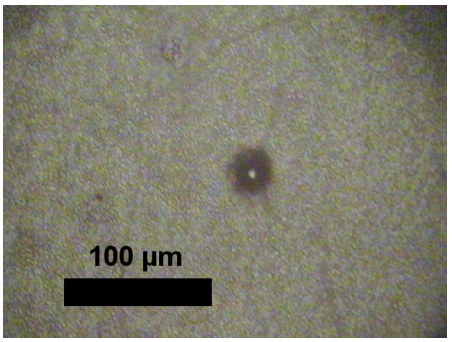

FIGURE C.2: Micrograph of a "bubble" defect in CQD-doped PMMA.

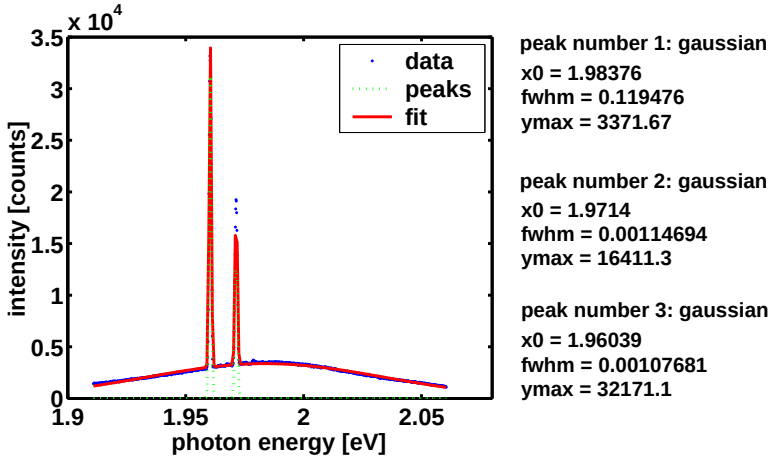

FIGURE C.3: Spectrum from the defect shown in figure C.2 under pumping at 1.25 mJ/cm^2, fitted with the peak decomposition tool described in appendix A.

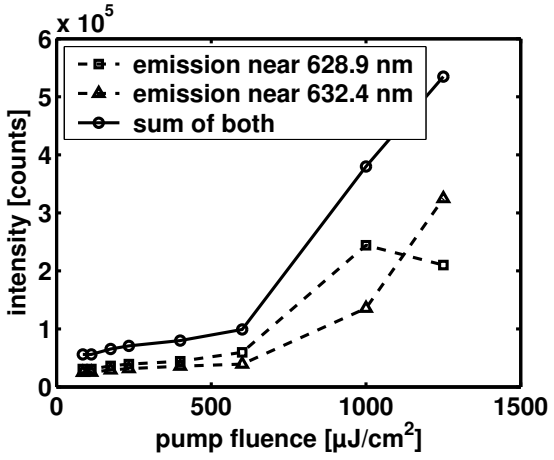

FIGURE C.4: Power transfer function of the laser emission from the defect shown in figure C.2. Compare figure C.3 for identification of the laser peaks.

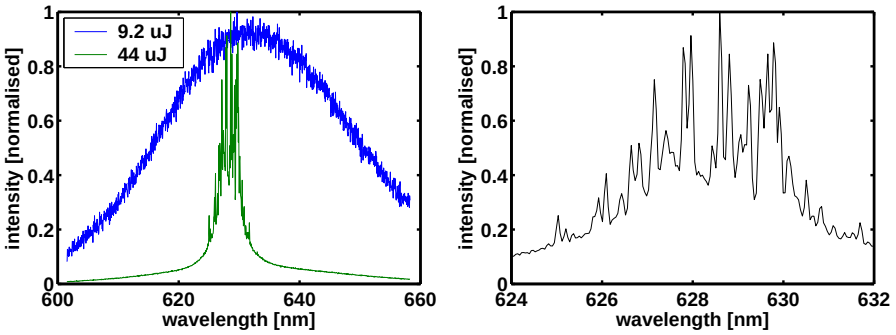

FIGURE C.5: *Left:* Spectra below and above threshold under stripe excitation. *Right:* Detail of the spectrum.

C.3 ASE/RL from Pure Red CQD Films on Glass Substrates

Optical gain from solution processible gain media is often first assessed in neat films without feedback. When pumping above threshold for optical gain, amplified spontaneous emission (ASE) can be observed. In high gain media such as CQDs, the observed emission often has characteristics of random laser action (RL) rather than plain ASE, which is an effect of the interplay in between film inhomogenities and gain saturation [5].

C.3.1 Structured Glass Substrates

Strathclyde results of random laser action in drop-cast CQD films on a glass substrate with scratched grooves [1] were successfully reproduced. The drop-coating process was repeated three times to yield a thick CQD layer and the main purpose of the grooves is to facilitate dense aggregation of dots. The samples were pumped in stripe-format with stripe aligned parallel to the scratched grooves.

Random laser action in the wavelengths region 625–640 nm could repeatedly be achieved with typical thresholds on the order of 25 μJ. Exemplary spectra and power transfer functions are shown in figures C.5 and C.6. Often, the ASE/RL appears at the same wavelength as the PL peak. It should be noted however, that the PL peak in edge emission is redshifted by about 5 nm compared to the PL peak in top emission, presumably a result of self absorption.

In conclusion, optical gain can be achieved from films of red CdSe/ZnS gradient shell CQDs. DFB lasers based on this material are therefore feasible and have been realised as described below in section C.4.

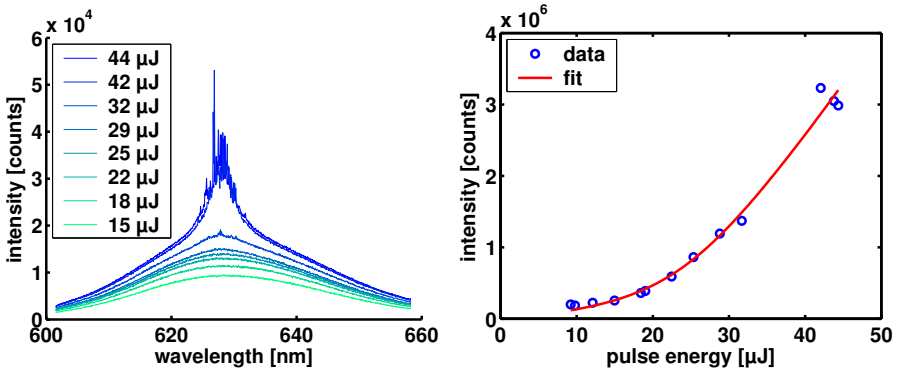

FIGURE C.6: *Left:* Evolution of the spectra in stripe excitation with increasing pump pulse energy. *Right:* Power transfer function.

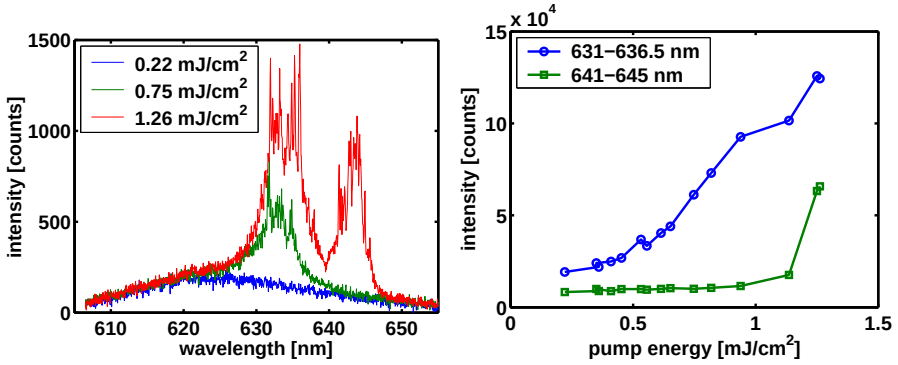

FIGURE C.7: RL spectrum and power transfer function measured in the micro-PL setup.

Some samples were also tested in the micro-PL setup. Optical gain could normally be achieved, but often only in a limited area of the sample, even when gain in stripe-excitation was obtained in many pump spots. One sample however stood out, yielding gain on large areas of the sample. At maximum pump intensity, some areas even showed two stimulated emission peaks, centered at 633 nm and 643 nm. As can be seen in figure C.7, the 643 nm peak has an about two times higher pump threshold than the 633 nm peak (1.2 and 0.6 mJ/cm^2, respectively). This may explain why the second peak was not observed on a large area - its threshold elsewhere may be too high.

C.3.2 Smooth Glass Substrates

So far, ASE/RL was observed on samples employing a structured (scratched by diamond pen) substrate to facilitate accumulation of dots. Three samples with drop coated CQD films on a smooth glass surface were prepared to see if optical gain can still be achieved in this format. The CQDs are red-emitting CdSeZnS alloy CQDs with a PL peak

	stripe-excitation (edge emission)	spot-excitation (top emission)
PL peak	630 nm	623 nm
ASE/RL sample 1	623–629 nm	–
ASE/RL sample 2	630–640 nm	626–636 nm
ASE/RL sample 3	626–631 nm	622–631 nm

TABLE C.1: Emission wavelengths of the various samples of drop coated CQD films on smooth glass.

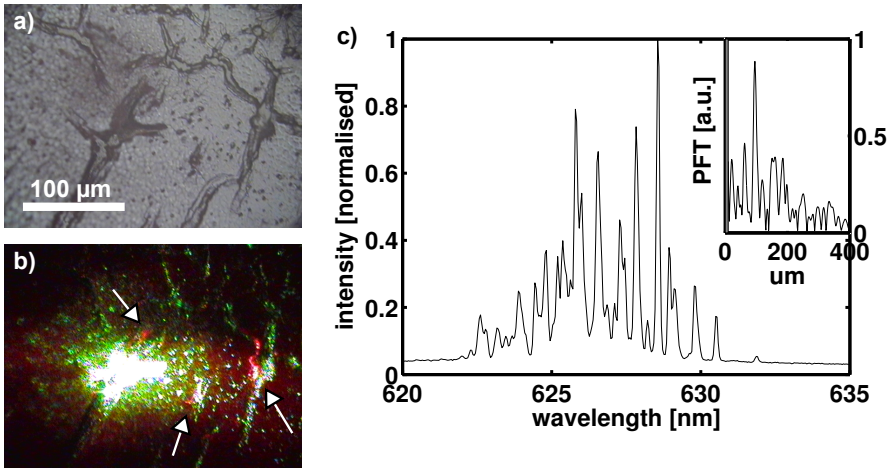

FIGURE C.8: Pump spot on sample 3. *a)* White light illumination, showing defects in the film. *b)* Pumping the same area with 532 nm light above threshold, parts of the laser mode are visible (indicated by arrows). *c)* stimulated emission spectrum corresponding to the micrograph *b)*. The inset shows part of the PFT of the spectrum (the values near 0 μm are excluded for better clarity).

wavelength of 623 nm in top emission and 630 nm in edge emission from a drop-cast film. The difference is psobably due to self absorption.

Samples were excited both in stripe excitation (edge emission detected) and in the micro-PL setup. In general, it was easier to obtain a stimulated emission signal in stripe-excitation format (sample 1 showed no signs of gain in the micro-PL setup at all). With the micro-spot, much fewer pump spots worked, often (though not exclusively) within the coffee stain rings formed during the drop casting process. On sample 3, the coffee stain area had crack-like defects, along which parts of the laser mode were actually visible in the micro-PL setup. This is shown in figure C.8. The - relative to other RL spectra - regularity of the spectrum and its power Fourier transform (PFT) and also the pronounced peak in the PFT at 100 μm suggest that in this case a closed path for coherent feedback, i.e. a random cavity may have formed.

Observed wavelength ranges for the stimulated emission observed are summarised in table C.1, indicating that optical gain can be provided from 622 nm to 640 nm.

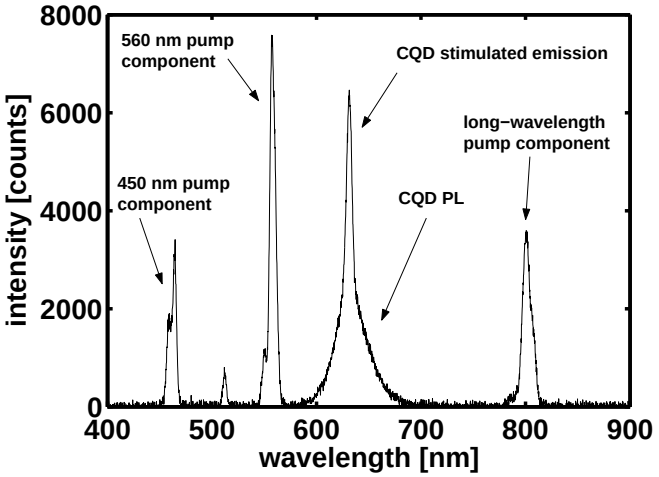

FIGURE C.9: Spectrum demonstrating optical gain from red CQDs under fs-pumping. Various wavelength components of the 450/560 nm pump can be seen.

Gain was also observed when pumping with femtosecond pulses at 450/560 nm, see figure C.9. It should be pointed out, that previous attempts by Ta Van Duong using dye-doped polymer showed no gain up to damage threshold in structures that were capable of lasing when pumped with nanosecond pulses. In this aspect, CQDs appear to behave fundamentally different compared to organic gain media.

C.3.3 Other Wavelengths

No optical gain from green-yellow CQDs was observed when pumping with the femtosecond laser at 450/560 nm and 490 nm. In the latter case, mechanical damage (ablation) by the pump laser occured before gain was reached. Also, no gain was observed with nanosecond excitation. A drop-cast film of yellow (566 nm) discrete-shell CQDs on smooth glass was examined with nano-second pump in stripe-configuration, but no laser action was observed in this case.

Previous laser reports of CQDs in the literature are primarily using red dots as well. CQD lasing at other wavelengths was reported by carefully adapting the pumping conditions – in particular the wavelength – [6] or by using dots with unusual properties, in particular single-exciton gain [7], which are typical for type-II dots.

C.4 DFB Laser Operation

Encouraged by the results in section C.3.2, red CQDs were used for fabrication of a CQD DFB laser on the basis of the gratings supplied by the IOP, University of Strathclyde.

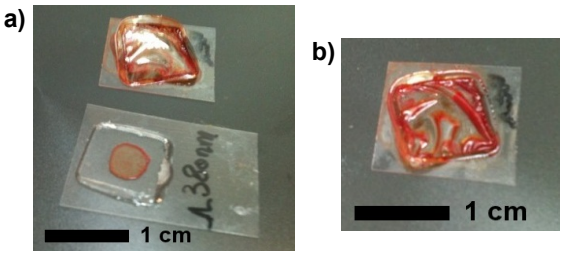

FIGURE C.10: *a)* Photographic image of grating 1 (top) and grating 2 (bottom) after drop coating of CQD solution. *b)* Another photo of grating 1.

C.4.1 Sample preparation

Two gratings ("grating 1" and "grating 2") with 380 nm period and 50 nm modulation depth in an NOA65 epoxy film were available. The epoxy film was on top of an acetate sheet that served as substrate. During the grating fabrication process, a 254 nm UV source was used for photo-curing due to technical problems with the 370 nm source. On arrival at NTU, it was noticed that some of the epoxy was slightly sticky, in particular for grating 1. Diffraction of the room light by the grating structure was visible confirming existance and quality of the grating structure.

In a first attempt, a large quantity of CQD solution (oleic acid ligands, solvent: toluene) was drop cast onto grating 1, wetting the whole epoxy area. After a few minutes, the bond in between the epoxy and the acetate broke and the solution including the CQDs moved underneath the epoxy film which almost completely detached from the acetate. In figure C.10 it can be seen how the sample looked like after the this happend.

Consequently, grating 2 was coated with a small drop so that only a small area was wetted. This device, shown also in figure C.10, yielded the laser results below in section C.4.2. After the first laser test, it was attempted to raise the CQD density by another drop-coating step. This time however the wetting area was about three times as large as in the first step and while lasing still was observed, device performance was inferior to before the second drop coating.

C.4.2 Laser pumping results

Device 2 was pumped in the micro-PL setup and in a modified stripe-setup (modified because top- rather than edge emission had to be detected) but no lasing was observed. However, when positioning the sample in the pump laser beam close to the aperture of the pump laser, a clear fan-shaped DFB laser beam - shown in figure C.11 - was seen. Possibly, the combined effects of beam divergence, poor beam quality, aperturing effects

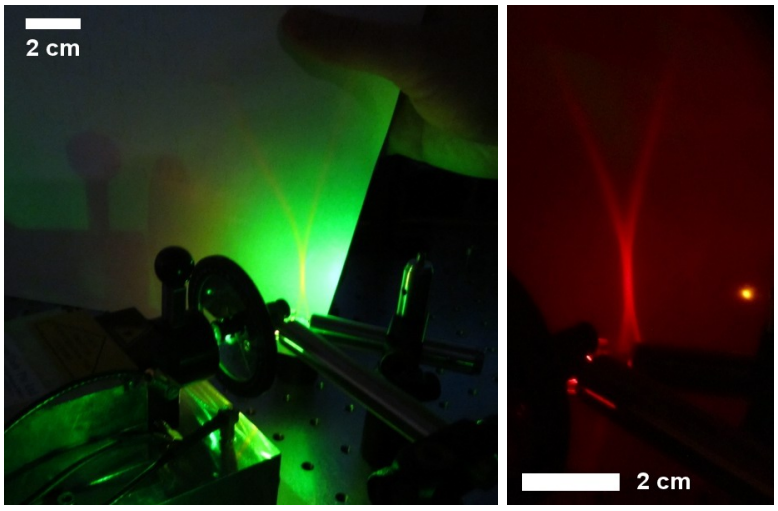

FIGURE C.11: Photographic images of the CQD DFB laser beam. The photo on the right was taken through laser safety goggles in order to eliminate green pump light, giving better clarity.

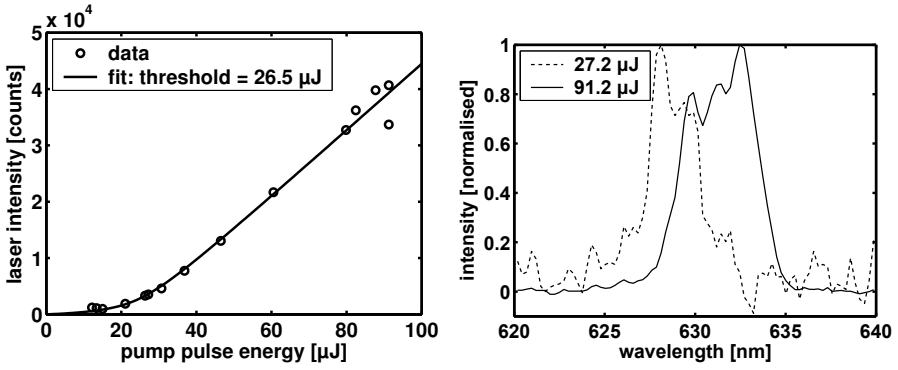

FIGURE C.12: *Left:* Power transfer function of the CQD DFB laser (see figure C.11). *Right:* CQD DFB laser spectra close to threshold and at 3.4× threshold.

and other losses at mirrors and lenses caused a too high loss in pump energy to reach threshold in the other configurations.

A fibre spectrometer was used to monitor the laser emission with the fibre tip begin placed in the center of the beam. Laser spectra and power transfer function are plotted in figure C.12. Laser emission is at 630 nm, redshifts by about 3 nm from lasing onset to 3.4× threshold and the linewidth broadens at the same time from 3 nm to 5 nm. The threshold is about 26.5 μJ corresponding to a fluence on the order of 9 mJ/cm^2). It was noticed that a large fraction (not measured) of the pump light passed through the sample without being absorbed. The bright spot in the right photo of figure C.11 is where this transmitted pump beam hits the paper screen.

C.4.3 Subsequent attempts

After the laser measurements, grating 2 was cleaned by rinsing with toluene. The sample appeared clean apart from a faint stain and the room light diffraction by the grating was visible. The grating was overcoated again two times. Both times, optical gain was observed and grating-coupled stimulated emission yielded a fan-shaped beam. However, the laser emission was not at the stop-band wavelength of the DFB and the fan appeared separated/crossed, depending on the pump spot position. This indicates, that in these cases the observed emission was ASE/RL coupled out by the grating rather than laser oscillation. It should be noted that the first device operated reliably at the stop-band wavelength for a variety of pump spots, although the film quality did not appear better in quality than the subsequent devices. This indicates that the emission of the first device was strongly influenced by the feedback from the grating.

One of the later devices was also pumped with 450/560 nm femtosecond pulses and optical gain was observed, confirming that this pumping regime is suitable.

C.4.4 Conclusions

A CQD DFB laser was achieved emitting at 630 nm based on a 380 nm second order DFB grating. The observed DFB laser emission has a broad linewidth of up to 5 nm which is probably due to variations in the film thickness (the increase in linewidth with increasing pump power may be more areas of different thickness reaching threshold). Threshold was however high, requiring the sample to be placed in close proximitiy to the pump laser. This may be caused by low dot density and therefore low pump absorption. Attempts will be made to develop a method of generating higher dot densities. It should be noted that one of the two available 380 nm gratings detached from the acetate and is possibly destroyed. It cannot be excluded that the same thing happens to grating 2. As a precaution, wetting of the actetate/epoxy boundary by CQD solution should be avoided.

C.5 Summary

In conclusion, the following results were achieved:

- Optical gain using CdSeZnS alloy CQDs was obtained at wavelengths 625–640 nm, pumping with 1 ns pulses at 532 nm
  - Threshold was 25 μJ using a stripe of dimensions <10×0.3 mm
  - Attempts at other wavelengths were not successful
  - Gain was also seen when pumping with 100 fs pulses at 450/560 nm
    - In this aspect, CQDs seem to behave differently than dyes
- A CQD-based DFB laser was successfully created
  - Threshold was 26.5 μJ, 9 mJ/cm^2
- WGM lasing from defects (possibly bubbles) in a CQD-doped PMMA film was observed
  - Threshold was bout 600 μJ/cm^2

Important tasks still to do are recording of absorption and photoluminescence spectra, ideally both in solution and film.

Future work may include the following:

- Create DFB lasers more reliably and with lower threshold
  - This work will include pumping at 355 nm (5 ns pulses) as in sections 3.2.4 and 4.3, allowing also comparison with commercial CQDs
- Access to other wavelengths
  - This may include investigations on other types of dots (e.g. type-II)
- Investigation of repeatability and controllability of the WGM lasing observed in doped PMMA films

References

[1] Yujie Chen, Johannes Herrnsdorf, Benoit Guilhabert, Yanfeng Zhang, Ian M. Watson, Erdan Gu, Nicolas Laurand, and Martin D. Dawson. Colloidal quantum dot random laser. *Opt. Express*, 19(4): 2996, 2011.

[2] Yujie Chen, Benoit Guilhabert, Johannes Herrnsdorf, Yanfeng Zhang, Allan R. Mackintosh, Richard A. Pethrick, Erdan Gu, Nicolas Laurand, and Martin D. Dawson. Flexible distributed-feedback colloidal quantum dot laser. *Appl. Phys. Lett.*, 99:241103, 2011.

[3] Wan Ki Bae, Kookheon Char, Hyuck Hur, and Seonghoon Lee. Single-Step Synthesis of Quantum Dots with Chemical Composition Gradients. *Chem. Mater.*, 20(2):531–539, 2008.

[4] Van Duong Ta, Rui Chen, and Han Dong Sun. Self-Assembled Flexible Microlasers. *Adv. Mater.*, 24:OP60–OP64, 2012.

[5] Johannes Herrnsdorf, Yujie Chen, Benoit Guilhabert, Nicolas Laurand, and Martin D. Dawson. Stripe Excitation of High Gain Media With Disorder. *IEEE J. Quantum Electron.*, 48(9):1184–1192, 2012.

[6] Ryan R. Cooney, Samuel L. Sewall, D. M. Sagar, and Patanjali Kambhampati. Gain Control in Semiconductor Quantum Dots via State-Resolved Optical Pumping. *Phys. Rev. Lett.*, 102:127404, 2009.

[7] Cuong Dang, Joonhee Lee, Craig Breen, Jonathan S. Steckel, Seth Coe-Sullivan, and Arto Nurmikko. Red, green and blue lasing enabled by single-exciton gain in colloidal quantum dot films. *Nature Nanotechnology*, 7:335–339, 2012.

List of Publications

Journals

[1] J. Herrnsdorf, B. Guilhabert, J. J. D. McKendry, Z. Gong, D. Massoubre, S. Zhang, S. Watson, A. E. Kelly, E. Gu, N. Laurand and M. D. Dawson, *Hybrid organic/GaN photonic crystal light-emitting diode*, Appl. Phys. Lett., **101**, 141122 (2012)

[2] Johannes Herrnsdorf, Yujie Chen, Benoit Guilhabert, Nicolas Laurand and Martin D. Dawson, *Stripe Excitation of High Gain Media With Disorder*, IEEE J. Quantum Electron. **48** (9), 1184 (2012)

[3] B. Guilhabert, N. Laurand, J. Herrnsdorf, Y. Chen, A. L. Kanibolotsky, C. Orofino, P. J. Skabara and M. D. Dawson, *Mechanically Flexible Organic Semiconductor Laser Array*, IEEE Photon. J. **4** (3), 684 (2012)

[4] Yujie Chen, Johannes Herrnsdorf, Benoit Guilhabert, Yanfeng Zhang, Alexander L. Kanibolotsky, Peter J. Skabara, Erdan Gu, Nicolas Laurand and Martin D. Dawson, *Modification of emission wavelength in organic random lasers based on photonic glass*, Org. Electron. **12**, 1129 (2012)

[5] Yujie Chen, Benoit Guilhabert, Johannes Herrnsdorf, Yanfeng Zhang, Allan R. Mackintosh, Richard A. Pethrick, Erdan Gu, Nicolas Laurand and Martin D. Dawson, *Flexible distributed-feedback colloidal quantum dot laser*, Appl. Phys. Lett. **99**, 241103 (2011)

[6] Yujie Chen, Johannes Herrnsdorf, Benoit Guilhabert, Yanfeng Zhang, Ian M. Watson, Erdan Gu, Nicolas Laurand and Martin D. Dawson, *Colloidal quantum dot random laser*, Opt. Express **19** (4), 2996 (2011)

[7] Yujie Chen, Johannes Herrnsdorf, Benoit Guilhabert, Alexander L. Kanibolotsky, Allan R. Mackintosh, Yue Wang, Richard A. Pethrick, Erdan Gu, Graham A. Turnbull, Peter J. Skabara, Ifor D. W. Samuel, Nicolas Laurand and Martin D. Dawson, *Laser action in a surface-structured free-standing membrane based on a π-conjugated polymer-composite*, Org. Electron. **12**, 62 (2011)

[8] J. Herrnsdorf, B. Guilhabert, Y. Chen, A. L. Kanibolotsky, A. R. Mackintosh, R. A. Pethrick, P. J. Skabara, E. Gu, N. Laurand and M. D. Dawson, *Flexible blue-emitting encapsulated organic semiconductor DFB laser*, Opt. Express **18** (25), 25535 (2010)

[9] Benoit Guilhabert, Nicolas Laurand, Johannes Herrnsdorf, Yujie Chen, Allan R. Mackintosh, Alexander L. Kanibolotsky, Erdan Gu, Peter J. Skabara, R.A. Pethrick and Martin D. Dawson, *Amplified spontaneous emission in free-standing membranes incorporating star-shaped monodisperse π-conjugated truxene oligomers*, J. Opt. **12**, 035503 (2010)

Conferences

(Presenter highlighted by bold letters)

[10] **J. J. D. McKendry**, S. Zhang, S. Watson, J. Herrnsdorf, D. Massoubre, A. Cogman, B. Guilhabert, N. Laurand, E. Gu, R. K. Henderson, A. E. Kelly and M. D. Dawson, *Micro-pixellated light-emitting diode arrays: novel sources for data transmission over POF* (invited, detailed paper in Proceedings), POF 2012

[11] **Johannes Herrnsdorf**, Benoit Guilhabert, Jonathan McKendry, Zheng Gong, David Massoubre, Yujie Chen, Shuailong Zhang, Alexander L. Kanibolotsky, Allan R. Mackintosh, Peter J. Skabara, Anthony E. Kelly, Erdan Gu, Nicolas Laurand and Martin D. Dawson, *Hybrid GaN/organic polymer photonic crystal LED* (oral), IEEE Photonics 2011

[12] B. Guilhabert, **N. Laurand**, A. Kanibolotsky, J. Herrnsdorf, Y. Chen, P.J. Skabara and M.D. Dawson, *Flexible Organic Semiconductor Laser Array* (oral), IEEE Photonics 2011

[13] Yujie Chen, Johannes Herrnsdorf, Benoit Guilhabert, Yanfeng Zhang, Allan R. Mackintosh, Richard A. Pethrick, Erdan Gu, Nicolas Laurand, and **Martin D. Dawson**, *Fabrication and Optical Characterization of a Flexible Colloidal Quantum Dot Laser* (invited, detailed paper in Proceedings), IEEE Nanotechnology 2011

[14] Yujie Chen, Johannes Herrnsdorf, Benoit Guilhabert, Yanfeng Zhang, Alex L. Kanibolotsky, Peter J. Skabara, Erdan Gu, Nicolas Laurand, and **Martin D. Dawson**, *Tunable Random Laser Action in a π-Conjugated Polymer-based Photonic Glass Gain Medium* (poster, detailed paper in Proceedings), IEEE Nanotechnology 2011

[15] **Yujie Chen**, Benoit Guilhabert, Johannes Herrnsdorf, Yanfeng Zhang, Allan R. Mackintosh, Richard A. Pethrick, Nicolas Laurand and Martin D. Dawson, *Flexible distributed feedback colloidal quantum dot laser patterned by a submicron grating structure* (oral), CLEO Europe 2011

[16] B. Guilhabert, N. Laurand, A. R. Mackintosh, **Y. Chen**, J. Herrnsdorf, A. Kanibolotsky, P.J. Skabara and M. D. Dawson, *Low threshold all-organic composite laser* (oral), CLEO Europe 2011

[17] **Yujie Chen**, Benoit Guilhabert, Johannes Herrnsdorf, Yanfeng Zhang, Ian M. Watson, Erdan Gu, Nicolas Laurand and Martin D. Dawson, *Flexible DFB colloidal quantum dot laser patterned by DVD submicron grating structure* (oral), One Day Quantum Dot Meeting 2011

[18] Johannes Herrnsdorf, Benoit Guilhabert, Alexander L. Kanibolotsky, Allan R. Mackintosh, Richard A. Pethrick, Peter J. Skabara, Nicolas Laurand, Erdan Gu and **Martin D. Dawson**, *Flexible blue-emitting DFB laser* (oral), IEEE Photonics 2010

[19] **Allan R. Mackintosh**, Peter J. Skabara, Alex Kanibolotsky, Richard A. Pethrick, Yujie Chen, Benoit Guilhabert, Erdan Gu, Nicolas Laurand, Martin Dawson, Johannes Hernsdorf, Ifor D. Samuel and Graham Turnbull, *Laser Action in a Surface-structured Free-standing Membrane Based on a pi-Conjugated Polymer-composite* (poster), MRS Fall meeting 2010

[20] **J. Herrnsdorf**, B. Guilhabert, Y. Chen, A. L. Kanibolotsky, A. R. Mackintosh, R. A. Pethrick, P. J. Skabara, E. Gu, N. Laurand, and M. D. Dawson, *DFB laser action from truxene-core chromophores in an encapsulating polymer matrix on a flexible substrate* (oral), Photon10, 2010

[21] **Y. Chen**, J. Herrnsdorf, B. Guilhabert, A. L. Kanibolotsky, Y. Zhang, E. Gu, P. J. Skabara, N. Laurand and M. D. Dawson, *Random laser action in π-conjugated polymer-based photonic glasses system* (oral), Photon10, 2010

[22] Johannes Herrnsdorf, Yujie Chen, **Nicolas Laurand**, Benoit Guilhabert, Erdan Gu and Martin D. Dawson, *Stimulated emission from colloidal quantum dots in a light-emitting polymer film* (poster), QD 2010

[23] **Y. Chen**, J. Herrnsdorf, N. Laurand, B. Guilhabert, E. Gu and M. D. Dawson, *Random lasing action in colloidal quantum dots* (poster), QD 2010

[24] **Johannes Herrnsdorf**, Yujie Chen, Nicolas Laurand, Benoit Guilhabert, Erdan Gu and Martin D. Dawson, *Stimulated emission from colloidal quantum dots in a light-emitting polymer film* (oral), One Day Quantum Dot Meeting 2010

[25] **Yujie Chen**, Johannes Herrnsdorf, Nicolas Laurand, Benoit Guilhabert, Erdan Gu, and Martin D. Dawson, *Random lasing action in colloidal quantum dots* (poster), One Day Quantum Dot Meeting 2010

[26] **B. Guilhabert**, J. Herrnsdorf, Y. Chen, N. Laurand, A. L. Kanibolotsky, P. J. Skabara, A.R. Mackintosh, R.A. Pethrick, E. Gu, I.M. Watson and M.D. Dawson, *Free-standing light-emitting organic nanocomposite membranes* (oral), IEEE Photonics 2009

[27] **Johannes Herrnsdorf**, Yujie Chen, Benoit Guilhabert, Nicolas Laurand, Erdan Gu, Alexander Kanibolotsky, Peter J. Skabara and Martin D. Dawson, *Optical gain from light-emitting nanocomposite membranes* (oral), SID Organic Electronics 2009

[28] **Yujie Chen**, Johannes Herrnsdorf, Nicolas Laurand, Benoit Guilhabert, Alexander L. Kanibolotsky, Erdan Gu, Graham Turnbull, Peter J. Skabara, Ifor. D. W. Samuel, and Martin D. Dawson, *Green-emission organic/inorganic composite as a random lasing medium* (oral), SID Organic Electronics 2009

Others

[29] B. Guilhabert, N. Laurand, J. Herrnsdorf, Yujie Chen, A. R. Mackintosh, A. L. Kanibolotsky, E. Gu, P. J. Skabara, R. A. Pethrick and M. D. Dawson, *Free-standing 'plastic-like' photonic membrane*, Euro Physics News **41** (3), 14 (2010)